



University of Kentucky
UKnowledge

University of Kentucky Doctoral Dissertations

Graduate School

2007

MOLECULAR TRANSPORT PROPERTIES THROUGH CARBON NANOTUBE MEMBRANES

Mainak Majumder
University of Kentucky, mm20@rice.edu

[Right click to open a feedback form in a new tab to let us know how this document benefits you.](#)

Recommended Citation

Majumder, Mainak, "MOLECULAR TRANSPORT PROPERTIES THROUGH CARBON NANOTUBE MEMBRANES" (2007). *University of Kentucky Doctoral Dissertations*. 557.
https://uknowledge.uky.edu/gradschool_diss/557

This Dissertation is brought to you for free and open access by the Graduate School at UKnowledge. It has been accepted for inclusion in University of Kentucky Doctoral Dissertations by an authorized administrator of UKnowledge. For more information, please contact UKnowledge@lsv.uky.edu.

ABSTRACT OF DISSERTATION

Mainak Majumder

The Graduate School
University of Kentucky

2007

MOLECULAR TRANSPORT PROPERTIES THROUGH CARBON NANOTUBE
MEMBRANES

ABSTRACT OF DISSERTATION

A dissertation submitted in partial fulfillment of the
requirements for the degree of Doctor of Philosophy in the
College of Engineering
at the University of Kentucky

By
Mainak Majumder

Lexington, Kentucky

Director: Dr. Bruce J. Hinds, William Bryan Professor of Materials Engineering

Lexington, Kentucky

2007

Copyright © Mainak Majumder 2007

ABSTRACT OF DISSERTATION

MOLECULAR TRANSPORT PROPERTIES THROUGH CARBON NANOTUBE MEMBRANES

Molecular transport through hollow cores of crystalline carbon nanotubes (CNTs) are of considerable interest from the fundamental and application point of view. This dissertation focuses on understanding molecular transport through a membrane platform consisting of open ended CNTs with ~ 7 nm core diameter and $\sim 10^{10}$ CNTs/cm² encapsulated in an inert polymer matrix.

While ionic diffusion through the membrane is close to bulk diffusion expectations, gases and liquids were respectively observed to be transported ~ 10 times faster than Knudsen diffusion and ~ 10000 - 100000 times faster than hydrodynamic flow predictions. This phenomenon has been attributed to the non-interactive and frictionless graphitic interface.

Functionalization of the CNT tips was observed to change selectivity and flux through the CNT membranes with analogy to 'gate-keeper' functionality in biological membranes. An electro-chemical diazonium grafting chemistry was utilized for enhancing the functional density on the CNT membranes. A strategy to confine the reactions at the CNT tips by a fast flowing liquid column was also designed. Characterization using electrochemical impedance spectroscopy and dye assay indicated ~ 5 - 6 times increase in functional density. Electrochemical impedance spectroscopy experiments on CNT membrane/electrode functionalized with charged macro-molecules showed voltage-controlled conformational change. Similar chemistry has been applied for realizing 'voltage-gated' transport channels with potential application in trans-dermal drug delivery. Electrically-facilitated transport (a geometry in which an electric field gradient acts across the membrane) through the CNT and functionalized CNT membranes was observed to be electrosmotically controlled.

Finally, a simulation framework based on continuum electrostatics and finite elements has been developed to further the understanding of transport through the CNT membranes.

KEYWORDS: *carbon nanotube membrane, nano-scale hydrodynamics, diazonium grafting, voltage-gated membrane, finite element analysis*

Mainak Majumder

Date: 12th November, 2007

MOLECULAR TRANSPORT PROPERTIES THROUGH CARBON NANOTUBE
MEMBRANE

By

Mainak Majumder

Dr. Bruce J. Hinds
Director of Dissertation

Dr. Douglass Kalika
Director of Graduate Studies

12th November, 2007

DISSERTATION

Mainak Majumder

The Graduate School
University of Kentucky

2007

MOLECULAR TRANSPORT PROPERTIES THROUGH CARBON
NANOTUBE MEMBRANE

DISSERTATION

A dissertation submitted in partial fulfillment of the
requirements for the degree of Doctor of Philosophy in the
College of Engineering
at the University of Kentucky

By
Mainak Majumder

Lexington, Kentucky

Director: Dr. Bruce J. Hinds, William Bryan Professor of Materials Engineering
Lexington, Kentucky

2007

Copyright © Mainak Majumder 2007

Dedicated to my grand-father, 'dada', who guided and inspired me during my formative years. He passed away on 25th July 2007, after a prolonged battle with Alzheimer's disease.

ACKNOWLEDGEMENTS

First and foremost, I am indebted to my advisor, Professor Bruce J. Hinds, for his guidance, enthusiasm and excellent problem selection. I gratefully acknowledge the funding provided by the National Science Foundation (NSF), National Institutes of Health (NIH), ARO Advanced Carbon Nanotechnology Program and the dissertation year fellowship from the University of Kentucky. I also acknowledge Central Glass and Ceramic Research Institute, a CSIR laboratory in Kolkata, India for allowing me a leave of absence for the first two years of my Ph.D. studies.

I thank Dr. Nitin Chopra, a former graduate student of our laboratory for realizing the synthesis of the CNT membranes, without which this dissertation would not have reached the present form. Other collaborators from our laboratory include Xin Zhan, Dr. Karin Keis and Xin Su. Dr. Karin Keis was particularly involved in much of the electrochemistry work discussed in Chapter 5. Undergraduate students who helped me were Corey Meadows, Jeggan Cole and Wendy Satterwhite.

A person very special to my academic growth and support at the University of Kentucky is Professor Dibakar Bhattacharyya (Department of Chemical Engineering). In fact, he was responsible for recruiting me to this university and has been a strong mentor. Members of the Bachas lab (Chemistry Department, University of Kentucky), Dr. Vasilis Gavalas, Dr. Pramod Nednoor, and Professor Leonidas Bachas, are acknowledged for some very fruitful discussions. Professor Audra Stinchomb at the Department of Pharmacy, University of Kentucky, is acknowledged for some preliminary drug diffusion studies through functionalized carbon nanotube membranes. My collaborators from the Center for Applied Energy Research, Drs. Rodney Andrews and Dali Qian, are also credited for supplying the aligned carbon nanotube samples.

My sincere thanks to Bing Hu, who often helped me in Scanning Electron Microscopy experiments and obtaining clear and beautiful pictures of the nanotubes or membranes; Professor Steven Rankin (Chemical Engineering, University of Kentucky) for using the FTIR Spectrometer (Chapter 4); Professor Todd Hastings (Electrical Engineering, University of Kentucky) for the use of EIS simulation software (Chapter 5); and Professor Pinar Menguic (Mechanical Engineering, University of Kentucky) and members of his laboratory for allowing me to use the finite element software FEMLAB (Chapter 7). The infrastructure provided by the Department of Chemical and Materials Engineering and the Center for Nano-scale Science and Engineering at the University of Kentucky is beneficial for undertaking cutting edge research and is, therefore, acknowledged.

There are many friends, including Kaustav Ghosh, Dr. Sumod Kalakkunath, Dr. Venkat Koganti., Pawan Tyagi, and Saurav Dutta, who made my stay in Lexington a memorable one. My mother has been a tower of strength, braving every crisis that came my way. Her faith and devotion have strengthened me and made me what I am today. My wife, Amrita, has not only provided me emotional support, but also brought structure and enrichment to my life.

TABLE OF CONTENTS

Acknowledgements	iii
Table of Contents	v
List of Tables	ix
List of Figures	xi
Preview	xx
Chapter 1: Introduction	1
1.1 Discovery of Fullerene and Carbon Nanotubes	1
1.2 Carbon Nanotubes as Nano-scale Containers or Mass Transport Channels	4
1.3 Synthesis of Aligned Carbon Nanotube Structures	7
1.4 Vertically Aligned and Ordered Membranes	9
1.4.1 What are membranes?	9
1.4.2 Anodization of Aluminium	10
1.4.3 Track-etch Membranes	12
1.4.4 Template Synthesis Approach	14
1.4.5 Fabrication of Vertically Aligned Carbon Nanotube Membrane	15
1.5 Goals of the Dissertation	18
Chapter 2: Experimental Methods	20
2.1 Synthesis of CNT Membranes.	20
2.2. Ionic Transport Measurements.	20
2.3. Electrochemical Impedance Spectroscopy Measurements.	23
2.4. Liquid Transport Measurements	23
2.5 Gas Transport Measurement	25
2.6.KCl Diffusion Experiments for Estimation of Porosity	27
2.7 Functionalization of CNT Membranes	28
2.8 FTIR Studies	30
2.9 U-tube Permeation Experiment.	30
2.10 Synthesis of 4-carboxy phenyl diazonium tetra fluoroborate	32
2.11 Electrochemical Grafting.	32

2.12 Dye Adsorption-Desorption Assay	34
2.13 Functionalization of CNT Membrane/Electrodes.	36
2.14 Estimation of Porosity of Membranes from Methyl Viologen flux	39
2.15 Transport Measurements for Voltage Gating and Electrically Facilitated Transport	39
Chapter 3: Ionic, Liquid and Gas Transport	43
3.1 Introduction	43
3.2 Results and Discussions	44
3.2.1 Integrity of the CNT Membrane Structure	44
3.2.2 Ionic Transport	45
3.2.3 Estimation of Charge Density of Plasma-Oxidized Membrane.	45
3.2.4 Analysis of the ionic flux using resistance-in-series model	49
3.2.5 Liquid Transport	53
3.2.6 Gas Transport	60
3.3 Conclusions	65
Chapter 4: Ionic-Transport through ‘Gate-keeper’ Functionality	66
4.1 Introduction.	66
4.2. Results and Discussions	67
4.2.1 FTIR Spectroscopic Studies	67
4.2.2 Effect of functional molecule chain length on flux and selectivity	70
4.2.3 Effect of charge and functional molecule aqueous solubility	74
4.2.4 Effect of solvent ionic strength on transport through CNT-dye membrane	75
4.2.5 Comparison of observed selectivity to hindered diffusion model	77
4.3 Conclusions	81
Chapter 5: Electro-chemical Functionalization and Characterization	83
5.1 Introduction	83
5.2. Results and Discussions	85
5.2.1 Estimation of COOH density by pH dependent dye adsorption-desorption	85

5.2.2 Interfacial Capacitance Measurements	87
5.2.3 Voltage Dependent Capacitance Measurements.	93
5.2.4 Ionic Transport Measurements	96
5.2.5 Switchable Impedance Spectroscopy of Dye Functionalized CNT Membrane/Electrode	98
5.2.6 Equivalent Circuit Diagram Analysis	102
5.3 Conclusions	109
Chapter 6: Voltage Controlled Transport	111
6.1. Introduction	111
6.2. Results and Discussions	113
6.2.1 Ionic Screening Effects on CNT Membranes with Enhanced Functional Density	113
6.2.2 Voltage-Gated Chemical Transport	116
6.2.3 Electric-Field Assisted Transport through Carbon Nanotube Membrane	122
6.3 Conclusions	133
Chapter 7: Finite Element Calculations	135
7.1 Introduction	135
7.2 Defining the Problem	136
7.2.1 Partition of a spherical particle in a cylindrical pore.	136
7.2.2 Setting up the differential equation and problem	138
7.2.3 Computational Geometry and Boundary Conditions	139
7.2.4 Computational Technique	142
7.3 Results and Discussions	142
7.3.1 Comparison of the finite element solution with analytical solution	142
7.3.2 Partition coefficient as a function of Debye screening length	151
7.3.3 Effect of particle shape: Sphere, Cube and Cylinder	151
7.3.4 Transport of ions in segmented and sandwich membranes	152
7.4 Conclusions and Future Work	160
Chapter 8: Conclusions and Future Work	162
Appendices:	165

A3: Appendix to Chapter 3	165
A3.1 UV-vis Calibration for Ionic Transport Measurements	165
A3.2 Liquid-Flow Decline Studies Through CNT Membrane	169
A3.3. Estimation of Permeable Pore Density	176
A6: Appendix to Chapter 6	177
A6.1. Effect of position of the ‘gate-keeper’ chemistry: feed side and permeate side	177
A7: Appendix to Chapter 7	180
A7.1 Matlab with Femlab program for evaluation of the energy of the sphere and cylinder in the sphere in cylinder system as a function of reduced pore diameter	180
A7.2 Matlab with Femlab program for evaluation of the energy of the sphere with zero charge on the cylinder as a function of reduced pore diameter	181
A7.3 Matlab with Femlab program for evaluation of the energy of the cylinder with zero charge on the sphere as a function of reduced pore diameter	182
References	183
Vita	202

LIST OF TABLES

Table 2.1	Molecules with varying size and charge density for probing the carbon nanotube transport channels through diffusion experiments. Their bulk diffusivity and experimentally-obtained apparent diffusivity through the CNT membrane are shown. 21
Table 3.1	Tabular summary of pressure-driven flow of liquids through CNT membrane. Water flow at ~0.001-0.02 bar measured by U-tube permeation experiment with positive column height and quantified by Ru(bipy) ₃ ²⁺ dye permeation 55
Table 3.2	Pressure flow of water through CNT membranes as a function of progressive chemical functionalization. Flow velocity is measured in the range of (0.001-0.2 bar) using a U-tube permeation cell with positive column height using an Ru(bipy) ₃ ²⁺ probe molecule. The enhancement factors are based on calculated Newtonian flow through a pipe with 7 nm inner diameter and a length similar to the thickness of the membrane. Note that progressive functionalization decreases the flow velocity and causes the transport to be closer to conventional hydrodynamics. The right-most column shows the observed diffusive flux after functionalization is normalized to the diffusive flux through the unmodified CNT membrane for these series of experiments 59
Table 4.1	Summary of diffusive transport measurements across CNT membrane as a function of tip-functionalization (0.3cm ² area, 5mmol of each source) from a 2-component source solution. Simultaneous flux of permeate is calculated from linear fit of solute concentration vs. time. The separation factor was experimentally measured for the membranes and pore size was calculated from the model using the separation factor and hindered diffusion model at the CNT entrance (model i). The error bars are the standard deviation of the linear fit from the experimental flux data at 90% confidence 71
Table 4.2	Transport measurement across CNT-dye in different concentration of electrolyte (KCl). The error bars represent the standard deviation of the linear fit from the measured experimental values 76
Table 5.1	Comparison of functional site densities of carbon nanotube systems 92
Table 5.2	Parameters estimated by fitting the model circuit to the experimentally obtained EIS spectra shown in figure 5.6(a) 108
Table 6.1	Electrical facilitated permeability of CNT membranes for different functionalization treatments, calculated from figure 5.12 for the negative potentials using $P_E = \frac{J_T - J_d}{C \cdot A_p \cdot V}$ where J_T and J_d are the transport rates in mole/s and have their usual meaning, C is the concentration in moles/s, A_p is the permeable pore area of the membrane in cm ² , V is the applied potential in volts. The observed electric field assisted flow velocity has been calculated from P_E , at 0.2 V. The zeta-potential has been calculated from estimated charge density of plasma oxidized and diazo-grafted membranes using interfacial capacitance measurements in 0.1M of 1:1

electrolyte. The electro-osmotic velocity at 0.2V has been calculated from,

$$v_{eo} = \frac{\varepsilon\zeta\Delta V}{\eta\Delta l} 129$$

Table 6.2	Parameters and formulae used for calculation of electro-osmotic and electrophoretic flux through the CNT membrane. for utilization of electroosmotically driven flux in micro-fluidic devices with interconnects provided by CNT channels.	132
Table 7.1	Analytical solution developed by Smith and Deen for a charged colloid in a charged pore using center line approximation	145

LIST OF FIGURES

Figure 1.1.	Schematic of (a) spheroidal and (b) tubular forms of fullerene discovered in 1985 and 1991, respectively. The tubular form or carbon nanotube (CNT) is composed of rolled up graphene sheets. Shown is a single-walled CNT. This dissertation investigates the molecular transport behavior through the central core of the CNTs in a membrane platform consisting of substantially large numbers of MWCNT encapsulated in a polymer matrix. (Graphics using Argus Lab, www.planaria-software.com/).	3
Figure 1.2	(a) Schematic of the CVD reactor used for growing multiwalled carbon nanotubes at the Center for Applied Energy Research, University of Kentucky. The aligned CNT array is deposited in quartz pieces (1" x 1") placed inside the furnace. (b) SEM micrograph of an array of CNTs.	8
Figure 1.3	Schematic representation of a separation process by a membrane. The driving force for the transport can be pressure, concentration, potential or thermal energy. The purpose of the membrane is to selectively transport one species over another based on various mechanisms including steric, electrostatic, affinity or solubility-diffusivity. (Adapted from <i>Basic Principles of Membrane Technology</i> by Marcel Mulder)	11
Figure 1.4	Schematic of methods to fabricate ordered porous membranes: (a) anodized alumina and (b) track-etch mica.	13
Figure 1.5	Schematic for fabrication of CNT Membrane	17
Figure 1.6	(a) Scanning electron micrograph of the vertically-oriented CNT membrane and (b) schematic of the targeted structure. Transport through the CNTs is investigated on this macroscopic structure consisting of $\sim 10^{10}$ nanotubes/cm ² with ~ 7 nm inner diameter encapsulated in an impervious polymer matrix. The CNTs are opened via a water plasma oxidation process.	19
Figure 2.1	In-situ UV-vis based U-tube permeation cell for studying ionic/molecular transport through a CNT membrane. A quartz cuvette is converted into the permeate cell for direct measurement of the diffusion rate. For the diffusion experiments, simultaneous diffusion of two component source solutions containing 5 mM of iso-valent ions were used as the source. For rhodamine, a single component source was used. The exposed membrane area was 0.7 cm ² .	22
Figure 2.2	(a) Schematic of the apparatus used for the liquid transport measurements; (A) Piston Pump (WPI Inc.), (B) Pressure sensor (Omega, PX 603), (C) Precision Needle Valve (Ideal valve), (D) Home made SS Flow cell (membrane area 0.785 cm ²), (E) Pan Balance (Denver Instruments, APX-1502), (F) Beaker for collecting permeate, (G) Lap top for data acquisition, (H) beaker for collecting by-pass liquid. (b) Photograph of pressure flow cell (D). The aligned CNT membrane is supported on porous metal disk (right) and the top seal is made of a viton o-ring.	24
Figure 2.3	Experimental set-up for studying gas transport through CNT membranes. Different components of the apparatus are: (A) pressure regulator, (B) pressure transducer (Omega, PX603), (C) on-off valve, (D) precision	

	needle valve, (E) home made flow cell (membrane area $\sim 0.78 \text{ cm}^2$), (F) horizontal glass bore capillary of 2 mm diameter, (G) liquid marker, (H) Distance of 10 cm on the capillary. A purge protocol was followed to displace the air inside the flow cell and fill with gas from the cylinder. The flow rate through the membrane was measured by timing the movement of a fixed volume (30 μl) of liquid marker inside the glass capillary. 26
Figure 2.4	Schematic of the molecules used for functionalizing nanotube membrane (A) C9; (B) Dye; (C) C22; (D) ACA (E) C40 (polypeptide) (formed after four sequential reaction of ACA, followed by C9) 29
Figure 2.5	(a) Schematic of permeation cell, the feed solution is 5 mM in $\text{Ru}(\text{bipy})_3^{2+}$ and 5mM in MV^{2+} . The permeate volume is 1.3 ml, and exposed membrane area is 0.3cm ² . (b) The probe molecules have similar charges, but different sizes and shapes. $\text{Ru}(\text{bipy})_3^{2+}$ is a spherical molecule of about 11 Å diameter; MV^{2+} is a cylindrical molecule of 5 Å equivalent spherical diameter (10 Å long, 3 Å diameter). 31
Figure 2.6	(a) Schematic of the aligned multiwalled CNT membrane structure and (b) Scanning Electron Micrograph (SEM) of the cross-section of the CNT membrane. The CNT membranes have significant in-plane conduction due to modest tortuosity allowing CNTs to cross. (c) Schematic of electrochemical reduction of (4-carboxyphenyl)-diazonium tetrafluoroborate on the carbon nanotube membrane leading to covalent attachment of benzoic acid groups to the conducting graphitic surface. 33
Figure 2.7	Apparatus for (a) Static Grafting (SG); and for (b) Flow Grafting (FG). H determines the height of the liquid column, hence, the high flow velocity through the membrane, forcing preferential reaction at the CNT tips. 35
Figure 2.8	Schematic of the functionalizing molecules (a) dye; (b) 8-amino caprylic acid; (c) CNT- DG-dye formed by sequential diazo-grafting and dye functionalization; (d) CNT-DG-spacer-dye formed by sequential diazo-grafting, 8-amino caprylic acid and dye functionalization. 37
Figure 2.9	(a) Schematic of the actuator molecule formed on the CNT membranes by four sequential reactions: (i) 4-carboxy phenyl diazonium ⁺ grafted onto a conducting CNT surface by electrochemical grafting to form a surface 4-carboxy phenyl group; (ii) Attachment of ACA (b) using carbodiimide mediated coupling between COOH group of electrochemically grafted 4-carboxy phenyl group and NH ₂ group of ACA (b) (iii) Coupling of COOH group of ACA (b) and NH ₂ group of ACA (b) ; (iv) Carbodiimide coupling of terminal COOH of ACA and NH ₂ group of the highly anionic dye (c) molecule. 38
Figure 2.10	Schematic of experimental set-up for measuring transport through membranes as a function of applied voltage. Note that the CNT-membrane placed between the fed and permeate solution is the working electrode. The permeate volume is 0.8 ml and the exposed membrane area is 0.7 cm ² 41
Figure 2.11	Experimental set-up for studying electro-phoretic and electro-osmotic transport across carbon nanotube membranes. The permeate concentration

	is measured as a function of time by UV-vis spectroscopy. The experiments are carried out potentiostatically using a Potentiostat/Galvanostat (Model 263A, Princeton Applied Research). Both the working and counter electrode are Pt wires and the reference electrode is an Ag/AgCl (sat. KCl) electrode. 42
Figure 3.1	UV-vis absorption monitoring of nc-Au (10nm diameter) diffusion across aligned CNT membrane. Photograph of the feed and permeate after 25h 46
Figure 3.2	Interfacial capacitance of the CNT membrane (measured by electrochemical impedance spectroscopy) was evaluated as a function of pH for the plasma oxidized membrane. The interfacial capacitance increases with increasing pH due to the ionizable carboxylic acid groups formed on the CNTs. From the difference in capacitance and the active electrode area, a charge density of $\sim 6 \times 10^{-3} \text{C/m}^2$ at pH 12 is estimated. 48
Figure 3.3	Electrostatically-hindered diffusion analysis of the ionic transport measurements. Flux of the probe molecules normalized to KCl flux. The Stokes-Einstein diameters are calculated from their bulk diffusivities. Reduced pore diameter (λ) varies from 0.04 to 0.24. Data from left to right are KCl, MV^{+2} , NDS^{-2} ; Ru-bipy $^{+2}$; RhodamineB; Green Dye $^{-2}$. The error bars at 95% confidence. The calculations are based on the analytical solutions developed by Smith and Deen ¹¹³ for constant charge density on the pore and molecule. Model (i) assumes that the entire path length contributes to the electrostatic partitioning and hindrance of the molecules, whereas, model (ii) assumes a fixed length at either end contributes to the rate process. Model (ii) with a length approximately equal to 7% on either side, predicts the fluxes quantitatively. 52
Figure 3.4	Slip length of the liquids on CNT calculated from the pressure flow experiments. Slip length is a measure of the deviation of liquid flow from the no-slip condition in the Haagen-Poiseuille equation and denotes the extent of interfacial friction of liquid on carbon-nanotube walls. Slip length for various liquids were observed to decrease with increasing hydrophobicity of the solvent. The quantities in brackets on the x-axis are the solubility parameter ($\text{Mpa}^{0.5}$) of the liquid. 57
Figure 3.5	(a) Permeability of the gases showed significant correlation with their molecular weights and not with their viscosities. The experimental permeability scaled with molecular weight of the gases by an exponent of 0.42 (which is close to 0.5 for ideal Knudsen type diffusion transport). Inset: Plot of experimental flux through CNT membrane. The slope of the lines is the permeability (in $\text{cm}^3/\text{cm}^2\text{-s-psi}$) of gas through the membrane. (b) Histogram of observed permeability in ($\text{mole}/\text{m}^2\text{-s-Pa}$) and enhancement factor for each gas. 63
Figure 3.6	(a) Schematic of diffuse reflection on rough surface and specular reflection on smooth surface. Knudsen diffusion is based on diffused reflection of gases and is applicable for most porous materials with rough surfaces. (b) Calculated Knudsen type diffusivity of hard spheres in smooth pores as a function of 'f' defined as the fraction of the gas collisions that reflect diffusely with the walls. 64

Figure 4.1	(a) FTIR spectra and (b) expanded and smoothed view of region of C=O stretch. Spectra is identified as (i) as received CNT; (ii) plasma oxidized; (iii) CNT-dye; (iv) CNT-9 membrane. The functionalized membranes show a peak at 1630 cm^{-1} and shoulder at 1600 cm^{-1} indicative of amide (I) and amide (II) stretches. Data shown in expanded region is smoothed with 11 point boxcar routine. 69
Figure 4.2	Representative plot of $\text{Ru}(\text{bipy})_3^{2+}$ and MV^{2+} transport through CNT-dye membrane in 0.1M KCl; Separation factor (α) is the ratio of the slopes of the linear fit of flux with time. 72
Figure 4.3	(a) Schematic and (b) separation factor (α) versus pore size for (i) hindered diffusion at the entrance and exit to the nanotubes; (ii) hindered diffusion throughout the nanotube; Model (ii) predicts higher α , than model (i) due to longer hindered diffusion path length. 80
Figure 5.1	(a) Chemical assay for the estimation of carboxylic-acid density of CNT membranes by pH dependent adsorption/desorption of charged-dye molecule; (b) Functional density ($\#/\text{cm}^2$) of CNT membrane as a function of the concentration of the adsorbing dye solution. Increase by 4-5 times in functional density is observed with electrochemical diazonium (static) grafting. Area used for functional density calculation is the geometric planar area of the sample. Lines are added to aid visual clarity. 86
Figure 5.2	(a) Nyquist and (b) Bode plots for as-made CNT membrane and diazonium (static) grafted CNT membrane electrode. The electrolyte is 0.1(M) KCl in an aqueous 10mM K_2CO_3 buffer. A semi-circle in the Nyquist plot indicates an electrochemical circuit consisting of a resistor (R_{el}) and double-layer capacitor (C_{dl}) in parallel. An increase in total capacitance of ~ 2 times is observed. 88
Figure 5.3	Interfacial capacitance as a function of pH. The electrolyte is 0.1M KCl in an aqueous 10mM K_2CO_3 buffer and pH is controlled by the addition of KOH or HCl. The estimated charge density of fully deprotonated -COOH groups of diazonium-grafted CNT membrane is $4 \times 10^{-2}\text{ C/m}^2$ compared to $\sim 6.4 \times 10^{-3}\text{ C/m}^2$ for as-made CNT membrane, indicating ~ 6 fold increase in carboxylic group density. 90
Figure 5.4	Interfacial capacitance of the diazonium-grafted CNT membrane as a function of applied potential, measured in an aqueous 10 mM K_2CO_3 (pH =10.8) buffer solution with various KCl concentrations. A compact Debye length of $\sim 0.9\text{ nm}$ at 0.1M KCl compared to $\sim 3\text{ nm}$ at 0.01M KCl increases the measured interfacial capacitance. 95
Figure 5.5	Selective spatial functionalization of CNT membranes by static grafting (SG) and flow grafting (FG) and the effect on $\text{Ru}(\text{bipy})_3^{2+}$ diffusion across the membrane. The static-grafted membrane shows > 2 fold increase in diffusive flux of positively-charged $\text{Ru}(\text{bipy})_3^{2+}$ by the attraction to anionic carboxylate groups. The electrostatic attraction is screened in a 0.1M KCl solution. 97
Figure 5.6	Comparison of non-faradaic impedance spectra of (a) CNT-DG-dye and (b) CNT-DG-spacer-dye membrane electrode. The impedance spectra were recorded at the bias voltage indicated in the figure and an AC impulse of 10 mV rms. The electrolyte solution is 0.1 in KCl and 10 mM in K_2CO_3 . The experiments were conducted on two membrane samples,

	hence the difference in their absolute impedances. Note that the CNT-DG-dye membrane electrode exhibits switchable impedance effect, while CNT-DG-spacer-dye does not. 99
Figure 5.7	Plot of $\omega^{-1/2}$ against the real and imaginary Z for the EIS recorded at 0 volt for the CNT-DG-dye carbon nanotube membrane/electrode in the frequency range of 10^3 to 10^4 Hz indicating a diffusion-limited transport of counter-ions to the functionalized electrode. 101
Figure 5.8	Comparison of faradaic impedance spectra (Nyquist plot) measured in 0.1M KCl and 10mM K_2CO_3 in the presence of 5 mM $[Fe(CN)_6]^{3-/4-}$ redox couple, at bias potential of 230mV vs Ag/AgCl for (a) CNT-DG-dye and (b) CNT-DG-spacer-dye membrane/electrode. For the CNT-DG-dye, the charge transfer resistance is larger than the bare membrane, indicating blocking of the electrode by the dye molecule, whereas, the spacer molecule keeps the bulky-dye molecule away from the surface in CNT-DG-spacer-dye membrane. 103
Figure 5.9	(a) Equivalent circuit diagram of a dye-functionalized CNT electrode. It consists of the double-layer resistor (R_{dl}) and capacitor (C_{dl}) and a subcircuit of the functional molecule (C_m and R_m). A Warburg contributing to the overall circuit (W_t) was added. Instead of pure capacitors, constant-phase elements representing leaky capacitors were used. (b) Warburg conductance (W_t) for CNT-DG-dye electrode was estimated by fitting the model of figure 5.9(a) with the experimental values of figure 5.6(a). The increase of Warburg conductance with increasing negative potential, indicated charged dye molecule changes from a 'lying down' to a 'standing-up' position, which allow easier diffusion of counter-ions to the functionalized electrode. 105
Figure 5.10	Typical fit of the experimental impedance spectra with the simulated (solid red line) Nyquist plots using the equivalent circuit diagram in figure 5.6(a). The simulation has been carried out using Gamry Echem Analyst software and the figure is screen printed from the software. 107
Figure 6.1	Estimated COOH density on CNT membrane using a grafting technique similar to SG. The TBO concentration in this experiment is about 0.12 mM. There is about a 2-3 times increase in COOH functional density and the reaction proceeds to saturation with increasing time of reaction. 115
Figure 6.2	Variation of transport of $Ru(bipy)_3^{2+}$ through CNT membranes as a function of chemical treatment and ionic screening. Experiments have been conducted on two separate membranes and the fluxes are normalized to their pre-grafting transport rates. Also shown is the schematic representation of the electrochemical grafting techniques: CNT-FG (Flow Grafting) and CNT-SG (Static Grafting). The yellow color represents the aqueous diazonium solution and blue color the flowing inert solution inside the CNTs. The flowing inert liquid column restricts the reaction to the CNT tips only.. . . . 117
Figure 6.3	(a) Cross-sectional SEM image and (b) idealized schematic of free-standing membrane with CNT array passing across a solid polymer film, (c) charged dye molecule tethered to CNT surface 120
Figure 6.4	(a) Change in separation co-efficient with voltage applied to the CNT-FG- spacer (polypeptide)-dye membrane. Also shown are the modest

	changes in the observed separation factor for CNT-spacer(polypeptide)-dye membrane in plasma-oxidized membrane (no electrochemical grafting), due to limited functional density in plasma-oxidized membranes	
Figure 6.5	(a) Change in separation coefficient with voltage applied to the CNT-SG-spacer(polypeptide)-dye membrane; (b) Fluxes of the two permeates at applied voltages across CNT-FG membrane. Membrane area is 0.7 cm ² . The line joining the data points are to aid visual clarity.	121
Figure 6.6	A representative UV-vis spectra of permeate through CNT-SG-spacer(polypeptide) membrane as a function of applied voltage and permeation time. Both MV ²⁺ (peak at 260 nm) and Ru-(bipy) ₃ ²⁺ (peak at 286 and 452 nm) are transported at 0 V, with a separation factor ~ 3. Application of a bias of +/-130 mV to the membrane causes the transport of Ru-(bipy) ₃ ²⁺ to be reduced, as evident from the lower intensity of the 286 peak, thereby increasing the separation factor to > 20 at -130 mV. The control experiment with nonfunctionalized membranes showed a similarly-modest change in separation factor or flux with applied voltage up to ± 300mv	123
Figure 6.7	Methyl viologen flux in the potential range (-400 to +400 mV) for CNT-SG-spacer-dye membrane. Note that at positive applied potential the flux is diffusion limited, while at negative potentials the flux is electro-osmotically enhanced over the diffusion flux. The separation factor does not change appreciably (~ 40%)..	124
Figure 6.8	Methyl viologen flux through carbon nanotube membrane as a function of applied negative potential to the working electrode with different functionalization treatments. The feed solution is 5 mM in Ru(bipy) ₃ ⁺² , 5 mM in MV ⁺² and 0.1 (M) in KCl. The permeate is 0.1M KCl. The membranes have been: (i) as-made without any functionalization (ii) with spacer-dye functionalization (iii) flow grafted and spacer-dye functionalized (iv) static-grafted with spacer dye functionalization	126
Figure 6.9	Experimentally-obtained electrical permeability of the CNT membranes and calculated zeta potential. The calculation for zeta potential is based on the experimentally-obtained charge density of plasma oxidized and dizonium core grafted membranes. Note that the electrically-facilitated permeability increases monotonically with the zeta potential, providing evidence to electro-osmotically driven transport through the CNT membrane.	130
Figure 7.1	The geometry for the finite element analysis. The sphere ABCD represents the particle inside the infinite cylindrical pore EFHG. For the analysis, a finite volume of the pore IKLJ, corresponding to the length L _c is considered. For the cube and cylinder (L/D =1), a similar geometry with the particle at the center of the cylinder was considered..	131
Figure 7.2	Typical finite element solution of the Poisson-Boltzmann equation of the sphere in cylinder geometry, with constant surface charge density on the walls of the cylinder and colloid. The solution is in dimensionless quantities.	140
		143

- Figure 7.3 Effect of length to diameter of the cylinder on the computed Boltzmann factor. Insignificant variation in the computed Boltzmann factor is observed with varying L/D of the cylinder from 2 to 20. . . . 144
- Figure 7.4 Quadratic Lagrangian elements used for generating the mesh for the finite element analysis. The mesh can be made finer by decreasing the maximum height (h_{\max}) of the element. Finer meshes require longer computational time, but the errors are minimized. . . . 148
- Figure 7.5 Comparison of Deen's analytical solution to the Finite-Element Analysis in this study. Calculations are for a cylinder with 10 nm pore radius with a charge density of $0.5 \times 10^{-2} \text{ C/m}^2$ and spherical particle with 1.02×10^{-2} charge density in presence of 0.1M of a 1:1 electrolyte. The maximum height of the mesh utilized for the finite element calculations is denoted by h_{\max} 149
- Figure 7.6 Boltzmann factor for a charged-spherical particle (charge density $1.02 \times 10^{-2} \text{ C/m}^2$) inside a cylindrical pore of 10 nm diameter with charge density ($5 \times 10^{-3} \text{ C/m}^2$). Partition co-efficient calculations are for different concentration of the screening (1:1) electrolyte. As expected, at higher concentration of the electrolyte, the charges are screened and the electrostatic effects are diminished. Values close to one indicate minimum interaction and values close to zero indicate that the particles are totally rejected by the charged pore especially at low values of τ . . . 150
- Figure 7.7 Boltzmann factor for different shapes of the particle: sphere, cube and cylinder ($L/D = 1$). For similar charge densities on the membrane ($1.02 \times 10^{-2} \text{ C/m}^2$) and on the cubical shape is electrostatically most hindered. . . . 153
- Figure 7.8 (a) Schematic of the computational geometry for calculating the partition coefficient as a function of position inside the pore. The red color indicates the presence of a charged-boundary condition, while the black line indicates a zero-charge boundary condition. A pore radius of 3.5 nm with a surface-charge density of $3.2 \times 10^{-3} \text{ C/m}^2$ and reduced-molecule radius of 0.135 with surface-charge density of 0.113 C/m^2 are considered. These values are analogous to those for a plasma-oxidized CNT membrane and $\text{Ru}(\text{bipy})_3^{2+}$. Ionic concentrations of 0.1M, 0.01M and 0.001M of 1:1 electrolyte are considered. (b) The Boltzmann factor for the molecule as a function of position in the segmented pore geometry. In this figure, the calculated Boltzmann factor is plotted against the dimensional position. Also shown by dashed line in the figure, is the Boltzmann factor for a homogenous cylinder for a position $z = 14 \text{ nm}$ 154
- Figure 7.9 (a) A sandwich pore structure of radius 1.5 nm with surface charge density of $1.28 \times 10^{-2} \text{ C/m}^2$ and $7.72 \times 10^{-2} \text{ C/m}^2$, reduced molecule radius of 0.31 with surface charge density of 0.113 C/m^2 are considered. . . . 157
 Boltzmann factor as a function of the dimensional position of the sphere in the sandwich-pore structure for charge density of (b) 1.28×10^{-2} and (c) $7.72 \times 10^{-2} \text{ C/m}^2$ on the 1.5 nm pore. The red legends are for 0.1M and the blue legends are for 0.01M of the screening electrolyte. Calculations were performed for the blue legend on either side of the sandwich structure for figure 7.9 (a) and was found to be symmetric. Therefore, calculations were

performed only for the negative z axis, while for positive values they were substituted from the symmetry of the solution. The Boltzmann factor has also been calculated for a uniformly-charged cylinder for the position $z=0$. Since the partition co-efficient should not change for a uniformly charged sphere, it is denoted by dashed lines 158

Figure A3.1.1	Calibration curve of (a) MV^{2+} absorbance (at 260 nm); (b) $Ru(bipy)_3^{2+}$ absorbance (at 286 and 452 nm) in the Ocean Optics USB-UVvis	166
	(c) Predicted/actual separation factor of MV^{2+} to $Ru(bipy)_3^{2+}$, from the protocol used for estimation of $Ru(bipy)_3^{2+}$ and MV^{2+} from the peaks at 286 and 260 nm as in Chapter 6. Note that the protocol successfully predicts the separation factor at higher ratio of MV^{2+} to $Ru(bipy)_3^{2+}$, but overestimates the separation factor at lower values of the separation factor.. . . .	166
Figure A3.1.2	Calibration curve of (a) NDS^{-2} absorbance (at 230 nm) and (b) Dye^{-2} absorbance (at 620 nm) in the Ocean Optics USB-UVvis	167
Figure A3.1.3	Calibration curve of RhodamineB absorbance (at 456 nm) in the Ocean Optics USB-UVvis	168
Figure A3.2.1	(a) Flow decline kinetics of water through CNT membrane (b) flow revival when the flow system was de-pressurized	171
Figure A3.2.2	Water flow measurements using vacuum boiled DI water in the flow set-up through two commercial membranes (a) Anodised alumina oxide membrane (with 20 nm top pores and 200 nm bottom pores) and (b) PAN membrane (24,000 molecular weight cutoff)	172
Figure A3.2.3	Cumulative volume of different solvents collected over a balance per unit area (cm^3/cm^2) of the membrane flowing through the CNT membrane as a function of time at (0.7-1bar applied pressure). Water flow data shown here has been normalized by permeable pore density. Reduction in the flow of associated liquids (water and alcohols) with time can be attributed to flow-induced solvent ordering or formation of bubbles. This mechanism is currently under investigation	173
Figure A3.2.4	Permeability decline during measurement of (a) water; (b) iso-propyl alcohol, and (c) ethyl alcohol using the apparatus described in Section 3.2.4?. The error bars represent the error in measurement of the liquid permeability resulting from the weight of each drop of the liquid coming out of the flow cell.	175
Figure A3.3	1 Representative plot of KCl diffusion as measured by the conductivity of the permeate solution as a function of time	176
Figure A6.1	Separation factor between MV^{2+} and $Ru(bipy)_3^{2+}$ as a function of applied potential to the CNT-FG-spacer-dye membrane with (a) Chemistry side on the permeate; (b) Chemistry side on the feed	178
Figure A6.2	Fluxes of the probe molecules through CNT-FG-spacer-dye as a function of applied potential for (a) Chemistry side on the permeate; (b) Chemistry side on the feed	179

Preview

The general theme of this dissertation is based on the experimental investigation for the understanding and modulation of the molecular transport phenomena through carbon nanotube membranes. Carbon nanotubes are a promising, unique material for membrane applications with cores composed of atomically-smooth graphitic tubes, functional chemistry at tube entrances, and the ability to conduct electrical current. Ability to control flux and selectivity through membrane structures are at the heart of membrane processes. Demonstrated in this dissertation are various methods to control flux through the membrane, including dramatically enhanced pressure induced transport of liquids and gases, as well as ‘chemically-gated’ and ‘voltage-gated’ diffusional transport of aqueous ions. The dissertation is composed of eight chapters.

Chapter 1 aims to provide a description of the importance and offer a perspective of this dissertation. It takes the reader into the history of fullerenes and carbon nanotubes chronologically, with an emphasis on the concept of utilizing the hollow core as nano-containers or molecular-conduits. Membranes as the rate-controlling step of mass transport in separation processes are discussed. The importance of vertically-oriented membranes with well-defined pore structure for understanding fundamental mass transport in the nano-scale is highlighted. Different methods used to fabricate vertically-oriented porous membranes like anodization, track etch, and template synthesis are elaborated upon and the process for fabrication of the membranes composed of a large array of aligned CNTs, is introduced. The goals of the dissertation are also discussed.

Chapter 2 discusses the experimental techniques employed in the research for this dissertation. These include brief descriptions of the membrane fabrication, experimental set-ups to investigate pressure-driven liquid and gas transport, diffusive transport of ions, and methods for functionalizing the membranes.

Chapter 3 focusses on the ionic, liquid, and gas transport properties of the membrane structure. Ionic diffusion of ions of different size and charge is experimentally determined. Charge density at the membrane pores is estimated from interfacial

capacitance measurements. The experimental results are analyzed by electrostatic partitioning and hindered diffusion theory of large molecules in small pores. The permeable pore density of the membrane structure is estimated from diffusion of small ions, while the absence of macro-scale defects is confirmed by size exclusion of 10 nm gold colloids to validate a membrane structure comprising CNT transporting channels of ~ 7 nm diameter. A key assumption of this estimation (i.e. bulk diffusivity of ions in 7 nm diameter CNT channels) is established from the ionic transport behavior of a variety of ions. Transport measurements of liquids and gases are analysed based on hydrodynamic models of liquid transport in porous membranes (Haagen-Poiseuille flow) and kinetic theory (Knudsen theory) of gas transport in small pores. The experimentally-observed, dramatically-enhanced flow rates are compared with molecular dynamic (MD) predictions of enhanced transport by other research groups.

Chapter 4 elaborates on ‘gate-keeper’ like transport through the membrane structure. Transport of ions or molecules in biological membranes are regulated by protein transporter molecules that lie at the entrances to the hydrophobic lipid channels. Plasma-oxidation during the fabrication of the CNT membrane structure introduces carboxylic acid functional groups at the CNT entrance, making them amenable to easy functionalization chemistry approaches. Specifically, the CNT membranes were functionalized with molecules of different size, hydrophilicity and hydrophobicity, and the transport of two positively charged ions were studied as a function of ‘gate-keeper’ chemistry. The results are analyzed using hindered diffusion theory.

Chapter 5 focuses on the powerful tools of electrochemistry to functionalize and characterize the CNT membranes. One conclusion from chapter 4 is that as-made (plasma-oxidized) membranes had limited functional groups at the CNT entrance. This was deduced from their modest separation performance. The CNT membranes are electronically-conducting due to crossing of the CNTs in the polymer matrix and can be used as a working electrode in an electrochemical cell. A diazonium-grafting chemistry was utilized to increase the functional density of carboxylic-acid groups. Increase in functional density was confirmed and quantified by interfacial capacitance and dye

adsorption-desorption measurements. The membrane/electrode with enhanced functional density was covalently coupled to an anionically-charged dye molecule with and without a spacer. The functionalized electrodes were probed by faradaic and non-faradaic impedance spectroscopy. Switchable impedance spectroscopy, attributed to the potential induced conformational change of the charged molecule at the polarized electrode, is demonstrated.

Chapter 6 discusses the effect of applied potential and electric fields on transport through the CNT membrane. ‘Voltage-gated’ channels are one of the primary mechanisms to the highly selective transport of biological membranes. This is achieved by an electrostatically actuated ‘paddle-like’ motion of charged-protein residues in the membrane channels. Electrostatically-actuated motion of tethered macro-molecules at the CNT membrane could in principle mimic ‘voltage-gated’ transport in artificial porous channels. The CNT membranes with enhanced functional density from diazonium grafting were functionalized with a molecular actuator consisting of a long poly-peptide tether attached to a highly-charged dye molecule. Transport measurement of ions of dissimilar sizes demonstrates controlled ‘voltage-gated’ transport.

Chapter 7 provides a numerical framework based on finite elements to study transport through the membrane structure. A series-in-resistance model with electrostatic hindrance a few nanometers down the core can predict ionic flux through the CNT membrane (Chapter 3 and Chapter 4). The rationale for choosing the finite element approach is flexibility of boundary conditions, (e.g. constant surface-charge density on the pore wall as pertinent to ionic diffusion studies in Chapter 3) or constant electrical potential on the pore wall as pertinent to voltage-gated transport in Chapter 6. Different geometry of the transporting molecule or pore can also be looked into by this technique. A finite element algorithm is developed for electrostatic partitioning of charged molecules in charged pores with constant surface charge density on the molecule and pore and compared to an analytical solution. The effect of Debye screening length on the equilibrium partitioning of charged molecules in charged pores is also calculated. A sandwich and a segmented pore structure analogous to the ‘gate-keeper’ geometry were

also analyzed based on the finite element approach. The finite element approach could be the framework for future simulation studies of ‘voltage-gated’ transport in conjunction with other techniques (e.g., Molecular Dynamics or Brownian Dynamics) to simulate the potential dependent conformational change of the molecular actuator.

Chapter 8 concludes the dissertation and discusses the potential scope and directions for future research on CNT membranes.

Chapter 1

Introduction

1.1 Discovery of the Fullerene and Carbon Nanotubes

Carbon, with its ability to bond with several elements like hydrogen, nitrogen and carbon itself, forms the basis of all life on earth, starting with the tiniest of viruses to the largest of mammals. There is also significant interest in carbon materials from the perspective of physics and chemistry. Before 1985, all carbon-crystalline materials were known to exist in two allotropic forms: diamond and graphite. In diamond, the C atoms are sp^3 hybridized and hence its coordination is fully satisfied in all three dimensions, whereas graphite is a planar sheet of sp^2 hybridized carbon with the mobile pi-electrons contributing to the in-plane conductivity of graphite. The difference in their crystal structures result in their diverse properties, hence both are of significant interest to materials scientists. For example, diamond is the hardest material known, while graphite is one of the softest; graphite is electrically conducting whereas diamond is insulating. In the fall of 1985, a group of scientists at Rice University discovered that carbon vapor, if allowed to condense under the right conditions, could form spheroidal carbon clusters, which are different from diamond or graphite. A new truncated icosahedron form of sp^2 hybridized graphite containing 60 carbon vertices was discovered. Of the 32 faces that this structure contains, 12 are pentagonal and 20 are hexagonal. The shape of the C_{60} molecule is similar to a soccer ball with a hollow core and was consequently named after Buckminster Fuller, the architect who designed geo-desic domes.¹ For the discovery of this new form of carbon, Kroto, Curl and Smalley shared the Nobel prize in 1996. The structure was found to be extra-ordinarily stable and exciting electronically or optically considering the abundance of π -electrons inside and outside the carbon shell. Efforts were soon underway to incorporate other materials inside the carbon cage shell often referred as endohedral fullerene chemistry, with the basic aim of altering their electronic properties.² Several elements including La, Sc, Y, La, Ca, Sr, etc. have been successfully incorporated and applications in biological and materials sciences have been predicted.³

After the discovery of the fullerene, what followed was a deluge of research characterizing different forms of C_{60} formed during the electric-arc process for synthesis

of fullerenes^{4,5} and efforts to mass produce these materials.⁶ With the advances in the resolution of Transmission Electron Microscopy (TEM), various forms of carbon clusters were soon identified. Among them, the discovery of carbon nanotubes by Sumio Iijima⁷ in 1991 stands out. This paper was the first to report a detailed TEM image of a multi-walled carbon nanotube, which was found to grow at the cathode during electric arc experiments to produce fullerenes. The micrographs had resolution high enough to distinguish individual graphene layers ($\sim 3\text{\AA}$). Two years later, single-shell carbon nanotubes, now known as single walled carbon nanotubes (SWNT), were reported by Iijima's group⁸ and a research group from California.⁹ Coincidentally, both these reports were published in the same issue of 'Nature'. Schematics of a fullerene and single walled CNT are shown in figure 1.1.

With one of the dimensions in the quantum regime (diameter often less than 10 nm), significant effort has been made to investigate and understand their electronic properties. Several international groups began to investigate their electronic, mechanical and thermal properties. Applications, including sensors based on field-effect transistor effect in the semi-conducting nanotubes, composites, and field emission devices, were designed. It is noteworthy that in their Nobel lecture in December 1996, Richard Smalley and Robert Curl envisioned emerging applications utilizing the facile functionalization of the end-caps of the fullerene tubes and their electronic conductivity.^{10,11} Apparently they realized that the fullerene tubes were perhaps more amenable to practical applications than fullerene spheres. However, the tubular form of graphite would not have interested scientists had fullerenes not been discovered.

It is important to point out that the formation of the filamentous form of carbon had been known for quite some time. A US patent disclosing formation of carbon filaments was reported almost two centuries ago. French scientific literature also stakes a claim to some early reports of carbon filaments. Russian scientists have shown some early TEM images of carbon nanotubes as early as 1952. Endo et al. reported the formation of filamentous forms of carbon as early as 1976.¹² Details about such early reports of filamentous and hollow carbon structure are provided by Monthieux and

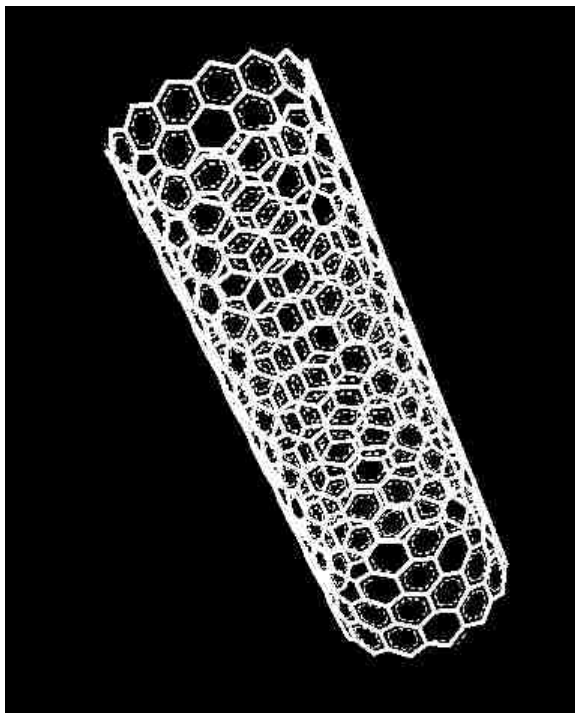
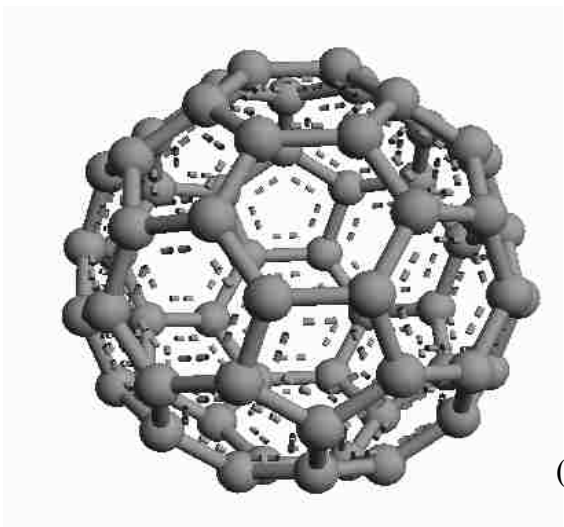


Figure 1.1 Schematic of (a) spheroidal and (b) tubular forms of fullerene discovered in 1985 and 1991, respectively. The tubular form or carbon nanotube (CNT) is composed of rolled up graphene sheets. Shown is a single-walled CNT. This dissertation investigates the molecular transport behavior through the central core of the CNTs in a membrane platform consisting of substantially large numbers of MWCNT encapsulated in a polymer matrix. (Graphics using Argus Lab, www.planaria-software.com/)

Kuznetsov.¹³ However, Ijima's report of carbon nanotubes in 1991, aided by several favorable factors including a wide audience of a prestigious journal, prior discovery of fullerenes, and the availability of novel investigation tools, kindled the imagination of the 'nano-science' community and impacted the field in a way that no other prior report can lay claim to. Several research groups have studied the electrical, magnetic and electronic properties of carbon nanotubes in the form of bundles¹⁴ or individual nanotubes^{15,16} ever since its discovery. There has also been significant interest in the hollow, tubular interior of the CNTs as nano-scale containers or conduits for mass transport, which is the principal concept on which this dissertation is based.

1.2 Carbon Nanotubes as Nano-scale Containers or Mass Transport Channels

The earliest experiments demonstrating the feasibility of liquids to infiltrate the inner cores of CNTs and act as nanoscale containers was by Ajayan and Ijima in 1993.¹⁷ In a subsequent publication that same year, the group reported that unlike metals, inorganic materials were hard to incorporate inside open-ended carbon nanotubes.¹⁸ This could be rationalized in terms of the higher surface energy mismatch of inorganic materials with the graphitic nanotubes compared with liquid metals. An important conclusion from this work was the feasibility of opening the carbon nanotubes using gas-phase oxidation. Direct application of such infiltration behavior is template-assisted synthesis of nanoscale materials.¹⁹

Dujardin et al.^{20, 21} studied the wetting behavior of carbon nanotubes and reported their findings in 1994 and 1998. Experiments involved infiltration of molten metals in bulk multiwalled nanotube (MWNT) samples with diameters of 2-20 nm. It was concluded that liquids with surface tension less than 180 mN/m would wet the MWNTs. Hence, liquids like water and organics could easily wet the MWNT, but not all molten metals. A follow-up article illustrated that SWNT samples did not behave differently. However, the critical surface tension shifted to a wider range (~ 130-190 mN/m).

Carbon nanotubes as conduits for molecular transport caught the imagination of scientists and engineers. With rapid improvement and development of molecular simulation techniques, several research groups in the US and UK started looking into the transport properties of carbon nanotubes. Prominent among them are David Sholl and

Karl Johnson at the Carnegie Melon University, Pittsburgh. They looked into the transport of gases like N₂, Ar, CH₄, etc. through nanoporous materials including carbon nanotubes. The rationale for their studies was to screen potential inorganic materials for gas separation applications. In 2002, they reported that the transport diffusivities of argon through carbon nanotube membranes were almost 3-4 orders of magnitude larger than through zeolitic pores.²² They reasoned that the smooth and frictionless graphitic interface would allow specular reflection of the gases and contribute to its enhanced transport diffusivity. Some work on gas transport through carbon nanotubes using molecular dynamics were also conducted by the Susan Sinnott group at the University of Kentucky.²³ Their simulations also predicted extremely fast transport of gases through CNTs.²⁴

Nick Quirke's group at Imperial College in the United Kingdom investigated hydrodynamics of low Knudsen number fluid flow through graphitic pores. Their simulation results indicated the presence of large slip lengths for such fluids.²⁵ In 2002 they proposed for the first time, the presence of slip-boundary conditions on smooth carbon nanotube surfaces.²⁶ With applications including nano-fluidics in mind, the same group reported extremely rapid imbibition kinetics of oil in CNTs not explainable by the Washburn equation.²⁷

At the National Institute of Health in Maryland, Gerard Hummer's interest in water transport through carbon nanotubes was primarily from their hydrophobic nature and similarity to protein channels. Possibly CNTs provided a much simpler model for Molecular Dynamics simulations compared to the complex protein channels. Their seminal publication in 2001, suggested that hydrophobic CNT channels transport water at an extraordinary speed through the co-operative movement of a hydrogen-bonded network through the frictionless walls of carbon nanotubes.²⁸ Kalra et al.²⁹ studied the osmotically-driven transport of water through CNTs. The water-flow velocities were very close to those found in natural water channels like aquaporin. Klaus Schulten's group at the University of Illinois Urbana-Champaign studied the water and proton transport behavior through CNTs. The water dipoles were found to be highly aligned unidirectionally in pristine nanotubes, which was somewhat disturbed in modified CNTs.³⁰ Several publications on water transport through CNTs have appeared since and

are beyond the scope of this dissertation topic. Some simulations work by other groups will be referred to in the subsequent chapters, especially those relevant to the experimental studies in this dissertation.

In this context it might be pointed out that an Indian research group studied the transport of liquids in single walled carbon nanotube (SWNT) bundles. Their observation of induced voltage in the direction of the flow was not consistent with standard electrokinetic phenomena and was explained by an induced charge mechanism at the polarizable liquid-electrolyte interface.³¹ The observed voltage is a function of the liquid ionic properties and hence this device could serve as a flow sensor.

Behavior of water inside hydrothermally synthesized CNTs by in-situ microscopy techniques has been studied by Gogotsi et al. of Drexel University. In 2002,³² the group reported flow velocities of water to be $\sim 0.5 \times 10^{-4}$ cm/s in 50 nm inner diameter nanotubes. Though it conclusively proved the presence of water in equilibrium with a gas inside the carbon nanotubes, uncertainty remained as to the driving force for the transport measurements. The same group also studied the dynamics of water inside disordered carbon nanopipes using an environmental scanning electron microscope. In this work, the carbon nanotubes were hydrothermally filled with water, frozen at -80 °C and examined by HR-TEM and EELS.³³ Couple of observations from these experiments are worth mentioning. There was a segmented filling of water (with intermittent air-pockets) inside CNTs with pore diameter (20-100 nm) and a complete filling for pore diameter in the range of 5-10 nm. For highly crystalline nanotubes a gap of ~ 4 Å was also observed between the graphitic walls and frozen water.³⁴ This suggests that water molecules did not wet crystalline CNTs of small diameter, but could effortlessly fill them.

The earliest experimental mass transport measurements through carbon nanotubes appear to be on single pore carbon-nanotube membranes with ~ 120 nm pore diameter.³⁵ This large-diameter nanotube did not exhibit any unusual transport properties and was synthesized for Coulter counting applications. A Coulter counter is a device that can count biological cells or colloidal particles. The single-pore device is placed in an electrical potential gradient. Passage of the colloidal particle through the nanopore is detected by ion-current measurements.³⁶ Though necessary to fundamentally understand

mass transport at the nanoscale, such a single-pore membrane with a large diameter would have limited applicability in small molecules or in large-scale separations. It is important to devise strategies for synthesizing membrane platforms with smaller diameter carbon nanotubes for large-scale chemical engineering or medium-scale drug delivery applications.

A significant challenge therefore remained to develop and characterize CNT membranes with a large array of CNTs for fundamental mass-transport studies, verifying some of the MD predictions and developing large-area platform applications. Interested readers in fluid transport through carbon nanotubes are referred to an excellent review article by Whitby et al.³⁷

1.3 Synthesis of Aligned Carbon Nanotube Structures

In the early 1990s, along with efforts to synthesize carbon nanostructures in large-scale production capabilities, efforts were also undertaken to make controlled nanostructures composed of aligned CNTs. Such efforts were primarily made to investigate their anisotropic electrical, optical and magnetic properties. A direct application for such aligned nanotubes was for field-emission devices. The earliest report of aligned MWCNT films was from a French group in 1995 using the arc evaporation process.³⁸ Subsequently, other groups started synthesizing such aligned CNT structures using other processes. Among them the Chemical Vapour Deposition (CVD) method was a scalable and industrially-viable process for synthesis of CNTs. Vertically aligned CNT films were reported to grow from a substrate containing nanoscale iron catalysts embedded in a silica matrix.³⁹ Ren et al. reported the formation of aligned MWNTs on nickel-coated glass substrates by plasma-enhanced hot-filament chemical-vapor deposition from a mixture of acetylene and ammonia below 666 °C.⁴⁰ The CNTs had significant bamboo-type structures as a consequence of low-temperature formation. Similarly, aligned CNT arrays were produced with hydrocarbons mixed with ferrocene catalyst sources.⁴¹ Efforts at the Center for Applied Energy Research (CAER) at the University of Kentucky were focused on perfecting and scaling-up production of MWNT arrays from a continuous source of ferrocene and xylene at about 650 °C.⁴² The ferrocene catalyst decomposes to form ‘floating’ metal particles, which are deposited on the substrate (quartz). The carbon

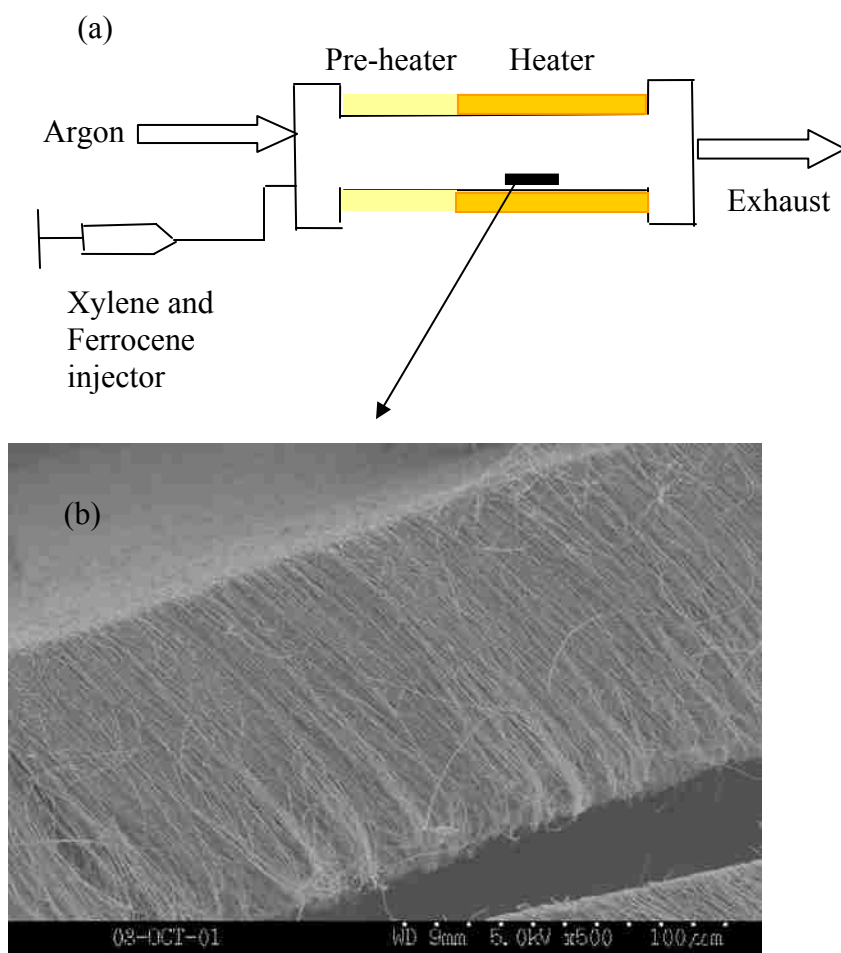


Figure 1.2 (a) Schematic of the CVD reactor used for growing multiwalled carbon nanotubes at the Center for Applied Energy Research, University of Kentucky.⁴² The aligned CNT array is deposited in quartz pieces (1" x 1") placed inside the furnace. (b) SEM micrograph of an array of CNTs.⁸⁰

sources then form interstitial compounds with the catalyst and finally shoot crystalline graphite with basal planes tangential to the catalyst nano-particle. Hence, the size of the catalyst determines the inner diameter of the CNTs. The nanotubes were found to grow via a mixture of tip- and base-growth mechanisms, with the Fe nanoparticle located at the top end of the growing CNT.⁴³ A schematic of the process and an SEM micrograph are shown in figure 1.2.

The other strategy for alignment of CNTs would entail the application of some external forces. Partial alignment of CNTs (~ 50%) inside a polymer matrix was achieved by mechanical stretching. These anisotropic nanostructures were also found to be aligned along the flow direction during extrusion of a polymer-nanotube composite melt.⁴⁴ Alignment of CNTs could also be achieved by extruding a polymer melt of polystyrene and nanotubes in the direction of the extrusion.⁴⁵ However, a high degree of alignment for samples containing a large-volume fraction of the nanotube would be difficult to achieve because of the limited fluidity of the melt. Researchers at Rice University were able to align in-plane, purified SWNT bundles using a magnetic field (~ 7 T) during filtration of a nanotube suspension.^{46,47} Such an aligned structure would not be appropriate for filtration applications, which require an out-of-plane alignment of CNTs.

1.4 Vertically Aligned and Ordered Membranes

1.4.1 What are membranes?

From a physical chemistry perspective, a membrane is a continuous 2 D material (e.g. graphite sheets). For biological scientists, it is a cellular film of lipids containing highly-selective protein channels, while for chemical engineers it is a continuous film allowing separation of materials of importance to society. For the sake of this dissertation, it would be instructive to define membranes as a 2D continuous film that allows selective mass transport under the influence of a driving force including concentration, pressure, or electric field gradient as shown in figure 1.3. The main aim of a membrane is to selectively transport one species over another. For example, a reverse-osmosis membrane is a polymer film of cellulose acetate, which allows water to pass through but salt to be retained and is used to desalinate sea water. A coarse micro-

filtration membrane will retain colloidal particles and bacteria and is used to filtrate drinking water. Problems of complex magnitude include separation of H_2 from CH_4 or EtOH from H_2O . Suffice to say, a membrane acts as a rate limiting step of mass transport under a driving force with the ultimate goal of kinetically separating one substance (or phase) from the other. Various physical factors including size-based exclusion in porous membrane, solubility-diffusivity in dense polymeric membrane, and electrostatic interactions in nanofiltration are operative often in conjunction with each other.

Understanding transport processes at the nanoscale is a significant challenge, especially since these processes often interplay between chemical, electrical and mechanical effects. Problems are compounded when the solute or solvent molecule is of similar dimension to the pores and the continuum physics are not valid at these length scales. Membranes composed of ordered pores that are uniform and well-defined are platforms of interest for fundamental investigation of membrane transport. Besides, such membrane structures hold promise for simultaneously increasing flux and selectivity. Methods to synthesize such ordered-membrane structures are therefore discussed.

1.4.2 Anodization of Aluminium

The formation of an oxide barrier layer over metal surfaces is well known and contributes to their corrosion resistance and barrier properties. Stresses formed on the oxide layer may be compressive or tensile, depending upon positive or negative volume expansion upon oxidation. In general, metals show a positive-volume expansion upon oxidation; hence the mechanical stability of the layer depends on the exact amount of volume change, the figure of merit for which is the Pilling Bedworth (PB) ratio. For metals like iron or tantalum, it is > 2 and the oxide layer is unstable. Stable oxide layers are formed on Al (PB ratio ~ 1.28) or Ti (~ 1.78)⁴⁸ and usually form a planar barrier layer over the metal surface. Under certain electrolytic and anodic polarization conditions, caused primarily by the migration of the Al^{3+} ions out of the polarized barrier electrode and negative O^{2-} and OH^- ions into the barrier, a porous structure with tubular pores perpendicular to the substrate are formed.^{49,50} Chemical or electrochemical⁵¹ etching then removes the underlying Al layer and the Al_2O_3 barrier layer to provide transporting porous channels.⁵² While 85% phosphoric acid is the preferred etchant for

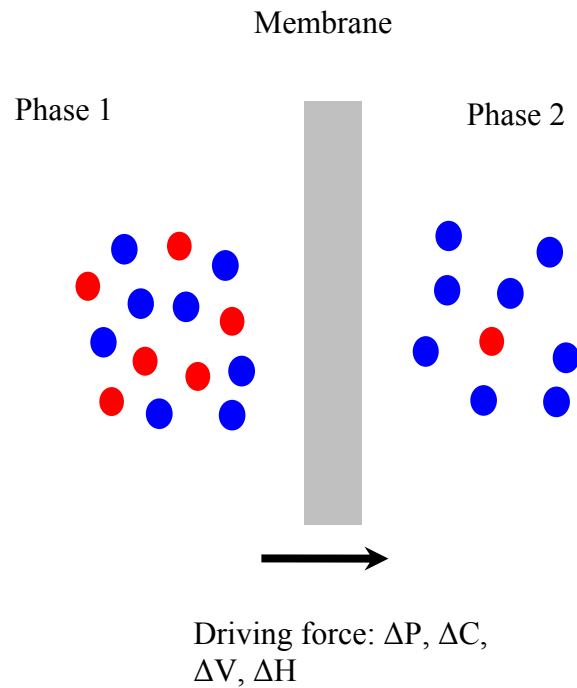


Figure 1.3 Schematic representation of a separation process by a membrane. The driving force for the transport can be pressure, concentration, potential or thermal energy. The purpose of the membrane is to selectively transport one species over another based on various mechanisms including steric, electrostatic, affinity or solubility-diffusivity. (Adapted from *Basic Principles of Membrane Technology* by Marcel Mulder⁵³)

the alumina barrier layer, Al was etched by an HgCl_2 solution. The pore size is tunable from 8 nm to > 100 nm and depends upon a variety of factors including anodization potential (usually in the range of 25-40 V) and choice of electrolyte (like sulfuric acid, oxalic acid or phosphoric acid). Anodized alumina membranes are sold by Whatman (<http://www.whatman.com/>) under the name Anopore®. The smallest pore size available is 20 nm pores with a support of 120 nm. A very instructive and practical guide for setting up a laboratory apparatus for anodization is provided by Knaack et al.⁵⁴ A brief schematic of the process is shown in figure 1.3(a). An interesting feature of the anodization process is the long-range planar hexagonal symmetry of the porous structure. The ordering effect in this self-assembly process has been related to the PB ratio. Using different electrolyte and anodic oxidation conditions, it was observed that the long-range order increased with increasing volume expansion of the oxide layer.⁵⁵ Such ordered porous structure can be exploited as templates for synthesizing nano-scale photonic devices⁵⁶ or nanowires.⁵⁷ The key advantages of this method are: facile formation of a wide variety of 1 D nanostructured materials like nanotubes; nanowires of controlled dimensions set by the pore dimensions of the template membrane; and the possibility of having different functionality on the inside and outside of the nanotubes, etc.⁵⁸

From the perspective of membranes, the porosity of the anodized membrane is extremely small ($< 10\%$) and very brittle. Laboratory experiences indicate that membranes with smaller pore size are often highly irreproducible. Nevertheless, anodization of aluminium is an interesting approach to synthesize ordered membrane structures with narrow pore-size distribution and small tortuosity and could be extended to other material like titanium or zirconium. These membranes have found applications in size-based separations⁵⁹ and catalytic membrane reactors.⁶⁰

1.4.3 Track-Etch Membranes

A different method for fabricating ordered porous membranes is the track-etch process. When a high energy fission particle traversed a continuous film of mica, it was observed that the track produced areas of high disorder and low crystallinity. These relatively disordered areas could be selectively etched by HF acid to produce hollow channels as shown in figure 1.4 (b). Formation of membranes using the track-etch

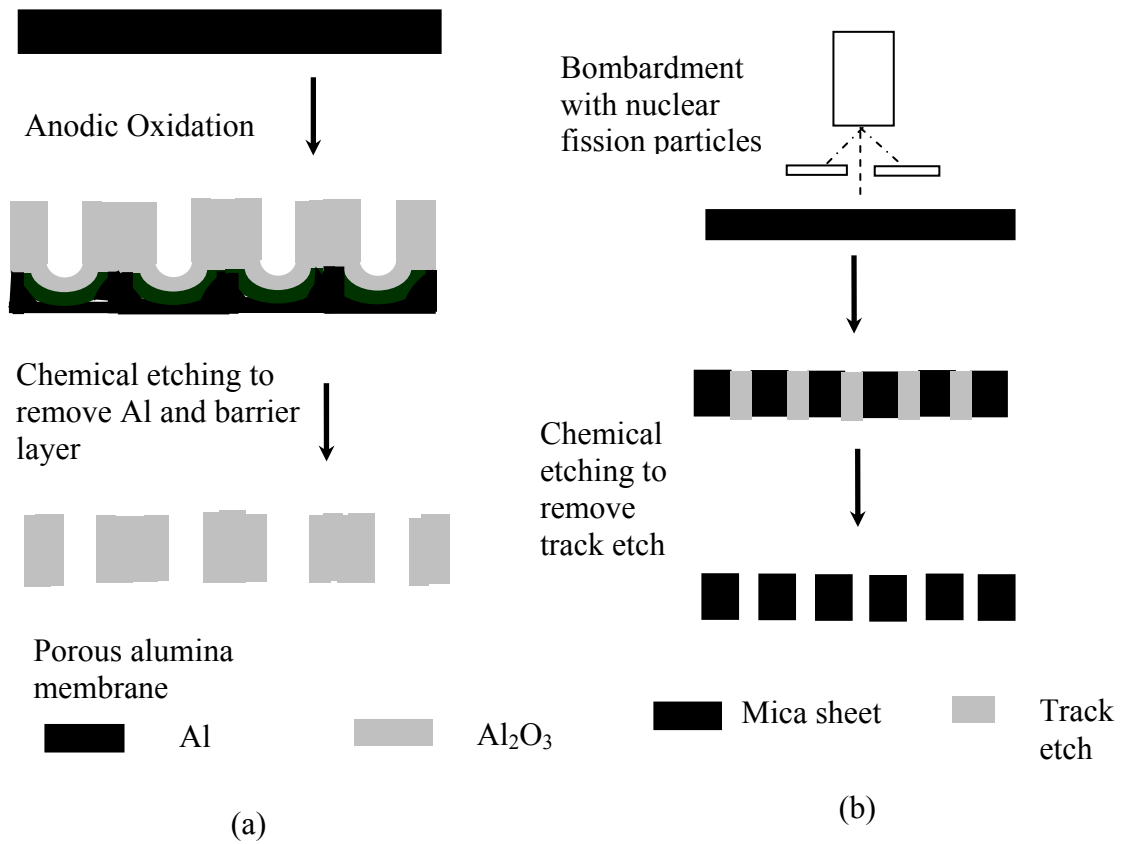


Figure 1.4 Schematic of methods to fabricate ordered porous membranes: (a) anodized alumina and (b) track-etch mica.

process was discovered by Price and Walker.^{61,62} Track-etched mica membranes have served as model membranes to study hindered transport^{63,64,65}, electrolyte transport⁶⁶ and liquid⁶⁷ and gas transport⁶⁸. The pores formed in mica membranes typically have a rhombohedral shape and could be varied from 25 Å to as large as microns depending upon the etching time. The porosity of these membranes is small (< 10%) and is a function of the irradiation time. Parameters like pore density (#/cm²), pore size and pore length can be accurately determined for these membranes. Hence, they are of interest as model membranes.

The process of track etching can be extended to other materials, notably polymer films.⁶⁹ In this case, lower-energy fission particles are used. Commercial membranes are sold by Sterlitech (<http://www.sterlitech.com/>) in the form of polycarbonate and polyester track etch membranes with pore sizes as small as 20 nm. Since the number of pores formed is the same as the number of ions that have impinged, the track-etch process can be controlled to form single pores. Swizy et al.⁷⁰ have carried out fundamental mass-transport studies on conical single-nanopore membranes formed in poly-ethylene terephthalate films. The conical nanopores allow an electric field to be concentrated for non-linear ion-current behavior and rectification.⁷¹

1.4.4 Template Synthesis Approach

Deposition of materials inside the ordered-porous materials formed from anodization or the track-etch process is an interesting approach to synthesizing membranes with smaller pore size. Approaches for deposition of materials inside the existing ordered nanoporous material include: electroless deposition and chemical vapor deposition (CVD). In electroless deposition, the membrane surface is sensitized by an SnCl₂ solution. The Sn²⁺ ions adsorbed on the surface reduce the Au⁺ or Ag⁺ to metallic Au or Ag and form a uniform deposition inside the pores. The most important aspect is that the deposition starts from the walls. Therefore, unlike electro-deposition, hollow tubes are formed (with diameters as small as 0.8 nm), which allow transport of molecules. Such nanotubule membranes have exhibited size-based selectivity⁷² and electrochemically-switchable transport.⁷³ The deposition of Au also allows exploitation of the facile thiol chemistry to chemically change the environment of the transporting

pores.^{74,75} Electric potential applied to these conducting membranes have shown ion-permselectivity, in which the surface charge of the membrane was controlled by the applied potential to control the transport through the membrane.⁷⁶ Single pore conical membranes, discussed earlier, have also been used as templates for forming Au nanotubule membranes. Change in surface charge via chemisorption of thiols with COOH and NH₂ groups have demonstrated change in directionality of ion-current rectification behavior.⁷⁷ A considerably difficult challenge is to design robust surface chemistry strategies on conducting membranes, such that the conformational change of functional molecules could be changed by applied potential for ‘voltage-gated’ control of transport.

A similar approach is to deposit carbon materials inside the pores by CVD.^{78,79} However, the carbon nanotubule membranes synthesized by this method contain amorphous or partially graphitized CNTs and is therefore significantly different from the highly ordered graphite cores of the membranes studied for the present dissertation.

1.4.5 Fabrication of Vertically Aligned Carbon Nanotube Membranes

A contemporary approach is to use as-formed crystalline CNTs and fill up the space between the CNTs by using a polymer⁸⁰ or ceramic filler⁸¹ maintaining the alignment of the carbon nanotubes and open up the CNTs using plasma oxidation chemistry. Researchers in the Hinds group at the University of Kentucky synthesized the first large platform vertically-aligned CNT membrane in an inert polymer matrix. The membranes contained $\sim 10^{10}$ CNTs/cm² with pores ~ 7 nm in interior diameter and allowed macroscopic measurement of transport of ions and gases through the membrane structure.⁸⁰

Since this dissertation is focused on a membrane structure composed of CNTs in a polymer matrix, a brief paragraph on polymer nano-composites is included. Polymer nano-composites are defined as the combination of a polymer matrix and inclusions that have at least one dimension (i.e. length, width or thickness) in the nanometer size. Polymer nano-composites are improved materials in terms of moduli, thermal endurance, flame resistance, barrier properties, abrasion resistance and altered optical and electronic properties. Carbon nanotubes are materials with their diameter in nanoscale and have

exceptionally high mechanical strength, high aspect ratio and electrical conductivity making them attractive candidates as additives in polymer matrices.⁸² Randomly oriented CNTs as reinforcements on polymers have been developed in polymer like poly-vinyl alcohol,⁸³ and polystyrene.⁸⁴ Significant interest is also on developing aligned CNT-polymer composites⁸⁵ for applications including field emission and electromagnetic shielding devices⁸⁶ and membranes.⁸⁰ A very thorough article discussing the mechanism of infiltration of monomers of methyl acrylate in MWNT arrays and subsequent polymerization are discussed by Ravarikar et al.⁸⁷ The choice of polystyrene in this work was dictated by its high wettability⁸⁸ with CNTs and easy film fabrication by a spin-coating process. However, other mechanically-robust polymers and other conformal deposition techniques can be substituted in the membrane fabrication process. The vertically-oriented carbon nanotubes in the polymer matrix often have a graphitic end cap or the catalyst metal particle sealing the graphitic interiors. In order for the vertically-oriented membrane structure to have the nanotubes as transporting channel, it is necessary to remove these materials. Liming Dai and co-workers have demonstrated the feasibility of using the mild plasma oxidation process to remove amorphous carbon layers and open CNTs without destroying the mechanical structure of the CNTs.⁸⁹ Other oxidation processes, including high temperature oxidative treatment⁹⁰ or acidic oxidation treatments, would however, destroy the membrane structure. The elegance of the plasma-oxidation process stems from its controllable oxidation kinetics, and ability to fabricate a macroscopic CNT array device to be fabricated. This plasma-oxidation process, inherent to the membrane fabrication process, performs three very important functions (i) It removes excess polymers by oxidative trimming, since the oxidation kinetics of the polymer (CNT) is faster than that of the CNTs. The CNTs are exposed out of the polymer matrix. (ii) It removes amorphous carbon, Fe impurity (aided by the HCl treatment). (iii) Finally, it introduces functional groups (mainly –COOH) at the CNT tips, which makes them amenable to facile Functionalization-chemistry approaches. The CNT membrane structure after the plasma oxidation process showed a BET pore-size distribution of $\sim 6 \pm 2$ nm, which is consistent with TEM observations of the inner core of ~ 7 nm.⁸⁰ A schematic of the membrane-fabrication process is shown in figure 1.5.

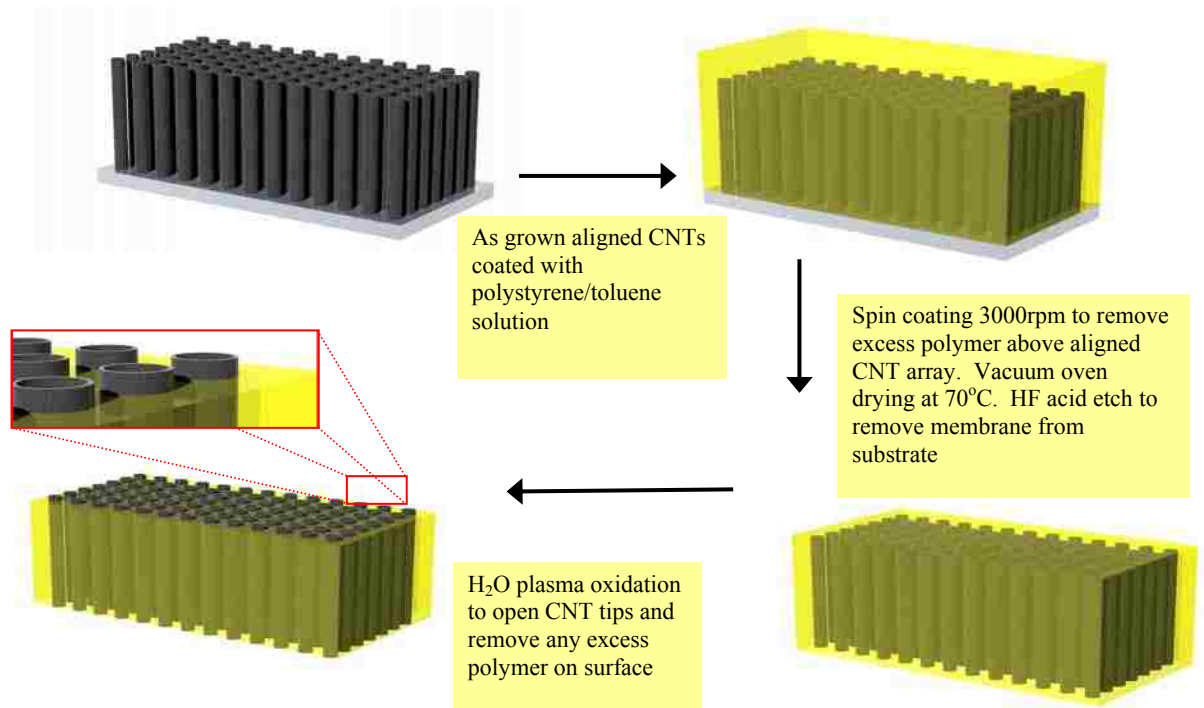


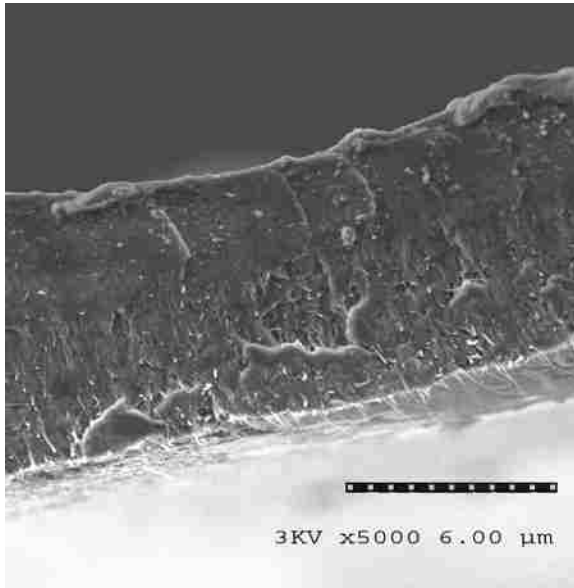
Figure 1.5 Schematic for fabrication of CNT membrane.⁹¹

Further, the CNT membrane showed transport of gases and ionic species. This indicates that the above process is capable of forming a viable membrane structure composed of vertically-oriented open-ended CNT channels, which serve as conduits for molecular transport.

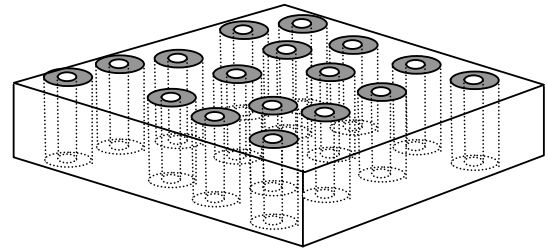
1.5 Goals of the Dissertation

This Ph.D. dissertation focuses on understanding the molecular transport properties through CNTs. Central to the study is the CNT membrane structure, that contains a significantly large number of vertically-aligned carbon nanotubes ($\sim 10^{10} / \text{cm}^2$) allowing macroscopic measurement of transport across the membrane. An SEM image of the membrane structure with aligned CNTs is shown in figure 1.6 (a). Also shown is the pictorial view of the targeted membrane structure with open-ended CNTs and space-filling inner polymer layers.

The principal goals of the dissertation are: to show extremely fast mass transport through the atomically-smooth CNT cores and; confirm that charged molecular tethers attached to the conducting CNT membranes can be changed by applied potential for ‘voltage-gated’ control of molecular transport.



(a)



(b)

Figure 1.6 (a) Scanning electron micrograph of the vertically-oriented CNT membrane and (b) schematic of the targeted structure. Transport through the CNTs is investigated on this macroscopic structure consisting of $\sim 10^{10}$ nanotubes/cm² with ~ 7 nm inner diameter encapsulated in an impervious polymer matrix. The CNTs are opened via a water plasma oxidation process.

Chapter 2

Experimental Methods

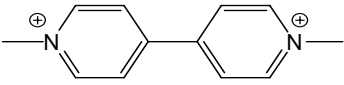
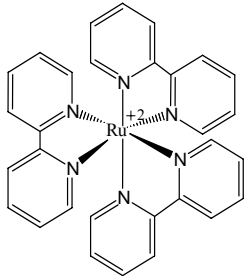
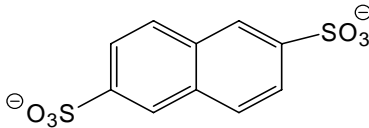
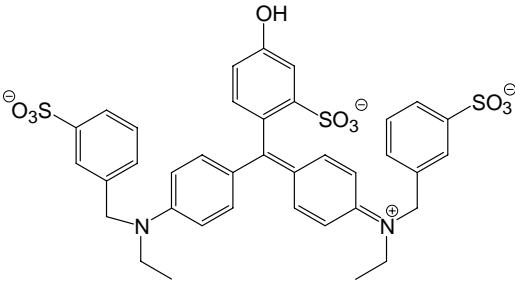
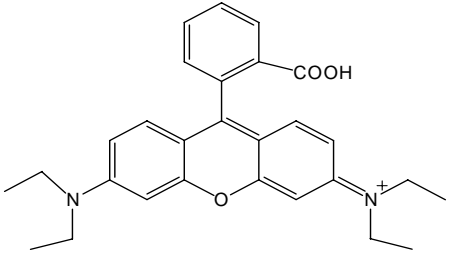
2.1 Synthesis of CNT Membranes

CNT membranes were fabricated using the previously described method. Briefly, a vertically-aligned array of multiwalled CNTs (with ~ 7 nm core diameter) was grown on quartz substrate by chemical vapor deposition (CVD) using a ferrocene/xylene feed gas. The space between the CNTs was filled with a solution of polystyrene and toluene, without disrupting the initial alignment. The composite film was removed from the quartz substrate by HF etching after drying to remove the solvent. Excess surface polymers, as well as Fe nano-crystals at the tips of the CNTs, were removed by H₂O plasma oxidation. This resulted in a membrane structure with open ended CNTs traversing the polystyrene film and carboxylate functionality at the CNT tips. Scanning electron micrographs and a schematic of the targeted structure are shown in figures 1.6 (a) and (b).

2.2. Ionic Transport Measurements

The probe molecules for ionic transport measurements were: Methyl Viologen dichloride hydrate (98 %, Aldrich) [MV²⁺], tris (2,2'-bipyridyl)dichlororuthenium(II) hexahydrate [Ru(bipy)₃²⁺] (Aldrich), 2,6-Naphthalenrdisulphonic acid, disodium salt (97 %, Aldrich) [NDS²⁻], Fast Green FCF (99%, Alfa Aesar), [Dye²⁻], Rhodamine B (Sigma-Aldrich) [Rhod]. The structure of the probe molecules are shown in table 2.1. Figure 2.1 shows the U-tube diffusion cell for in-situ measurement of the probe molecules by UV-vis (USB-ISS-UV/Vis, Ocean Optics Inc.), which was used for these experiments. A quartz cuvette was converted into the permeate cell and inserted into the UV-vis spectrophotometer to obtain the permeate concentration as a function of time. UV-vis spectra were collected at regular intervals after stirring with a glass pipette. Three different solutions were used for the ionic diffusion studies: (i) 5 mM in Ru(bipy)₃²⁺ and 5 mM in MV²⁺ for the +ve charged ions; (ii) 5 mM in NDS²⁻ and Dye²⁻ and; (iii) 5 mM of neutral molecule Rhodamine B. Nine or ten point calibration curves were used for

Table 2.1 Molecules with varying size and charge density for probing the carbon nanotube transport channels through diffusion experiments. Their bulk diffusivity and experimentally-obtained apparent diffusivity through the CNT membrane are shown.

Probe	Structure	Bulk Diffusivity (cm ² /s)	Stoke-Einstein Diameter (Å)	Apparent Diffusivity (cm ² /s)
Methyl Viologen (MV ²⁺)		7.74 x 10 ⁻⁶	6.3	7.92 x 10 ⁻⁶
Ruthenium bi-pyridine (Ru(bipy) ₃ ²⁺)		5.16 x 10 ⁻⁶	9.5	4.78 x 10 ⁻⁶
2,6 naphthalene di-sulfonic acid (NDS ²⁻)		5.77 x 10 ⁻⁶	8.5	4.26 x 10 ⁻⁶
Fast Green (Green Dye ²⁻)		2.90 x 10 ⁻⁶	16.9	1.10 x 10 ⁻⁶
Rhodamine B (Rhod)		3.60 x 10 ⁻⁶	13.62	1.98 x 10 ⁻⁶

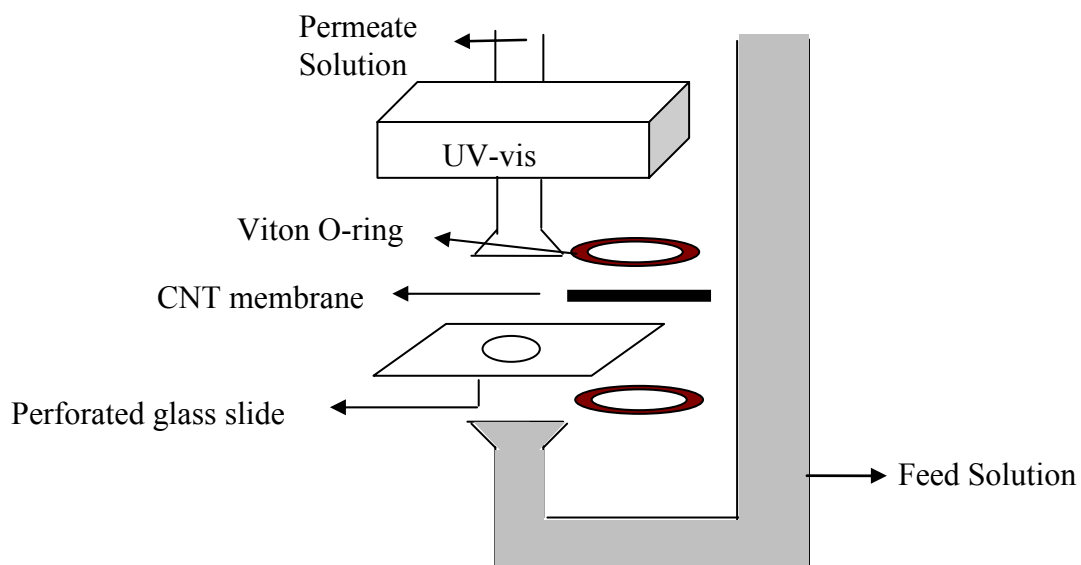


Figure 2.1 In-situ UV-vis based U-tube permeation cell for studying ionic/molecular transport through a CNT membrane. A quartz cuvette is converted into the permeate cell for direct measurement of the diffusion rate. For the diffusion experiments, simultaneous diffusion of two component source solutions containing 5 mM of iso-valent ions were used as the source. For rhodamine, a single component source was used. The exposed membrane area was 0.7 cm^2 .

each analyte as shown in Section A2.1. Flux rates were obtained by fitting a straight line to the time vs. nanomoles transported plot.

2.3 Electrochemical Impedance Spectroscopy Measurement of CNT Membranes

Electrochemical impedance measurements (EIS) were carried out in the frequency range of 100kHz-0.2Hz with sinusoidal amplitude modulation of 10mV using a model 263A Potentiostat and FRD 100 frequency response analyzer from Princeton Applied Research. The electrochemical cell consisted of: as-prepared CNT membrane or diazo-grafted CNT membrane on a platinum support plate as a working electrode; Ag/AgCl (sat. KCl) as a reference electrode; and a platinum wire as a counter electrode. Non-Faradaic EIS measurements were performed at various potentials in aqueous 0.1M KCl and 0.01M KCl solutions with 10mM K₂CO₃ (pH=10.8). The pH of the solution was altered by adding small quantities of HCl or KOH in solution. The stabilization time was found experimentally and the CNT membrane was soaked for at least 6 hours in electrolyte solution before taking the measurements. All reported values are averaged from at least 10 measurements. The capacitance was calculated from the slope of the linear part in the log|Z| vs the log(ω) plot at intermediate frequencies, corresponding to electrode/electrolyte interface electric double layer capacitance.⁹² Faradaic impedance spectra was measured in 0.1M KCl and 10mM K₂CO₃ in the presence of 5 mM [Fe(CN)₆]^{3-/4-} redox couple, at bias potential of 230mV vs Ag/AgCl.

2.4 Liquid Transport Measurements

Pressure-driven liquid transport through the CNT membranes were measured in an experimental set-up detailed in figure 2.2. Briefly, the membrane was assembled in the flow cell and a syringe pump provided the required pressure to drive the liquid through the membrane. The weight of the liquid permeating the membrane was measured in real time on a pan balance interfaced with a laptop computer using Balance Talk SL[®] software from Labtronics.

All associative liquids (water, isopropyl alcohol (IPA), ethanol (EtOH)) were treated in a vacuum oven for 12-24 hours and allowed to cool in the vacuum. For

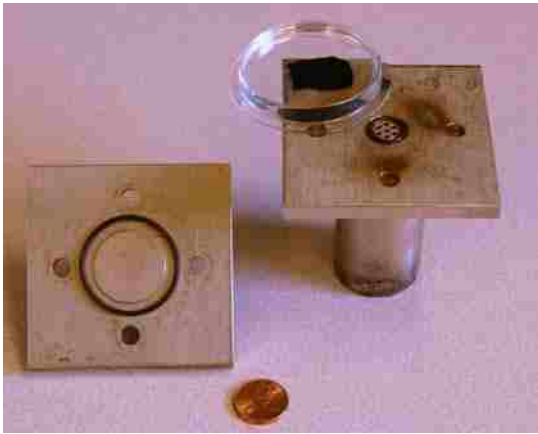
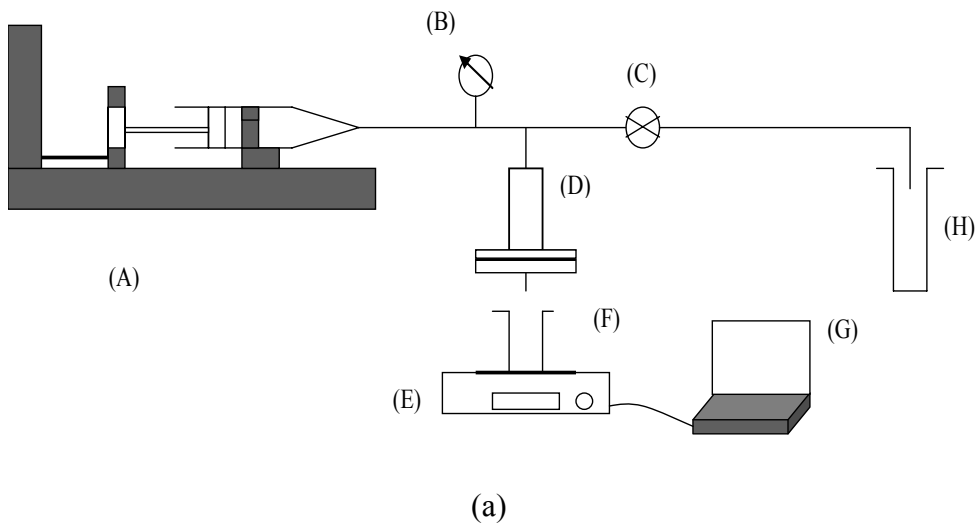


Figure 2.2 (a) Schematic of the apparatus used for the liquid transport measurements; (A) Piston Pump (WPI Inc.), (B) Pressure sensor (Omega, PX 603), (C) Precision Needle Valve (Ideal valve), (D) Home made SS Flow cell (membrane area 0.785 cm^2), (E) Pan Balance (Denver Instruments, APX-1502), (F) Beaker for collecting permeate, (G) Lap top for data acquisition, (H) beaker for collecting by-pass liquid. (b) Photograph of pressure flow cell (D). The aligned CNT membrane is supported on porous metal disk (right) and the top seal is made of a viton o-ring

measurements of different liquids on the same membrane, the membrane was dried in air for 12 hours and then soaked in the solvent for 1-2 hours prior to the experiment. The syringe was then filled with the liquid and the pipe-line is purged with the liquid at 2.5 ml/min flow rate, keeping the valve completely open so that any air in the pipes was driven away. Thereafter, the valve was gradually closed manually to increase pressure inside the flow cell. Once a drop of liquid was seen coming out of the nipple, the data acquisition in the computer began. Time-dependent pressure data was also collected manually. The zero time for the flow experiments was the time to notice the first drop of liquid coming out of the nipple. So, there was a systematic error (due to the hold-up volume) in determining the initial permeability. This was significant for the associative liquids, where the flow rate declined with time. Therefore, an estimate of the hold-up volume was also made. The weight of the bottom plate with a small piece of paraffin was first taken. In place of CNT membrane, PAN membrane was used and pressure flow was conducted. The pump was next stopped and the last drop was allowed to fall out of the nipple. The piece of paraffin was used to close the opening of the nipple and then the flow cell was disassembled. Water poured from the top cell and water from the bottom cell was dried with Kimwipes and weighed. The difference between the initial and final weights gives the hold-up volume and was found to be $\sim 0.5 \text{ cm}^3$.

2.5 Gas Transport Measurement

For gas transport measurements, the same flow cell and gas cylinders were used instead of the syringe pump. A small (2mm) diameter glass capillary was attached to the exit of the flow cell. A liquid droplet of $\sim 30 \mu\text{l}$ was placed inside the capillary, and the volumetric flow of gas permeating was found by timing the movement of the water meniscus between two fixed marks on the glass capillary (figure 2.3).

A 3-step purging protocol was followed to fill the flow cell with gas from the cylinder. (i) The gas line was purged with the gas for 2-3 minutes. (ii) The control valve was fully opened and the on-off valve was closed so that gas was allowed to fill the flow cell. The pressure rose to $\sim 15 \text{ psi}$. (iii) The valve on the cylinder was closed and the on-off valve was opened to relieve the pressure. Steps (ii) and (iii) were repeated ~ 10 times to dilute any residual of the held-up gas volume in the flow cell. The flow rate through

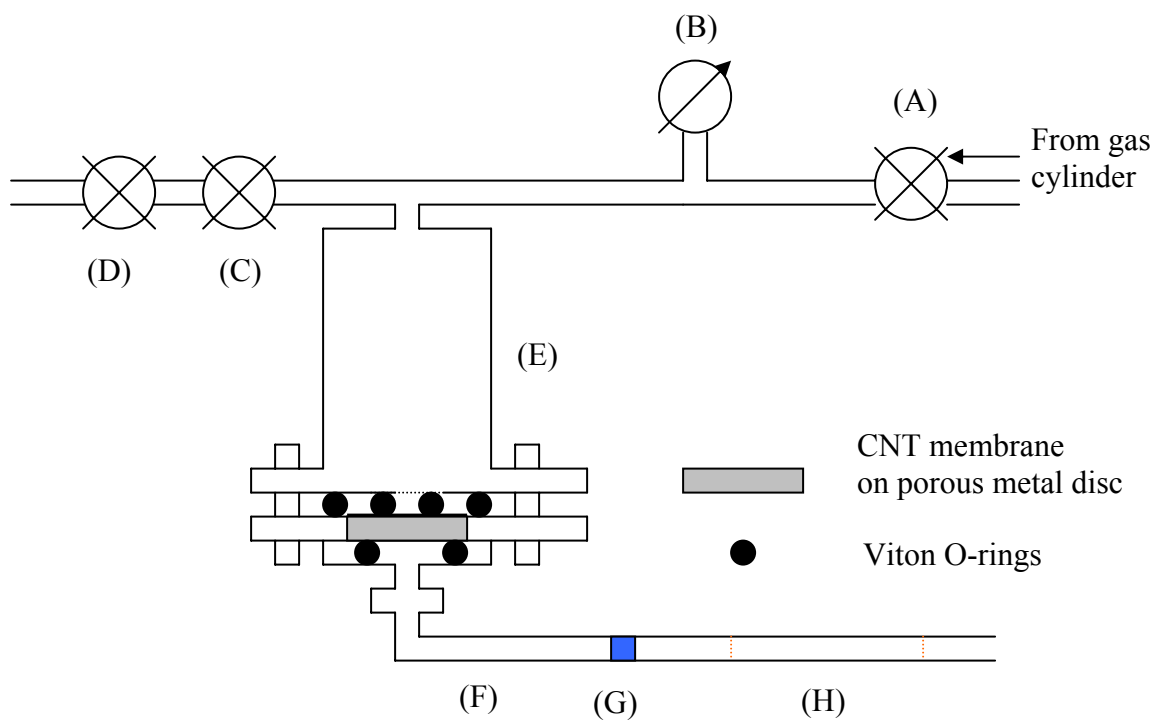


Figure 2.3 Experimental set-up for studying gas transport through CNT membranes. Different components of the apparatus are: (A) pressure regulator, (B) pressure transducer (Omega, PX603), (C) on-off valve, (D) precision needle valve, (E) home made flow cell (membrane area $\sim 0.78 \text{ cm}^2$), (F) horizontal glass bore capillary of 2 mm diameter, (G) liquid marker, (H) Distance of 10 cm on the capillary. A purge protocol was followed to displace the air inside the flow cell and fill with gas from the cylinder. The flow rate through the membrane was measured by timing the movement of a fixed volume (30 μl) of liquid marker inside the glass capillary.

the glass capillary was calibrated using a syringe pump. The volumetric flow rate through the membrane was measured as a function of the pressure. A linear plot of volumetric flow rate per unit area of the membrane vs. pressure was obtained, and the slope of the plot described the permeability of the membranes.

2.6 KCl Diffusion Experiments for Estimation of Porosity

The pore density and porosity of the membranes were estimated using KCl diffusion through the membrane. The feed solution was 7.5 cm³ of 669 ppm of KCl (standard solution). The permeate volume was 1.5 cm³. The maximum concentration measured was 25 ppm. Thus, the total mass of KCl in the feed solution was about 2 orders of magnitude greater than that in the permeate, eliminating depletion effects. Both the feed and the permeate cells were stirred with a magnetic stirrer. The conductivity of the permeate was monitored by a conductivity electrode (Microelectrodes Inc.), connected to a conductivity meter (Orion 150 A+ conductivity meter) and the data were collected in a spreadsheet using Balance Talk SL (Labtronics) every 15 minutes. The conductivity meter was calibrated using 66.9 ppm standard solution before the start of any experiment. The conductivity data were converted into flux data using an appropriate calibration plot of ppm of KCl vs. conductivity. Typical experimental data of KCl diffusion are shown in figure A2.3.1. The permeable pore area (A_p) can be estimated from the equation:

$$A_p = \left(\frac{J \times l}{D \times C} \right)$$

where D is the bulk diffusivity of KCl at 21 °C (~ 1.96 x 10⁻⁵ cm²/s); C is the concentration of the feed (8.97 x 10⁻³ M); l is the membrane thickness (from SEM cross sectional pictures); and J is the experimental steady state flux of KCl (mole/s). The porosity (ε_p) of the membrane and the permeable pore density can be calculated from:

$$\varepsilon_p = \left(\frac{A_p}{A_m} \right)$$

$$\text{Permeable pore density (\#/cm}^2\text{)} = \frac{\left(\frac{A_p}{A_m}\right)}{\frac{\pi d^2}{4}}$$

where d is the pore diameter (7 nm); and A_m ($\sim 0.3 \text{ cm}^{20}$) is the membrane area exposed in the diffusion experiment. Salt rejection of the CNT membranes was determined by analyzing the permeate during pressure flow of 1.7×10^{-2} (M) KCl. Minimal ($\sim 4\%$) salt rejection was observed. Thus, there is not a significant underestimation of A_p from surface charge repulsion.

2.7 Functionalization of CNT Membranes

The CNT membranes were functionalized using well known carbodiimide chemistry. The following chemicals were used for these reactions: 1-[3-(dimethylamino)propyl]-3-ethylcarbodiimide hydrochloride (EDC, 98%, Aldrich), nonyl amine (C9, 98%, Aldrich), Direct Blue 71 (dye, Aldrich), 8-amino caprylic acid (ACA, 99%, Aldrich), Kemamine P-298D, (C22, Crompton Corporation, USA), 2-N-morpholino ethanesulfonic acid (MES, 99%, Sigma), isopropyl alcohol (99.5%, EMD), and Ethyl alcohol (Aaper Alcohol and Chemical Co., Kentucky). For reactions in water, D.I. water ($\sim 18 \text{ M}\Omega$ resistance) was used. The functional molecules are shown in figure 2.4.

For the water-soluble molecules, 8 mg of EDC was dissolved in a 50 mM aqueous solution of C9 or dye in 0.1M MES buffer and then the membrane was added to it. The reaction was carried out for 12 hours at ambient temperature after which the membrane was washed with MES buffer and IPA to remove the excess reagents. EDC-based coupling reactions were carried out in an alcohol medium.⁹³ The functionalized membranes will henceforth be referred as CNT-C9 and CNT-dye. Kemamine is a commercial fatty amine containing about 90% C22. It is insoluble in water, but soluble in IPA at 35 °C. 32.36 mg of C22 and 8 mg of EDC was added to 4 ml of IPA along with the membrane and kept in a water bath at 35 °C for 12 hours and then washed with ethyl alcohol. The functionalized membrane will henceforth be referred as CNT-C22.

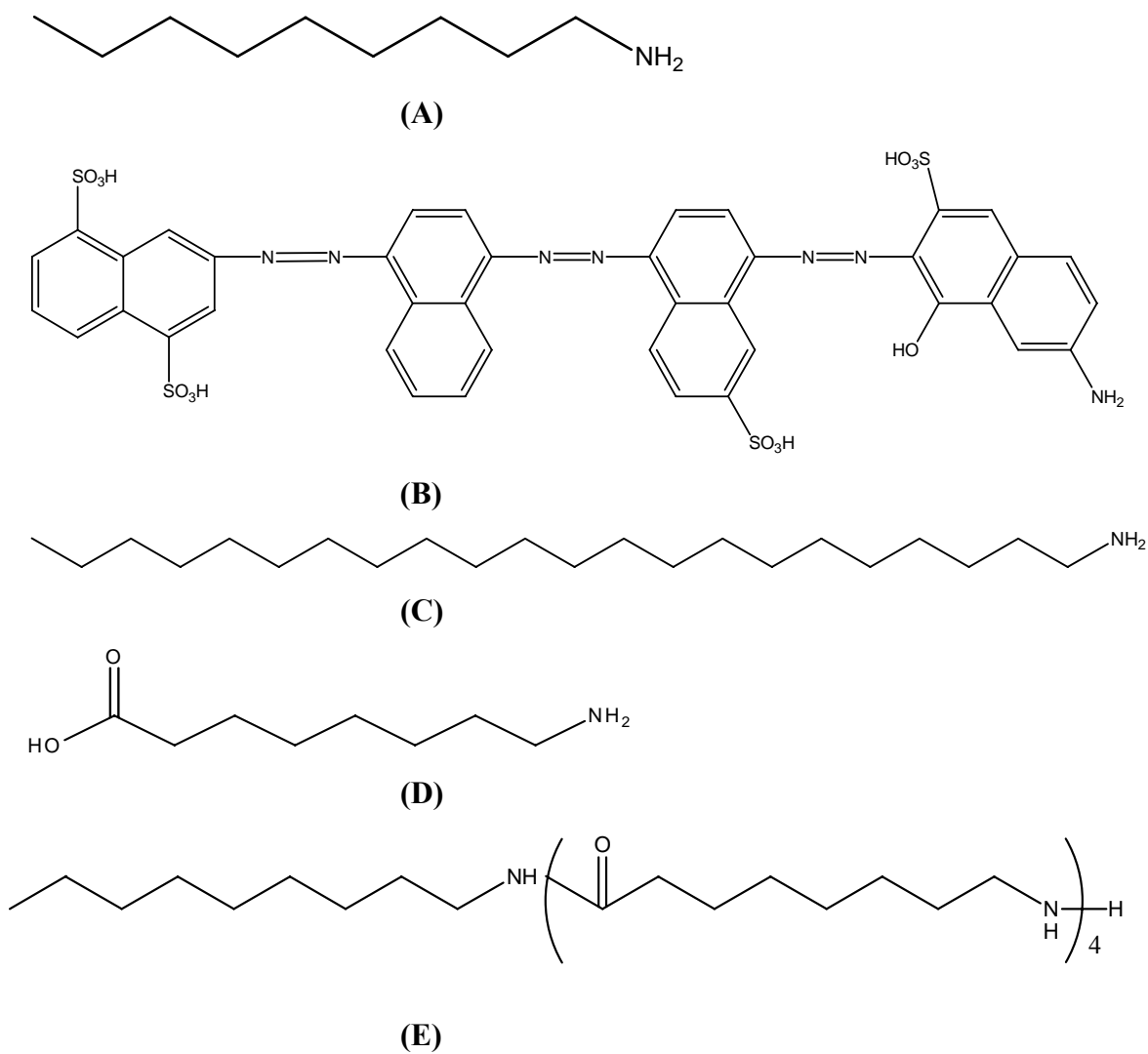


Figure 2.4 Schematic of the molecules used for functionalizing nanotube membrane (A) C9; (B) Dye; (C) C22; (D) ACA (E) C40 (polypeptide) (formed after four sequential reaction of ACA, followed by C9)

ACA is an 8 carbon atom molecule, containing terminal COOH and NH₂ groups. The membrane was first surface activated in 4 ml of 0.1M MES by 8 mg EDC. The membrane was then placed into a 50 mM solution of ACA in a 0.1M MES buffer. Functionalization was thus carried out in two steps: activation with terminal COOH groups with EDC and; then a reaction with ACA. This process avoids polymerization of ACA and sequentially adds peptides to the membrane surface.

These two steps were repeated four times to increase the spacer length and then finally functionalized with C9 according to the method described earlier. The membrane was washed with MES buffer and then with IPA. The functionalized membrane will henceforth be known as CNT-C40 (polypeptide). Tip functionalization molecular length was estimated by minimizing conformational energy using MM₂ routine.

2.8 FTIR Studies

The membrane was dissolved in toluene and (Mallinckrodt, 100%), then centrifuged to remove the polymer. The purified nanotubes in toluene were then mixed with FTIR-grade KBr (Sigma-Aldrich, >99%) and dried in the vacuum oven. The dried powder was then examined in ThermoNicolet Nexus 4700. FTIR spectra were analyzed after subtraction of KBr spectra from each.

2.9 U-tube Permeation Experiment

A schematic of the U-tube cell is shown in figure 2.5. The seal between membrane and cell is made with a vitron o-ring and the liquids in the two chambers were maintained at the same level to avoid any pressure induced transport. The probe molecules (Methyl viologen dichloride hydrate and Ruthenium bi-pyridine hexahydrate) were purchased from Aldrich. The probe molecules were chosen for their ease of detection by UV-vis and direct comparison of fluxes and selectivities with other nanoporous systems.⁷³ The permeate was periodically pipetted out, the probe molecules readily quantified by UV-vis spectroscopy (HP 8543 Spectrophotometer) and then transferred back to the chamber. Ru(bipy)₃²⁺ has two peaks at wavelengths of 452 and 286 nm, whereas MV²⁺ has a peak at 260 nm. The peak at 452 nm is used to quantify the

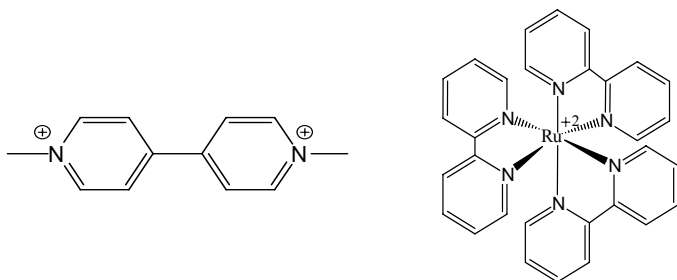
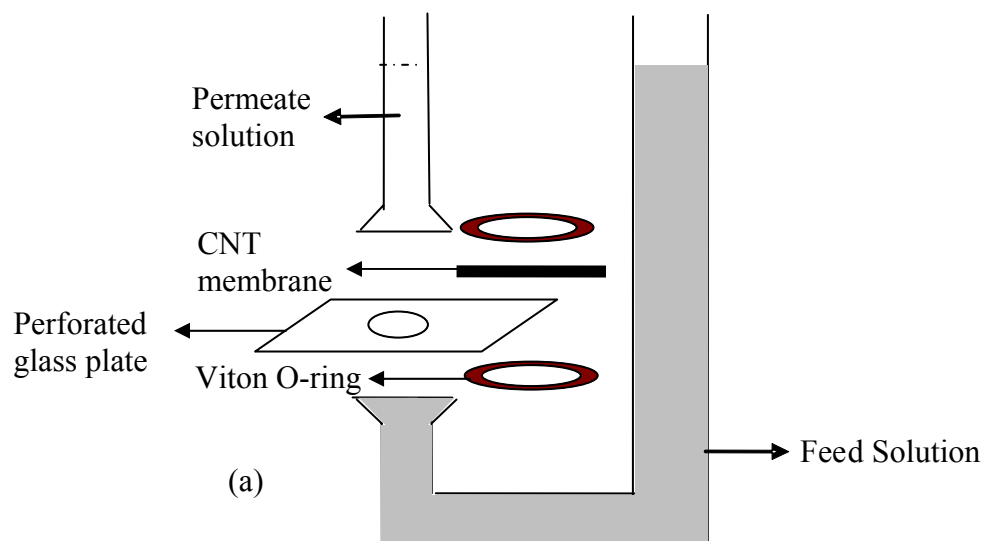


Figure 2.5 (a) Schematic of permeation cell, the feed solution is 5 mM in $\text{Ru}(\text{bipy})_3^{2+}$ and 5mM in MV^{2+} . The permeate volume is 1.3 ml, and exposed membrane area is 0.3cm². (b) The probe molecules have similar charges, but different sizes and shapes. $\text{Ru}(\text{bipy})_3^{2+}$ is a spherical molecule of about 11 Å diameter; MV^{2+} is a cylindrical molecule of 5 Å equivalent spherical diameter (10 Å long, 3 Å diameter).

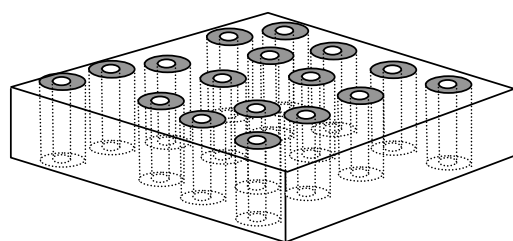
amount of $\text{Ru}(\text{bipy})_3^{2+}$. The MV^{2+} peak at 260 nm has interference from the amount of $\text{Ru}(\text{bipy})_3^{2+}$, due to the peak at 286 nm. So, the contribution at 260 nm from the peak at 452 nm is deducted from the absorbance value at 260 nm and then used to quantify MV^{2+} . For quantifying the amounts of $\text{Ru}(\text{bipy})_3^{2+}$ and MV^{2+} , 6 point calibration curves (from $5 \times 10^{-4} \text{M}$ to $1 \times 10^{-6} \text{M}$) were used.

2.10 Synthesis of 4- carboxy phenyl diazonium tetrafluoroborate

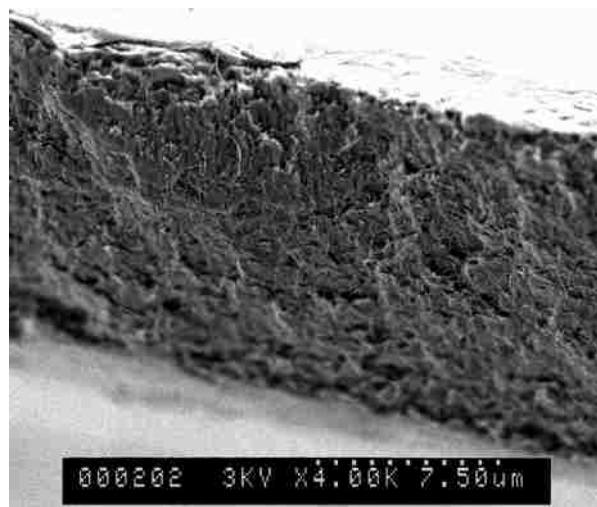
Synthesis of the diazonium compound from p-aminobenzoic acid was carried out following a method of Belanger et al.⁹⁴ About 2.74g (0.02 mole) p-aminobenzoic acid (Aldrich) was dissolved in 20ml water, which was heated to about 50 °C until it was dissolved. Then, 0.044 moles of concentrated HCl was added dropwise to the solution, followed by the cooling of the solution to -3 °C. Thereafter, 0.022 mole NaNO_2 (Sigma) in 10ml water at 0 °C was added slowly to the solution. The reaction was allowed for 1 hour. The solution was filtered; then 0.022 mole of NaBF_4 (Aldrich) solution was added to the filtrate at -3 °C. A light yellow precipitate was formed. The precipitate was filtered and washed with ice water and cold ether. Starting from 2.75g of p-aminobenzoic acid, about 1.52g of the diazonium salt (F.W. 236) is obtained. This gives a molar yield of ~ 30%. The white (or slightly yellow) crystals was dried in a vacuum and preserved in a dessicator at 4 °C. Care should be taken not to mechanically agitate the white crystals as the product is potentially explosive. NMR H^1 (CDCl_3): (4-carboxyphenyl)-diazonium tetrafluoroborate, two doublets, 8.87-8.83 and 8.46-8.42 ppm.

2.11 Electrochemical Grafting

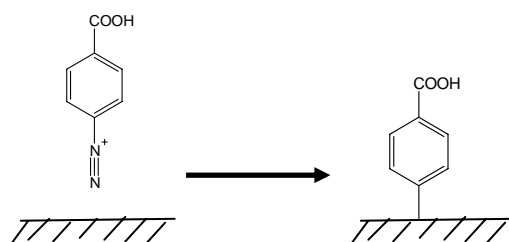
The aligned multiwalled CNT membranes have significant in-plane conduction due to crossing of the CNTs, allowing it to be used as a working electrode in a three-electrode cell (figure 2.6 (a) and (b)). A schematic of the electro-reduction diazonium grafting chemistry is shown in figure 2.6(c). In most literature precedences, acetonitrile was used as the solvent. However, suspected mechanical instability of the polymer (polystyrene) in acetonitrile required us to use an aqueous recipe similar to Corgier et al.¹⁸⁹ Cyclic voltammetry at 200 mV/s in 5 mM of the 4-carboxy phenyl diazonium tetrafluoroborate, 0.1M KCl and 0.1M HCl showed an irreversible reduction at -0.6 V,



(a)



(b)



(c)

Figure 2.6 (a) Schematic of the aligned multiwalled CNT membrane structure and (b) Scanning Electron Micrograph (SEM) of the cross-section of the CNT membrane. The CNT membranes have significant in-plane conduction due to modest tortuosity allowing CNTs to cross. (c) Schematic of electrochemical reduction of (4-carboxyphenyl)-diazonium tetrafluoroborate on the carbon nanotube membrane leading to covalent attachment of benzoic acid groups to the conducting graphitic surface.

which is quite close to the voltages reported for reduction of diazonium compounds. The apparatus used for the electro-chemical grafting reactions was a 3 electrode cell, with Ag/AgCl as the reference electrode, a Pt wire as the counter electrode and the CNT membrane as the working electrode (Fig.2.7). The glass support plate was covered with a Cu tape and a wire was attached to the Cu tape using Ag paste. An alligator clip was connected to this wire. Such an arrangement was necessary to maintain the mechanical integrity of the membranes for further experiments. For FG, the perforated glass plate was covered with a perforated Cu tape. In both cases a clamp held all the pieces together. All grafting reactions were carried out potentiostatically at -0.6 V with constant Ar purging. For the static-grafted membrane, [figure 5.2(a)] henceforth referred to as CNT-SG, the reaction time was 2 minutes for each side of the membrane. For flow grafted membrane [figure 5.2(b)], henceforth referred to as CNT-FG, a liquid column 0.1M in KCl and 0.1M in HCl and 8-13 cm height (H) provided a positive pressure on the membrane to concentrate the grafting reaction on the tips of the CNTs. For direct comparison with the CNT-SG, the time of grafting was a total of 4 minutes on one side only. After the grafting reaction the membranes were rinsed with water, 0.1M KCl and IPA to dissolve any unwanted byproducts.

2.12 Dye Adsorption-Desorption Assay

CNT membrane was incubated in a Toluidine Blue O (TBO, Sigma) solution at pH 10 and room temperature for 5 hours to coordinate the cationic dye with anionic carboxylate groups. The membrane was then rinsed with deionized water and kept in 0.1 M NaOH solution for 5 minutes to remove non-complexed TBO. The complexed TBO was desorbed in a 50 % (v/v) acetic acid solution. The concentration of desorbed TBO in acetic acid solution was determined by the absorbance at 632 nm using UV-vis Spectroscopy (USB-ISS-UV-vis, Ocean Optics Inc.). The calculation of carboxyl functional density was based on the assumption that positively charged TBO binds with carboxyl groups of CNT membrane at 1:1 ratio and on the planar geometrical area of the membrane.⁹⁵

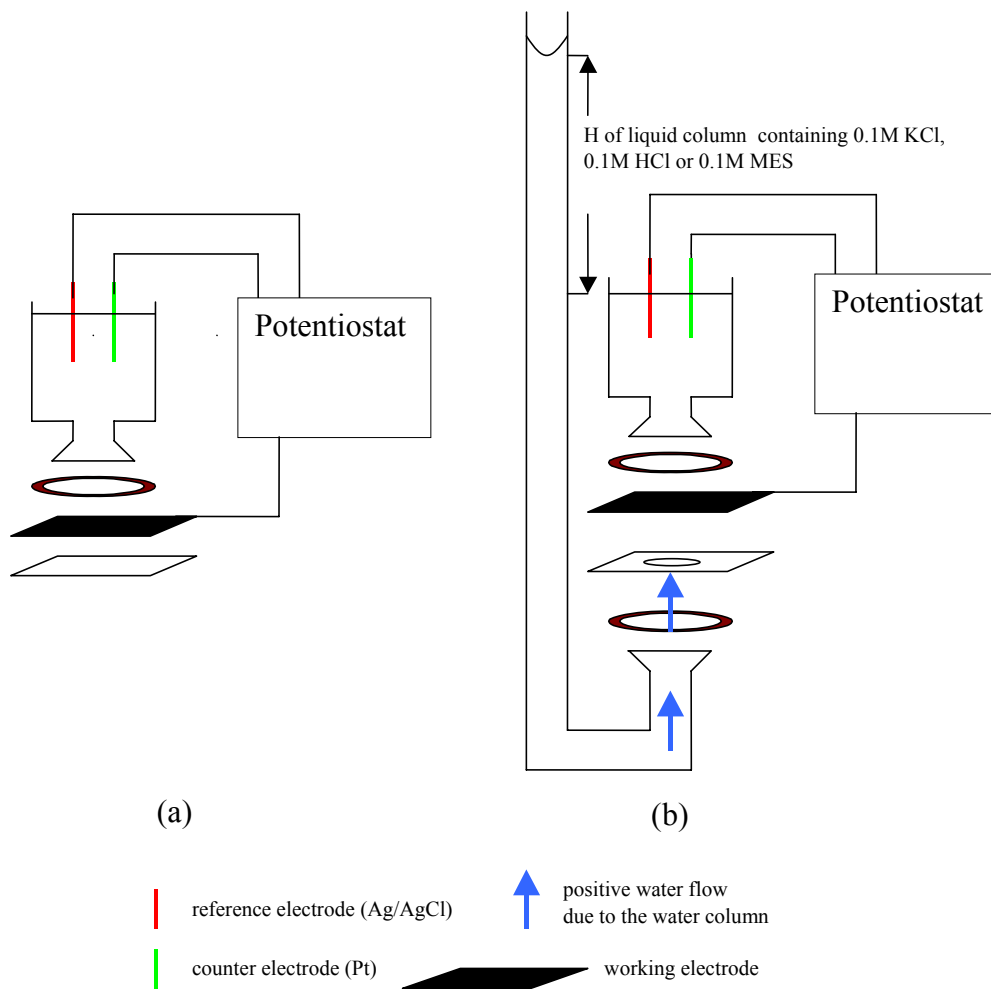


Figure 2.7 Apparatus for (a) Static Grafting (SG); and for (b) Flow Grafting (FG). H determines the height of the liquid column, hence, the high flow velocity through the membrane, forcing preferential reaction at the CNT tips.

2.13 Functionalization of CNT Membrane/Electrodes

After the diazonium grafting reaction the CNT membranes were functionalized using carbodiimide chemistry. The following chemicals were used for functionalizing the CNT-SG and CNT-FG membranes: 1-[3-(dimethylamino)propyl]-3-ethylcarbodiimide hydrochloride (EDC, 98%, Aldrich), Direct Blue 71 (dye, Aldrich), 8-amino caprylic acid (ACA, 99%, Aldrich), 2-N-morpholino ethanesulfonic acid (MES, 99%, Sigma). For all reactions, D.I. water (~18 M Ω resistance) was used. For dye functionalization, 8 mg of EDC was dissolved into 4 ml of 50 mM aqueous solution of the dye [figure 2.8 (a)] in 0.1M MES buffer. The membrane was added to the solution for 12 hours at ambient temperature, after which the membrane was washed with MES buffer and KCl containing water to remove the excess reagents. The spacer molecule was formed by sequential reaction of ACA [figure 2.8(b)]. For ACA functionalization, the membrane was first surface activated in 4 ml of 0.1M MES by 8 mg EDC. The membrane was then placed into a 50 mM solution of ACA in 0.1M MES buffer. Functionalization was thus carried out in two steps: 1) activation of terminal COOH groups with EDC and 2) reaction with ACA. This process avoids polymerization of ACA and sequentially adds the molecule to the membrane surface. This sequential additional step was carried out 2 times. Thereafter, the electrode was functionalized with the dye molecule. The functionalized membrane/electrode will henceforth be referred to as CNT-DG-dye (figure 2.8(c)) and CNT-DG-spacer(polypeptide)-dye (figure 2.8 (d)). For the voltage-gating experiments (Chapter 6) a similar chemistry was utilized. The idea behind the functionalization reactions was to form a molecular actuator with a rigid, but highly charged end-group, connected to the conducting CNT pores by a mechanically-flexible spacer [figure 2.9(a)]. The spacer molecule was formed by sequential reaction of ACA [Fig 2.9(b)]. The charged end-group was provided by the dye molecule [figure 2.9(c)] containing four SO₃⁻ groups per molecule. Earlier experiments indicated the need to increase the functional density on the CNT surfaces to provide a measurable response of 'voltage-gated' transport through CNT membranes. Functional density was increased by electrochemical grafting of the diazonium compound as discussed in the earlier section. Two sequential reactions of ACA followed by

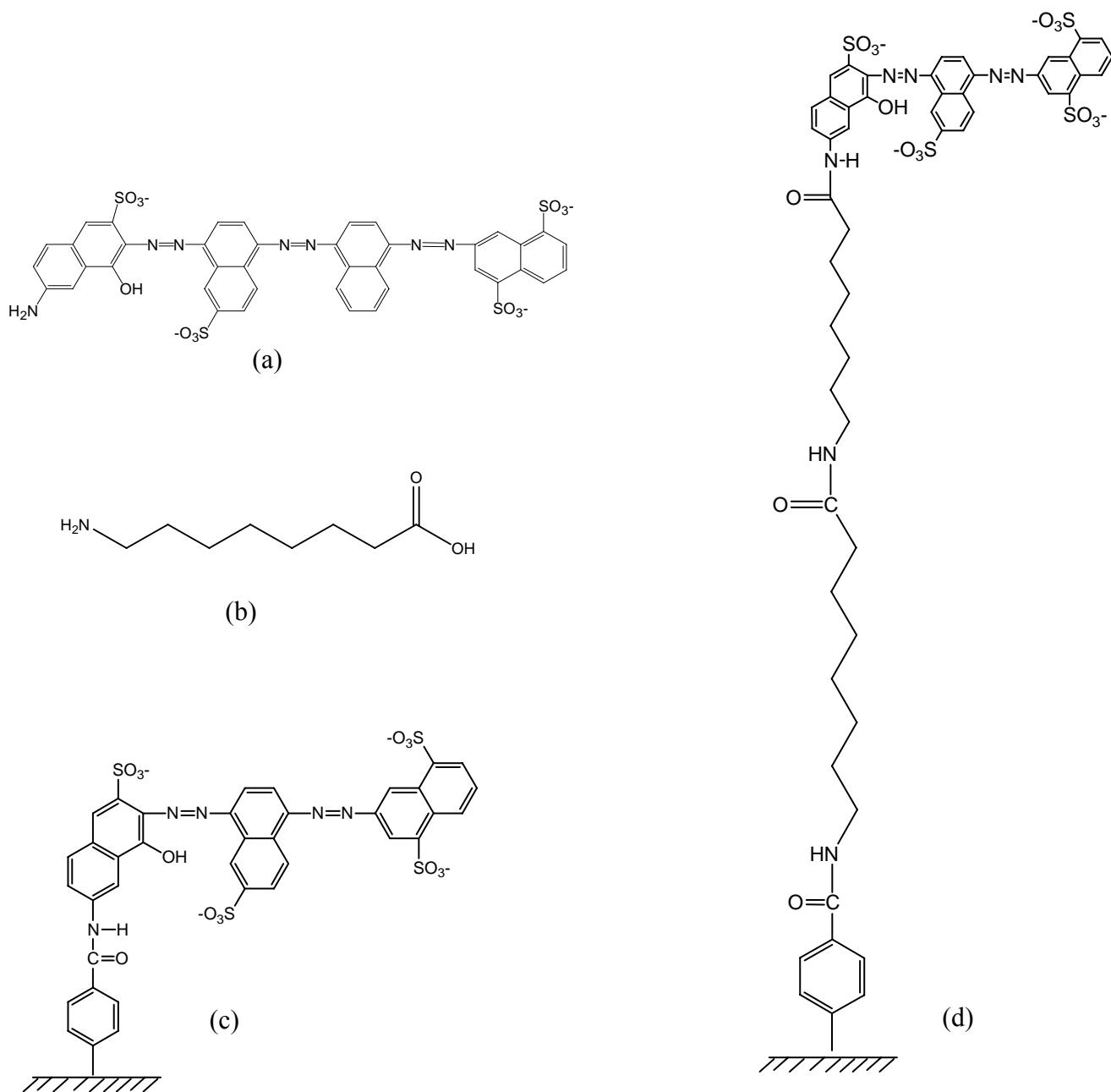


Figure 2.8 Schematic of the functionalizing molecules (a) dye; (b) 8-amino caprylic acid; (c) CNT- DG-dye formed by sequential diazo-grafting and dye functionalization; (d) CNT-DG-spacer-dye formed by sequential diazo-grafting, 8-amino caprylic acid and dye functionalization.

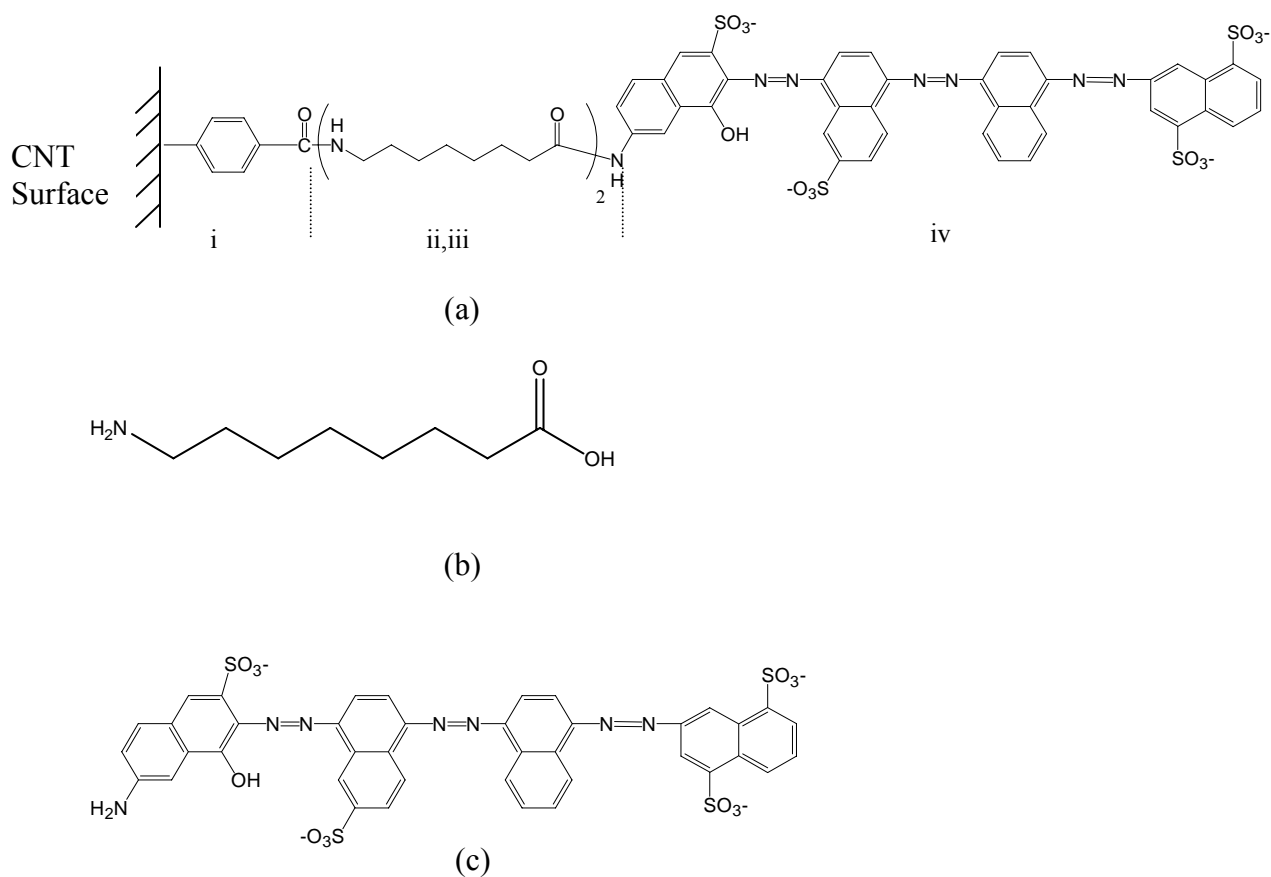


Figure 2.9 (a) Schematic of the **actuator molecule** formed on the CNT membranes by four sequential reactions: (i) **4-carboxy phenyl diazonium⁺** grafted onto a conducting CNT surface by electrochemical grafting to form a surface **4-carboxy phenyl group**; (ii) Attachment of **ACA** (b) using carbodiimide mediated coupling between COOH group of electrochemically grafted **4-carboxy phenyl group** and NH_2 group of **ACA** (b) (iii) Coupling of COOH group of **ACA** (b) and NH_2 group of **ACA** (b) ; (iv) Carbodiimide coupling of terminal COOH of **ACA** and NH_2 group of the highly anionic **dye** (c) molecule.

functionalization with dye were carried out following a procedure described in this section. The functionalized membranes will henceforth be referred to as CNT-SG-spacer (polypeptide)-dye. For flow grafted membrane, similar functionalization sequences and concentrations of reactants were used, except that a column of water containing MES buffer provided positive pressure on the membrane to preferentially functionalize the molecules at the tips of the CNTs (as shown in figure 2.7(a)). The functionalized membrane will henceforth be referred to as CNT-FG-spacer (polypeptide)-dye.

2.14 Estimation of Porosity of Membranes from Methyl Viologen Flux

The porosity of the membranes used in the voltage-gating studies in Chapter 6, were evaluated from the steady-state MV^{2+} flux through the plasma oxidized membrane from the relations:

$$A_p = \frac{J\Delta x}{D\Delta C} \quad \varepsilon = \frac{A_p}{A_m} \times 100$$

where, A_p (cm^2) is the available pore area, J (mole/s) is the experimental steady state flux of MV^{2+} , Δx (cm) is the thickness of the membrane evaluated from cross-sectional scanning electron micrographs, ΔC (mole/ cm^3) is the concentration of the difference between the feed and the permeate, ε is the porosity of the membrane, A_m (cm^2) is the membrane area exposed to the solution. For our case, the concentration of the feed is 5 mM and A_m is 0.3 cm^2 . An assumption implicit in this estimation, is bulk diffusivity of MV^{2+} ($D = 7.74 \times 10^{-6} \text{ cm}^2/\text{s}$) inside the CNTs with $\sim 7 \text{ nm}$ core diameter.

2.15 Transport Measurements for Voltage-Gating and Electrically Facilitated Transport

The probe molecules, ruthenium bipyridine hexahydrate $[\text{Ru}(\text{bipy})_3]^{2+}$ and methyl viologen dichloride hydrate $[\text{MV}^{2+}]$ were purchased from Aldrich. A solution 5 mM in $\text{Ru}(\text{bipy})_3^{2+}$, 5 mM in MV^{2+} and 0.1M in KCl (supporting electrolyte in voltage dependent experiments) was used as the feed solution. Deionized water containing 0.1M KCl was used in the permeate cell. For the voltage-gating studies, experiments were carried out in a U-tube permeation cell as shown in figure 2.10. The membrane served as the working electrode in a three-electrode cell, with a Pt wire counter electrode and an

Ag/AgCl (sat. KCl) reference electrode. For the transport studies in the cross-potential mode, a different geometry of the electrode was used. In this case, the working electrode was placed in the permeate cell (figure 2.11). This allowed an electrical potential gradient to be applied across the membrane allowing for experimentally studying electrically-facilitated transport across the membrane. Constant potential was applied using Potentiostat/Galvanostat Model 263, of Princeton Applied Research and the potentials reported are w.r.t. Ag/AgCl (sat. KCl) electrode. There is an inherent asymmetry in the functionality of the CNT-FG-spacer (polypeptide)-dye membrane, as the functional groups are concentrated at one end of the membrane. For the experiments on CNT-FG-spacer dye, the functional end of the membrane was placed on the permeate side of the cell. In Section A6 the opposite geometry; i.e., the functional end of the membrane on the feed side of the u-tube cell is compared. Concentration of $\text{Ru}(\text{bipy})_3^{2+}$ and MV^{2+} in the permeate was measured after 15-40 hours of diffusion experiments using UV-vis Spectrophotometer (USB-ISS-UV-vis, Ocean Optics Inc.). The porosity of the membranes used for this study is small ($\sim 10^{-4}\%$), so the overall transport through the membrane was extremely slow. In order to obtain consistent measurements in the UV-vis spectrophotometer, it was necessary for long measurement times so that sufficient amounts of the probe molecules had permeated. The MV^{2+} flux was calculated from the peak at 260 nm. The $\text{Ru}(\text{bipy})_3^{2+}$ has two peaks at 286 and 452 nm. For most experiments the intensity at 452 was too low to get consistent flux data. Hence, the more sensitive peak at 286 was used for estimating $\text{Ru}(\text{bipy})_3^{2+}$ flux. Contribution to the absorbance at 286, by the MV^{2+} peak at 260 is subtracted and used to calculate transport rate of $\text{Ru}(\text{bipy})_3^{2+}$. Both the molecules are iso-valent, but are different in size: Stokes-Einstein diameter of 11 Å for $\text{Ru}(\text{bipy})_3^{2+}$ to 6 Å for MV^{2+} . The separation factor is the ratio of MV^{2+} to $\text{Ru}(\text{bipy})_3^{2+}$ flux. Shown error bars have been calculated from 3-6 repeated UV-vis measurements of the permeate concentration in the solution for each run condition.

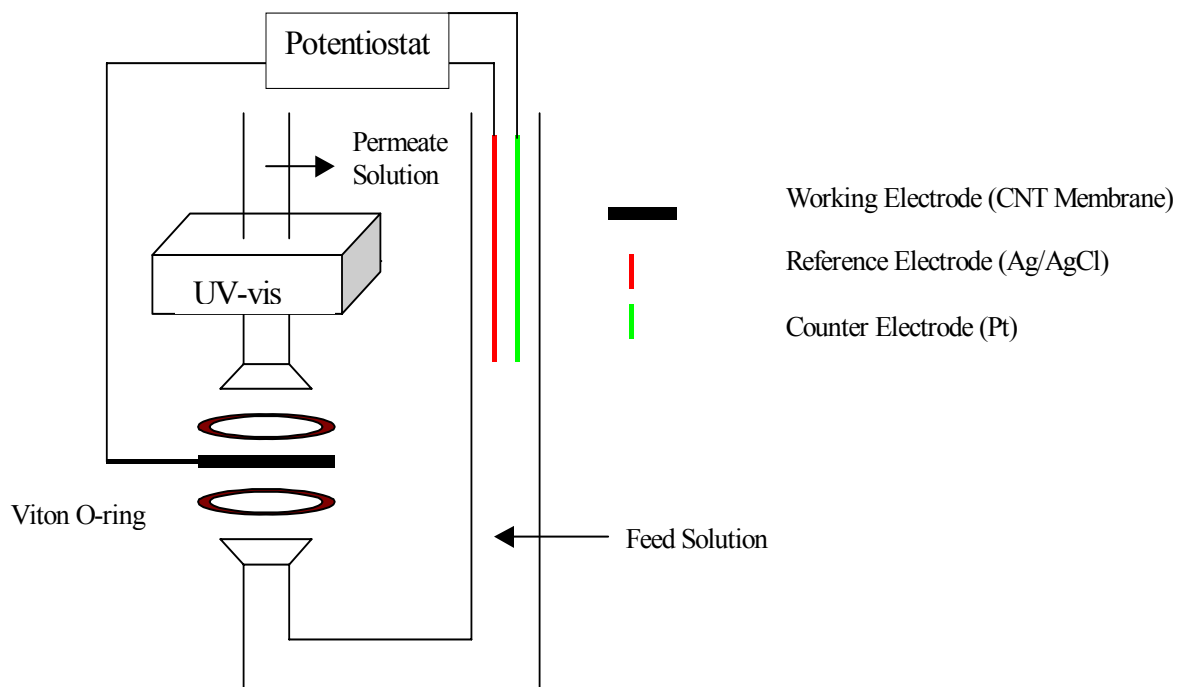


Figure 2.10 Schematic of experimental set-up for measuring transport through membranes as a function of applied voltage. Note that the CNT-membrane placed between the fed and permeate solution is the working electrode. The permeate volume is 0.8 ml and the exposed membrane area is 0.7 cm^2 .

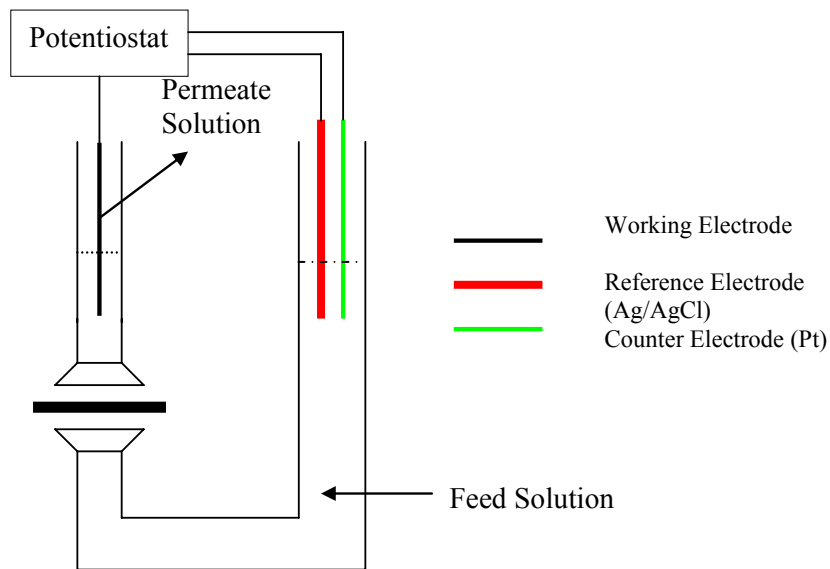


Figure 2.11 Experimental set-up for studying electro-phoretic and electro-osmotic transport across carbon nanotube membranes. The permeate concentration is measured as a function of time by UV-vis spectroscopy. The experiments are carried out potentiostatically using a Potentiostat/Galvanostat (Model 263A, Princeton Applied Research). Both the working and counter electrode are Pt wires and the reference electrode is an Ag/AgCl (sat. KCl) electrode.

Chapter 3

Ionic, Liquid and Gas Transport

This chapter is based on two manuscripts:

Majumder, M.; Chopra, N.; Andrews, R.; Hinds, B. J., Nanoscale hydrodynamics: Enhanced flow in carbon nanotubes. *Nature* **2005**, 438, (7064), 44.

Majumder, M.; Chopra, N.; Hinds, B. J. Mass transport through carbon nanotube Membranes in three different regimes: ionic, liquid and gas (to be submitted)

3.1 Introduction

Rapid transport and high selectivity in biological channels are worth mimicking in artificial systems for designing membranes with high selectivity and permeability. There are several instances of achieving high selectivity through steric⁷³ or chemical interactions.^{75, 76} The principal limitation to fast transport, however, arises from the inherent tortuosity and fluid-pore wall friction in these membranes. A possible way to reduce tortuosity is the synthesis of well-ordered and vertically-oriented porous membranes. Approaches include anodization of metal films;^{96, 97} track etching by energetic heavy ions in polymers⁷¹ or mica⁹⁸; selective dissolution of self-assembled structures from block co-polymers;⁹⁹ out-of plane self-assembly of surfactant templated nanopore arrays;¹⁰⁰ and template synthesized nanotubule membranes by CVD or electroless deposition.^{73, 77, 80} However, the goals of achieving both high selectivity and high permeability remain elusive.

A new class of membranes¹⁰¹ with as-formed graphitic CNTs as conduits for molecular transport offer possibilities of extremely fast transport¹⁰² analogous to biological channels like aquaporin.¹⁰³ The process entails encapsulation of vertically-oriented CNT arrays inside an inert polymer⁸⁰ or a ceramic matrix⁸¹ with a plasma cutting chemistry opening up the CNT tips. Mass-transport studies have been conducted on single-pore CNT membranes with pore diameter ~ 120 nm.³⁵ However, interest lies in

membranes with smaller diameters and substantial numbers of CNTs for large area applications.

Experimental investigations on mass transport through the aligned multiwalled CNT membrane structure with ~ 7 nm pore diameter, in the large spectrum of ionic diffusion, to liquid and gas transport are discussed in this chapter. The membrane structure of interest contains a substantially large number of CNT ($\sim 10^{10}$ /cm²), which allow macroscopic measurement of transport through the membrane. Gas adsorption-desorption indicates a membrane structure with a mean pore $\sim 6\pm 2$ nm and with the inner core of the multiwalled CNT contributing to the porosity of the composite structure.⁸⁰ Absence of large cracks or interfaces is also validated by several size-based exclusion experiments including retention of 10 nm Au colloids,¹⁰³ ligand gated ‘on-off’ transport behavior¹⁰⁴, as well as, ‘chemically-gated’¹⁰⁵ and ‘voltage-gated’ separation of small from large molecules.¹⁰⁶ Experimental transport properties are compared with conventional models of mass transport through membranes of comparable pore size and it is shown that nano-scale transport phenomena in these graphitic pores deviate significantly from these predictions.

3.2 Results and Discussions

3.2.1 Integrity of the CNT Membrane Structure

A diffusion experiment in the U-tube cell with a feed solution of 10nm diameter Au nanocrystals (Ted Pella Inc., 10 nm) containing ~ 0.005 wt% Au-nano crystal, showed no detectable visible absorption from nc-Au in the permeate solution, while the small-molecule citrate (UV active) was visible (figure 3.1). This indicated a nanoporous membrane without interfaces/pores larger than 10nm. The multiwalled CNTs used for the membrane fabrication process were ~ 7 nm in ID and $\sim 50 - 100$ nm in outside diameter (OD). After membrane fabrication, nitrogen adsorption-desorption showed a sharp pore-size distribution with a mean $\sim 6\pm 2$ nm.⁸⁰ Polystyrene rendered nanoporous during membrane fabrication would have contributed to pore sizes different from the inner diameter of the CNTs. Thus, the adsorption-desorption experiments indicated the absence of nanoporous polystyrene and also significant outer-wall CNT surfaces. The porosity of the CNT membrane structure is composed of the inner core of the MWCNT.

Further, membranes made from blocked MWCNTs (grown in a region of the furnace with high iron content) of the same thickness and polymer processing, showed no detectable ionic diffusion or pressure flow for all solvents. Hence, the polystyrene matrix was not rendered mesoporous during plasma oxidation, nor was there any transport through the polymer/CNT interface.

Other indirect-control experiments for the membrane structure include: (i) size-based molecular separation between $\text{Ru}(\text{bipy})_3^{2+}$ and MV^{2+} by progressive blocking of CNT tips;¹⁰⁵ (ii) enhanced molecular separation > 20 , through electro-conformation induced ‘voltage-gating’;¹⁰⁶ and (iii) blocking of ion-transport through attachment of bulky streptavidin molecules to the 7nm CNT core diameter.¹⁰⁴ These clearly demonstrate the absence of large cracks or interfaces through the membranes, and that the molecular transport is through the inner core of the CNTs.

3.2.2 Ionic Transport

The structure, bulk diffusivity, and apparent diffusivity through CNT membrane of the probe molecules are shown in Table 2.1. The apparent diffusivity of the probe molecules have been calculated from:

$$Diffusivity_{\text{Probe}} = \left(\frac{Flux_{\text{Probe}}}{Flux_{\text{KCl}}} \right) \times Diffusivity_{\text{KCl}} \quad [2.1]$$

The bulk diffusivity of KCl at 25 °C is assumed to be $1.7 \times 10^{-5} \text{ cm}^2/\text{s}$. Flux is experimentally measured across the CNT membrane according to methods discussed in section 2.2.

3.2.3 Estimation of Charge Density of Plasma-Oxidized CNT Membrane

The experimental methods for measuring the electrochemical spectra and calculation of the interfacial capacitance are discussed in section 2.3. The interfacial capacitance of the CNT membrane increases with increasing pH (figure 3.2) indicating the presence of charged ionizable groups on the CNT surface, presumably carboxylic

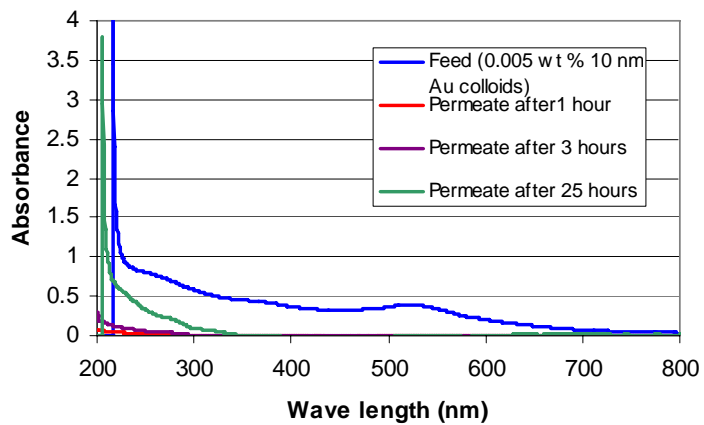


Figure 3.1 UV-vis absorption monitoring of nc-Au (10nm diameter) diffusion across aligned CNT membrane. Photograph of the feed and permeate after 25h.

acid. The total interfacial capacitance (C_T) at the CNT surface is a function of the film capacitance (C_F), the diffuse double layer capacitance (C_S) and the capacitance from the degree of protonation ($C(f)$) and can be represented by the equation:¹⁰⁷

$$\frac{1}{C_T} = \frac{1}{C_F} + \frac{1}{C_S + C(f)} \quad [2.2]$$

At low pH, the carboxylic acid groups are not ionized and would not contribute to the measured capacitance. Hence, the measured capacitance should be the same as the film capacitance. The specific capacitance of highly-ordered pyrolytic graphite in contact with a 0.2 M of 1:1 electrolyte was measured to be $\sim 3 \mu\text{F}/\text{cm}^2$.¹⁰⁸ Assuming that the graphitic nanotube in contact with 0.1(M) of 1:1 electrolyte behaves similarly, the area of the electrode can be estimated from the specific capacitance of $3 \mu\text{F}/\text{cm}^2$. From the difference in capacitances at pH 2 and 12 ($\sim 1.15 \times 10^{-8}$ F), and the active electrode area, the number of surface sites per cm^2 of the electrode is estimated ($\sim 4.4 (\pm 0.9) \times 10^{12}$ sites/ cm^2). It was employed to measure the density of COOH groups after covalent attachment of benzoic acid groups via a diazonium grafting reaction and showed that there was ~ 5 -6 fold increase in functional density from the as-made (plasma oxidized) membrane. The surface charge density of COOH groups would lead to a charge density of $\sim 6.35 \times 10^{-3}$ C/ m^2 on the CNTs at pH12. Assuming $\sim 50\%$ ionization at neutral pH¹⁰⁹ (i.e. the pH condition for the ionic transport measurements) one arrives at a charge density of $\sim 3 \times 10^{-3}$ C/ m^2 . For comparison, broken graphite sheets would contribute 3.5×10^{15} sites/ cm^2 and charge density ~ 2.4 C/ m^2 . For acid functionalized SWNT ~ 3 -8% of the carbon atoms are carboxylic-acid functionalized¹¹⁰ and the functional molecules would provide a charge density of $\sim 4 \times 10^{-1}$ C/ m^2 on a planar graphitic electrode. For the milder plasma oxidation conditions, in the case of membrane fabrication, the charge density obtained is almost two orders of magnitude smaller than acid-functionalized CNT. Flow through zeta potential measurements are usually used for measuring the surface charge density of membranes.¹¹¹ However, slip boundary condition of liquids on the CNT-walls¹⁰³ precludes the use of flow-through techniques for estimating surface charge density.¹¹² Nevertheless, the estimation of charge density from the capacitance measurements is independent of the functional groups on the oxidized polystyrene surface and represents the charge density on the electrically conducting pores and

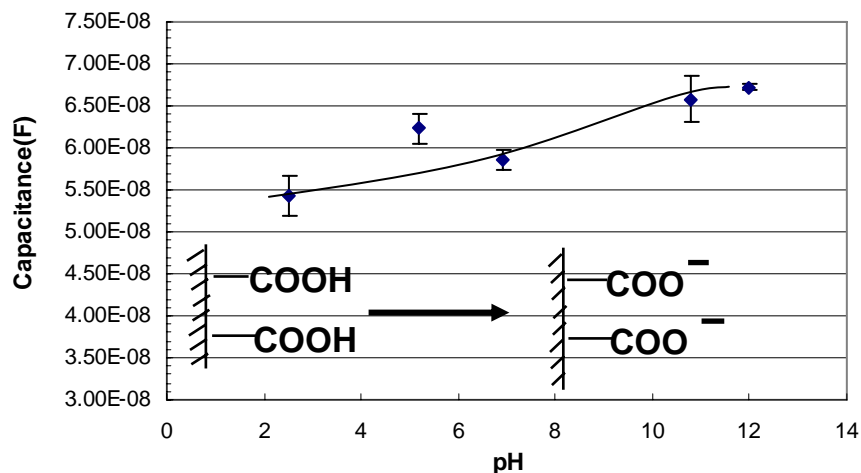


Figure 3.2 Interfacial capacitance of the CNT membrane (measured by electrochemical impedance spectroscopy) was evaluated as a function of pH for the plasma oxidized membrane. The interfacial capacitance increases with increasing pH due to the ionizable carboxylic acid groups formed on the CNTs. From the difference in capacitance and the active electrode area, a charge density of $\sim 6 \times 10^{-3} \text{C/m}^2$ at pH 12 is estimated.

surfaces which would influence the transport through the membrane.

3.2.4 Analysis of the ionic flux using resistance-in-series model

The diffusivity (D_0) of a solute in bulk solution is given by the Stokes-Einstein equation:

$$D_0 = \frac{kT}{6\pi\eta R_s} \quad [2.3]$$

where D_0 is the bulk diffusivity, k is the Boltzmann constant, η is the viscosity of the liquid and R_s is the spherical radius of the molecule. For transport in pores of molecular dimensions, there is enhanced interaction between the pore and the molecule. For purely steric interactions between the solute and pore wall, hindered diffusivity, D_h can be expressed by the Renkin equation as:

$$D_h = D_0(1 - \lambda)^2(1 - 2.104\lambda + 2.09\lambda^3 - 0.95\lambda^5) \quad [2.4]$$

where λ is defined as the reduced pore diameter defined by:

$$\lambda = \frac{\text{PermeateMoleculeDiameter}}{\text{PoreDiameter}} \quad [2.5]$$

Electrostatic interactions between the charged molecule and the charged pore significantly affect the electrostatic partitioning and hence, the transport through membranes. Quantitative understanding of ‘electro-static partitioning’ has been developed by solving the linearized Poisson-Boltzmann equation for a charged sphere in a charged cylindrical pore model.¹¹³ Assuming center line approximation, the electrostatically hindered diffusivity, D_{eh} , can be expressed by the equation:

$$D_{eh} = D_0(1 - \lambda)^2 \exp(-E/kT)(1 - 2.104\lambda + 2.09\lambda^3 - 0.95\lambda^5) \quad [2.6]$$

Where E is the energy of interaction for constant surface charge density at the cylindrical pore and sphere and k is the Boltzmann constant. The center line approximation can quantitatively explain transport of charged protein molecules through charged ultra-filtration membranes.¹¹⁴ The major variables in the model are the surface-charge density of the molecule and the membrane surface. The surface-charge density of the molecule (σ_s) was calculated from the molecule’s ionic charge divided by the sphere’s surface area with equivalent Stokes-Einstein diameter as shown in Table 2.1. The surface-charge

density on the membrane (σ_c) was estimated from the capacitance measurements, as discussed in the previous section. The reduced pore diameter is also calculated from the Stokes-Einstein diameter, since it accounts for the hydrated size of the molecule. Schematics of the two models for analyzing the ionic flux data are shown in figure 3.3. Model (i) assumes a uniform charge distribution along the CNT walls. For a resistance-in-series model (ii) we have,

$$\frac{L}{D} = \frac{L_1}{D_1} + \frac{L_2}{D_2} + \frac{L_3}{D_3} \quad [2.7]$$

where D is the effective diffusivity and L is the total path length of diffusion. L_1 , L_2 and L_3 are the individual path lengths which sum up to L . D_1 , D_2 , and D_3 are the respective diffusivities in each segment. Since, in the case of CNT membranes, charged functional groups are present only at the CNT tips, one expects the transport to be affected by these charged groups and limit the diffusion through the CNT membranes. One can expect similar behavior for the CNT entrance and exit. L_1 is assumed to be the functionalization length at each end, while L_2 is the non-functional length of the nanotube. Further, in accordance to our earlier studies, we assume bulk diffusivity inside the CNT cores (D_0).

$$\frac{L}{D} = \frac{2L_1}{D_{eh}} + \frac{L_2}{D_0} \quad [2.8]$$

In a prior work, the CNTs were functionalized with gold nanoparticles and imaged in TEM. The functionalization length of the nanotubes was estimated from the length upto which the Au nanoparticles were observed on the CNTs. It was found to be $\sim 7\%$ on each side of the nanotube and was this experimentally obtained parameter was used in modeling hindered diffusion of ionic transport through the CNT membrane.¹⁰⁵ Therefore, $L_1=0.07$ and $L_2=0.86$.

For model (i), assuming hindered diffusion along the entire pore length we would have:

$$D = D_{eh} \quad [2.9]$$

Ionic transport of similar charge but different size probes through CNT membrane could be modulated by chemical ‘gate-keeper’ functionality at CNT entrances.¹⁰⁵ Factors affecting transport were the chain length, solubility/conformation, charge of the functional molecule and solution ionic strength. The selectivity data were consistent with

diffusion limited by hindrances at the CNT entrance and close to bulk diffusion considerations along the length of the nanotube. It is important to understand the transport of a variety of ions of different size and charge through the 7nm carbon nanotube membranes. Probe molecules considered were ~ 6 to 13 \AA in Stokes-Einstein diameter, which provided reduced pore diameters up to ~ 0.24 (i.e. a quarter of the pore diameter) were filled with the molecule. The experiments were carried out on the same membrane and the fluxes are normalized to KCl flux of equimolar KCl feed. Adsorption of molecular species on the membrane pores are known to significantly affect the transport selectivity.¹¹⁵ However, for the molecules under investigation, the diffusion rates remained steady within the timeframe (3-4 hours) of the experiment. Hence adsorption related effects will not significantly dominate the transport measurements.

Apparently, the diffusivity of the positively charged species is closer to, and the negatively charged species are slower than, bulk diffusion predictions (Table 2.1). For the negatively charged species, the permeates are repelled by the negatively charged ‘gate-keeper’ molecules and hence are more hindered. The positively charged species are partitioned attractively in the pores, causing the flux to be closer to bulk diffusivity values. The experiments were performed using an equimolar (5mM) solution of the divalent ions. Hence, the Debye length is calculated based on a 2:1 electrolyte with a concentration of 10 mM. Calculations based on electrostatic hindrance throughout the core (i.e. model (ii)) over-predicts the electrostatic effects significantly, which indicates that the functional molecules are not present all along the core to influence transport. The calculations are based on the analytical solutions developed by Smith and Deen¹¹³ for constant-charge density on the pore and the molecule. This is consistent with plasma-oxidation chemistry of porous carbons, where high reactivity of the plasma precludes functionalization deep inside the pores and is limited to near-surface reaction only.¹¹⁶ The resistance-in-series model, a rather simplistic version of the actual case, predicts the fluxes reasonably (Figure 2.6). the following are the major drawbacks of the model: (i) assumption of a uniform charge density at the CNT tips, whereas, the plasma oxidation step would presumably provide a density gradient of surface charge a few nanometers into the core; (ii) it is extremely difficult to experimentally estimate the functionalization

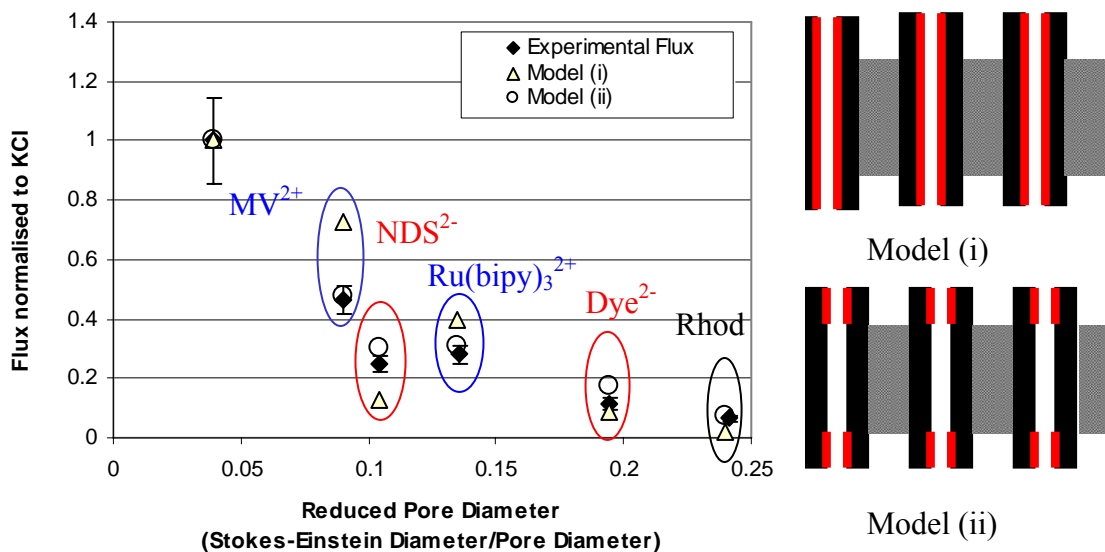


Figure 3.3 Electrostatically-hindered diffusion analysis of the ionic transport measurements. Flux of the probe molecules normalized to KCl flux. The Stokes-Einstein diameters are calculated from their bulk diffusivities. Reduced pore diameter (λ) varies from 0.04 to 0.24. Data from left to right are KCl, MV^{2+} , NDS^{2-} ; $Ru(bipy)_3^{2+}$; RhodamineB; Green Dye²⁻. The error bars at 95% confidence. The calculations are based on the analytical solutions developed by Smith and Deen¹¹³ for constant charge density on the pore and molecule. Model (i) assumes that the entire path length contributes to the electrostatic partitioning and hindrance of the molecules, whereas, model (ii) assumes a fixed length at either end contributes to the rate process. Model (ii) with a length approximately equal to 7% on either side, predicts the fluxes quantitatively.

length on the interior of the nanotubes, and has been estimated from Au-nc experiments on the *exterior* of the nanotubes. The functionalization length (L_1), is in fact, an adjustable parameter of this model.

Despite these drawbacks, the model successfully predicts the observed fluxes within an error of $\sim 30\%$ and definitively rules out functionalization along the entire CNT core. Important to the understanding of ionic transport through the CNTs is i) a rate limiting diffusion step described by electrostatics at the CNT entrances; and ii) close to bulk-like aqueous diffusion inside the non-interacting CNT cores. Ongoing research is directed to increase the limited functional density at the CNT entrances by electrochemical grafting techniques to influence the transport properties as described in Chapter 5. That the ionic diffusion of these species is close to bulk-diffusivity expectations is unique for carbon nanotubes with a 7nm inner diameter. In contrast, 200 nm Anopore membrane or 2 nm Au nanopore membrane made hydrophobic by chemical functionalization would not allow transport of ionic species,¹¹⁷ whereas in nanoporous silica's apparent diffusion co-efficient of dye molecules has been found to be of the order of 10^{-10} cm²/s, due to strong adsorption effects.¹¹⁸ Theoretical work by Hummer et al. suggests that the energy barrier needed for ions to move from a high dielectric region (solution) to the low dielectric (pore) can be substantially reduced for carbon nanotube channels larger than 1 nm and furthermore, near-bulk diffusion would be expected.¹¹⁹ Transporting molecules through carbon-nanotube channels with minimum mass transport limitations and the presence of charged functional groups at the channel entrance, makes the CNT-membrane structure an ideal scaffold to mimic biological 'gate-keeper'-like transport. The subtle, but important, conclusion of non-interacting CNT cores, will have important manifestations in the subsequent pressure-driven liquid-transport studies, where flow velocities were observed to be tremendously enhanced by the 'frictionless non-interacting' cores of the CNT.

3.2.5 Liquid Transport

Flow of liquids (J) through porous membranes can be predicted using the Haagen Poiseuille equation⁵² and is given by:

$$J = \frac{\varepsilon_p \cdot \mu \cdot r^2 \cdot \Delta P}{8 \cdot \mu \cdot \tau \cdot L} \quad [2.10]$$

where ε_p is relative porosity; r_0 is pore radius (3.5 nm for our system); P pressure applied; μ dynamic viscosity; τ tortuosity (1.1) and L length of pore. The basic assumptions of this equation are laminar flow and ‘no-slip’ at the boundary layer (i.e. the velocity of the fluid at the CNT wall is zero).

The implication of the equation for nanoporous materials (small radius) is that the transport rate is limited by the pressure drop across the pores. The ‘no-slip’ boundary condition is not true for a large number of cases including flow through hydrophobic capillaries, providing possibilities to design membranes with small pore size, but enhanced liquid transport. However, it has been difficult to make such hydrophobic membranes with enhanced slip flow, as surface energies would not allow water to enter the transporting channels. The atomically-smooth graphite cores, theory, and experimental observations of water inside CNT cores described in Chapter 1 make it possible to see enhanced slip flow across CNT membranes. Slip flow can be characterized by slip length, which is an extrapolation of the extra pore radius required to give zero velocity at a hypothetical pore wall (the boundary condition for conventional materials). It indicates the deviation of the liquid flow from the hydrodynamic prediction and denotes the extent of interfacial friction between the liquid and the pore walls. It can be estimated from the equation: ¹¹²

$$\frac{V(\zeta)}{V_{ns}} = 1 + \frac{4 \cdot \zeta}{r_0} \quad [2.11]$$

where, $V(\zeta)$ is the experimentally-observed flow velocity (cm/s); V_{ns} is the flow velocity calculated from the Haagen-Poiseuille Equation; ζ is the slip length and r_0 is the radius of the nanotube.

Estimation of permeable pore density is based on the validity of close to bulk diffusion characteristics of ions inside CNT pores as discussed in the preceding section. In general, the flow velocities were 4-5 orders of magnitude larger than hydrodynamic predictions (Table 3.1). The trend of flow velocities could not be explained by

Table 3.1 Tabular summary of pressure-driven flow of liquids through CNT membrane. Water flow at ~0.001-0.02 bar measured by U-tube permeation experiment with positive column height and quantified by Ru(bipy)₃²⁺ dye permeation

Liquid	Permeable pore density (# per cm ²)	Membrane thickness (micron)	Initial permeability (cm ³ /cm ² -min-bar)	Flow velocity normalized at 1 bar (cm/s)	Viscosity (cP)	Enhancement Factor	Slip length (micron)
Hexane	3.4 x 10 ⁹	126	0.44	5.6	0.3	1.09 x 10 ⁴	9.5
Decane	3.4 x 10 ⁹	126	0.053	0.67	0.9	3.9 x 10 ⁴	3.4
Water (0.7-1bar)	1-3.4 x 10 ⁹	34-126	0.77(±0.22)	26.1 (±17.2)	1.0	6 (±1.6) x 10 ⁴	53.3(±14.5)
Water (0.001-0.02 bar)	2.4 x 10 ⁶	81	----	10.9 (±5.1)	1.0	4.6 (±2.1) x 10 ⁴	40.4(±18.5)
EtOH	3.4 x 10 ⁹	126	0.35	4.5	1.1	3.2 x 10 ⁴	28
IPA	3.4 x 10 ⁹	126	0.088	1.12	2	1.4 x 10 ⁴	13

parameters like viscosity or hydrophobicity. For instance, hexane is less viscous and more hydrophobic than water and should flow faster than water in a hydrophobic channel. However, the hexane flow rate is less than the water flow rate through the carbon nanotube membrane. Molecular dynamic simulations have shown that water can be transported through carbon-nanotube channels at extremely high speeds by the cooperative movement of a hydrogen-bonded network through the frictionless and smooth graphitic cores.²⁸ Most interestingly, the flow velocity of water (i.e. volumetric flow rate through individual nanotubes) divided by the pore area was found to be comparable to those observed in protein channels like aquaporin and the MD simulation prediction. However, these experiments do not confirm the presence of ordered water inside the CNT channels, though we observed that the water flow rates through the carbon nanotube membranes declined over time for the polar liquids. For this specific reason, the flow rates are calculated from their initial permeability (i.e. the time we observed the first drop of liquid to come out of the flow cell).

The experimental results of liquid flow can be explained qualitatively by the presence of slip-flow conditions at the CNT walls (figure 3.4). Theoretically, existence of micron scale slip-lengths have been explained by the presence of a ‘gas-liquid’ interface, which gives rise to a non-zero velocity at the walls.^{120,121} The observed slip flow of water is consistent with independent measurements in sub 2nm carbon nanotube channels.¹⁰² The slip length for the liquids was found to correlate qualitatively with the hydrophobicity of the solvent indicated by the solubility parameter, which is frequently used in the polymer literature to find appropriate solvents and is a measure of its hydrophilicity.¹²² Water is the most hydrophilic of the solvents, has higher solubility parameter, and the maximum slip length of the liquid on the CNT surface. The observed slip lengths are consistent with the contact angle of polar liquids on carbon nanotubes [Water (79°), > EtOH (12°) > IPA (8°)]¹²³. For the hydrocarbons, the slip lengths are qualitatively consistent with their hydrophobicity. Greater interaction (wetting) of the liquid with the graphite surface leads to a decrease in the slip lengths and decreased transport rates.¹²⁴

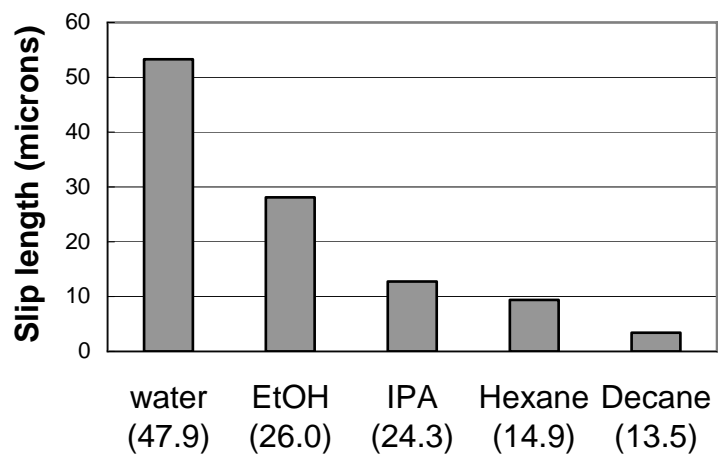


Figure 3.4 Slip length of the liquids on CNT calculated from the pressure flow experiments. Slip length is a measure of the deviation of liquid flow from the no-slip condition in the Haagen-Poisueille equation and denotes the extent of interfacial friction of liquid on carbon-nanotube walls. Slip length for various liquids were observed to decrease with increasing hydrophobicity of the solvent. The quantities in brackets on the x-axis are the solubility parameter (Mpa^{0.5}) of the liquid.

In order to test the hypothesis that the enhanced flow observed through the CNT membranes is due to slipping of the liquid at the CNT walls, flow velocities of liquids through the CNT membrane were determined with progressive functionalization of the tips and the core of the CNTs. In the diffusion experiments (figure 2.1) the liquids in the feed and the permeate cell were maintained at the same level to ensure minimum pressure-driven flux. In order to determine the pressure-flow velocities, the height of the feed column was deliberately kept ~ 0.5 -20 cm higher than the permeate. The results of these experiments are shown in Table 3.2. The pore area was estimated from the diffusive flux measurements with no height difference and assumption of bulk diffusivity of the probe ($\text{Ru}(\text{bipy})_3^{2+}$) in the CNT cores. The flow velocity of 5mM $\text{Ru}(\text{bipy})_3^{2+}$ for as-made membrane was found to be $8.8(\pm 4.1)$ cm/s (normalized to 1 bar), which is remarkably consistent with the flow velocity of pure water, estimated from the syringe pump experiments. The as-made membrane has functional groups at the CNT tips and was functionalized by a polypeptide spacer and a charged dye molecule containing SO_3^{2-} groups. The method of functionalization and the structure of the functional molecules are described in Chapter 2. After the functionalization with the bulky, charged-dye molecule, pressure-flow experiments showed that the flow velocity of 5 mM $\text{Ru}(\text{bipy})_3^{2+}$ solution had decreased to $0.04 (\pm 0.007)$ cm/s. These experiments were carried out in the presence of 0.1M of KCl electrolyte in order to screen the electrostatic effects. In order to fully functionalize the entire core of the CNTs, the membrane was grafted electrochemically using a highly aggressive diazonium grafting chemistry. Capacitance measurements, indicated an almost 5 to 6 times increase in functional density. The membrane was thereafter functionalized with a polypeptide spacer and the anionically charged dye molecule. Suffice to say that these treatments decrease the inherent smoothness of the graphitic nanotubes and increase the interaction between the solvent molecules and modified-nanotube surface. No detectable pressure-driven transport of the probe molecules were detected (< 0.0005 cm/s) in the pressure range of the experiment. Shown in the table is also the normalized diffusive flux of $\text{Ru}(\text{bipy})_3^{+2}$, defined by a ratio of the diffusive flux after a functionalization treatment to that of the unmodified (plasma-oxidized) membrane. Hence, by definition, this ratio is 1 for the as-made membrane.

Table 3.2 Pressure flow of water through CNT membranes as a function of progressive chemical functionalization. Flow velocity is measured in the range of (0.001-0.2 bar) using a U-tube permeation cell with positive column height using an Ru(bipy)₃²⁺ probe molecule. The enhancement factors are based on calculated Newtonian flow through a pipe with 7 nm inner diameter and a length similar to the thickness of the membrane. Note that progressive functionalization decreases the flow velocity and causes the transport to be closer to conventional hydrodynamics. The right-most column shows the observed diffusive flux after functionalization is normalized to the diffusive flux through the unmodified CNT membrane for these series of experiments.

Chemical Functionalization	Flow Velocity normalized at 1 bar (cm/s)	Enhancement over Newtonian flow	Normalized Diffusive Flux
As made (plasma-oxidized)	10.9(±5.1)	4.6 (±2.1) x 10 ⁴	1
Spacer-dye (tip region)	4.7 (±0.7) x 10 ⁻²	2 (±0.3) x 10 ²	0.93
Spacer-dye (core and tip)	< 1.26 x 10 ⁻³	< 5.3	1.03

The experiments for the spacer-dye functionalization were carried in the presence of 0.1 M KCl for screening the electrostatic charges.. Therefore, the ratios are close to 1. It indicates that the membrane functionalization did not block the pores completely, but instead modified the surface to decrease the pressure-driven flux. This conclusively proves in a single set of experiments on the same membrane that the graphitic, noninteracting cores of the CNTs are responsible for the enhanced flow velocities of liquid through the CNT membrane.

3.2.6 Gas Transport

Gas transport through mesoporous materials is generally a combination of: (i) viscous or Poiseuille Flow; (ii) Knudsen diffusion; and (iii) surface diffusion.^{125,126} From the perspective of separations, higher flux with lower separation for viscous flow and lower flux with higher separation for surface diffusion is obtained and in the order described. Viscous or Poiseuille permeability, the preferred mechanisms in large pores, can be mathematically described by:

$$J_p = \frac{\varepsilon_p \cdot \mu_{kn} \cdot r^2}{8 \cdot R \cdot T \cdot \eta \cdot L} P_m \quad [3.12]$$

where J_p is the Poiseuille permeation ($\text{mol} \cdot \text{m}^{-2} \cdot \text{s}^{-1} \cdot \text{Pa}^{-1}$); μ_{kn} is the reciprocal tortuosity; η is the gas viscosity ($\text{N} \cdot \text{s} \cdot \text{m}^{-2}$); L is the thickness (m) of the membrane; and P_m is the mean pressure (Pa) (i.e. the mean of the inlet and outlet pressure). Importantly, the Poiseuille permeation scales inversely with the viscosity. Knudsen diffusion becomes prominent when mean free path of the diffusing species is larger than the pore diameter. Knudsen permeability can be expressed by the following equation:

$$J_{kn} = \frac{2 \cdot \varepsilon_p \cdot \mu_{kn} \cdot v \cdot r}{3 \cdot R \cdot T \cdot L} ; V = \left(\frac{8 \cdot R \cdot T}{\Pi \cdot M} \right)^{0.5} \quad [3.13]$$

where J_{kn} is the Knudsen permeation ($\text{moles} \cdot \text{m}^{-2} \cdot \text{s}^{-1} \cdot \text{Pa}^{-1}$); ε_p is the porosity; μ_{kn} is a shape factor equal to $1/\tau$, r is the the pore radius (m); τ is the tortuosity; v is the average molecular velocity ($\text{m} \cdot \text{s}^{-1}$); L is the layer thickness (m); M is the molecular mass ($\text{Kg} \cdot \text{mole}^{-1}$) of the gas molecule; and T is the absolute temperature (K). Characteristics of Knudsen-type transport are the inverse scaling with square root of molecular weight of the gases, which parallels arguments for the kinetic theory of gases. In some cases of

porous membranes, a surface-adsorption based preferential diffusion may lead to highly selective transport.^{127,128} A representative equation is:

$$J_s = -\rho_{app} \cdot D_s \cdot \mu_s \cdot \frac{dq}{dl} \quad [3.14]$$

where J_s is the surface diffusion flux component ($\text{mol} \cdot \text{m}^{-2} \cdot \text{s}^{-1}$); ρ_{app} is the apparent density ($\text{Kg} \cdot \text{m}^{-3}$); D_s is the surface diffusion coefficient ($\text{m}^2 \cdot \text{s}^{-1}$); μ_s is the reciprocal tortuosity and dq/dl is the surface concentration gradient ($\text{mol} \cdot \text{Kg}^{-1} \cdot \text{m}^{-1}$)

Permeability ($\text{cm}^3/\text{cm}^2\text{-min-psi}$) of a gas through the membrane is estimated from the slope of the flow rate ($\text{cm}^3/\text{cm}^2\text{-min}$) versus differential pressure (psi) across the membrane. (Inset figure 3.5(a)). Along with the mean permeability (slope of the linear fit), the (\pm) uncertainty at 99 % confidence level from 30-35 different measurements is reported. The equation $ts/n^{0.5}$ where n is the number of observations, t is the student's t value at $n - 1$ degrees of freedom, and s is the standard deviation of the measured values from the linear fit is reported (figure 3.5(a)). The slope of the linear fit is corrected for by the calibration curve of the capillary with the syringe pump. For convenience and easy comparison with other nanoporous systems, we report the gas permeability in the units of moles/ $\text{m}^2\text{-s-Pa}$.¹²⁹ In order to eliminate experimental uncertainty arising from sample to sample variability, all the gas flow measurements were carried out on a single piece of membrane. Compressed air transport experiments repeated 4 to 5 times on the same piece of membrane showed a standard deviation of $\sim 8.5\%$ in the measurements.

For most gases at room temperature, the mean free path is significantly larger than the pore diameter of the CNT membrane ($\sim 70 \text{ \AA}$). For example, air at room temperature will have a mean free path of $\sim 600 \text{ \AA}$, which is almost an order of magnitude larger than the pore diameter of the CNT membrane. Hence, one expects the gas transport through the CNT membranes to be in the Knudsen regime. For transport dominated by viscous flow, the gas permeability should scale linearly with the inverse of viscosity of the gases.¹³⁰ Instead, the experimental gas permeability scaled with the molecular weight of the gases by an exponent of 0.42, (figure 3.5 (a)), which is close to the predictions of Knudsen diffusion (0.5). Surface-based adsorption-diffusion may play an important role in the transport of these gases, which might be responsible for the exponents differing from 0.5.^{131,132} This observation (i.e. scaling of the gas permeability with molecular

weight and non-correlation with viscosity) indicate the absence of significant viscous transport through the CNT membrane, which would be the case if gas transport was through large cracks or interfacial porosity.¹³³ The results are also consistent with MD simulations, suggesting insignificant viscous contributions in gas transport through 8.1 nm diameter carbon nanotubes.¹³⁴

The expected Knudsen permeability through a pore 7 nm in diameter and 126 micron in length (estimated from Scanning Electron Micrographs) $T= 298\text{K}$, tortuosity factor ~ 1 , and 0.0015 porosity (estimated from KCl diffusion experiments) was calculated from eq.3.13. The enhancement factor was calculated by the following relation:

$$\text{Enhancement factor} = \text{Experimental permeability} / \text{Calculated Knudsen permeability}$$

Enhancement factors for the gases ranged from 20-30 for most gases (figure 3.5 (b)). It is worth emphasizing that the theory of Knudsen transport is based on the kinetic theory of gases, where momentum transfer is dominated by collisions with the wall. In the case of very smooth surfaces, collisions with the wall will not be totally specular and have a tangential momentum component (figure 3.6). For an amorphous carbon coated (20-30 nm thick) alumina membrane (200 nm pore dia), gas transport measurements of argon, oxygen and nitrogen and modeling approaches indicated that approximately 50% of the gas collisions were specular.¹³⁵ Specular momentum transfer will cause the diffusivities to exceed those predicted from the kinetic theory.^{136,137} The observed enhancement factors are in close agreement with other simulations work in graphitic carbon nanotubes. For instance, transport diffusivity of Ar (using MD simulations) through a carbon nanotube of ~ 1.6 nm diameter is $\sim 10^{-1}$ cm^2/s , which is almost 2 orders of magnitude larger than predicted from the Knudsen diffusivity equation (4×10^{-3} cm^2/s).¹³⁸ The present observations are also consistent with some recent experimental work on sub 2 nm CNT membranes, where enhancement by 2-3 orders of magnitude was observed.¹⁰² Interestingly, for AAO membrane of comparable pore sizes (~ 10 nm), Knudsen diffusion was observed, whereas a factor of 10 enhancement over Knudsen Diffusion was observed for 10 nm PC membranes.¹³⁹ This suggests that the material surface characteristics of the

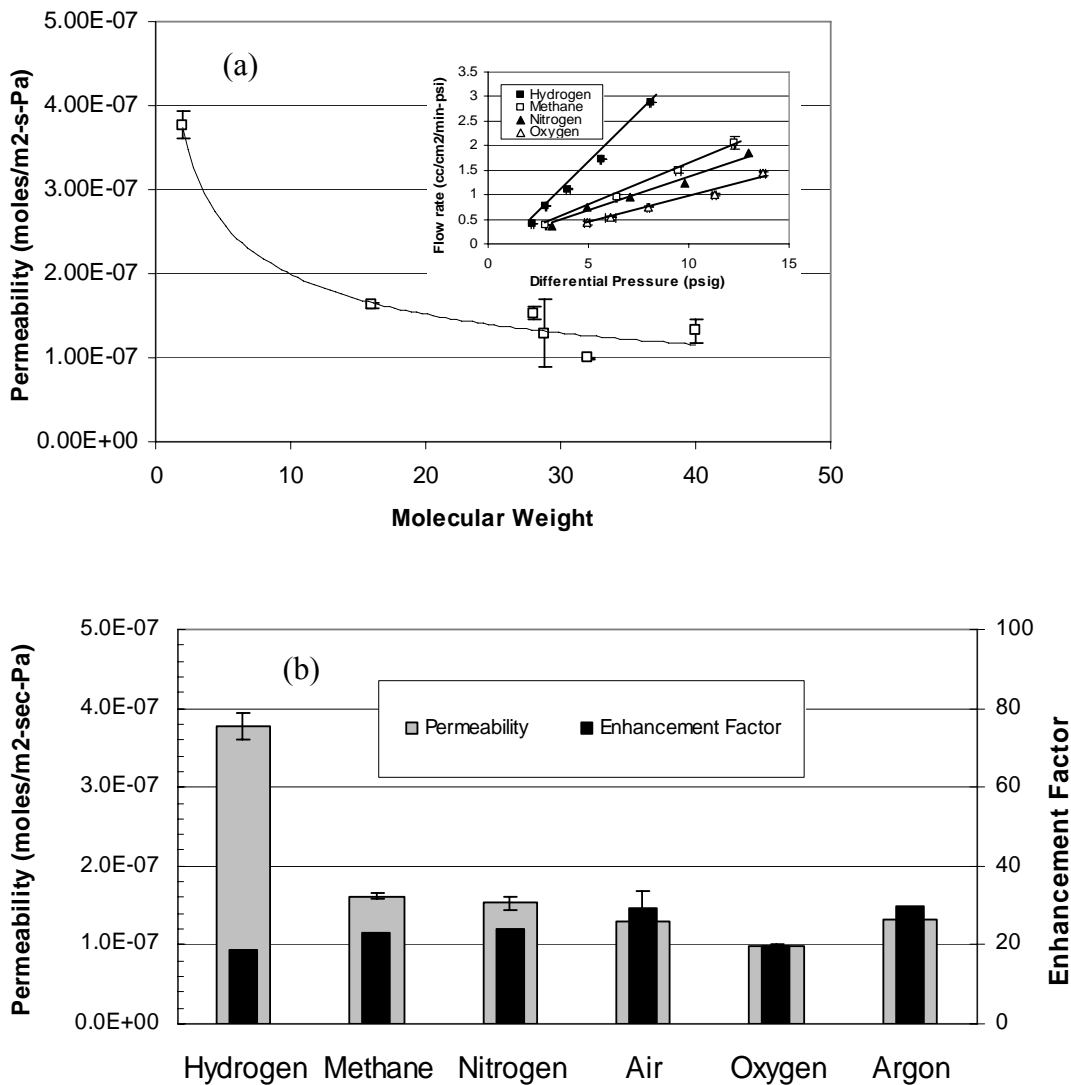


Figure 3.5(a) Permeability of the gases showed significant correlation with their molecular weights and not with their viscosities. The experimental permeability scaled with molecular weight of the gases by an exponent of 0.42 (which is close to 0.5 for ideal Knudsen type diffusion transport). Inset: Plot of experimental flux through CNT membrane. The slope of the lines is the permeability (in cm³/cm²-s-psi) of gas through the membrane. (b) Histogram of observed permeability in (mole/m²-s-Pa) and enhancement factor for each gas.

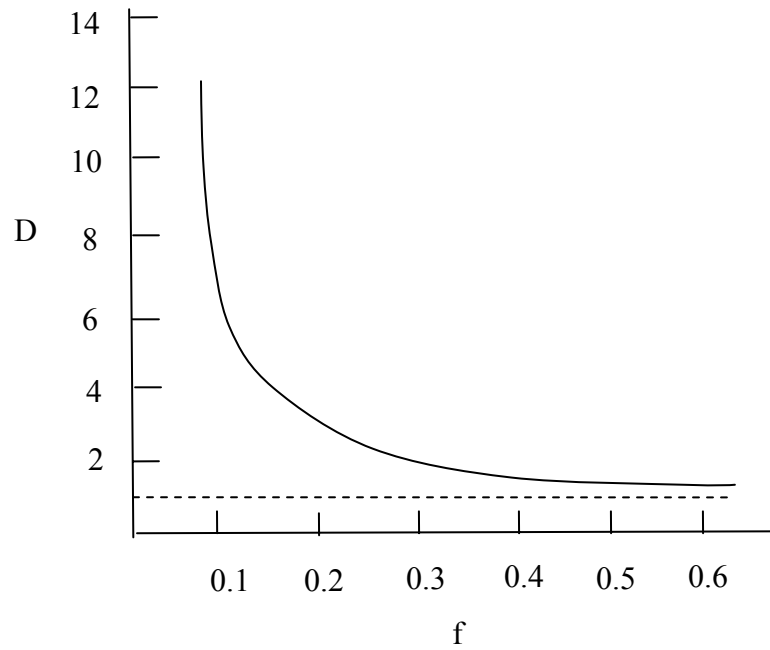
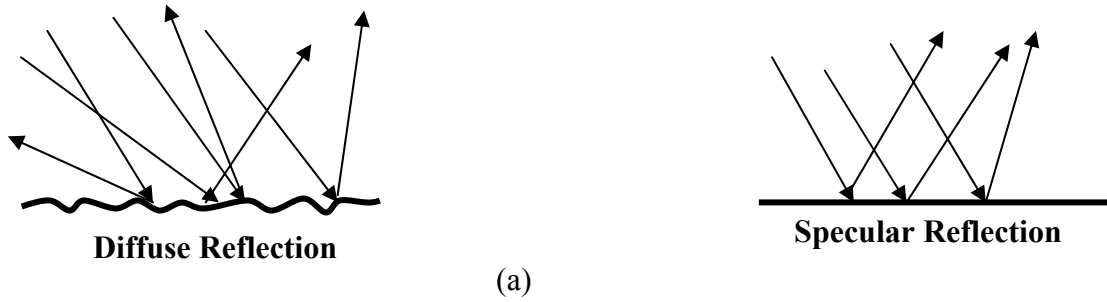


Figure 3.6 (a) Schematic of diffuse reflection on rough surface and specular reflection on smooth surface. Knudsen diffusion is based on diffused reflection of gases and is applicable for most porous materials with rough surfaces. (b) Calculated Knudsen type diffusivity of hard spheres in smooth pores as a function of ‘ f ’ defined as the fraction of the gas collisions that reflect diffusely with the walls. (Figure adapted from Arya et al. ¹³⁶)

vertically oriented nanoporous materials are very important to obtain the enhanced diffusivities. Apparently, the graphitic carbon nanotubes with their large van der Waals Enhancements by ~ 2 orders of magnitude over calculated Knudsen permeability has been observed for the gases under study. In summary, the observed permeability of gases scales down with the molecular weight by an exponent ~ 0.4 , but the diffusivities are ~ 1 order of magnitude larger than Knudsen diffusivity predictions. Thus a Knudsen-type diffusion transport, with highly specular reflection along the CNT walls is the dominating gas transport mechanism. Also important to the evidence of a membrane structure with molecular channels provided by the inner core of the CNTs, is the absence of correlation between transport rates and viscosity.

3.3 Conclusions

The following are the conclusions of the present work: Ionic diffusion through the CNT membranes is close to bulk diffusion expectations and electrostatically influenced by charged carboxyl functionality at the CNT entrance. The observed fluxes can be quantitatively predicted by a resistance-in-series model of electrostatic hindered partitioning within a few nanometers of the entrance and exit while bulk diffusivity in the cores. Liquids flow ~ 1000 - $10,000$ fold faster than predictions of liquid transport from 'no-slip' hydrodynamic predictions. The extent of slip decreases with increasing hydrophobicity of the liquid. Progressive functionalization of the CNT tips and cores cause the water transport rates in the CNT membranes to approach those of hydrodynamic predictions. These indicate a frictionless, non-interacting CNT surface contributes to the enhanced liquid flow rate through the membrane. Gases are transported by a Knudsen like transport mechanism but are ~ 15 - 30 fold faster than Knudsen diffusion predictions due to highly specular reflection at the smooth CNT walls. The CNT membrane with their high mass transport characteristics, small pore size and possibility of attaching selective 'gate-chemistry' at the CNT tips has the potential to achieve the holy-grail of membrane science, i.e., combine high selectivity and high permeability. These membranes are the first demonstration of man-made channels which can approach the extremely fast transport seen in biological channels.

Copyright © Mainak Majumder 2007

Chapter 4

Ionic-Transport across ‘Gate-keeper’ Functionality

This chapter is based on a published manuscript:

Majumder, M.; Chopra, N.; Hinds, B. J., Effect of Tip Functionalization on Transport through Vertically Oriented Carbon Nanotube Membranes. *J. Am. Chem. Soc.* **2005**, 127, (25), 9062-9070.

4.1 Introduction

Synthesis and characterization of ordered nanoporous materials with nontortuous and well-controlled pore diameters is an active research area with applications that include separations, catalysis, molecular sensing, and controlled drug delivery.^{141, 142} Synthesis of a suitable membrane structure with highly ordered vertical pore orientation is a difficult challenge.^{143,144} A promising approach for obtaining vertically-oriented membrane structure has been controlled reduction of pore size of existing ordered porous structures like anodized alumina or track-etched polycarbonate membranes.⁷² A flurry of research activity for reducing pore size by electroless deposition¹⁴⁵ or CVD⁷⁸ has demonstrated improvements in O₂/N₂ and water vapor/oxygen separation coefficients. Critical to membrane separations is fine control of pore size. The inner core of carbon nanotubes offer an alternative route to uniform membrane pore diameter with fine control determined by catalytic particle size.¹⁴⁶ Transport mechanisms of gaseous²² and liquid molecules,^{28, 29} through the graphitic cores of the CNTs, are of interest and need further experimental verification of theoretical studies. Transport of polystyrene particles in an aqueous medium through single-pore membrane composed of carbon nanotubes with ~ 100nm diameter³⁵ and ionic transport through carbon-plated porous alumina⁷⁹ indicate the ability for aqueous systems to function in carbon systems, but it is of interest to study core dimensions less than 10nm and with smoothness inherent in graphitic carbon nanotubes. Recently, vertically-aligned carbon nanotube membranes with CNT cores (~7 nm diameter) traversing a thin, solid, polymer film have been synthesized.⁸⁰ Ionic and gas transport through CNTs is consistent with the geometry. Not only pore size, but also functional molecules attached to the pore surfaces, can lead to highly selective

separations by forcing chemical interactions between the permeate and the functional molecule.^{147,148,149} Since the oxidation process selectively functionalizes the entrances/tips of CNT cores, these membranes offer a unique nanoscale scaffolding to permit ‘gate-keeper’ type interactions, possibly increasing both flux and selectivity. Transport through hydrophobic carbon nanotubes is analogous to biological membrane channels. Biological membrane systems are abundant in examples where protein molecules facilitate transport of ions or molecules.¹⁵⁰ Opening of gated-ion channels are determined by voltage-dependent movement of charged arginine residues within membrane pores.¹⁵¹ Recently, transport of water and electrolyte (KCl) through carbon nanotubes containing charged groups at their ends using MD simulations, have been studied.¹⁵² The motivation for the present study stems from biological systems, in which molecules regulate the transport properties of molecules or ions in highly hydrophobic environments

The CNT membranes thus provide an ideal membrane structure with hydrophobic cores having entrances that can be functionalized by molecules of desired length, hydrophilicity or functionality. Since the tips are functionalized with carboxylate groups from an oxidation process, simple carboimide chemistry can be performed with desired functional molecules containing accessible amines. These functional molecules can be utilized to investigate a ‘gate-keeper’ mechanism for controlling the flow and selectivity of chemical transport through the CNT-membranes. In this study we focus on the effect of functional molecule size, hydrophilicity, and charge on the flux and relative selectivity of two similarly-charged, but differently-sized permeate molecules through the CNT membranes.

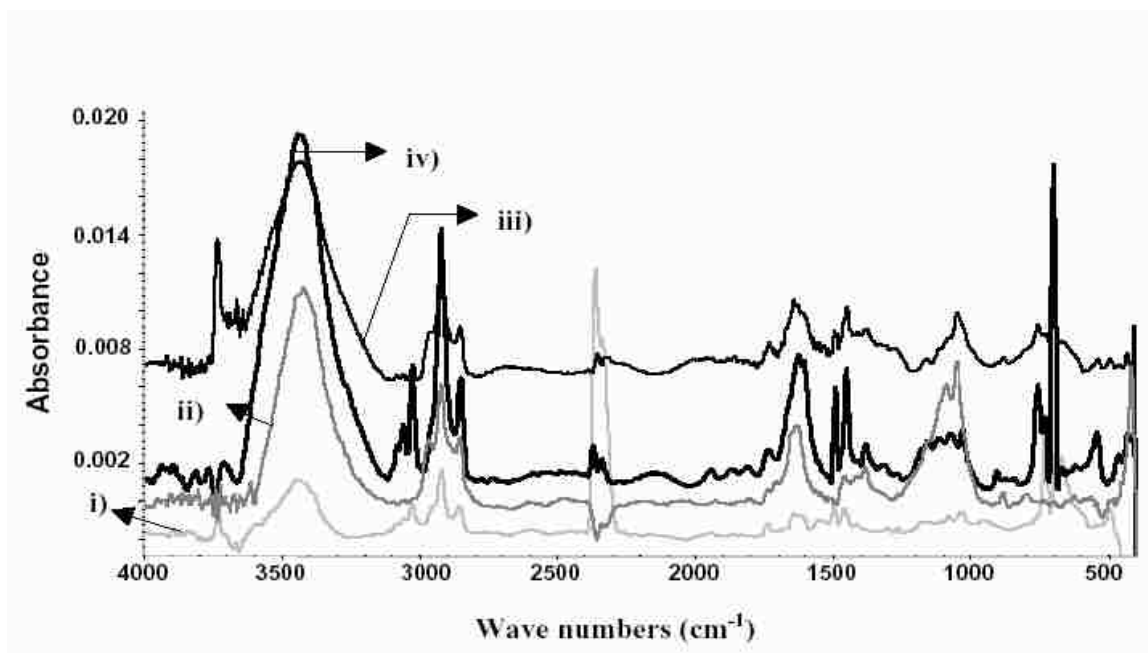
4.2 Results and Discussions

4.2.1 FTIR Spectroscopic Studies

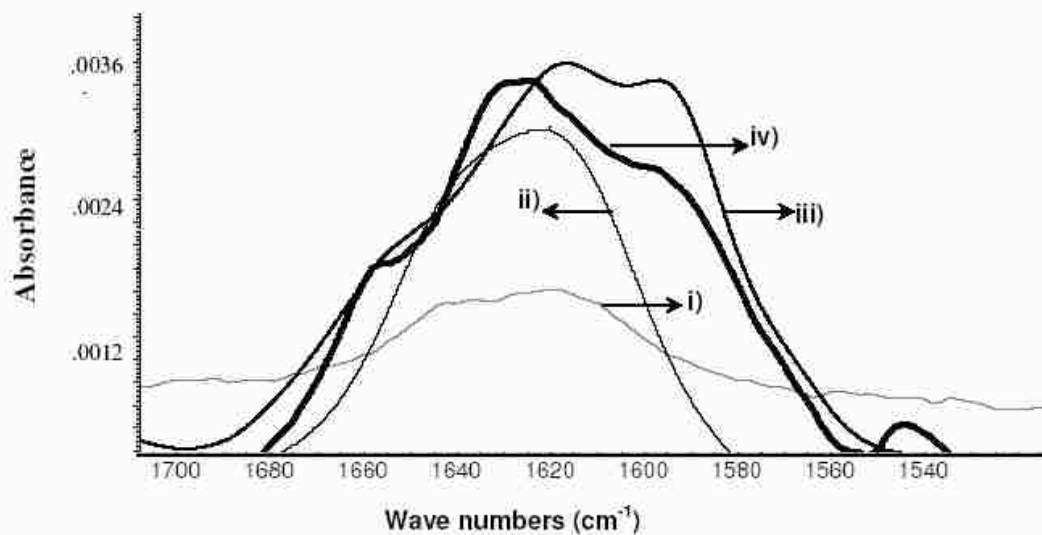
To monitor the functionalization reaction, FTIR spectra of CVD grown as-received CNT, plasma-oxidized CNT, CNT-dye, CNT-C9 and CNT-C22 are shown in figure 4.1a. The expanded and smoothed view of the region of C=O stretch is shown in figure 4.1b. As received CNTs show minimal C=O stretch. In the case of plasma-oxidized CNT, a peak at 1630 cm^{-1} was found. This can be attributed to C=O stretch in

carboxylic acid. For chemically-oxidized single-walled CNTs (SWCNTs), carbonyl stretch for carboxylic acid groups¹⁵³ has been found in the range of 1700-1750 cm^{-1} . This was not observed in our case since we used the much larger diameter multiwalled CNTs (MWCNTs). A shift of C=O stretch to lower frequencies can occur with larger aromatic groups.¹⁵⁴ Carbonyl peaks near 1630 cm^{-1} have also been observed near 1635 cm^{-1} in MWCNTs¹⁵⁵ and our observed shift after carbodiimide functionalization is consistent with carboxylate assignment. Also noticed was OH peak intensity at 3400-3500 cm^{-1} consistent with carboxylic acid groups, but conclusive interpretation is limited by overlap with peaks of absorbed water in the KBr pellets.

The peaks between 3000-3100 cm^{-1} are characteristic of aromatic C-H stretches, thus indicating an experimental difficulty of removing all the polystyrene or toluene solvent, adsorbed on or within (toluene) opened nanotubes. Polystyrene and toluene also have characteristic absorptions at 2850-2950, 1715, 1600, 1495, 1450, 1270 and 1050 cm^{-1} . Many of the similarities in spectra (iii, iv, and v) can be attributed to residual polystyrene or toluene. Functional molecules would primarily have peaks in the region 2800-3050 cm^{-1} (C-H stretches) and carbonyl stretches in 1600-1700 cm^{-1} . In the case of the dye molecule, aromatic peaks overlapping with polystyrene/toluene would also be expected. The expanded view of the region of C=O stretch for the functionalized membranes showed that the peak had broadened with the maximum at 1630 cm^{-1} and a shoulder at 1600 cm^{-1} , (for CNT-dye) and 1604 cm^{-1} (for CNT-C9) whose intensity is less than the peak at 1630 cm^{-1} . These peaks can be assigned amide (I) and amide II bands, respectively.¹⁴⁹ However for CNT-C22, a sharp peak at 1600 cm^{-1} is observed. Both the intensity and location of amide (I) and amide (II) stretches can be dependent on the local chemical environment. For instance, lower hydrogen bonding lengths (higher hydrophobicity) has been found to shift amide (I) stretches to lower frequencies in proteins.¹⁵⁶ In our case the presence of the highly-hydrophobic environment of CNT-C22 (in a conformation absorbed along the wall of CNT, is consistent with the transport studies), may shift the amide (I) stretch to a lower frequency, resulting in the sharp peak at 1600 cm^{-1} . However, interference from residual polystyrene or toluene (C-C aromatic stretch at 1600 cm^{-1}) makes this line of analysis inconclusive.



(a)



(b)

Figure 4.1 (a) FTIR spectra and (b) expanded and smoothed view of region of C=O stretch. Spectra is identified as (i) as received CNT; (ii) plasma oxidized; (iii) CNT-dye; (iv) CNT-9 membrane. The functionalized membranes show a peak at 1630 cm^{-1} and shoulder at 1600 cm^{-1} indicative of amide (I) and amide (II) stretches. Data shown in expanded region is smoothed with 11 point boxcar routine.

4.2.2 Effect of functional molecule-chain length on flux and selectivity

Measurement of the transport of molecules through a porous material is an effective method of probing the size and chemical state of pore interiors.¹⁵⁷ Hindered diffusion occurs in pores when the size of the permeating species is large enough to force significant interaction with the pore walls. Transport of two molecules having similar charge but different size ($\text{Ru}(\text{bipy})_3^{2+}$ and MV^{2+}) can show the relative hindrance provided by functional molecules at the entrance of the CNT cores. The summary of the transport properties through the membranes as a function of chemical functionalization are shown in Table 4.1. Figure 4.2 shows a representative plot of the transport of $\text{Ru}(\text{bipy})_3^{2+}$ and MV^{2+} through the membrane as a function of time.

The UV-vis measurements were not carried out *in-situ*. Specifically, they were not made continuously using the U-tube as a UV-vis cell. Instead, the flux experiment was interrupted to analyze the entire volume of the analyte cell. Due to time constraints of sequential analysis, each flux series (figure 4.2) has only 6-7 data points. This increases the amount of uncertainty in predicting the flux rates (slope of linear fit) from the measured values. Along with the mean-sample transport rate, we showed the (\pm) uncertainty at 90% confidence level. We used the equation $ts/n^{0.5}$, where n is the number of observations, t is the student's t value at n-1 degrees of freedom and s is the standard deviation of the measured values from the linear fit.

It is also important to note that the Fe-catalyzed CVD process for synthesizing aligned CNTs can lead to the presence of iron nanoparticles in the CNT-cores causing sample-to-sample variation in membrane transport. Plasma oxidation and HCl treatment are used to remove iron particles, but in extreme cases they remain to reduce the absolute flux values. As a control experiment, we made 'membranes' using an identical process steps (and thickness) from regions of the deposition reactor where all CNTs are blocked by Fe. No flux (either MV^{2+} or $\text{Ru}(\text{bipy})_3^{2+}$) was detected, even after three days of diffusion experiments. The detection limit of the instrument was 5.15×10^{-8} M for $\text{Ru}(\text{bipy})_3^{2+}$. Using the cell volume of 1.3 ml, the diffusion through the blocked membrane was less than 0.009 nmole/h. This indicated that diffusion through or defects in polystyrene polymer film were not significant transport mechanisms. The selectivities

Table 4.1 Summary of diffusive transport measurements across CNT membrane as a function of tip-functionalization (0.3cm² area, 5mmol of each source) from a 2-component source solution. Simultaneous flux of permeate is calculated from linear fit of solute concentration vs. time. The separation factor was experimentally measured for the membranes and pore size was calculated from the model using the separation factor and hindered diffusion model at the CNT entrance (model i). The error bars are the standard deviation of the linear fit from the experimental flux data at 90% confidence.

Membrane Tip Functionality	Size of Molecule (Å)	MV²⁺ Flux (nmole/h) (90% confidence)	Ru(bipy)₃²⁺ Flux (nmole/h) (90% confidence)	α	Pore Diameter calc. from α (Å)
CNT	0	4.21(±1.0)	2.45 (±0.39)	1.7	67
CNT-9	11.4	6.40 (±2.18)	2.12 (±0.90)	3.0	37
CNT-dye	28	21.05 (±2.32)	9.57 (±0.91)	2.2	47
CNT-22	26	1.84 (±0.48)	0.93 (±0.22)	1.97	50
CNT-40	52	0.65 (±0.13)	0.18 (±0.02)	3.6	33

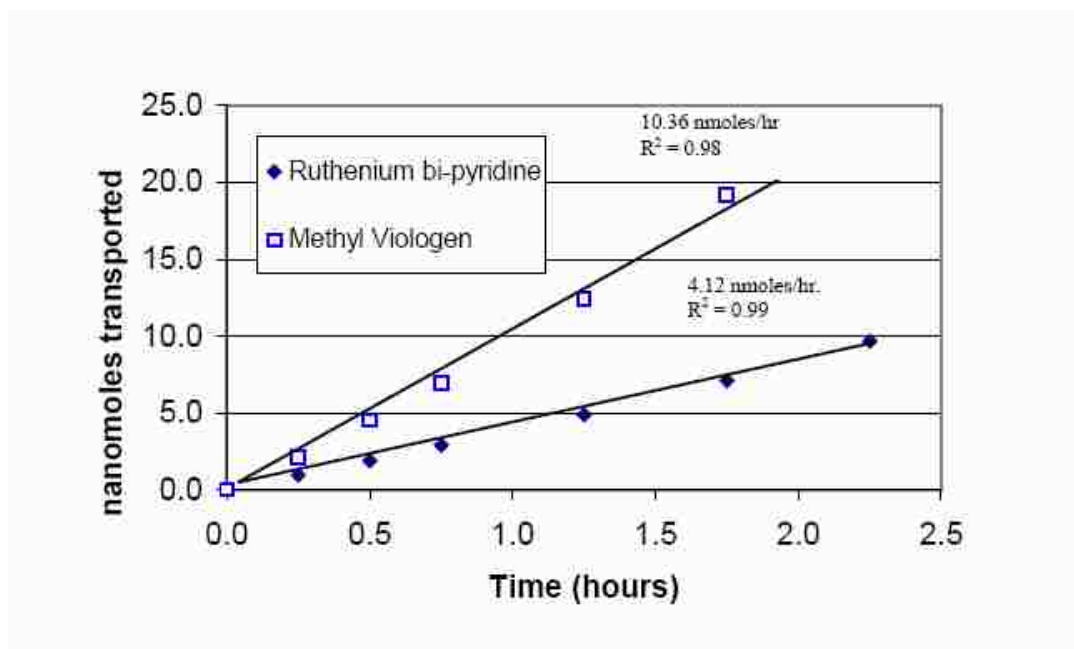


Figure 4.2 Representative plot of $\text{Ru}(\text{bipy})_3^{2+}$ and MV^{2+} transport through CNT-dye membrane in 0.1M KCl; Separation factor (α) is the ratio of the slopes of the linear fit of flux with time.

(α , the ratio of the transport rates of the two species) in these simultaneous flux experiments would not be affected by any CNTs that were blocked by iron.

In general the separation coefficients between MV^{2+} and $Ru(bipy)_3^{2+}$ were modest (1.7-3.6) compared to porous alumina where separation coefficients were as high as 1500.⁷² In the case of alumina membrane, pore-size reduction was accomplished by solid plating to sizes less than the diameter of $Ru(bipy)_3^{2+}$. In our case, the areal density of the functionalized molecule may not be complete (as it would be in the case of solid pore plating) and the conformation of the molecules may change with solvent conditions. The observed selectivity is consistent with ‘gate-keeper’ functionality at the CNT tips. In optimized systems, the tip functionality would have the advantage of short path length of hindered diffusion, thereby increasing overall permeate flux.

From established hindered diffusion studies, an increase in the separation factor would be expected from a decrease in pore size by the attachment of a functional molecule. The separation factor for the initial CNT membrane with COOH functionality is $\alpha=1.7$. This increases to $\alpha=3$ in the CNT-C9 case. Purely geometric arguments using the diameter of the CNT core would give a pore size of 47 Å (7 nm nominal core diameter minus twice the molecule). Pore-size reductions by depositing molecules in mesoporous-silica materials using silane chemistry have been reported to be consistent with the length of the molecule.¹⁵⁸ However, when a longer aliphatic amine of length ~ 28 Å (CNT-C22) was attached to the CNT membrane, the selectivity actually declined to $\alpha=2.0$. The $Ru(bipy)_3^{2+}$ flux also decreased compared to that of CNT-C9, by a factor of about 2.2. The overall flux through CNT-C22 was reduced by increased hydrophobicity at the pore entrances. This has also been the case with C_{18} modified porous alumina¹¹⁷ having very little transport of water and hydrophilic permeates. Liquid permeation experiments in hydrophobic membranes have also shown lower permeability of polar molecules such as water and alcohols as compared to alkanes, while the reverse is true for hydrophilic membranes.¹⁵⁹ Since the separation factor is a function of the pore diameter at the CNT entrances, attachment of a larger molecule should ideally give a reduced pore size as was observed in hydrophilic mesoporous silica (as measured by BET).¹⁴⁹ In all our cases, it is possible that a molecularly-dense functionality was absent at the CNT core entrance due to a relatively small number of carboxylic acid groups at the CNT tips.

This gave a reduced separation coefficient as compared to pore-plating methods. For long-chain alkanes, van der Waals interaction of the chains with the walls of the graphitic CNT core was expected to dominate, compared to chain-chain interaction. The reduction of the separation factor in CNT-C22 compared to CNT-C9 was consistent with the long hydrophobic alkyl chains preferring the surface of the hydrophobic CNTs and not protruding into the aqueous channel. This was in contrast to the case of alumina or silica pores, where the long-chain alkane interactions with the pore wall would be relatively weak.

4.2.3 Effect of charge and functional molecule aqueous solubility

Functionalization of the membrane with the anionically-charged dye molecule (CNT-dye) led to increased flux of positively-charged species. It increased ~ 4 fold compared to the unmodified CNT membrane. Potential dependent transport of charged species was demonstrated in gold nanotubule membranes.⁷⁶ $\text{Ru}(\text{bipy})_3^{2+}$ flux increased ~ 2.8 fold in 3.2 nm diameter and ~ 3.3 fold in 1.5 nm gold nanotube membrane when the applied potential was -0.4 V. This was compared to the flux in the membranes without any bias. Comparable increase of flux in CNT-dye indicated that there are electrostatically attractive forces acting on the positively-charged permeate species by the negatively-charged dye molecule. Along with an increase in flux, an increase of separation factors in CNT-dye compared to CNT-C22 was also observed, despite the fact that the dye molecule is slightly smaller than C22. The presence of the charged functional molecule would not lead to an increase in the separation factor based on electrostatic attractions because of the identical charges on MV^{2+} and $\text{Ru}(\text{bipy})_3^{2+}$. Instead, the increase is due to the conformation of the charged, soluble dye molecule. Molecules in favorable solvents are entropically stable and want to be in an open position as opposed to a folded one. This contributes to a larger decrease in pore size, which increases the separation factor. Conformational changes of molecules in solvents have been reported to regulate accessibility of microcavities in long-chain monolayers formed by molecular imprinting.¹⁴⁹ In CNT-C40, sequential addition of ACA (4 times) was followed by a reaction with C9 amine, so that the terminal group was an alkane group and not COOH. The long-chain molecule was about 52 Å long with a relatively

hydrophilic peptide bond, which should geometrically block the pores. Compared to CNT-C22, the CNT-C40 had a decrease in $\text{Ru}(\text{bipy})_3^{+2}$ flux (~5 times) and an enhancement in the separation factor to $\alpha=3.6$. Thus, the separation factor could be increased by attaching relatively hydrophilic long-chain molecules. In the case of long-aliphatic chain lengths (C22) the separation factors do not increase significantly ($\alpha=2.0$) because the molecules prefer to be oriented along the carbon-nanotube walls, instead of protruding into the aqueous channel.

4.2.4 Effect of solvent ionic strength on transport through CNT-dye membrane

By functionalizing the entrance to the CNT core with anionically-charged dye molecules, the flux of cationic permeates dramatically increased. The length of space-charge layer (ionic strength of the solution) should affect flux of permeates and separation factors as shown in Table 4.2.

There was nearly a three fold decrease in $\text{Ru}(\text{bipy})_3^{2+}$ flux when the electrolyte strength increased to 0.01M KCl. This is consistent with short screening lengths (at high ionic strength) reducing the Coloumbic attraction of the cationic permeate to the anionic functional groups, which reduces the overall flux. A theoretical study¹⁵² of SWCNTs of 2.2nm diameter found strong enhancement of ionic flux into the CNT core with charged carboxylate groups. Though the inner-core diameters of MWCNTs in this experimental study were about 7nm, the dye molecules were about 2.6nm long, resulting in an effective diameter of 1.8nm (diameter minus twice the functional molecule). This suggests that the length scales between theoretical SWCNT and this experiment are appropriate for comparison. It is unclear if anionic-carboxylate groups of ‘as made’ membranes (~7nm inner diameter) help cationic flux as compared to neutral entrances. The CNT-C9 membrane would have a neutral charge at the entrance (if completely functionalized) and does not show dramatically reduced cationic flux compared to as made CNT membrane. In the case of CNT-C22 a dramatic decrease in flux is seen, which may be due to more efficient functionalization in the IPA solvent or increased hydrophobicity. Since the tetravalent-dye molecule extends into the core cross-section, the CNT-dye membrane appears to have a higher efficiency for cation attraction compared to the ‘as made’ membrane. The ionic strength of the solution can also alter

Table 4.2 Transport measurement across CNT-dye in different concentration of electrolyte (KCl). The error bars represent the standard deviation of the linear fit from the measured experimental values.

Electrolyte	MV⁺²	Ru(bi-py)₃⁺²	
Conc. (M)	Flux (nmol/hr)	Flux (nmol/hr)	Å
KCl	(90 % confidence)	(90 % confidence)	
0	21.05 (±2.32)	9.57 (±0.91)	2.2
0.01	8.88 (±0.4)	3.24 (±0.17)	2.7
0.1	10.36 (± 0.97)	4.12 (±0.275)	2.5

wetting hydrophobic surfaces. A reduced rate of nitrogen-bubble nucleation and coalescence on hydrophobic surfaces is seen at increasing potassium chloride concentrations¹⁶⁰. Thus, in the presence of increased electrolytes, the phenomena of air bubbles should result in an increase in the flux of cationic species due to a decrease in air bubbles at hydrophobic CNT surfaces. Our experimental observations are a decreased flux of the cationic species in electrolytic solutions, thus suggesting that electrostatic effects are dominant.

Electrostatic interactions should be equal for divalent cations and should not lead to an increase in selectivity. A modest observed increase in permeate selectivity with increased solvent ionic strength indicated that there was also a pore-size reduction. This may be a result of the electrostatic conformation of the dye molecule. An increase in the molecular-interaction area in salt solutions due to dipolar coupling between the polar groups and ions has been reported in Langmuir/Langmuir-Blodgett films.¹⁶¹ Such interactions would be prominent in the charged dye molecule leading to conformational changes with a corresponding decrease in pore size. For a reported flux of a neutral molecule (phenol) through a larger carbon nanotube membrane (120 nm pore diameter)⁷⁸, there was not any change in diffusional flux with a change in electrolyte ionic strength. However, they found electroosmotic velocity decreased with increasing ionic strength. In our case there was no applied potential and thus we would not expect electroosmosis to be significant. This suggests that the conformation of the dye molecule is significant.

4.2.5 Comparison of observed selectivity to hindered diffusion models

Observed separation coefficients between differently-sized permeate molecules can give insight into the geometry of the membranes pores. The transport studies have been analyzed using equations 2.4 and 2.5

It is interesting to compare experimental-separation coefficients (α) to predictions of hindered diffusion at the CNT-tip entrances to verify a ‘gate-keeper’ transport limited mechanism. The first model considered was hindered diffusion only at distances $L_1/2$ at the two ends of the CNT and normal diffusion along the length L_2 . The total length of the nanotube is thus $L_1 + L_2$. The other model was hindered diffusion throughout the nanotube. Schematics for the two models are shown in figure 4.3a. We assume steady-

state conditions for this model. Since the cross-sectional area inside the nanotube is changing, $W=NxA$ is constant, where W is the molar-transport rate (mol/hr), and N is the flux and A is the pore area (cm^2). We also assume that the concentration of a species changes along the nanotube, with C_1 (mol/cm^3) at the entrance and C_4 (mol/cm^3) at the exit, which are the same as the feed and permeate concentration, respectively. C_2 (mol/cm^3) and C_3 (mol/cm^3) are the concentrations at the end of the first functional layer at the entrance and at the beginning of the second functional layer at the exit. The cross sectional area of the non-functionalized nanotube is A_0 (cm^2) and the area where hindered diffusion occurs is A_h (cm^2). These areas are given by:

$$A_0 = \pi d_0^2/4; \quad A_h = \pi d_p^2/4 \quad [3.1]$$

Where d_0 is the diameter (\AA) of the inner core of the nanotube and d_p is the pore diameter (\AA) at the entrance and exit. Thus,

$$\begin{aligned} W &= -D_h A_h (C_1 - C_2) / 0.5 L_1 = -D_0 A_0 (C_2 - C_3) / L_2 = -D_h A_h (C_3 - C_4) / 0.5 L_1 \quad [3.2] \\ &= -(C_1 - C_2) / (0.5 L_1 / D_h A_h) = -(C_2 - C_3) / (L_2 / D_0 A_0) = -(C_3 - C_4) / (0.5 L_1 / D_h A_h) \\ &= -(C_1 - C_4) / (L_1 / D_h A_h + L_2 / D_0 A_0) \end{aligned}$$

For two molecules with bulk diffusivities, $D_{0,1}$ and $D_{0,2}$ respectively, the following separation factor (α) is proposed:

$$\alpha = (L_1 / D_{h,2} A_h + L_2 / D_{0,2} A_0) / (L_1 / D_{h,1} A_h + L_2 / D_{0,1} A_0) \quad [3.3]$$

This equation can be simplified for model (ii) in which $L_2=0$, thus

$$\alpha = D_{h,1} / D_{h,2} \quad [3.4]$$

For the probe molecules, Ruthenium bi-pyridine is a spherical molecule with a diameter of about 11.8 \AA . MV^{2+} is a cylindrical molecule with length 11 \AA and breadth 3.3 \AA . The equivalent spherical diameter for the molecule is about 5.2 \AA . Diffusion

studies in porous alumina⁷³ saw a flux reduction for MV²⁺ of 10³ when pore size was reduced from 5.5nm to 0.6nm. Their data is remarkably consistent for an expected flux reduction of 1000. This is based on a factor of 83 (for reduction of pores size) and a factor of 13.8 (for reduction due to hindered diffusion) using the equivalent spherical diameter of MV²⁺ of 5.2 Å. Thus, reduced pore diameter for each species can be closely approximated as a function of d_p based on an equivalent spherical diameter. The bulk diffusivity of Ru-(bipy)₃²⁺ is 5.16x10⁻⁶ cm²/s.¹⁶² The bulk diffusivity⁷³ of MV²⁺ is 1.5 times that of Ru(bipy)₃²⁺ (i.e. D_{0,1}/D_{0,2}=1.5).

Experiments were carried out to estimate the functional density and the length up to which the nanotube tips were oxidized. The carbon-nanotube membrane was dissolved in toluene and centrifuged to remove the polymer. Thereafter, the nanotubes were functionalized with 2-aminoethanethiol using the same carbodiimide chemistry and decorated¹⁶³ with gold nanoparticles (10 nm diameter) by covalent linkage with the thiol group of 2-aminoethanethiol. By TEM the nanoparticle density was observed as the number of nc-Au particles/length of CNT for 30 different CNT's of 10 μm length.¹⁶⁴ The Au nanoparticle density decreased from 526 particles/micron at the tips to negligible (<7 particles/micron) at a location 700 nm from the carbon nanotube tips. At the tips, the surface coverage of nc-Au was ~52%. This is consistent with the previous argument that the functional molecules at the tips of the CNTs are not likely to be molecularly dense (packed). However, this gold nanoparticle decoration experiment is only a lower limit since several functional molecules (2-aminoethanethiol) may be attached to the same gold nanoparticle. The carbon nanotubes were also functionalized at each end at a distance ~ 7% of the total length of the nanotube. This is consistent with experimental observation of CNT tips slightly above the polystyrene matrix due to differing oxidation rates of CNT and polystyrene.⁷⁹ Though the exterior of the CNT's were decorated with gold particles, here we assume that the same oxidation process occurred inside during functionalization with molecules. Thus, L₁ is ~ 14% and L₂ is ~86% of the total length of the nanotubes. The selectivity vs. pore size (d_p) plots for the two models are shown in figure 4.3b. Consistent pore sizes of the different membranes can be calculated from the first model and the experimentally-observed separation factors. These calculated values are also shown in Table 4.1. Importantly, in the case of the as-oxidized (carboxylate only

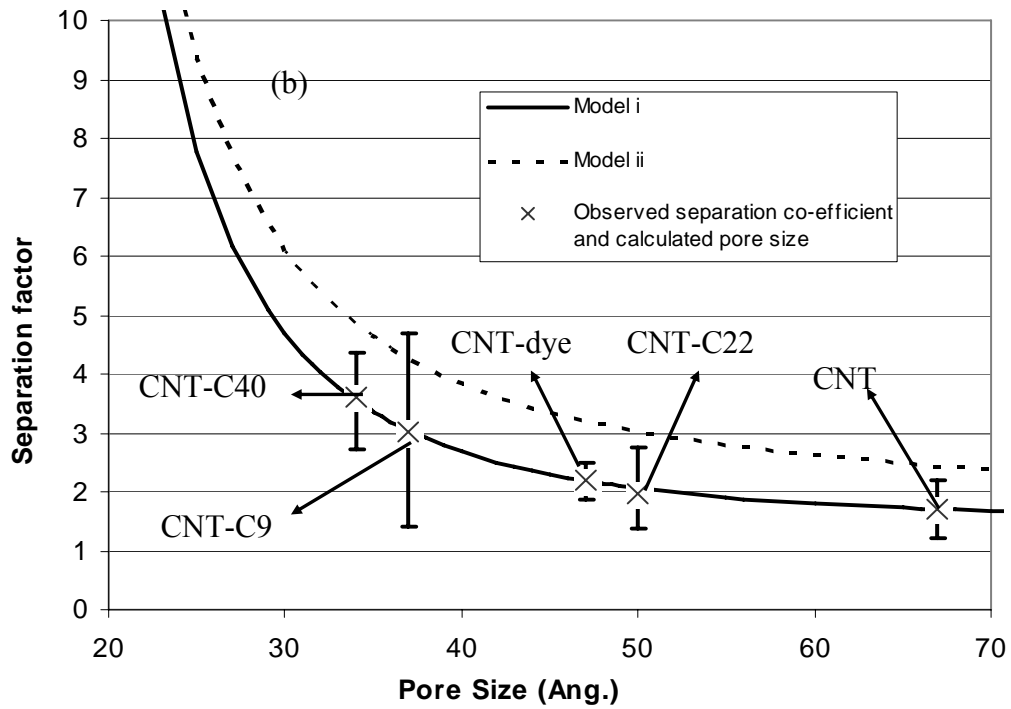
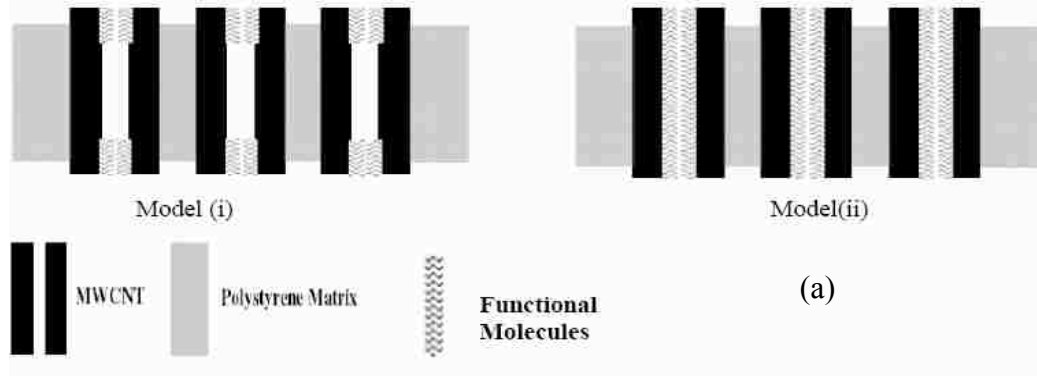


Figure 4.3 (a) Schematic and (b) separation factor (α) versus pore size for (i) hindered diffusion at the entrance and exit to the nanotubes; (ii) hindered diffusion throughout the nanotube; Model (ii) predicts higher α , than model (i) due to longer hindered diffusion path length.

functionality) membrane, model (i) gives a calculated pore size of 67 Å, which is consistent with microscopic characterization of MWCNT cores. Using model (ii), the calculated core diameter of as-oxidized carbon nanotubes is 20nm. Furthermore, the functional molecules would not be physically long enough to give the observed higher separation coefficients as seen in the chemically-modified membranes. The higher flux observed with the anionic dye molecule supports this model of tip functionalization. If the CNT cores were lined with an attractive anionic charge, we would expect a reduction in flux of cations due to partitioning onto pore wall with a decrease in effective diffusion coefficients. This effect is commonly seen in ion exchange membranes.¹⁶⁵ A somewhat subtle point of model (i) is the assumption of bulk diffusivity D_0 in the non-functionalized region of the CNT core. This would indicate that the permeate molecules have little interaction with the CNT wall since hindered diffusion is based largely on frictional interaction of the permeating molecule with the pore wall.⁶⁵ This would be expected from theoretical studies predicting that water molecules have a several Å gap with the CNT wall due to surface energy mismatch.²⁸ Polyethylene monomers diffusing in a CNT core are also predicted to keep a distance of about 4 Å from the CNT walls.¹⁶⁶ Other theoretical studies predict much higher diffusivities than in other nanoporous materials^{24,27} due to minimal frictional resistance between the inherently smooth potential-energy surfaces of the graphitic CNT interiors. Implicit in our hindered diffusion model (with hindrance only at the entrances to CNT cores) is that increases in overall flux across the membrane due to high diffusivities predicted inside CNT cores may be limited by the chemical interactions ('gate-keeper' functionality) at the tips of the CNT. The data and model shown here are self-consistent, but are not definitive proof of the nature of conduction through the CNT due to the experimental uncertainty of the areal density and the conformation of functionalized 'gate keeper' molecules.

4.3 Conclusions

Chemical functionalization at the entrance to CNT cores affects the selectivity of chemical transport across an aligned-membrane structure. The CNT tips are modified using broadly applied carboimide chemistry, which is confirmed by FTIR and electron microscopy of nc-Au decorated-site observations. Since the selectivity of transport is

modified through chemical functionality, the observed flux through the CNT membrane cannot be through macroporous cracks in the polymer matrix. Additionally, the lack of flow through membranes using CNTs that are blocked by iron catalyst particles indicates that the polystyrene polymer matrix is not rendered mesoporous by the fabrication steps. Increasing the length of the 'gate-keeper' molecule at the CNT core entrance improves size-based selectivity. However, longer aliphatic functional molecules have poor aqueous solvation resulting in reduced selectivity. This indicates the importance of functional-molecular configuration. Use of anionically-charged dye molecules as 'gate-keepers' dramatically improves cationic transport through the membrane due to Coloumbic attraction. A hindered-diffusion model with lowered diffusivity near the entrances of CNT cores, and with bulk diffusion along the length of CNTs, was consistent with observed-separation coefficients (α) as a function of chemical functionality. Thus, the overall chemical flux through CNT membranes is largely limited by chemical interactions of functional molecules at the CNT core entrances.

Longer aliphatic lengths of functional molecules have poor solvation resulting in reduced selectivity, indicating the importance of functional molecular configurations. Using anionically-charged dye molecules as 'gate-keepers' dramatically improves cationic transport through the membrane due to Coloumbic attraction. A hindered-diffusion model with lowered diffusion near the entrance to CNT cores, and with bulk diffusion along the length of CNTs, was consistent with observed separation coefficients (α) as a function of chemical functionality. Thus, the overall chemical flux through CNT membranes is largely limited by chemical interactions of functional molecules at the CNT core entrances.

Chapter 5

Electrochemical Functionalization and Characterization

This chapter is based on two manuscripts:

Majumder, M.; Keis, K., Zhan, X.; Meadows, C; Cole, J.; Hinds, B. J., “Enhanced electrostatic modulation of ionic diffusion through carbon nanotube membrane by diazonium grafting chemistry” *Journal of Membrane Science* (accepted) **2007**

Majumder, M.; Keis, K., Zhan, X.; Hinds, B. J., “Switchable impedance spectroscopy of functionalized vertically oriented CNT membrane/electrode” (*in preparation*), **2007**

5.1. Introduction

Transport processes modulated by electrostatics are central to several separation processes including nano-filtration¹⁶⁷, adsorption¹⁶⁸, ion-exchange¹⁶⁹ and electro-osmosis.⁷⁹ Interest is also in ionic transport through pores with dimensions close to the Debye screening length, which causes overlap of the electrical double layer. Ion-permselective membranes⁷³ and energy-conversion devices¹⁷⁰ rely on high-charge density in geometrically well-defined pore structures.

The membrane structure⁸⁰ consisting of an array of open-ended carbon nanotubes (~ 7 nm i.d.) spanning across an inert polymer matrix offers possibilities of extremely fast mass transport through the non-interacting and atomically planar graphitic inner core.¹⁰³ A plasma oxidation step, inherent to the membrane-fabrication process, introduces carboxylate functionality at the CNT entrances. This allows for facile covalent attachment of functional ‘gate-keeper’ molecules of different size, charge, hydrophilicity, and hydrophobicity at the CNT tips. Initial studies, as discussed in Chapter 3, showed that ionic transport (flux and size selectivity) through the membrane structure can be modulated by this ‘gate-keeper’ functionality.¹⁰⁵ However, the observed separation factors were modest, indicating less than ideal density of functional molecules tethered to the CNT core. For numerous applications, including ionic-separations and engineering a

membrane with 'voltage-gated' control of transport,¹⁰⁶ it is imperative to increase the surface charge density of the functional molecules on the carbon nanotubes.

Various methods for introducing functional sites on the chemically-inert carbon nanotubes have been reported in the literature.^{171, 172} Functionalization chemistry of CNTs has primarily relied on derivatizing the CNTs by oxidation in HNO₃,¹⁷³ or by strong oxidizers like SOCl₂¹⁷⁴ to generate oxygenated functional groups as for example carboxylic acid. Other strategies include plasma activation¹⁷⁵ and high temperature halogenation.¹⁷⁶ Derivatized CNTs can then be easily further functionalized with proteins, enzymes, or peptide, through a covalent-coupling chemistry between the surface-bound groups and functional groups on the molecule of interest. An alternative, more controllable strategy to functionalize CNTs, is the electrochemical covalent modification of these conducting surfaces.¹⁷⁷ Electrochemical approaches for modification of glassy carbon or other graphitic surfaces include oxidation of amines,¹⁷⁸ reduction of aryl diazonium cations,¹⁷⁹ or oxidation of arylacetates.¹⁸⁰ Aryl diazonium salts are well known to react covalently with glassy-carbon¹⁸¹, graphite¹⁸², CNFs and CNTs,^{183,184} by a one-electron reduction mechanism to form a covalent C-C linkage. The covalently-linked molecule is usually one monolayer and stable in a wide potential window.¹⁸⁵ However, there are reports of the formation of multilayers under certain over-voltage potentials.¹⁸⁶ CNTs have been used to modify glassy-carbon electrodes by deposition from a solution,¹⁸⁷ in the form of composites with a conducting polymer like Nafion,¹⁸⁸ or a binder like Chitin.¹⁸⁹ Of interest, even from the perspective of electrochemistry, is the membrane structure⁸⁰ consisting of an array of open-ended carbon nanotubes (~ 7 nm i.d.). A plasma-oxidation step, inherent to the membrane fabrication, removes excess polymers, and exposes and opens the CNT tips. In this membrane system, the CNTs protrude about 70nm above the PS surface, increasing the area of exposed CNTs.¹⁶⁴ Importantly, the CNTs cross each other with modest tortuosity, thereby introducing in-plane conductivity. Hence, this membrane structure can be used as an electrode in an electrochemical cell.

In this chapter, an electrochemical grafting technique is demonstrated to enhance the functional density on the CNT membrane structure. Increase in functional density is confirmed by dye adsorption-desorption tests and interfacial capacitance measurements.

Anionically-charged dye molecules are then attached covalently to these grafted carboxylic acid groups and the resulting functionalized membrane/electrode is characterized by faradaic and non-faradaic impedance spectroscopy. Direct evidence of an electrochemically switchable surface is demonstrated and is the basis for electrostatically-gated membranes discussed in the next chapter.

5.2. Results and Discussions

5.2.1 Estimation of COOH density by pH dependent dye adsorption-desorption

The understanding and manipulation of surface-chemistry density at the entrance to CNT pores is critical for engineered-separation applications. Figure 5.1(a) describes the mechanism for estimation of carboxylic acid density. The experimental procedure for this measurement is discussed in section 2.12. In basic pH, the carboxylic acid groups are deprotonated. Toluidine Blue O is positively charged and forms an electrostatic complex with the charged COOH groups. The experiments were carried out at varying concentrations of TBO (from 1.2×10^{-4} M to 2.5×10^{-3} M) to insure a monolayer coverage corresponding to charge density and physisorption. Figure 5.1(b) shows a lack of dependence of absorbed TBO dye on the concentration of incubation solution, which is expected for Langmuir-type isotherms for adsorption of a monolayer. The functional density is based on the planar area of the membrane and assuming a 1:1 correspondence between the amount of dye desorbed and the number of functional groups. It is important to point out that the true surface area of membranes is significantly higher than the planar area. In this membrane system, the CNTs protrude about 70nm above the polystyrene surface¹⁶⁴ increasing the area of exposed CNTs. Also, this estimation will not discriminate between carboxylate groups on the polymer and the CNTs as both form carboxylic-acid groups in the plasma-oxidation process. The conductive CNTs, however, are the only active sites for diazonium grafting. Dye assay experiments indicated ~ 4-5 times increase in functional density of COOH groups by electrochemical diazonium grafting to $\sim 1 \times 10^{15}/\text{cm}^2$ (planar area). These experiments also demonstrate the feasibility

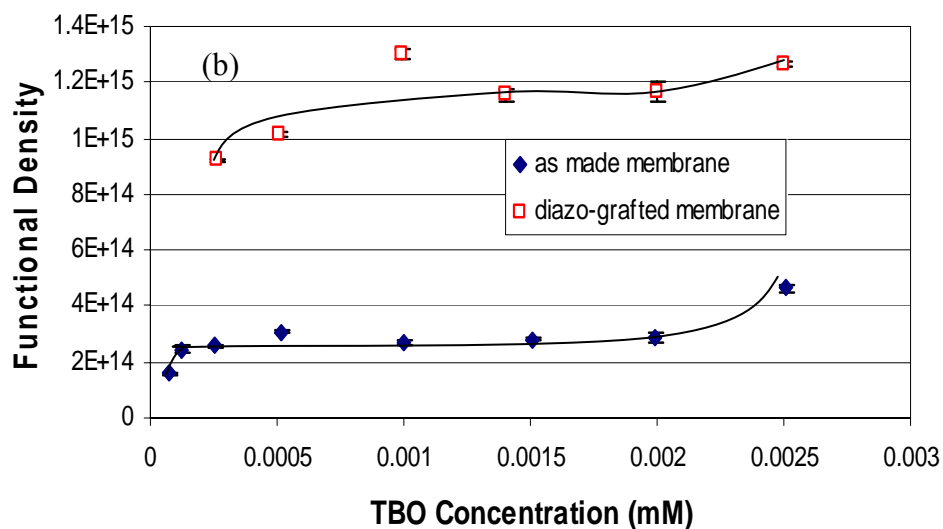
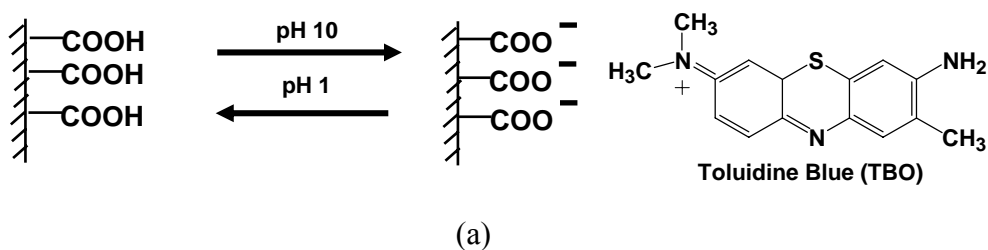
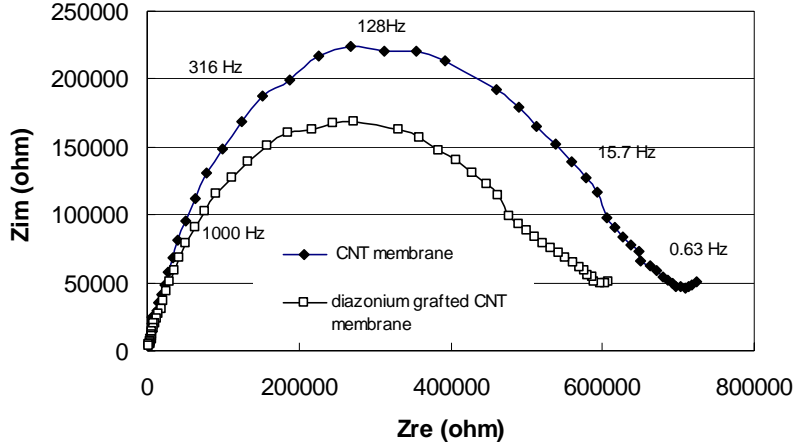


Figure 5.1 (a) Chemical assay for the estimation of carboxylic-acid density of CNT membranes by pH dependent adsorption/desorption of charged-dye molecule; (b) Functional density ($\#/cm^2$) of CNT membrane as a function of the concentration of the adsorbing dye solution. Increase by 4-5 times in functional density is observed with electrochemical diazonium (static) grafting. Area used for functional density calculation is the geometric planar area of the sample. Lines are added to aid visual clarity.

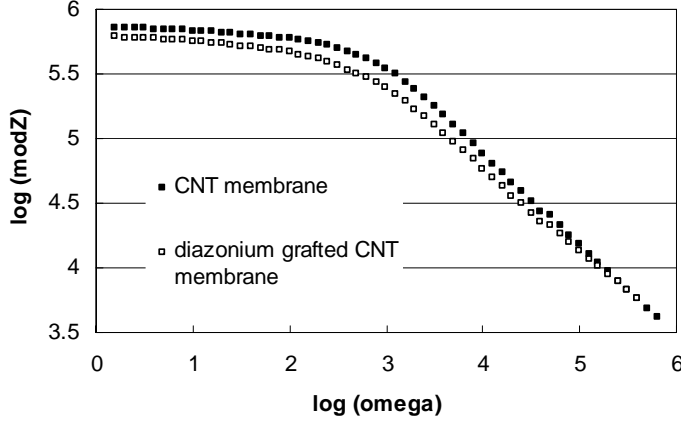
of membrane adsorbers based on CNTs with facile regeneration by pH-dependent desorption.

5.2.2 Interfacial Capacitance Measurements

Electrochemical capacitance is a powerful method that allows the measurement of active electrode surface area; charge density; dimensions of the space charge layer; and ionic diffusions rates. This can be used to quantify the functional density of modified CNT membranes and probe the conformational state of long-tethered molecules. The typical electrochemical impedance spectroscopy (EIS) plots for as-prepared CNT membrane and diazonium-grafted CNT membrane measured at 0V vs. Ag/AgCl in 0.1M KCl (pH=10.8) are shown in figure 5.2. The Nyquist plot (Figure 5.2 (a)) indicate an electrical circuit consisting of a resistance (R_{el}) from the electrolyte and a capacitor corresponding to the electrical double layer (C_{dl}) in parallel.¹⁹⁰ The presence of a single semicircle is attributed to the kinetics of charging and discharging of the electrochemical double layer at the CNT electrode/electrolyte interface with a RC time constant of ~ 8 msec.¹⁹¹ A typical Nyquist plot for an array of CNT (not impregnated with a polymer) showed a semicircle (i.e., a capacitor and a resistor in parallel) and a vertical tail at lower frequencies (from 10 Hz to 0.1 Hz).¹⁹² Such a vertical tail was not observed for the membrane electrodes in this study. The Bode plots of $\log|Z|$ vs $\log(\omega)$ demonstrate the plateaus at low frequencies associated with the sum of the resistance of the electrolyte solution and the contact resistance, while the straight declining line at intermediate frequencies characterizes the double layer capacitance (figure 5.2(b)). For the CNT membrane, the calculated capacitance from the intermediate frequency region of the Bode plot was estimated to 1.86×10^{-8} F. After the diazonium grafting, the capacitance increased to 4.2×10^{-8} F, (an increase by a factor of 2.2 at pH 10.8). This is consistent with ~ 3 fold increase in capacitance for surface (COOH) functionalized carbon nanotubes.¹⁹³ Capacitance increase due to an increase in functional-group density on carbon nanotubes was demonstrated earlier using cyclic voltammetry measurements.¹⁹⁴ Also in our study, the presence of a large density of carboxylic groups can be shown by cyclic voltammetry, where oxidation/reduction of surface carboxylic groups appear as two distinct broad



(a)



(b)

Figure 5.2 (a) Nyquist and (b) Bode plots for as-made CNT membrane and diazonium (static) grafted CNT membrane electrode. The electrolyte is 0.1(M) KCl in an aqueous 10mM K_2CO_3 buffer. A semi-circle in the Nyquist plot indicates an electrochemical circuit consisting of a resistor (R_{el}) and double-layer capacitor (C_{dl}) in parallel. An increase in total capacitance of ~ 2 times is observed.

peaks at potentials around -0.3 to -0.4 V that are very difficult to quantify analytically. It is important to point out the EIS measurements in our study are carried out in a potential range (-200 mV to 200 mV) where no surface redox reactions would occur.

In the dye adsorption-desorption experiments, it was shown that the surface carboxylic-acid groups could be deprotonated at high pH and protonated at low pH. It is interesting to study the changes in interfacial capacitances with progressive deprotonation of the carboxylic-acid groups. It is also pertinent to estimate the functional density of the surface carboxylic-acid groups due to mild plasma oxidation conditions and strong diazonium grafting chemistry. The dye assay described in the preceding section would not specifically estimate the functional density on the CNTs, since the plasma-oxidized polystyrene polymer would also adsorb and desorb the dye molecule. Figure 5.3 shows the measured capacitances of the CNT membranes normalized to the capacitance at pH ~ 2 . The interfacial capacitance of the diazonium- grafted CNT membrane increases with increasing pH by $\sim 128\%$ compared to 20% for the as-made plasma-oxidized membrane, indicating the presence of charged ionizable groups on the CNT surface. The total interfacial capacitance (C_T) at the CNT surface is a function of the film capacitance (C_F), the diffuse double-layer capacitance (C_s) and the capacitance from the degree of protonation ($C(f)$), represented by the equation ¹⁰⁷:

$$\frac{1}{C_T} = \frac{1}{C_F} + \frac{1}{C_s + C(f)} \quad [5.1]$$

The presence of carboxylic acid groups, which can be ionized at higher pH leads to increase in $C(f)$ and hence C_T . The presence of larger amounts of carboxylic-acid groups via diazonium grafting leads to the greater increase in pH-dependent capacitance compared to the as-made membrane. At low pH, the contribution of ionized groups is significantly less. Hence, both C_{θ} and its corresponding C_s should be small. The total capacitance measured at low pH should be the film capacitance. The differential capacitance of highly-ordered pyrolytic graphite in contact with a 0.2 M of $1:1$ electrolyte was $\sim 3 \mu\text{F}/\text{cm}^2$.¹⁰⁸ Assuming that the graphitic nanotube in contact with 0.1 M of another (tetrapropylammonium tetrafluoroborate) $1:1$ electrolyte exhibits similar behavior; one

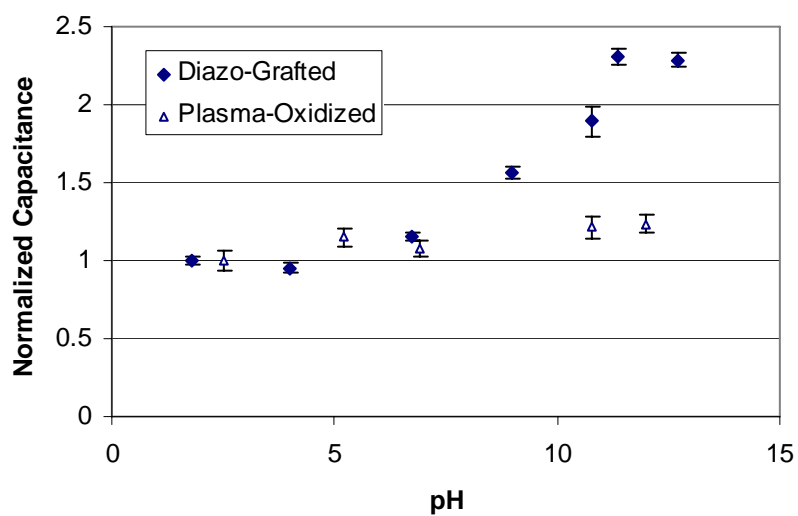


Figure 5.3 Interfacial capacitance as a function of pH. The electrolyte is 0.1M KCl in an aqueous 10mM K_2CO_3 buffer and pH is controlled by the addition of KOH or HCl. The estimated charge density of fully deprotonated -COOH groups of diazonium-grafted CNT membrane is $4 \times 10^{-2} \text{ C/m}^2$ compared to $\sim 6.4 \times 10^{-3} \text{ C/m}^2$ for as-made CNT membrane, indicating ~ 6 fold increase in carboxylic group density.

can estimate the active electrode area, A_e (cm^2), from the measured capacitance at pH 2 using the equation:

$$A_e = \frac{C_T(\text{pH} \sim 2)}{3 \times 10^{-6}} \quad [5.2]$$

The difference in capacitances at pH 2 and 12 (in Farad) represents the degree of protonation with change in pH. Assuming that the increase in capacitance is proportional to the amount of surface charge generated due to deprotonation of the carboxylic acid groups, the number of surface sites ($\# \text{ sites}/\text{cm}^2$) can be estimated from the equation:

$$\# \text{ sites} / \text{cm}^2 = \frac{[C_T(\text{pH} \sim 12) - C_T(\text{pH} \sim 2)]}{e \times A_e} \quad [5.3]$$

where, e is the electronic charge (i.e. the charge carried by each COO^- group).

The measurement of charge density from the capacitance measurements accounts for the actual electrically-active CNT area and is independent of functional groups on the oxidized-polystyrene surface, while the dye assay is not. Comparisons of the capacitance-based measurement of functional sites on CNT surfaces are shown in Table 5.1 with the carboxyl density increasing from 4×10^{12} to 2.4×10^{13} after diazonium grafting. The maximum possible functional sites on the edge planes of a cut-graphite surface are on the order of $10^{15}/\text{cm}^2$. Also for comparison, commonly used strong-acidic oxidation to cut and functionalize CNTs result in $\sim 14\%$ of oxidized carbon atoms ($\sim 10^{14} \text{ sites}/\text{cm}^2$)¹⁹⁵ but that process damages the polymer matrix, thus is generally unsuitable for this membrane system. The plasma-oxidation process used in the membrane fabrication scheme is limited to the exposed graphite surfaces near the CNT tips only. This is because high reactivity of the free radicals generated by the plasma process precludes its entrance deep into to the meso- or micro-pores.¹¹⁶ Electrochemical grafting of diazonium salts is a facile technique for increasing the functional density of the CNT membranes without compromising the integrity of the membrane structure.

Table 5.1 Comparison of estimated functional-site densities of carbon-nanotube systems.

	Capacitance pH~2 (F)	Capacitance pH~12 (F)	Active Electrode Area (cm ²)	Functional site density (#/cm ²)
Plasma Oxidized CNT Membrane	$5.4 (\pm 0.2) \times 10^{-8}$	$6.7 (\pm 0.03) \times 10^{-8}$	0.018	$4.4 (\pm 0.9) \times 10^{12}$
Diazo-Grafted CNT Membrane	$5.5 (\pm 0.1) \times 10^{-9}$	$12.7 ((\pm 0.07) \times 10^{-8}$	0.00185	$2.4 (\pm 0.07) \times 10^{13}$
Acidic Oxidation of CNTs ²⁸				$1 - 2.5 \times 10^{14}$
Cleaved Graphite Edge Planes				1.5×10^{15}

Surface pK_a of carboxylic-acid groups on SWNT or MWNT by atomic force titration measurements was reported to be close to the bulk pK_a of benzoic acid (4.5).¹⁹⁶ Defining pK_a as the pH at which 50 % of the groups are ionized, we observed the pK_a of the surface-bound carboxylic-acid groups to be ~ 9 . Shifts in pK_a of surface-bound benzoic-acid groups on carbon surfaces are well known. Benzoic-acid groups on graphitic carbon synthesized by the same diazonium-grafting chemistry have shown pK_a shifts to $pH \sim 6.5$.¹⁹⁷ The determination of surface-bound pK_a depends strongly upon the experimental-measurement technique; and the higher-surface pK_a observed here is consistent with double-layer capacitance measurements of mercaptoundecanoic acid on the gold surface ($pK_a > 10$).¹⁹⁸

The highly reactive electrochemical grafting is not selective to the CNT tips and would also functionalize the graphitic interior core of the CNTs. Because CNTs show dramatically-enhanced fluid flow through the cores of CNTs,¹⁰³ it is possible to protect the inner core of CNTs from the highly-reactive diazonium reagent with a fast-flowing inert solution in the core. This is simply achieved during electrochemical functionalization by using a U-tube electrochemical cell with a column of inert liquid (aqueous 0.1(M) KCl), 10 cm higher than the diazonium solution side of the membrane. Flow velocities are estimated to be 0.1 cm/s, which exceed the aqueous-diffusion characteristic length by an order of magnitude at the time scale of the grafting experiment.

5.2.3 Voltage-Dependent Capacitance Measurement

In the previous section the effect of pH dependent protonation, affecting the measured interfacial capacitance was discussed. Let us turn our attention to two other important parameters affecting the interfacial-capacitance measurements of the conducting-CNT membranes: ionic strength and applied potential (figure 5.4). It is well understood that the ion distribution at a charged surface depends on the ionic concentration of the electrolyte. The Debye screening length, often used to describe the double layer capacitor effects, is dependent upon the concentration of the electrolyte. At lower concentration of the electrolyte, the Debye length is large and consequently the interfacial capacitance is reduced. An increase in capacitance with increasing

concentration of electrolyte (from 0.01M to 0.1M KCl) is consistent with capacitance measurements with varying electrolyte concentration in porous carbon materials.¹⁹⁹ At higher ionic strength, diffuse double layer can be neglected, potential occur within the Helmholtz layer. Capacitance is large. Variation in capacitance with applied potential is a result of change in double-layer structure. At negative potential, the interfacial capacitance increases as the charged electrode attracts the counter ions and compresses the double layer. A higher rate of increase in capacitance is observed with a higher concentration of the electrolyte. At positive potential, the applied bias neutralizes the negative charge on the electrode and the double layer is large. Hence, the capacitance does not increase significantly with the potential.

For homogeneous surfaces, the sharp minimum in differential capacitance versus potential is observed in dilute electrolyte solutions, where a diffuse space-charge layer is formed. This minimum corresponds to an electrostatically-discharged interface and is generally interpreted as potential of zero charge. The presence of such a minimum can be explained by the general Gouy-Chapman theory. For heterogeneous systems with energetically-different surfaces, the flat, broad minimum in capacitance could be obtained.²⁰⁰ For diazo-grafted CNT membranes, the broad but small decrease in differential capacitance was observed in the region of +12 to +25 mV.

An estimate of the charge density from a PZC of 25 mV in 0.1(M) of a 1:1 electrolyte would lead to a charge density of $1.9 \times 10^{-2} \text{ C/m}^2$ (i.e. functional site density of $\sim 1.2 \times 10^{13} \text{ sites/cm}^2$),²⁰¹ which is consistent with the charge density estimates from pH-dependent capacitance measurements. However, the absence of a sharp minimum in the potential vs. capacitance measurements introduces large uncertainties in this method.

The functional density estimates from the pH-dependent capacitance measurements, discussed earlier, are more accurate. It is important to point out that the capacitance measurements were highly reversible, i.e. capacitance at 0 V was retained after measurements at ± 200 mV. This indicates the stability of the covalently-grafted molecules on the carbon-nanotube surface. An important observation from these measurements is the retention of electrochemical activity of the CNT-membrane structure

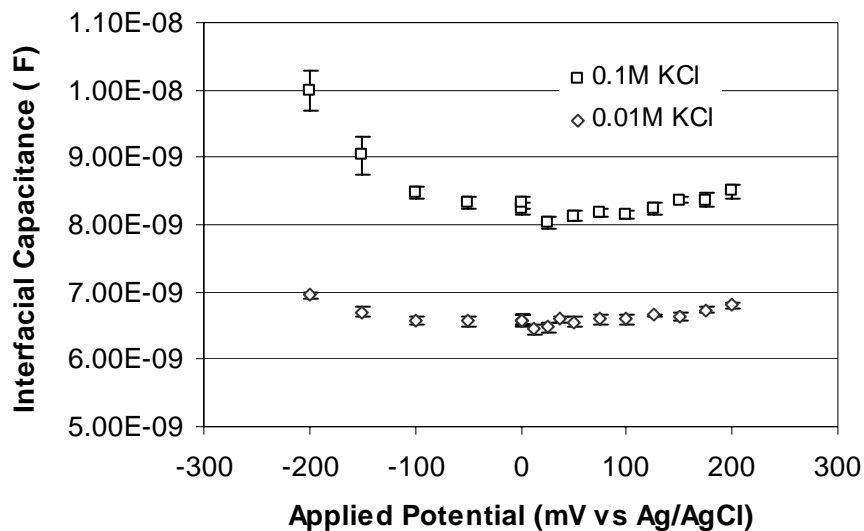


Figure 5.4 Interfacial capacitance of the diazonium-grafted CNT membrane as a function of applied potential, measured in an aqueous 10 mM K_2CO_3 (pH =10.8) buffer solution with various KCl concentrations. A compact Debye length of ~ 0.9 nm at 0.1M KCl compared to ~ 3 nm at 0.01M KCl increases the measured interfacial capacitance.

after increased functional density -- an important attribute for several applications of the CNT membrane.

5.2.4 Ionic Transport Measurements

The porosity (ϵ) of the membrane used for the diazonium grafting studies was estimated from MV^{2+} flux as discussed in section 2.14. The low porosity ($\sim 9 \times 10^{-4}\%$) is a result of a significant fraction of CNTs being blocked by iron-catalyst particles during the CNT growth process. The ionic transport measurements for the diazo-grafted membrane are shown in figure 5.5. The fluxes shown are normalized with respect to their as-made (plasma-oxidized) flux of $Ru(bipy)_3^{2+}$ without the screening electrolyte (i.e., without 0.1 M KCl), because of the sample-to-sample variation of porosity. For static-grafted CNT membrane the flux of positively charged- $Ru(bipy)_3^{2+}$ increased ~ 2.3 fold. This is consistent with our earlier observation of $\sim 4-5$ fold increase in the flux of $Ru(bipy)_3^{2+}$, when the plasma-oxidized membrane is functionalized with a large anionically-charged ($4e^-$) dye molecule.¹⁰⁵

When the diffusive transport measurements were performed in 0.1M KCl, the charged molecules on the membrane were screened and diffusive flux returned to near that of unmodified (plasma-oxidized) membranes. The transport measurements were carried out using a feed solution of 5mM $Ru(bipy)_3^{2+}$ and 5 mM MV^{2+} . The Debye screening length for a 2:1 electrolyte of 10 mM concentration is ~ 1.7 nm, which decreases to 0.8 nm in the presence of 0.1M KCl.²⁰² A better parameter for understanding the double-layer effects for small pores is the ratio of the Debye length to the pore radius. It is ~ 0.5 in the absence of the electrolyte and decreases to ~ 0.25 in the presence of 0.1M KCl, which explains why the fixed charges on the membranes are screened within a short distance of the pore walls. Thus, in ionic solutions with a very short Debye length of <1 nm, the positively charged permeates fail to be electrostatically attracted to the anionic surface charge and the diffusional-flux enhancement declines. However, for the case of flow grafting, where a fast fluid-flow protects the inner core and restricts the grafting reaction to the top tip surface, the number of surface carboxylic- acid groups are significantly less. Also the charges are spatially located on the surface and

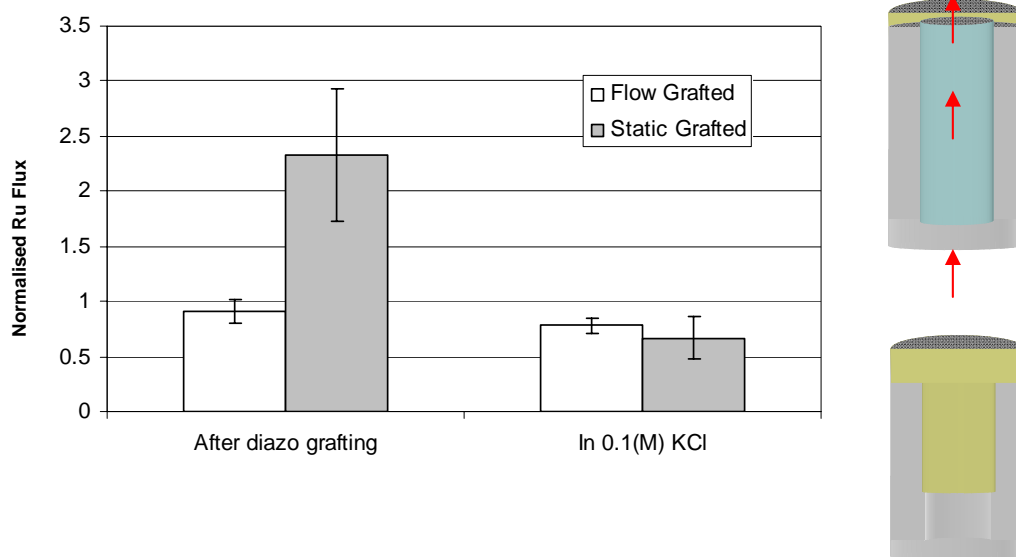


Figure 5.5 Selective spatial functionalization of CNT membranes by static grafting (SG) and flow grafting (FG) and the effect on $\text{Ru}(\text{bipy})_3^{+2}$ diffusion across the membrane. The static-grafted membrane shows > 2 fold increase in diffusive flux of positively-charged $\text{Ru}(\text{bipy})_3^{2+}$ by the attraction to anionic carboxylate groups. The electrostatic attraction is screened in a 0.1M KCl solution.

tips of the membrane, which will have significantly less electrostatic influence than inside the pores. Hence, the flux of $\text{Ru}(\text{bipy})_3^{2+}$ does not change significantly from the non-functionalized (plasma-oxidized) form. Likewise, screening the charge does not show significant change on the transport of the charged ionic species, within the error of the experiment.

5.2.5 Switchable Impedance Spectroscopy of Dye Functionalized CNT

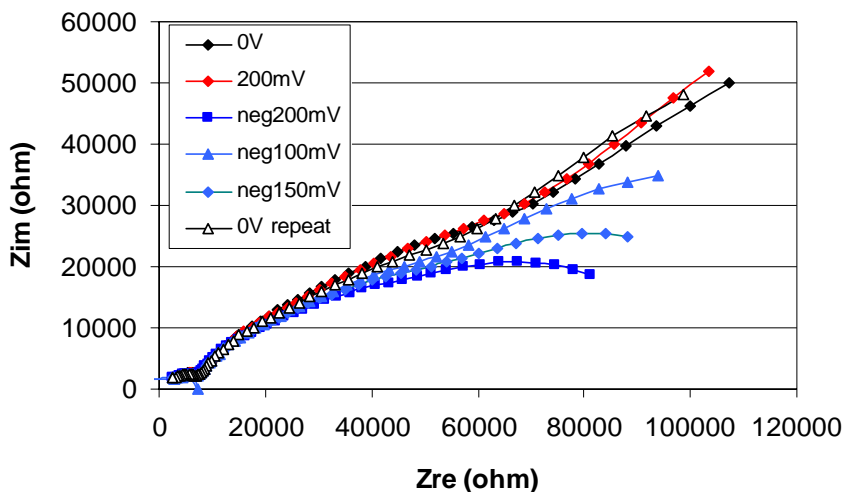
Membrane/Electrode

There is also considerable interest in surfaces, the properties of which can be switched in response to an external stimulus like light, temperature or electrical potential. Application in controlled-release devices, micro-fluidics, switchable surfaces and sensors have been demonstrated.^{203,204} Potential dependent switchable surfaces have been based on piezo-electric thin films²⁰⁵ or conformationally-free self-assembled monolayers on gold surfaces.^{206,207} Therefore, developing electrochemically-switchable surfaces based on other robust chemistry and substrates is a challenge worth pursuing.

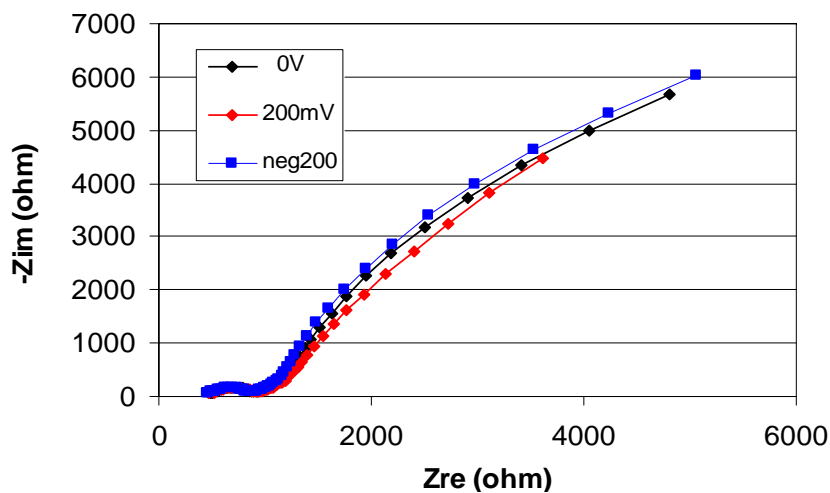
Carbon nanotubes (CNTs) are increasingly used for electrochemical sensing devices and electroanalysis²⁰⁸ underlining their importance in electrochemistry. Several studies have claimed the enhanced electrochemical performance of CNT-based electrodes in such sensing applications, probably because of the high proportion of edge plane sites in multiwalled carbon nanotubes (MWNTs).²⁰⁹ Hence, CNTs are potentially interesting materials from the viewpoint of developing switchable surfaces considering that the same chemistry could be applied to the tips of the open-ended CNTs for ‘voltage-gated’ molecular-transport channels.

As discussed in preceding sections, electrochemical diazonium grafting of 4-carboxyphenyl tetrafluoroborate is a facile way to increase the functional density of the CNT membranes. Comparison of capacitance based measurement of functional sites on CNT indicate an increase from $4.4 (\pm 0.9) \times 10^{12}$ in as-made (plasma-oxidized membrane) to $2.4 (\pm 0.07) \times 10^{13}$ for diazonium grafted CNT.

For the diazo-grafted membrane, one semi-circle in the Nyquist plots was observed, indicating an electrical equivalence of a double-layer capacitor in parallel with



(a)



(b)

Figure 5.6 Comparison of non-faradaic impedance spectra of (a) CNT-DG-dye and (b) CNT-DG-spacer-dye membrane electrode. The impedance spectra were recorded at the bias voltage indicated in the figure and an AC impulse of 10 mV rms. The electrolyte solution is 0.1 in KCl and 10 mM in K_2CO_3 . The experiments were conducted on two membrane samples, hence the difference in their absolute impedances. Note that the CNT-DG-dye membrane electrode exhibits switchable impedance effect, while CNT-DG-spacer-dye does not.

a resistor. A distinct difference in the non-faradaic impedance spectra, of the dye-functionalized CNT membrane electrode shown in figure 5.6, from the diazo-grafted membrane (figure 5.2(a)) is the presence of two semicircles, a smaller one at low frequency (with maximum ~ 7 KHz); and another incomplete semi-circle with a long tail at higher frequencies, indicating the presence of two separate processes at the functionalized-membrane electrode. These two processes would be: (i) the electrical double layer (EDL) formation on the electrode surface and; (ii) electrochemical-charge accumulation on the functional molecule. The tail at low frequency is due to mass transfer limitations and can be attributed to the tethered dye molecule. For diffusion-controlled impedance, the real and imaginary parts are linearly related to $\omega^{-1/2}$.²¹⁰ This is what is observed in the frequency range of 10 kHz to 100 KHz for the CNT-DG-dye membrane as shown in figure 5.7. It indicates a diffusion-controlled charge transfer of the counter ions at the functionalized electrode surface.²¹¹

A potential dependent switchable impedance effect was observed for the CNT-DG-dye membrane/electrode as shown in figure 5.6 (a). When the dye molecule was attached to the CNT surface via a large spacer molecule (~ 2 nm), one would expect this switching effect to be more pronounced due to the presence of the flexible spacer. On the contrary, no detectable switching effect was observed in that case as shown in figure 5.6(b). This is, however, consistent with EIS measurements of low density SAMs on a gold surface, where switching of impedance was greatly reduced when the length of the SAMs was increased from C11 to C 16.²¹² One likely explanation is that the spacer causes the charged molecule to lie sufficiently far away from the electrode surface, so that the electrostatic actuation does not affect the counter ion diffusion to the electrode surface and the double-layer charging process that dominates the impedance measurement. However, it is important to point out that the conformation of the dye or the spacer-dye molecule will depend upon a variety of factors including van der Waals and electrostatic interactions between the molecule and the nanotube surface.

To address the issue of the bulky dye molecule blocking the electrode surface, Faradaic impedance spectroscopy was conducted in 0.1M KCl and 10mM K_2CO_3 in the presence of a 5 mM $[Fe(CN)_6]^{3-/4-}$ redox couple probe, at a bias potential of 230mV vs

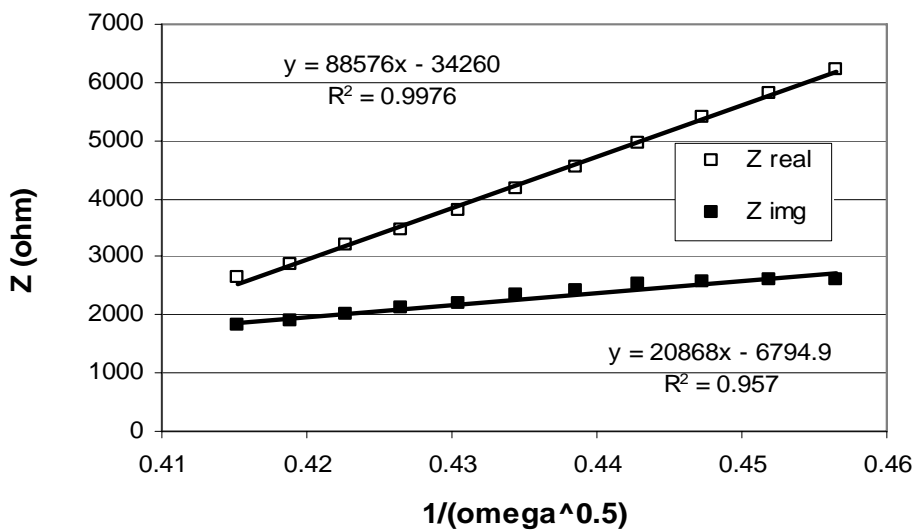


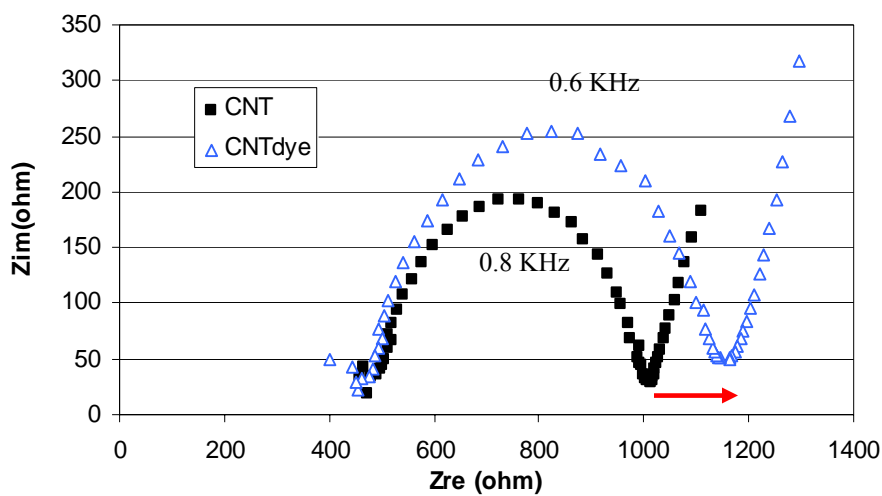
Figure 5.7 Plot of $\omega^{-1/2}$ against the real and imaginary Z for the EIS recorded at 0 volt for the CNT-DG-dye carbon nanotube membrane/electrode in the frequency range of 10^3 to 10^4 Hz indicating a diffusion-limited transport of counter-ions to the functionalized electrode.

Ag/AgCl and is shown in figure 5.8. Faradaic-impedance spectroscopy is considered to be a more sensitive technique to probe insulating properties of modified electrodes.²¹³ The electron-transfer resistance (R_{ET}) of the redox species increased when the membrane/electrode was functionalized with the dye, consistent with blocking the electrode surface by the bulky-dye molecule. In contrast, the spacer-dye membrane electrode saw a decrease in electron-transfer resistance. This observation is consistent with the spacer molecules keeping the large-dye molecule away from the electrode surface and allowing the probe molecules to easily diffuse to the electrode surface. One would not expect electrostatics to be significantly different in either case since both involve functionalization with the charged-dye molecule. A problem associated with this type of electrode fabrication is the presence of polymers on the top surface, introducing large sample-to-sample variation in the magnitude of the impedance. Note that the two membranes compared in figure 5.8 have significantly different resistances, however, this would not influence the shape of the Nyquist plots or the switching behavior observed here.

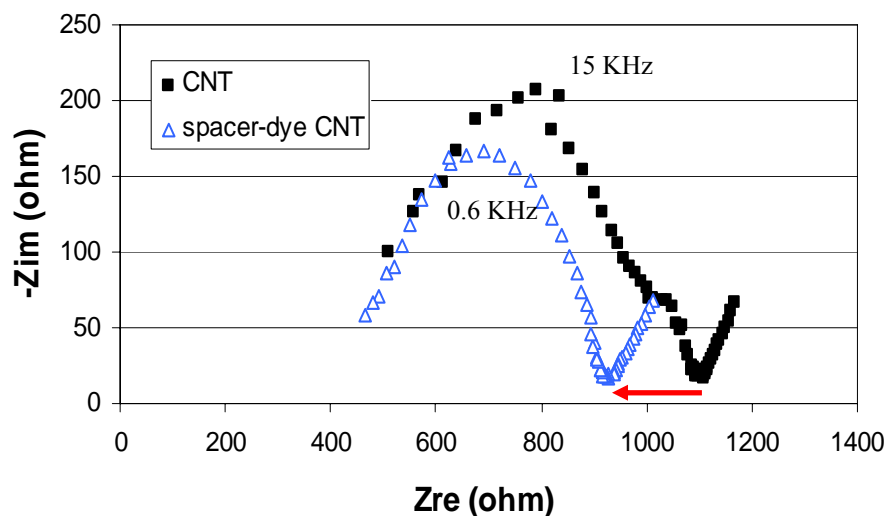
One of the major features of the impedance spectroscopy of the CNT-dye membrane is its remarkable switchability and reversibility. EIS measurements were started at 0 volt DC bias and ramped at 50 mV increments upto 200mV, and then the potential was switched to -negative 200mV and ramped at 50 mV increments upto 0 volt. The 0 volt EIS was retained after all these experiments and demonstrates the reversibility of the switching effect in the potential range of (+200 to -200 mV). This range of potential is much larger compared to those reported for ‘switchable monolayers’ (+ 40 mV to -40 mV) and demonstrates the robustness of the diazonium grafting and covalent carbodiimide functionalization scheme compared to the physisorbed thiol monolayers.²⁰⁶

5.2.6 Equivalent circuit diagram analysis

The switchable impedance spectroscopy has been modeled using an equivalent circuit diagram provided in figure 5.9 (a). The equivalent circuit consists of the double layer capacitance and resistance with a sub-circuit of the functional molecule. The model is similar to that used for adsorbed intermediate on electrodes.²¹⁴ However, unlike physi-



(a)



(b)

Figure 5.8 Comparison of faradaic impedance spectra (Nyquist plot) measured in 0.1M KCl and 10mM K_2CO_3 in the presence of 5 mM $[Fe(CN)_6]^{3-/4-}$ redox couple, at bias potential of 230mV vs Ag/AgCl for (a) CNT-DG-dye and (b) CNT-DG-spacer-dye membrane/electrode. For the CNT-DG-dye, the charge transfer resistance is larger than the bare membrane, indicating blocking of the electrode by the dye molecule, whereas, the spacer molecule keeps the bulky-dye molecule away from the surface in CNT-DG-spacer-dye membrane.

sorption, these molecules are covalently attached to the electrode and show reversible-impedance spectroscopy. Also in the model, constant-phase elements describing non-ideal capacitors are used. The impedance of a CPE can be represented by:

$$Z = \left(\frac{1}{Y_0} \right) \times \left(\frac{1}{j\omega^\alpha} \right); \quad (5.4)$$

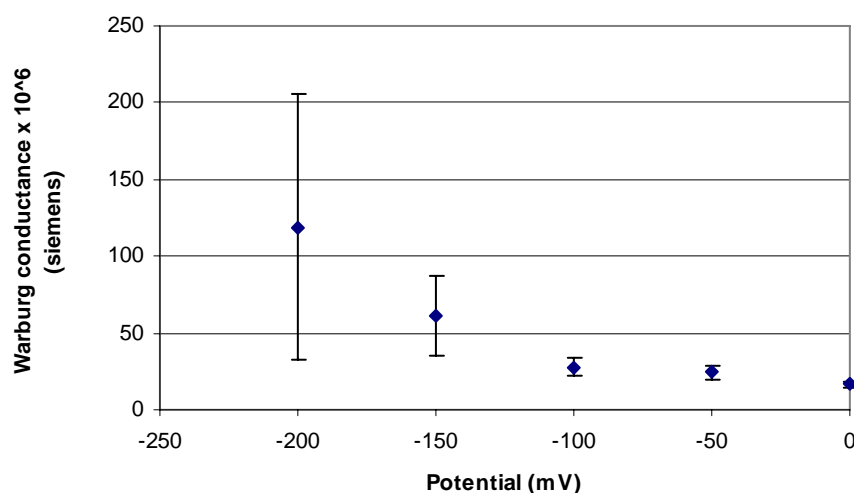
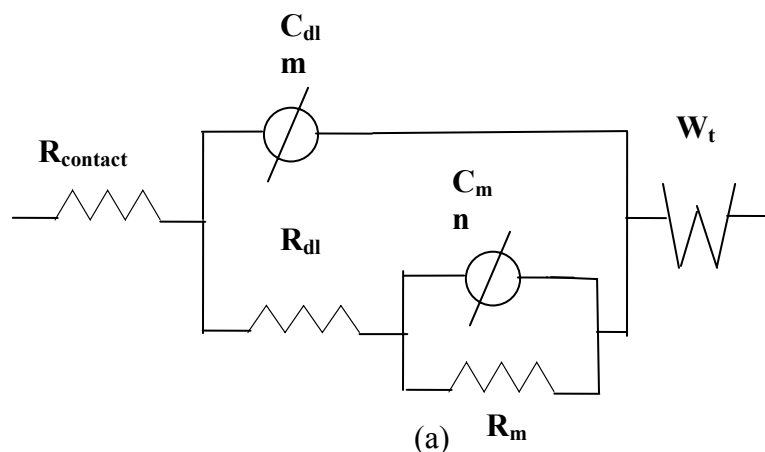
where Y_0 is the capacitance and α (<1) is an exponent describing the non-ideality. The circuit also includes a Warburg describing the kinetics of diffusion of counter-ions to the functionalized electrode.

The equation for the Warburg is:

$$Z = \left(\frac{1}{Y_0 (j\omega)^{\frac{1}{2}}} \right); \quad (5.5)$$

where Y_0 is the Warburg conductance and represents the diffusional mobility of the counter-ions. Note the $\omega^{-1/2}$ dependence of the Warburg impedance. The software used for the analysis (Gamry Echem Analyst) estimates the CPE and the Warburg in terms of the parameter Y_0 with units of siemens (Ω^{-1}).

Initial trial values for fitting the model were estimated from the 0 volt EIS spectra. R_{dl} , in this case is determined by the electrolyte resistance. One would not expect either $R_{contact}$ or R_{dl} to change significantly with applied potential, so parameters for other spectra were estimated by fitting the equivalent circuit using a simplex algorithm built within the software under the constraint of constant $R_{contact}$, R_{dl} . Typical fits of the experimental values with the equivalent circuit model are shown in figure 5.10. The fitted parameters are tabulated in Table 5.2. As discussed earlier, the Nyquist plots indicate two processes at the electrode surface. The smaller semi-circle is from the EDL, ($R_{dl} \sim 3k\Omega$), whereas the larger semi-circle is from the less conductive functional molecule ($R_m \sim 80-100 k\Omega$). The fitted parameters also indicate that the CPE exponent (m) is ~ 1 for the double layer indicating close to ideal capacitance behavior. The



(b)

Figure 5.9 (a) Equivalent circuit diagram of a dye-functionalized CNT electrode. It consists of the double-layer resistor (R_{dl}) and capacitor (C_{dl}) and a subcircuit of the functional molecule (C_m and R_m). A Warburg contributing to the overall circuit (W_t) was added. Instead of pure capacitors, constant-phase elements representing leaky capacitors were used. (b) Warburg conductance (W_t) for CNT-DG-dye electrode was estimated by fitting the model of figure 5.9(a) with the experimental values of figure 5.6(a). The increase of Warburg conductance with increasing negative potential, indicated charged dye molecule changes from a 'lying down' to a 'standing-up' position, which allow easier diffusion of counter-ions to the functionalized electrode.

capacitance of the EDL on the nanotube surface is $\sim 0.5 \times 10^{-9}$ S at 0 V. This is within an order of magnitude of the double-layer capacitance of the diazo-grafted membrane at pH 1.8 $\sim 5.5 \times 10^{-9}$ F obtained from the slope of the Bode plot. On the contrary, the capacitance of the sub-circuit is $\sim 10^{-6}$ S with an exponent (n) ~ 0.4 . The capacitance should be proportional to the number of molecules and hence capacitance per each molecule.

The fitted parameters indicate that the diffusional conductance (W_t) of the functionalized electrodes decrease with applied-negative potential (figure 5.9(b)). It is possible to estimate the hindered diffusivity of the counter ions to the functionalized electrode from the EIS measurements. From R_{dl} of the CNT-membrane electrode, membrane (~ 3.32 k Ω), which corresponds to the resistance of the electrolyte, and the

known conductivity of 0.1M KCl ($\sim 1.3 \Omega^{-1}\text{m}^{-1}$)²¹⁵, one can estimate $\frac{L}{A}$ (m^{-1}) of the

electrode. The mobility ($\text{m}^2\text{V}^{-1}\text{s}^{-1}$) can then be estimated from the equation,

$$\mu_{ion} = \left(\frac{\sigma_t}{e.n} \right); \text{ where } \sigma_t = W_t \times \frac{L}{A} \text{ (a)}$$

and W_t is the fitted Warburg conductance, e is the charge of the electron, and n is the number of counter ions per m^3 of solution for 0.1(M)

KCl. The mobility and diffusivity are related by the Einstein relation, $\frac{D_{ion}}{\mu_{ion}} = \frac{kT}{e}$ where

k , T and e are the Boltzmann constant, temperature and electronic charge. The diffusivity (D_{ion}) of the counter ion at 0 volts applied bias at 25⁰C was found to be $\sim 3.82 \times 10^{-7}$ cm^2/s and increased to 2.5×10^{-6} cm^2/s for negative 200 mV bias. For comparison, the diffusivity of K^+ ion (D_0) at 25⁰C was 1.96×10^{-5} cm^2/s ¹²² i.e a hindrance factor (D_0/D_{ion}) of 17.7 at 0V decreases to 2.7 at 0 V. This phenomena is quite different from increased diffusivity of positively-charged ions to a negatively-polarized electrode because of the $\omega^{-1/2}$ dependence explained earlier. The change in apparent diffusivity is based on the potential dependent conformational change of the dye molecule. An anionically-charged functional molecule, with increasing negative potential, changes from a ‘lying-down’ to a ‘standing-up’ position, allowing the counter-ions to diffuse easily to the electrode surface. Similar effects were also observed in transport measurements through the membrane structure, where molecular tethers on the CNT-membranes were observed

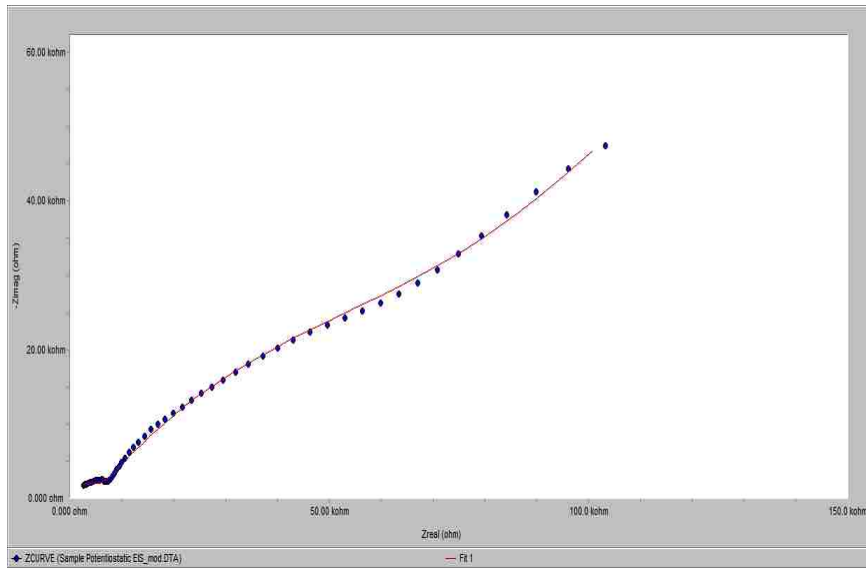


Figure 5.10 Typical fit of the experimental impedance spectra with the simulated (solid red line) Nyquist plots using the equivalent circuit diagram in figure 5.6(a). The simulation has been carried out using Gamry Echem Analyst software and the figure is screen printed from the software.

Table 5.2. Parameters estimated by fitting the model circuit to the experimentally obtained EIS spectra shown in figure 5.6(a)

Parameter	0 V	neg 50mV	Neg 100mV	neg 150 mV	neg200mV
R_{sol}	1.148 k Ω	1.148 k Ω	1.148 k Ω	1.148 k Ω	1.148 k Ω
R_m	84.39 (± 8.77) k Ω	97.28 (± 13.39) k Ω	99.55 (± 14.13) k Ω	104.2 (± 10.87) k Ω	98.99 (± 9.423) k Ω
R_{dl}	3.32 k Ω	3.32 k Ω	3.32 k Ω	3.32 k Ω	3.32 k Ω
C_m	3.655 (± 0.199) μ S	4.644 (± 0.236) μ S	4.337 (± 0.255) μ S	3.785 (± 0.17) μ S	3.762 (± 0.166) μ S
n	0.448 (± 0.0078)	0.414 (± 0.007)	0.422 (± 0.009)	0.436 (± 0.006)	0.439 (± 0.006)
C_{dl}	0.77 (± 0.21) nS	0.563 (± 0.15) nS	0.2 (± 0.43)	0.587 (± 0.15) nS	0.59 (± 0.15) nS
m	0.97 (± 0.02)	1 (± 0.002)	1 (± 0.17)	0.99 (± 0.02)	0.99 (± 0.02)
W_t	16.72 (± 1.87) μ S	24.38 (± 4.562) μ S	27.76 (± 6.192) μ S	61.54 (± 25.87) μ S	119.1 (± 86.62) μ S
Goodness of fit	2.1×10^{-3}	1.86×10^{-3}	97.18×10^{-3}	1.78×10^{-3}	1.59×10^{-3}

to undergo conformational change to directly affect flux and selectivity.¹⁰⁶ It will be discussed in detail in the subsequent chapter. Such membrane structures are being considered for voltage-gated control of trans-dermal drug delivery. The EIS measurements in this study provide additional evidence of controlled-conformational change of functional molecules attached to a conducting-graphitic surface via robust covalent-chemistry.

5.3. Conclusions

Electrochemical-diazonium grafting chemistry is a facile method to introduce functional groups onto the CNT membranes. The grafted-carboxylic acid groups demonstrate a pH-dependent protonation and deprotonation as confirmed by dye adsorption-desorption tests and interfacial-capacitance measurements. Diazonium grafting increases carboxylate density on carbon nanotubes by about 5- 6 fold (to $2.4 (\pm 0.07) \times 10^{13}/\text{cm}^2$) that of as-produced plasma-oxidized CNT membranes. Ionic transport of a positively-charged permeate is significantly increased by the presence of the anionic carboxylic-acid groups at the entrance and along the CNT core. The inner core of the CNTs can be protected by a positive flow of an inert water column (further discussed in Chapter 6) and thus restrict the aggressive electrochemical reaction to the CNT tip surfaces that are in contact with the diazonium salt. This allows the well-defined placement of chemical ‘gate-keepers’ with high functional density at the entrances of the CNT cores, thus enabling further advances in membrane design.

Electrochemical-diazonium grafting can significantly increase the functional density of carboxylic-acid groups on the CNT electrodes. Coupling of the grafted carboxylic-acid groups with the amine group of the anionically-charged dye molecule with and without spacer is demonstrated. Non-faradaic impedance spectroscopy indicates the presence of two double-layer charging processes with a prominent tail having $\omega^{-1/2}$ dependence, indicative of mass-transport limitations of counter ions to the electrode. The CNT electrode functionalized with the dye molecule shows potential dependent switchable impedance behavior of the tail. On the contrary, the CNT electrode that was functionalized with the 2nm-long spacer dye does not show measurable switching effect, which is attributed to the bulky-dye molecule being sufficiently away

from the electrode to observe the actuation behavior within the space charge layer ($\sim 0.8\text{nm}$). This is confirmed by the increase in charge-transfer resistance at the graphite surface of $\text{Fe}(\text{CN})_6^{3-/4-}$ couple at the dye-functionalized CNT electrode compared to a decrease for the spacer-dye functionalization. Equivalent-circuit modelling indicates that the Warburg conductance, representing mass-transport limitations, can explain the observed behavior. Estimation of counter-ion diffusivity indicates that the hindrance factor (D_0/D_{ion}) is ~ 18 at 0 V bias, but decreases to ~ 3 at negative 200mV, when the dye molecule is repelled by the polarized-electrode, allowing the counter-ions to diffuse easily to the graphitic-electrode surface. Thus, additional evidence to potential dependent-conformational change of functional molecules is provided. In the subsequent chapter, similar chemistry has been utilized for realizing voltage-gated membrane channels.

Chapter 6

Voltage-Controlled Transport

This chapter is based on the following published manuscript:

Majumder, M.; Zhan, X.; Andrews, R.; Hinds, B. J., Voltage Gated Carbon Nanotube Membranes. *Langmuir* **2007**, 23, (16), 8624-8631.

6.1. Introduction

Controlled and selective chemical transport across cell walls through biological channels is of fundamental importance and offers unique opportunities to mimic functionality in robust man-made platforms. These biological-protein channels are of remarkable complexity with highly-selective chemical transport regulated by chemical binding or voltage response. Voltage-gated K^+ ion channels, the basis for neural transmissions, have been among the most widely studied and the crystal structure of KcsA shows that charged protein segments induce ‘paddle-like’ conformation changes, thereby changing the transport through the channel.¹⁵¹ The critical essence for mimicking a voltage-gated channel is the electrostatically-induced motion, or actuation resulting in steric blocking of the channel.^{216,217,218}

A primary approach to mimic ion channels is the synthesis of intricately-designed macromolecule channels to span micelles that respond to input such as voltage, light and pH.²¹⁹ Such macromolecule/micelle structures can be incorporated into micro-machined platforms to be utilized in sensors, chemical separations, or drug delivery applications. However, micelles are inherently fragile and extremely difficult to incorporate into robust large-area applications. To form robust protein channel mimic, a promising approach is to use nanoporous materials as a scaffold to place selective-gating chemistry on the pore. Ordered anodized alumina and track-etch polycarbonate have been shown to perform size and chemically-selective separations by the modification of the surface chemistry along the pore wall.^{73,74} Responsive pores with surface-bound molecules that change conformation with pH can effectively act as gates.²²⁰ A promising system has been reported to change the conformation of surface molecules by applied bias^{207,221} and could have applications in conductive membranes. However, to have rapid chemical transport

across the membrane and thus to closely mimic protein channels, it is necessary to have a short gate-path length, ideally only at the pore entrance. Recent advances in track-ion etch fabrication allow for conical pores that have very narrow apertures (~ 2 nm) on one side of the membrane. This has the advantage of concentrating electric field to allow rectification of ionic current.⁷⁰ This has been further enhanced by grafting charged DNA along the pore walls, with the DNA conformation at the narrow aperture being most sensitive to a potential gradient across the membrane.²²² The effect of charged molecules at narrow apertures has also been seen with conical-electrode wells.²²³ However, it remains a challenge to place responsive-gating molecules directly in the pore entrance in a robust, large-area nanoporous material.

Membranes composed of aligned multiwalled carbon nanotubes (CNTs) crossing a solid polymer film⁸¹ can be an alternative platform for creating artificial chemical channels over a large mechanically-robust area. Importantly, CNTs offer the following unique physical properties unknown to other membrane systems: 1) atomically flat graphite planes with large van der Waals distance, allowing for extremely fast fluid flow;^{97,98} 2) the act of cutting CNTs places reactive broken carbon at the entrance to the CNT core for a well-defined geometry of ligands at the pore entrance; and 3) the CNTs are conductors inside an insulating matrix, allowing for the concentration of electric field at the tips of the CNTs for voltage gating or use as an electrode. The last step of CNT membrane fabrication requires a plasma-cutting process that removes iron-catalyst particles⁸⁹ and forms carboxyl end groups at the entrances to inner cores of CNTs (7nm I.D.). These can be readily chemically functionalized by a standard carbodiimide reaction, and have shown reversible biochemical reactions to ligand-gated ionic flux across the membrane.¹⁰⁴ The effect of the molecular tether length, hydrophobicity, and charge on the transport of differently-sized ions through CNT membranes was systematically studied.¹⁰⁵ The principle conclusions from this study were: 1) Tethered molecules at the entrance to CNTs can sterically hinder larger permeates; 2) negatively-charged ligands enhance the diffusion of positively-charged permeates, but this enhancement can be screened by the short Debye length in high ionic-strength solutions; 3) ligands are located near the tips of CNTs, but a hindered diffusion model is consistent with functionality tens of nanometers down the central core, possibly due to plasma

treatment; and 4) the functional density of carboxyl groups on CNTs is relatively small with only modest changes in separation between large and small permeate ($< \sim 3.6$).

To make the aligned CNT membrane an optimal platform for an ion channel mimetics, it is necessary to increase the functional density of tethered molecules only at the entrances to the CNT cores. This can be accomplished by electrochemical grafting of functional-diazonium salts to the exposed CNT tips where the interior core is masked from the reaction by a high velocity core flow of inert solution during grafting. Tethered molecules, that are charged, can be drawn into the channel by applied bias, thus acting as a voltage-gated channel. The primary hypothesis of this paper is that voltage-gated channels can be produced by tethering charged ‘gate-keeper’ molecules to the entrance of the CNT cores. Simultaneous experimental diffusion measurements of two iso-valent probe molecules, which differ in their sizes (i.e. $\text{Ru}(\text{bipy})_3^{2+}$ and methyl viologen $^{2+}$ (MV^{2+})) across the membrane as a function of bias, ionic strength and chemical treatment, demonstrate controlled electrostatically-induced steric hindrance at the entrance of the CNT cores. Practical applications of such bias-responsive membrane channels would include programmable transdermal drug delivery.

In the voltage-gating studies, the conducting CNT membrane is the working electrode in a three-electrode electrochemical cell. In order to understand electrically-facilitated transport and clearly distinguish between the ‘voltage-gating’ experiments, transport studies in these membrane structures in the presence of a potential difference across the membrane have also been carried out. Potential applications are in microfluidic devices, where the CNT channels can serve as transport controlling ‘gates.’

6.2. Results and Discussions

6.2.1 Ionic Screening Effects on CNT Membranes with Enhanced Functional Density

Diazonium grafting is routinely used to functionalize graphite electrodes²⁵ and has been demonstrated to efficiently graft on the sidewalls of the SWNTs²⁶ and MWNTs.²²⁴ Experiments by other groups have shown the formation of multilayers on glassy-carbon electrodes during reduction of diazonium salts at higher overvoltage potentials (~ -1.2 V) and longer reaction time (20-30 mins).¹⁸⁶ Experimental details for electrochemical

grafting are discussed in section 2.11. Adsorption/desorption assay of toluidine-dye molecules on the static-grafted membrane indicated at least a ~ 2 -3 times increase in functional density over as-prepared membranes. Kinetic studies using this assay indicated saturation at grafting times greater than 4 minutes, presumably at which point multilayer formation is occurring. It is also important to note that the electrochemical grafting is not tip-selective and would also functionalize the interior core of the CNTs. Because CNTs show dramatically-enhanced fluid flow through the cores of CNTs, it is possible to protect the inner core of CNTs from the highly reactive diazonium reagent by having a fast flowing inert solution in the core. This is simply achieved during electrochemical functionalization by using a U-tube electrochemical cell with a column of inert liquid (aqueous 0.1M KCl), 10 cm higher than the diazonium solution side of the membrane. Flow velocities are estimated to be 0.1 cm/s, which exceed the aqueous-diffusion characteristic length by an order of magnitude at the time scale of the grafting experiment. With a high density of surface carboxyl groups from electrochemical diazonium grafting, further modification of CNT tips is achieved by successive carbodiimide reactions. First, two peptide links are sequentially added (to give conformational flexibility) followed by the anionic ($4e^-$) dye molecule. The structure of the CNT 'gate-keeper' functionality and the molecules utilized to form it are shown in figure 2.9. The simultaneous diffusion of two isovalent, but different-sized cationic ions, $\text{Ru}(\text{bipy})_3^{2+}$ and MV^{2+} , with Stokes diameters of 1.1 and 0.6 nm respectively, are measured in a u-tube electrochemical cell by UV-vis absorption to quantify the effect of 'gate-keeper' functionality (figure. 2.5)). The first series of experiments were designed to study the effect of ionic-charge screening on the transport through membranes with enhanced CNT functional density from diazonium grafting. From a previous study, we found an enhancement by a factor of five in cation diffusion when the plasma-oxidized tip is functionalized with a anionically-charged dye molecule.¹⁰⁵ This columbic effect can be screened by free ions in solution, reducing the Debye screening length (<1 nm in 0.1 M KCl). Similar effects of charge screening in salt solutions on the transport of ionic species through multilayers of polystyrene sulfonate membrane have been observed.²²⁵ Diffusive transport of two membranes is shown in figure 6.2. The first had the tips

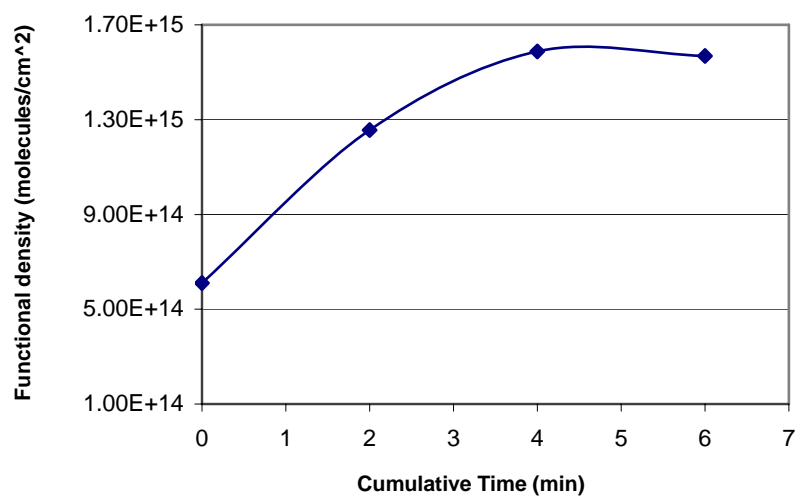


Figure 6.1 Estimated COOH density on CNT membrane using a grafting technique similar to SG. The TBO concentration in this experiment is about 0.12 mM. There is about a 2-3 times increase in COOH functional density and the reaction proceeds to saturation with increasing time of reaction.

preferentially-functionalized by using an inert fluid flow in the core during electrochemical grafting (Flow Grafted, FG). This geometry is schematically shown in figure 6.2, where the yellow solution has diazonium salt present for electrochemical grafting. In the second case, there was complete functionalization of the CNT in a static diazonium salt solution (Static Grafted, SG). $\text{Ru}(\text{bipy})_3^{2+}$ fluxes of the samples were normalized to that of untreated membranes to account for the difference in available pore area between samples. After initial diazonium grafting, the static-grafted sample saw ~ 2.3 fold increase in flux, consistent with an appreciable (~ 2 -3 times) increase in attraction of the cationic permeate by the anionic phenol-carboxyl groups. In the case of tip-only functionalization, negligible enhancement would be expected for a thin layer of charge at the edge of the 7nm-pore. When the ionic strength was increased to shield the charge, the fluxes returned to slightly below initial flux. After attachment of the ~ 3 nm long quad-valent charged dye tether, the tip-only (flow grafted) functionalized membrane saw a 2-fold increase in flux, consistent with charge attraction at the entrance to the pore. In the case of functionalization along the entire pore wall (static grafted) there was a dramatic decrease in $\text{Ru}(\text{bipy})_3^{2+}$ flux. This is typical of ion-exchange membranes, where lowering of the transport rate of counter ions have been observed at higher concentrations of the fixed charges on the membranes.²²⁶ The fluxes for both the membranes return to near original values with ionic screening. The important conclusions from these studies are: the CNT-FG membrane has significantly-less functional density of the grafted molecules, with the molecules concentrated at the reactive tips of the CNTs due to the effect of the fast flowing inert-liquid column. Consistent with our previous studies¹⁰⁵ and theoretical predictions,¹⁴⁸ the presence of hydrophilic functional groups at the CNT tips increases the transport rate of the cationic species. The CNT-SG has considerably higher functional density at both CNT tips and cores. The higher density of anionic sites has an electrostatic 'braking' effect on the transport of cations.

6.2.2 Voltage-Gated Chemical Transport

The steady-state flux $N(x)$ through a membrane in the x direction can be expressed by the Nernst-Planck Equation:

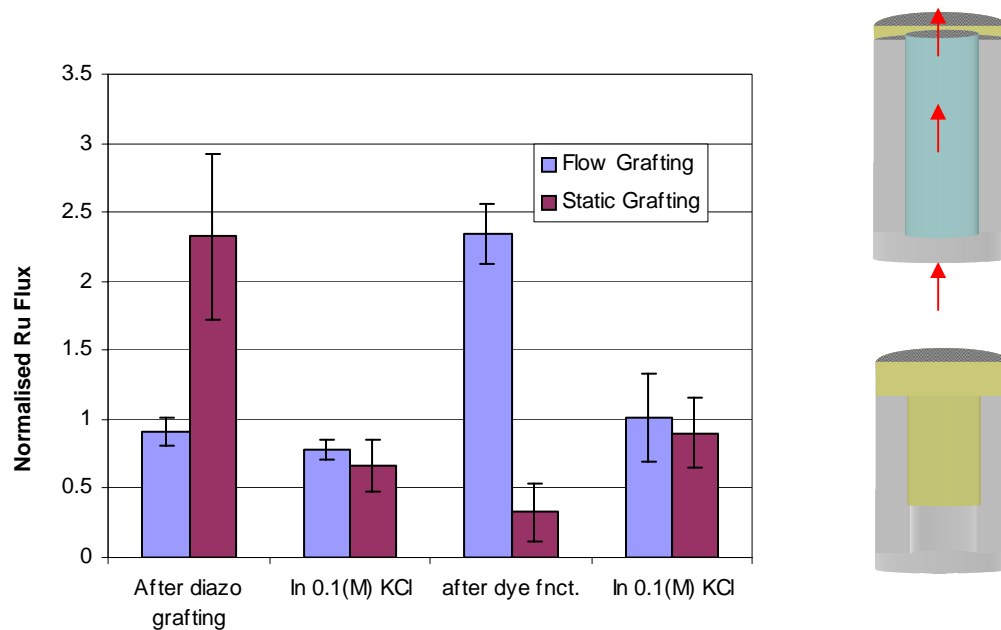


Figure 6.2 Variation of transport of $\text{Ru}(\text{bipy})_3^{2+}$ through CNT membranes as a function of chemical treatment and ionic screening. Experiments have been conducted on two separate membranes and the fluxes are normalized to their pre-grafting transport rates. Also shown is the schematic representation of the electrochemical grafting techniques: CNT-FG (Flow Grafting) and CNT-SG (Static Grafting). The yellow color represents the aqueous diazonium solution and blue color the flowing inert solution inside the CNTs. The flowing inert liquid column restricts the reaction to the CNT tips only.

$$N(x) = -D \frac{\partial C(x)}{\partial(x)} - \frac{z.F}{RT} DC(x) \frac{\partial \phi}{\partial x} + C(x)v_{eo}(x) \quad [6.1]$$

where D , C and z are the diffusion co-efficient, concentration and z the charge on the permeate. The three terms of the equation correspond to the diffusive, electrophoretic and electro-osmotic transport components, respectively. Both the electrophoretic and electro-osmotic terms are functions of the electric field across the membrane. For this case, the CNT membrane is conductive due to the crossing of CNTs within the polymer matrix. This allows the membrane to function as the working electrode in a 3-electrode cell (figure 2.10), by direct application of bias to the membrane. For electrophoretic or electroosmotic transport measurements, an electrical potential-gradient across the membrane is established by placing the counter and working electrode in the feed and permeate side. For these experiments, the membrane itself is the working electrode, hence a driving force for such electrically-facilitated transport will be absent, This will, in principle, eliminate any electrophoretic or electroosmotic effects, due to the absence of potential gradient across the membrane.

$$\text{Hence, } N(x) = -D \frac{\partial C(x)}{\partial(x)} \quad [6.2]$$

Factors affecting the transport would be: electrostatic charging and conformation of the tethered molecule at the charged surface. Cation and anion permselectivity with applied bias have been observed for gold nanotubule membranes.⁷⁶ However, this study's primary purpose is to understand the effect of the conformation of the large tethered charged molecule at the entrances to CNT cores on the molecular transport across the CNT membranes. Schematic of the targeted membrane structure and the actuator molecule are shown in figure 6.3. It is important to note that the conformational change of the charged dye molecule will induce two types of effects via: (i) electrostatic attraction and (ii) steric blocking by the bulk of the tethered molecule. The flux and separation factor [flux ratio of MV^{2+} to $Ru(bipy)_3^{2+}$] in the permeate will provide a direct

measure of the effects of the conformational change of the molecule tethered to the pores of the CNT and is essentially independent of available pore area.

The primary hypothesis of this report is that voltage-gated channels can be produced by tethering charged ‘gate-keeper’ molecules to the entrance of the CNT cores. Since the CNTs are conductors in an insulating matrix, electric fields can be concentrated at the CNT core entrance with applied bias. Figure 6.4 shows the voltage dependence of MV^{2+} and $Ru(bipy)_3^{2+}$ diffusion flux for flow-grafted dye-functionalized membranes. In the case of non-grafted membranes there is a very-low density of chemical functionality (*videinfra*) resulting from the H_2O plasma cutting process and we observe very modest voltage-dependent flux modulations. A dramatic increase in separation factor (>10) is seen for dye molecules drawn into the core at a positive bias. The bias (50 mV) that gives the maximum separation coefficient is near the self capacitance of the CNT ($\sim 80mV$). At a negative bias, a modest increase is seen as tethered dye molecules are repelled from the core wall. The flux of the larger $Ru(bipy)_3^{2+}$ is dramatically reduced by steric hindrance (*videinfra*). For example, at a gate voltage of 50 mV, the flux of $Ru(bipy)_3^{2+}$ decreases to $0.025 (\pm 0.001)$ nmole/h from $0.11 (\pm 0.03)$ nmole/h at 0 V. This corresponds to a flux decrease of $\sim 400\%$. At higher positive voltages, the gating effect is reduced. The flux of MV^{2+} increases slightly at the gate voltage of 50 and 100 mV, corresponding to the maximum observed separation factors. Both cations see electrostatic attraction from the anionic tethered molecules, but the larger permeate ($Ru(bipy)_3^{2+}$) is sterically hindered. At the negative bias, the maximum separation factor (~ 6) is observed at -50 and -100 mV. This is consistent with limited functional molecules lining the cores of the CNT. At a less negative bias, (-100, -150 mV), the flux of the smaller cationic species appears to increase. This again is likely the result of the tethered molecule causing steric hindrance of the larger permeate, but allows electrostatic attraction of the smaller species. There is an inherent asymmetry in the flow-grafted CNT membranes. The effect of the position of the ‘gate-keeper’ molecules either facing the feed or permeate side was also investigated. Details about the experimental results are discussed in Sec A6.1.

A dramatic increase in the separation factor (~ 22) was seen in the case of the completely-functionalized CNTs (static grafted), at a negative bias of 130 mV

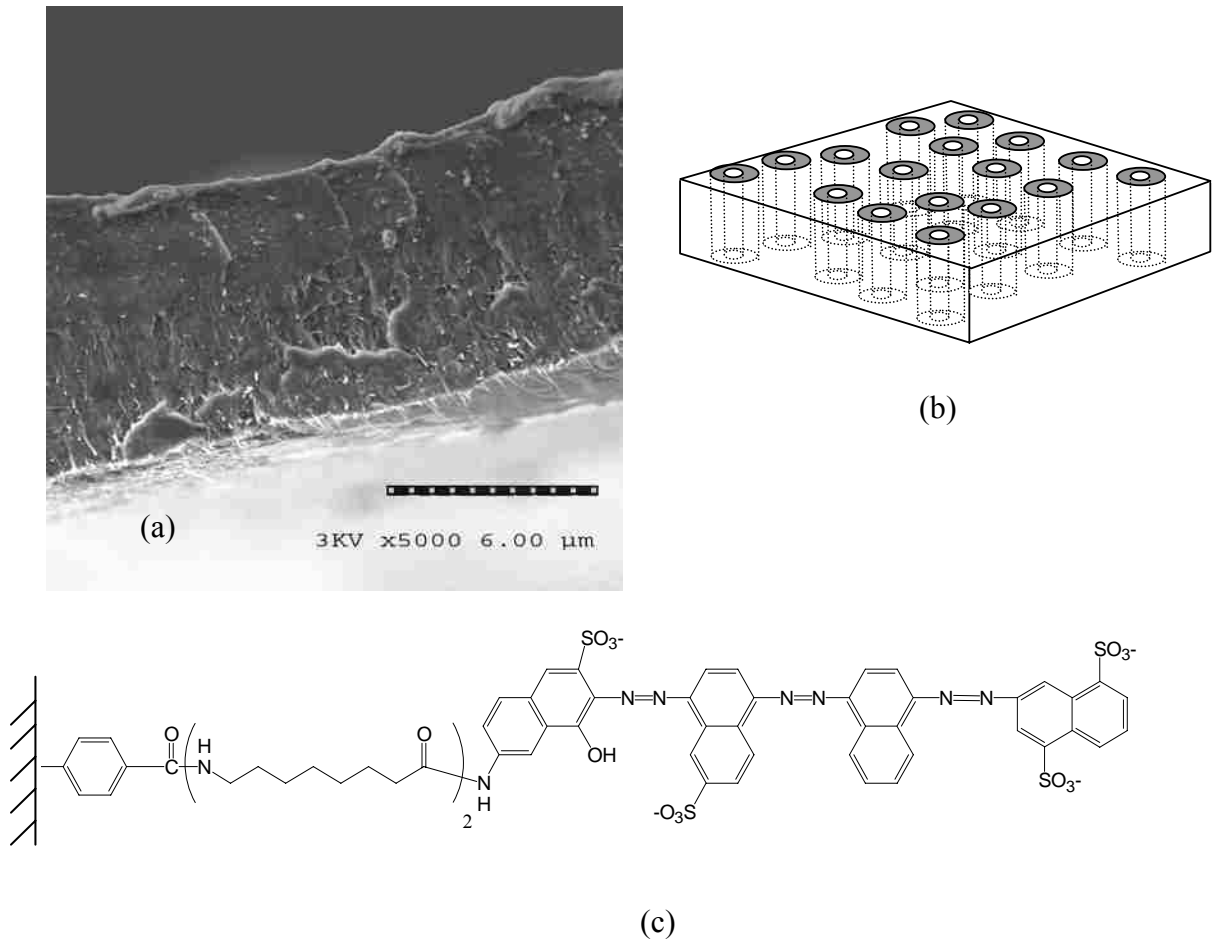


Figure 6.3 (a) Cross-sectional SEM image and (b) idealized schematic of free-standing membrane with CNT array passing across a solid polymer film, (c) charged dye molecule tethered to CNT surface.

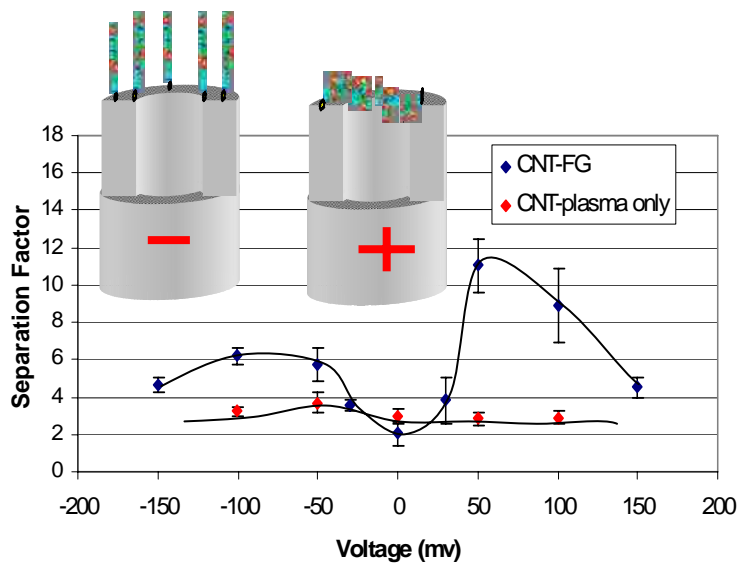


Figure 6.4 (a) Change in separation co-efficient with voltage applied to the CNT- FG-spacer (polypeptide)-dye membrane. Also shown are the modest changes in the observed separation factor for CNT-spacer(polypeptide)-dye membrane in plasma-oxidized membrane (no electrochemical grafting), due to limited functional density in plasma-oxidized membranes (b) Fluxes of the two permeates at applied voltages across CNT-FG membrane. Membrane area is 0.7 cm^2 . The line joining the data points are to aid visual clarity.

(figure 6.5 (a)). The flux of $\text{Ru}(\text{bipy})_3^{2+}$ decreases by an order of magnitude to $0.017 (\pm 0.003)$ nmole/h at an applied bias of -130 mV, compared to $0.19 (\pm 0.006)$ nmole/h, when no bias applied. The flux of the smaller MV^{2+} molecule decreases to $0.37 (\pm 0.034)$ nmole/h from $0.53 (\pm 0.03)$ nmoles/h. Interestingly, increases in separation are seen for both the positive and negative bias. A separation factor of ~ 14 is observed at an applied bias of $+100$ mV. For the positive bias, a similar mechanism to the tip-only functionalized sample would be expected. That is, any tip functionality would be drawn into the membrane entrance and would introduce steric hindrance. At negative bias, the ligands lining the core are repelled, thus introducing steric hindrance and the observed size-based separation. Unlike the case of flow-grafted membranes, in CNT-SG the fluxes of both the cations decrease with bias, which is also consistent with steric hindrance at both CNT tips and along the cores.

Figure 6.6 shows the UV-vis spectra of the permeates obtained during the transport measurement through CNT-CG-spacer dye membranes with strong voltage dependence. Interestingly, the steric effects of the dye tether are modest unless bias is applied, presumably with the electric field strongly placing the dye molecules in the channel. In the case of non-grafted membranes, there is a very low density of chemical functionality (*videinfra*) resulting from just the H_2O plasma cutting process. The voltage dependence on separation factor for the spacer-dye functionalized membrane is very modest ($\sim 15\%$ increase) as compared to grafted and functionalized membranes (as high as $\sim 800\%$). Thus, the use of the efficient electrochemical-diazonium grafting is critical in order to have enough functional density on the CNT for ‘voltage-gated’ control of transport.

6.2.3 Electric-Field Assisted Transport through Carbon Nanotube Membrane

The total transport (J_T) through a membrane in the direction of the membrane thickness, x , with permeable pore area, A_p , in an applied electric field $\frac{\partial\phi(x)}{\partial x}$, can be expressed by the Nernst-Einstein equation.

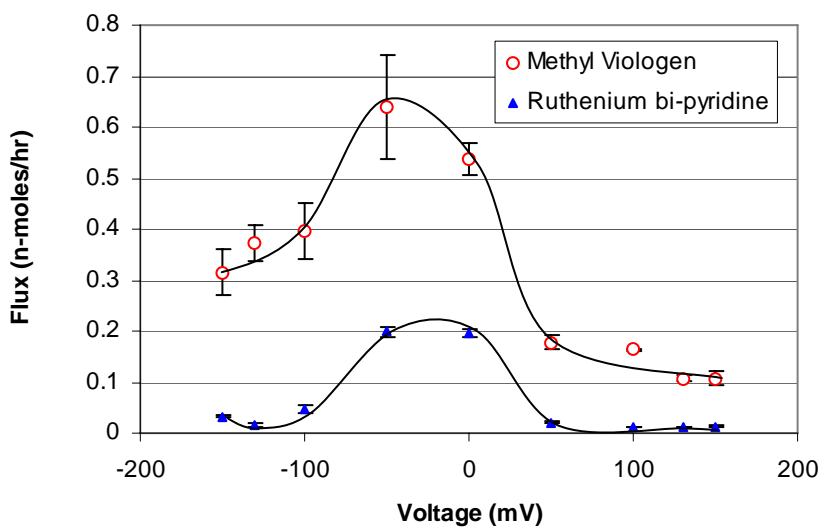
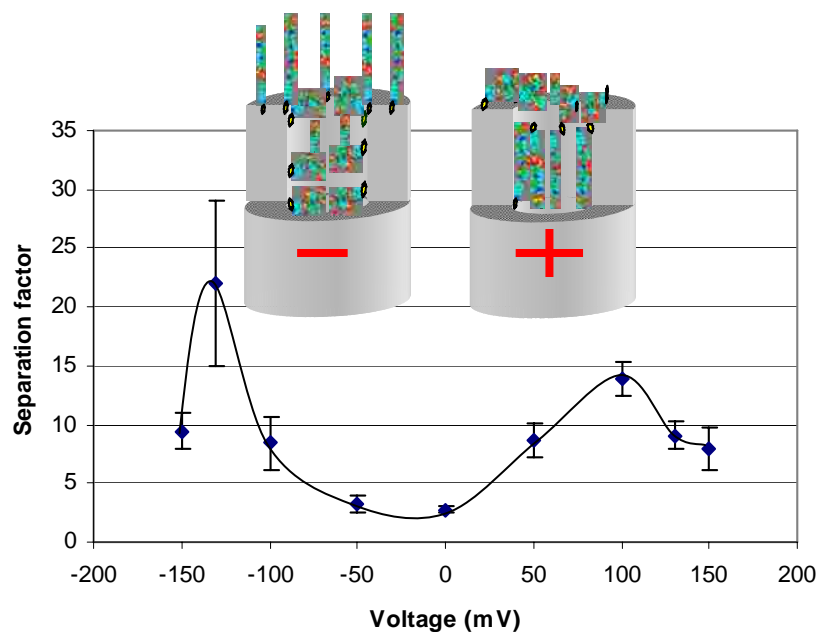


Figure 6.5 (a) Change in separation coefficient with voltage applied to the CNT-SG-spacer(polypeptide)-dye membrane; (b) Fluxes of the two permeates at applied voltages across CNT-FG membrane. Membrane area is 0.7 cm^2 . The line joining the data points are to aid visual clarity.

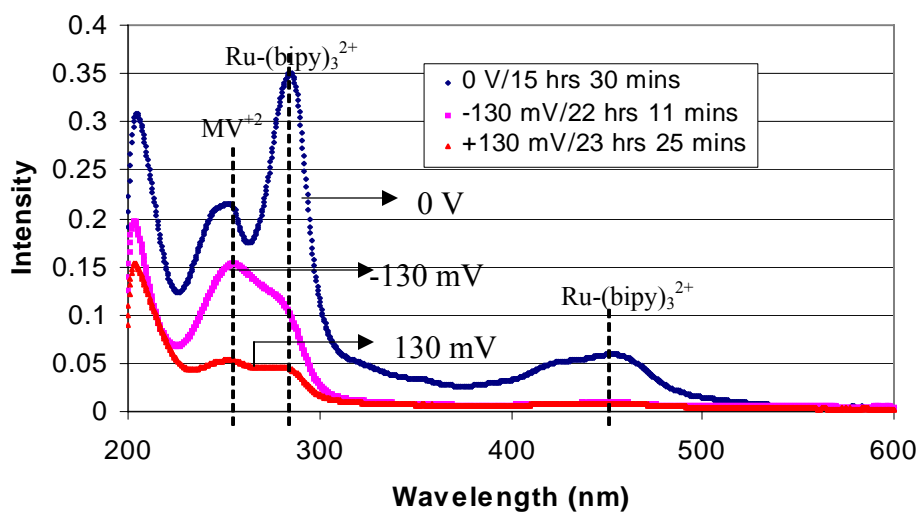


Figure 6.6 A representative UV-vis spectra of permeate through CNT-SG-spacer(polypeptide) membrane as a function of applied voltage and permeation time. Both MV²⁺ (peak at 260 nm) and Ru-(bipy)₃²⁺ (peak at 286 and 452 nm) are transported at 0 V, with a separation factor ~ 3 . Application of a bias of +/-130 mV to the membrane causes the transport of Ru-(bipy)₃²⁺ to be reduced, as evident from the lower intensity of the 286 peak, thereby increasing the separation factor to > 20 at -130 mV. The control experiment with nonfunctionalized membranes showed a similarly-modest change in separation factor or flux with applied voltage up to ± 300 mv.

$$J_T = -DA_p \frac{\partial C(x)}{\partial x} - \frac{z.F}{R.T} A_p .DC(x) \frac{\partial \phi(x)}{\partial x} + A_p C(x)v_{eo}(x) \quad [6.3]$$

Where D is the diffusivity of the permeate; C is the feed concentration; z is the charge on the permeate; F is the Faraday constant; R is the gas constant; ϕ is the potential difference across the membrane. The three terms on the right-hand side of the equation represent the diffusive transport J_d , electrophoretic transport, J_{ep} , and electro-osmotic transport, J_{eo} flux, respectively. Both electrophoresis and electro-osmosis are functions of the applied electric field. Electrophoresis is the migration of ions in a potential gradient and is explicit in the equation, whereas electro-osmosis, represents convective electric-field driven transport and is often explained by the equation $v_{eo} = \frac{-\varepsilon\zeta E(x)}{\eta}$, where ε is the dielectric-permittivity, ζ is the zeta-potential at the solid surface, $E(l)$ is the applied electric field and η is the viscosity of the solvent.⁷⁹ Electro-osmosis arises from the drag exerted by counter-ions on solvent molecules in response to an electric field and is in the direction of counter-ion migration. A major feature of electro-osmotic flow in contrast to pressure-driven convective flow is the plug flow type velocity profile in the flowing channels,²²⁷ which allow efficient mixing of reactants in micro-fluidic channels. For the experiments under consideration, the membrane is negatively charged. Therefore, the direction of electroosmosis will be in direction of cation migration.

In these experiments, the feed is 5 mM in MV^{2+} and $Ru(bipy)_3^{2+}$ with 0.1M supporting electrolyte, whereas, the permeate is 0.1M in KCl and the experimental set-up is shown in figure 2.11). A typical experimental data of the flux of MV^{2+} through the CNT membrane in an electric-field gradient is shown in figure 6.7. The potentials in this figure are that of the working electrode placed in the permeate side and with respect to the Ag/AgCl (saturated KCl). It is important to point out an inherent asymmetry in the experiment arising from the composition of the electrolyte in the feed and permeate which manifests in the experimental results. For positive potential applied to the working electrode on the permeate side, both J_{ep} and J_{eo} are in the direction from the permeate to the feed, in opposition to the diffusion flux

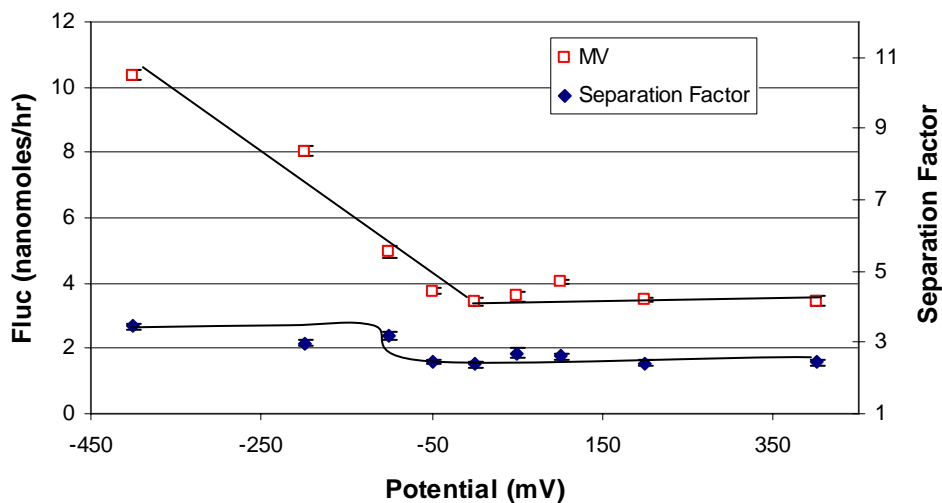


Figure 6.7 Methyl viologen flux in the potential range (-400 to +400 mV) for CNT-SG-spacer-dye membrane. Note that at positive applied potential the flux is diffusion limited, while at negative potentials the flux is electro-osmotically enhanced over the diffusion flux. The separation factor does not change appreciably (~ 40%).

$$J_T = J_d - J_{ep} - J_{eo} \quad [6.4]$$

while for negative potentials applied to the working electrode both J_{ep} and J_{eo} , are in the direction from the feed to the permeate in the same direction as the diffusion flux

$$J_T = J_d + J_{ep} + J_{eo} \quad [6.5]$$

At positive potentials, the concentration driving force for either J_{ep} or J_{eo} will be very small since the concentration of the probe molecules are $\sim 10^{-6}\text{M}$, whereas, the concentration in the feed is $\sim 10^{-3}\text{M}$. Therefore, the flux will be diffusion limited (i.e., $J_T = J_d$) as shown in figure 6.7. We will therefore concentrate the rest of the discussion on negative-applied potentials to the working electrode.

The effect of functionalization on the electric-field assisted transport (figure 6.8) is analyzed by the parameter electrically-assisted permeability with the units of $\text{cm s}^{-1}\text{V}^{-1}$, and can be estimated from the equation, $P_E = \frac{J_T - J_d}{C.A_p.V}$, where J_T and J_d are the flux in moles/s and have their usual meaning; C is the concentration in mole/s; A_p is the permeable pore area of the membrane in cm^2 ; and V is the applied potential in volts. The permeable pore area of the membrane can be estimated from the diffusive flux of the unmodified membrane. The estimation is based on the proven fact of close to bulk diffusion of the molecules like MV^{2+} and $\text{Ru}(\text{bipy})_3^{2+}$ inside the CNT pores. The electrically-assisted permeability of the CNT-membrane for different functionalization treatments are shown in Table 6.1. The data shown is an average of four negative potentials. For the plasma-oxidized membrane the permeability is $0.00132 (\pm 0.0002) \text{ cm sec}^{-1}\text{V}^{-1}$, which increases to $0.0047 (\pm 0.0028) \text{ cm s}^{-1}\text{V}^{-1}$ when functionalized with the spacer-dye molecule and to $0.0085 (\pm 0.0002) \text{ cm s}^{-1}\text{V}^{-1}$ for the sg-spacer-dye functionalization. Progressive functionalization is not expected to alter the electrophoretic fluxes significantly, since the electric field is not dependent upon chemical functionalization. The obvious effects of chemical functionalization are increases of charge density (σ_c) and the zeta potential, ζ , on the membrane walls. Hence, the increased electrical permeability of the membrane is attributed to electro-osmotically

driven flux through the membrane. There is insignificant change of the separation factor of the smaller MV^{2+} and larger $Ru(bipy)_3^{2+}$ ($\sim 43\%$) for CNT-sg-spacer-dye with the applied cross-potential, indicating the absence of conformational change of the functional molecule, whereas there is $\sim 800\%$ change in separation factor in the case of potential applied to the membrane.¹⁰⁶ This had been attributed to the conformation change of the tethered molecule causing steric blocking of the nanotube channels. However, in the cross-potential geometry, the electric field is either not concentrated enough to cause conformation change of the tethered macro-molecule or the majority of electric field is parallel to the CNT core, thus not inducing steric blocking from the charged tethers protruding into the center of the core.

For the plasma-oxidized membrane without any functionalization, an estimate of J_{eo} can be obtained. The charge density (σ_c) of the as-made membranes was estimated by interfacial capacitance measurements and was found to be $\sim 3 \times 10^{-3} \text{ C/m}^2$ at neutral pH.

Estimation of the zeta potential from the equation, $\zeta = \frac{2kT}{ze} \sinh^{-1}\left(\frac{\sigma_c ze}{2\epsilon kTK}\right)$; where k is

the Boltzmann constant, z and e are the valence and electronic charge and K is the inverse of the Debye length for 0.1M of 1:1 electrolyte provides a zeta potential of $\sim 4 \text{ mV}$. The electro-osmotic velocity at an applied potential of 200 mV and an estimated length of \sim

30 microns, is related to the zeta potential by the equation, $v_{eo} = \frac{-\epsilon\zeta E(x)}{\eta}$. The

resultant J_{eo} of MV^{2+} from the permeable membrane area (A_p), would lead to an electro-osmotic flux of $\sim 1.09 \text{ n-moles/hr}$. On the contrary, estimation of the electrophoretic flux

from the equation, $J_{ep} = \frac{z.F}{RT} A_p .DC(l)$, leads to $\sim 20 \text{ n-moles/hr}$ at -200 mV applied

potential. The observed flux $\sim 1.76 (\pm 0.02) \text{ n-mole/h}$ are consistent with calculated electro-osmotic fluxes across the membrane and not with the electrophoretic flux. The parameters used for the calculations are shown in Table 6.2. It is difficult to comment on why weak electrophoresis is observed in electrically-facilitated transport through conducting CNTs. Presumably in a metallic conductive material, the electric field gradient will not be linear across the length of the membrane since charge will accumulate at the electrode surface (i.e. no electric field exists in a metal). The potential

Table 6.1 Electrical facilitated permeability of CNT membranes for different functionalization treatments, calculated from figure 5.12 for the negative potentials using

$$P_E = \frac{J_T - J_d}{C \cdot A_p \cdot V}$$

where J_T and J_d are the transport rates in mole/s and have their usual meaning, C is the concentration in moles/s, A_p is the permeable pore area of the membrane in cm^2 , V is the applied potential in volts. The observed electric field assisted flow velocity has been calculated from P_E , at 0.2 V. The zeta-potential has been calculated from estimated charge density of plasma oxidized and diazo-grafted membranes using interfacial capacitance measurements in 0.1M of 1:1 electrolyte. The electro-osmotic velocity at 0.2V has been calculated from, $v_{eo} = \frac{\epsilon \zeta \Delta V}{\eta \Delta l}$.

Functionalization	Permeability ($\text{cmV}^{-1}\text{s}^{-1}$)	Observed velocity at 0.2 V (m/s)	Zeta- potential (V)	Electro-osmotic vel (m/s)
Plasma oxidation (as-made)	0.00132 (± 0.0002)	$2.64(\pm 0.4) \times 10^{-6}$	4.38×10^{-03}	2.32×10^{-6}
Plasma ox.-spacer- dye	0.0047 (± 0.0028)	$9.4(\pm 5.6) \times 10^{-6}$	1.72×10^{-02}	9.12×10^{-6}
fg-spacer-dye	0.0062 (± 0.0005)	$1.24(\pm 0.1) \times 10^{-5}$		
sg-spacer-dye	0.0085 (± 0.0002)	$1.7(\pm 0.1) \times 10^{-5}$	7.7×10^{-2}	4.09×10^{-5}

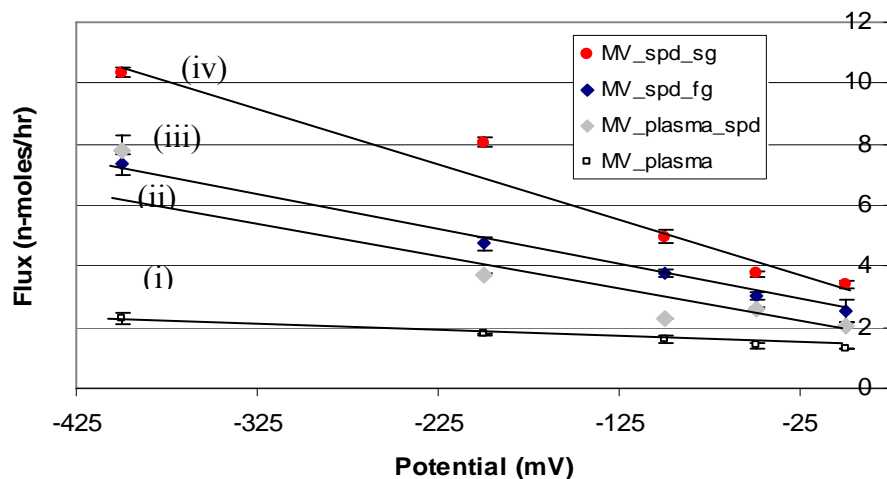


Figure 6.8 Methyl viologen flux through carbon nanotube membrane as a function of applied negative potential to the working electrode with different functionalization treatments. The feed solution is 5 mM in $\text{Ru}(\text{bipy})_3^{+2}$, 5 mM in MV^{+2} and 0.1 (M) in KCl. The permeate is 0.1M KCl. The membranes have been: (i) as-made without any functionalization (ii) with spacer-dye functionalization (iii) flow grafted and spacer-dye functionalized (iv) static-grafted with spacer dye functionalization.

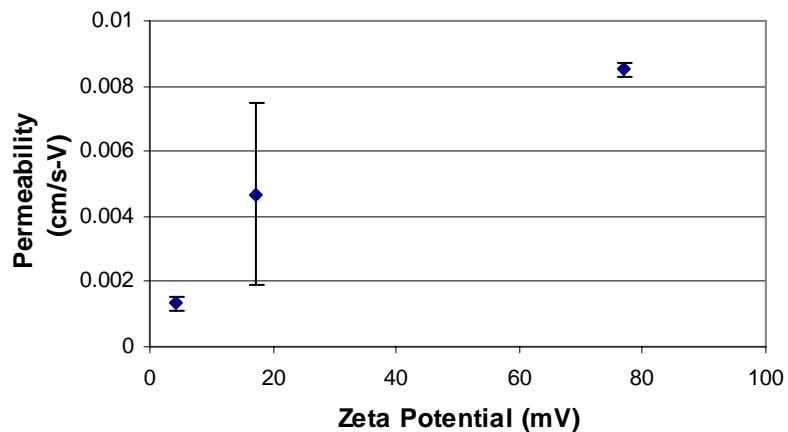


Figure 6.9 Experimentally-obtained electrical permeability of the CNT membranes and calculated zeta potential. The calculation for zeta potential is based on the experimentally-obtained charge density of plasma oxidized and dizonium core grafted membranes. Note that the electrically-facilitated permeability increases monotonically with the zeta potential, providing evidence to electro-osmotically driven transport through the CNT membrane.

Table 6.2 Parameters and formulae used for calculation of electro-osmotic and electrophoretic flux through the CNT membrane. for utilization of electroosmotically driven flux in micro-fluidic devices with interconnects provided by CNT channels.

Parameter	Values	How determined or calculated
Diffusive Transport, J , (moles/s)	3.61×10^{-13}	Experimentally determined
Concentration, ΔC , (moles/m ³)	5	Concentration of the feed solution
Pore area, A_p , (m ²)	2.79×10^{-8}	$A_p = \left(\frac{J \times \Delta l}{D \times \Delta C} \right)$
Membrane thickness, Δl , (m)	3×10^{-4}	From cross-section SEM
Potential Difference, $\Delta \phi$, (V)	0.2	With respect to Ag/AgCl reference electrode
Diffusivity of MV ²⁺ , D (m ² /s)	7.74×10^{-10}	Reference No. 72
Electro-phoretic Flux, N_{ep} (mole/m ² s)	2.01×10^{-4}	$N_{ep} = \frac{z.F}{R.T} D.C(l). \frac{\Delta \phi(l)}{\Delta l}$
Electrophoretic Transport, J_{ep} (moles/s)	20.25×10^{-9}	$J_{ep} = N_{ep} \cdot A_p$
Charge density, σ_c (C/m ²)	3.4×10^{-3}	From Interfacial Capacitance Measurements, Chapter 5.
Zeta potential, in 0.1 (M) of a 1:1 electrolyte, ζ (V)	4×10^{-3}	$\zeta = \frac{2kT}{ze} \sinh^{-1} \left(\frac{\sigma_c ze}{2\epsilon kTK} \right)$ $K = \left[\frac{F^2}{\epsilon RT} \sum (z_i^2 C_{i0}) \right]^{1/2}$
Electro-osmotic velocity, v_{eo} , (m/s)	2.46×10^{-6}	$v_{eo} = \frac{\epsilon \xi \Delta V}{\eta \Delta l}$
Electrosmotic transport, J_{eo} , (moles/s)	1.24×10^{-9}	$J_{el} = A_p \Delta C \cdot v_{eo}$

drop and electric field will be localized at the pore entrances and little electrophoresis deep within the membrane is expected (flat potential profile). For the case of electroosmosis, once electroosmotic flow velocity is set up in the tip region, there is continued plug flow in the CNT cores across the whole path-length of the nanotube. However, probing the CNT channels with negatively-charged and neutral molecules is necessary for future investigations to unravel electrically-facilitated transport through conducting CNTs. Further evidence to the presence of electro-osmotic transport in the CNT membranes is provided by figure 6.9, in which the experimentally determined electrically-facilitated permeability is plotted against calculated zeta-potential of the functionalized membrane and is found to monotonically increase with the calculated zeta potential for the experiments under consideration. The charge density of the membrane with surface COOH groups (i.e as-made (plasma oxidized) and diazo static grafted (sg)) was estimated from interfacial-capacitance measurements, as described earlier in Chapter 5. Further, it is assumed that the dye molecule provides 4 fold more charge density after coupling to the carboxylic-acid groups. The zeta-potential is calculated for a 0.1 (M) of a 1:1 electrolyte. This observation is further evidence that electrically-assisted transport of these probe molecules is electro-osmotically controlled. Also, note strong agreement between observed-flow velocity and electro-osmotic velocity for plasma-oxidized and plasma-oxidized-spacer dye membrane as shown in Table 6.1.

6.3 Conclusions

Aligned carbon-nanotube membranes are a promising platform to mimic natural protein channels with a well-defined scaffold to place selective ‘gate-keeper’ chemistry at the channel entrances. The conformation of the large anionically-charged molecules tethered to the CNT surfaces changes with applied bias and dramatically affects diffusional transport through the cores of the CNTs. The unique properties of the CNT cores, namely fast fluid flow and electrically-conductive tubes, allow preferential chemical functionality at the core entrance. The application of bias directly to the conductive CNT composite allows for concentration of an electric field directly at the conductive CNT tips. With the precise location of tethered functional groups, modest

voltages ($\sim 100\text{mV}$) can be applied to control the steric environment of the channel entrance. This is a subtle, but important, distinction from the more common geometry of a cross-membrane potential drop (voltage drop applied to solutions on each side of the membrane), where the electric field is essentially uniform down the length of the pore. In that case, the difference in energy for the conformational of charged ligands away from or towards the pore wall is small and is verified in the cross-potential experiments. In the case of potential applied to the CNT membrane, high electric fields effectively pin charged ligands' position in the channel. Electrically-facilitated transport through the CNT membrane structure appears to be electro-osmotically controlled with the observed fluxes being consistent with electro-osmotic fluxes calculated from the experimentally obtained charge density.

Since these membranes can be produced over a large area with mechanically-robust polymers, it is possible to apply the principles of natural channels to large-scale chemical separations and active drug delivery. For example, ongoing research efforts in this laboratory are to use the electrostatic 'gate-keeping' to control the diffusion flux of addictive substances such as fentanyl or nicotine. This will allow programmed transdermal-drug delivery over large areas with metabolically useful fluxes. The ability to electrochemically graft diazonium salts to CNT entrances also demonstrates the ability to use CNT tips as electrodes for electrochemical reactions with the advantage of forced mass transport of products across the membrane. A broader implication for these membranes, with tethered ligands only at the tips of conductive pores, is that applied bias can control the conformation of the tethered molecules, thus acting as an actuator for the selective transport of permeate molecules across the membrane. This mimics the fundamental mechanism of ion channels that can be applied to macroscopic chemical applications.

Chapter 7

Finite-Element Calculations

7.1. Introduction

Transport of ions of different size and charge through the CNT membrane structure has been studied as a function of CNT tip modification. An empirical resistance-in-series model of hindered diffusion for predicting transport through CNT membrane was described in Chapter 3. However, it is unclear whether the observed hindered diffusion is dominated by electrostatics or molecular-steric effects. Analytical techniques have been developed by Deen and co-workers in the 1980s to solve the electrostatic partitioning of charged particles in charged pores^{64,228}, which serves as the theoretical and quantitative basis for nearly all water purification applications. Here, we apply Deen's model to this system so that we can ascertain the maximum predicted diffusion hindrance due to electrostatics for the geometries involved in the CNT membrane. Deen's model assumes a uniformly-charged pore with ions being repelled from the surface. Since the geometry of the CNT membrane has non-uniform charge density (charge primarily located at CNT tips), it is necessary to revisit the Deen's model using a numerical technique based on finite elements. The key advantages of using the finite-element formalism are: flexibility of different boundary conditions like (a) constant surface-charge density on the molecule and pore walls (pertinent to ionic-transport studies in Chapter 2; or (b) constant surface-charge density on the transporting molecule, but constant potential boundary on the pore walls (pertinent to voltage-gating studies). The finite element approach also allows for flexible geometry regarding the pore and the transporting molecule. As a starting point to this modeling approach, a coarse-grained, finite-element formalism was developed to compare Deen's analytical solution of partitioning charged colloids in charged pores using a PC-based commercial, finite-element software (Femlab, COMSOL Inc.). Electrostatic partitioning of charged permeates in charged pores as a function of size of the permeate and concentration of screening electrolyte was studied using the finite-element framework. With the verification of the computational method by Deen's analytical model, the computations were applied to studying electrostatic partitioning in cylindrical pore structure containing

non-uniform charge density that resembles the CNT membrane geometry. This is best represented by a thin charged ring on an otherwise non-charged core. The motivation for this geometry is to mimick the ‘gate-keeper’ concept, prevalent in biological-cell channels, in which a thin layer of functional molecules can control selective transport through the membranes. Several chapters of this dissertation have been devoted to the application of the ‘gate-keeper’ concept in the CNT-membrane system. The primary question is whether a thin layer of charge at the entrance to the CNT pore provides enough electrostatic interactions to result in significant selectivity/flux changes or do steric effects dominate.

From a practical perspective, the effect of electrical-double layers (EDL) at the solid-liquid interface is extremely important in molecular transport through porous channels. The thickness of the double layer can vary from 1 nm in high-ionic strength to a few nanometers at low-ionic strength. The EDL effects become more prominent when the physical dimension of the molecule is a fraction of the pore size, thereby allowing strong interaction of the respective double layers, in addition to the steric factors. Such phenomena have been exploited for charge-based separation of protein molecules²²⁹ and designing ionic permselective membranes.⁷³ The significance of this research is that the finite-element technique allows for more flexibility in the geometries and boundary conditions; and allows application of electrostatic-partitioning theory in complex geometries or nonspherical molecules in membrane pores. It also lays the framework for future modeling of ‘voltage-gated’ transport through CNT membranes in conjunction with simulation techniques like Molecular Dynamics or Brownian dynamics to incorporate the conformational change of the ‘gate-keeper’ molecule.

7.2. Defining the Problem

7.2.1 Partition of a Spherical Particle in a Cylindrical Pore

The diffusion co-efficient of a particle in a solution can be predicted by the Stokes-Einstein equation (eq. 2.3). However, in a pore the apparent diffusion co-efficient (D) is strongly influenced by constraints of the pore and can be related by:

$$\frac{D}{D_0} = 2 \int_0^\lambda K(\lambda, r) \exp\left[\frac{E(r)}{kT}\right] r dr \quad [7.1]$$

which λ is the reduced-pore diameter given by the ratio of the diameter of the molecule to the diameter of the pore, and r is the dimensionless-radial position normalized to the radius of the pore. $E(r)$ is the potential at position r . The partition co-efficient is expressed as a combination of two factors: K is the enhanced hydrodynamic drag, and Φ is the equilibrium partition co-efficient. Considerable theoretical research is still being carried out to accurately predict the hydrodynamic drag co-efficient. For center line approximation (i.e. the particle at the center of the cylinder) $K(\lambda, r)$ can be approximated as $K(\lambda, 0)$. Therefore,

$$\frac{D}{D_0} = 2 K^{-1}(\lambda, 0) \int_0^\lambda \exp\left[\frac{E(r)}{kT}\right] r dr \quad [7.2]$$

For non-interacting sphere and cylinder, $E(r) = 0$, hence,

$$\frac{D}{D_0} = 2 K^{-1}(\lambda, 0) \int_0^\lambda r dr = K(\lambda, 0)(1 - \lambda)^2 \quad [7.3]$$

The hydrodynamic partition co-efficient K_d can be expressed by a number of equations, the most popular being the Renkin equation.

$$K_d = 1 - 2.105 \lambda + 2.09 \lambda^3 - 0.95 \lambda^5 \quad [7.4]$$

$$\text{Thus, } \frac{D}{D_0} = (1 - 2.105 \lambda + 2.09 \lambda^3 - 0.95 \lambda^5)(1 - \lambda)^2 \quad [7.5]$$

For interacting sphere and cylinder,

$$\frac{D}{D_0} = (1 - 2.105 \lambda + 2.09 \lambda^3 - 0.95 \lambda^5) \exp\left(\frac{\Delta E}{kT}\right)(1 - \lambda)^2 \quad [7.6]$$

The term $\exp\left(\frac{\Delta E}{kT}\right)$ also known as the Boltzmann Factor, represents the interaction energy term whereas, the term $(1 - \lambda)^2$ represents the steric factor in the equilibrium partitioning (Φ). This energy term will be dependent on long-range van der Waals and electrical double-layer interactions of the pore and the sphere. In this chapter, we revisit the problem of electrostatic partitioning using finite-element analysis and compare it with analytical solutions developed in the 1980s by Deen et al. for the linearised Poisson-Boltzmann equation. The finite-element approach also allows us to calculate the electrostatic partitioning of uni-dimensional geometries like a sphere, a cube, and a cylinder ($L/D=1$) and application in pores with non-uniform charge density.

7.2.2 Setting up the Differential Equation and Problem

The problem has been defined in the Cartesian co-ordinates (x,y,z). For the cylinder, we have $x=y$. For the particles, we considered symmetrical ($x = y = z$) 3 D objects (i.e. a sphere, a cube, and a cylinder with length to diameter ratio equal to one). One can define a characteristic length for these objects (i.e. the diameter of the sphere, the length of the cube, and the diameter of the base of the cylinder). The treatment of Deen *et al* was followed in defining the dimensionless quantities in terms of the cylinder radius X_0 . The reduced-pore dimension λ is defined as ratio of half the characteristic dimension to the cylinder diameter and the position (x) of the particle, located by its center, thus is a fraction of the cylinder radius.

The electrical potential Ψ^* , cylinder surface-charge density, q_c , and sphere-surface charge density q_s are expressed as dimensionless quantities:

$$\Psi = \frac{F\Psi^*}{RT} \quad \sigma_c = \frac{FX_0q_c}{RT} \quad \sigma_s = \frac{FX_0q_s}{RT} \quad [7.7]$$

Where F is the Faraday constant, R is the Universal gas constant, and T is the temperature. The non-linear dimensionless PB equation inside a cylindrical pore of radius X_0 is:

$$\nabla^2 \Psi = \tau^2 \sinh(\Psi) \quad [7.8]$$

The dimensionless parameter, τ is the ratio of pore radius to the Debye length ($\frac{1}{K}$) and is given by the equation

$$\tau = X_0 K = X_0 \left[\frac{F^2}{\varepsilon RT} \sum (z_i^2 C_{i0}) \right]^{1/2} \quad [7.9]$$

where z_i and C_i are the electronic charge and the concentration of the electrolyte.

7.2.3 Computational Geometry and Boundary Conditions

Figure 7.1 shows the computational geometry. For these calculations, a finite limit length of the cylinder was chosen. Therefore, the computational geometry requires an imposed boundary condition of zero-charge density on IJ and KL. Conforming to the center-line approximation, the sphere is placed on the axis of the cylinder and at the center of the cylinder. The interaction energy can be expressed by the following equation:

$$\Delta E = E_{sc} - E_s - E_c \quad [7.10]$$

where E_{sc} is the electrostatic energy of the sphere in the cylinder system, whereas E_s and E_c represent the energy of the sphere and the cylinder alone.

Energy of the sphere in the cylinder system

The boundary conditions are:

$$-n \cdot \nabla \Psi = \sigma_s \quad \text{for } d\Omega \in \text{ABCD}; \quad -n \cdot \nabla \Psi = \sigma_c \quad \text{for } d\Omega \in \text{IK, JL}$$

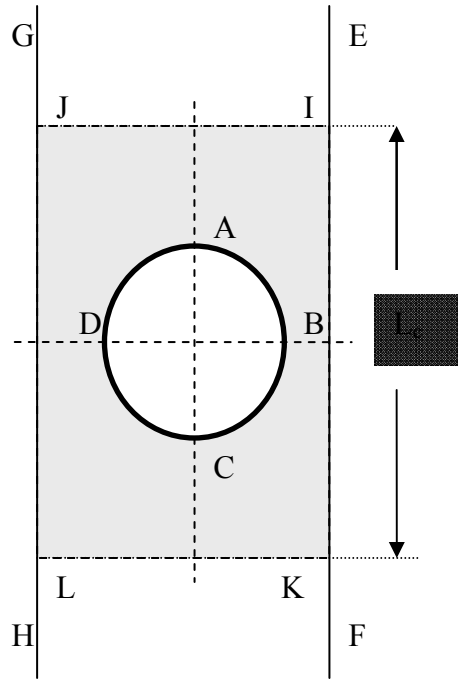


Figure 7.1 The geometry for the finite element analysis. The sphere ABCD represents the particle inside the infinite cylindrical pore EFHG. For the analysis, a finite volume of the pore IKLJ, corresponding to the length L_c is considered. For the cube and cylinder ($L/D = 1$), a similar geometry with the particle at the center of the cylinder was considered.

The imposed boundary condition is

$$-n.\nabla\Psi = 0 \quad \text{for } d\Omega \in \text{IJ, KL}$$

E_{sc} is the sum of the energy of the cylinder and the sphere in this system and given by:

$$E_{sc} = \frac{\sigma_c}{2} \int_{IK, JL} \Psi dA + \frac{\sigma_s}{2} \int_{ABCD} \Psi dA \quad [7.11]$$

Energy of the sphere

The boundary conditions are:

$$-n.\nabla\Psi = \sigma_s \quad \text{for } d\Omega \in \text{ABCD}; \quad -n.\nabla\Psi = 0 \quad \text{for } d\Omega \in \text{IK, JL}$$

The imposed boundary condition on the segment IJ, KL remains the same. The energy of the sphere is:

$$E_s = \frac{\sigma_s}{2} \int_{ABCD} \Psi dA \quad [7.12]$$

Energy of the cylinder

The boundary conditions are:

$$-n.\nabla\Psi = 0 \quad \text{for } d\Omega \in \text{ABCD}; \quad \text{for } -n.\nabla\Psi = \sigma_c \quad d\Omega \in \text{IK, JL}$$

The energy of the cylinder is:

$$E_c = \frac{\sigma_c}{2} \int_{IK, JL} \Psi dA \quad [7.13]$$

The dimensionless energy ΔE obtained from these calculations is converted into the dimensional form using the equation:

$$\Delta E^* = \left[\frac{RT}{F} \right]^2 \Delta EX_0 \varepsilon \quad [7.14]$$

The partition co-efficient for the center line approximation can be calculated from equations 7.6 and 7.10.

7.2.4 Computational Technique

The finite element analysis was carried out using a commercial package from FEMLAB (COMSOL Inc. USA). The software has provisions for a Matlab interface, which allows a script to run the FEMLAB solvers. The Matlab program is shown in Appendix to Chapter 6: A6.1, A6.2 and A6.3. The governing equation was formulated using the co-efficient form of PDE. The boundary conditions, as described in an earlier section, were entered as Neumann boundaries. The mesh was composed of quadratic Lagrange. elements and the GMRES solver were used. The energy was calculated from a boundary integration method available within the software. Ideally, one would have allowed a compiler to run the three programs simultaneously. However, a microsoft excel spreadsheet was used to tabulate the results obtained from the MATLAB + FEMLAB program. The calculations for the segmented pore structure were calculated with a graphical-user interface in the finite-element software and compiled manually in an excel file.

7.3 Results and Discussions

7.3.1 Comparison of the Finite Element Solution with Analytical Solution

There has been considerable interest in numerical solution of the Poisson-Boltzmann equation to obtain interaction between two colloidal particles in different geometries using finite difference or finite element techniques.^{230,231,232} Numerical techniques have been utilized for studying electrostatic interaction and predicting diffusivities of spheres in slit-pores.²³³ Monte-Carlo simulations have been performed to study electrostatic partitioning in slit pores.²³⁴ In this work, a finite-element approach is explored to study electrostatic partitioning of charged permeates in cylindrical pores. A typical solution of the dimensionless PB equation in the geometry discussed earlier using the finite element code is shown in figure 7.2.

First the effect of the imposed boundary condition (i.e. the Neumann boundary condition of zero charge density on IJ and KL) is explored. With this in view, the finite length of the cylinder is varied from $L/D = 2$ to 20 and the Boltzmann factor is calculated for different values of λ . The calculated Boltzmann factor remained invariant to the

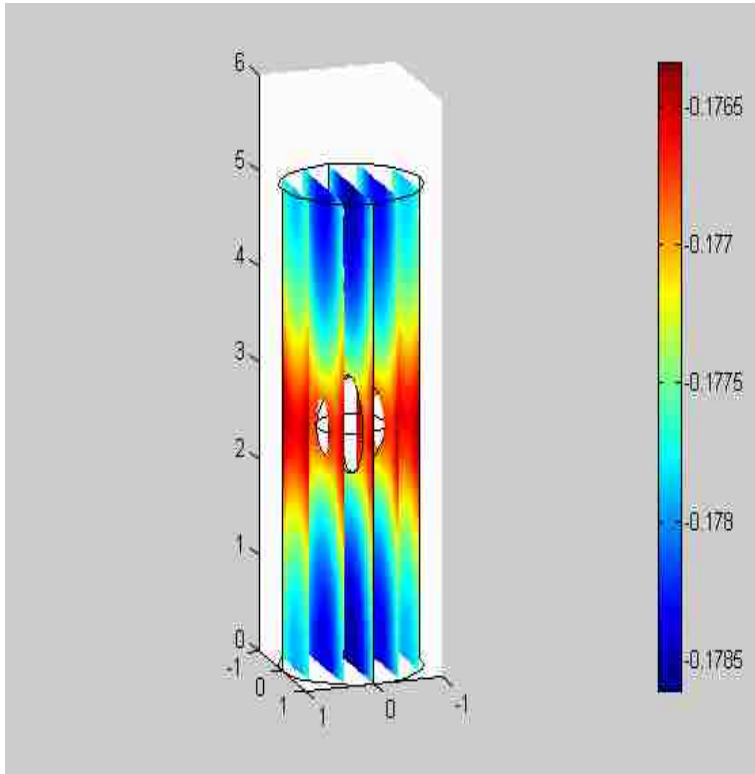


Figure 7.2 Typical finite element solution of the Poisson-Boltzmann equation of the sphere in cylinder geometry, with constant surface charge density on the walls of the cylinder and colloid. The solution is in dimensionless quantities.

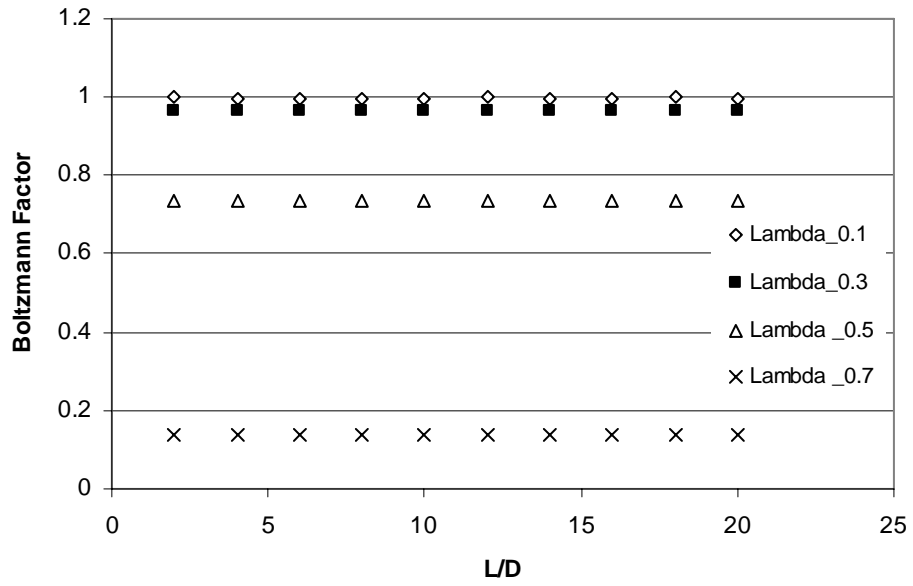


Figure 7.3 Effect of length to diameter of the cylinder on the computed Boltzmann factor. Insignificant variation in the computed Boltzmann factor is observed with varying L/D of the cylinder from 2 to 20.

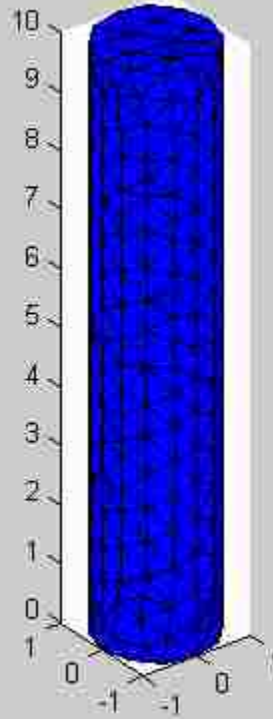
Table 7.1 Analytical solution developed by Smith and Deen for a charged colloid in a charged pore with center line approximation.

A_s	$\frac{4\pi\lambda^4 e^{\tau\lambda} S_0}{1 + \tau\lambda}$
A_{sc}	$\frac{4\pi^2 \lambda^2}{I_1(\tau)}$
A_c	$\frac{\pi^2 h(\tau\lambda)}{\tau^2 I_1^2(\tau)}$
A_{den}	$\pi\tau(1 + \tau\lambda)e^{-\tau\lambda} - S_0 h(\tau\lambda)$
$h(\tau\lambda) = (1 + \tau\lambda)e^{-\tau\lambda} - (1 - \tau\lambda)e^{\tau\lambda}$	
$S_0 = \int_0^{\text{inf}} \frac{K_1[(\tau^2 + \theta^2)^{1/2}]}{I_1[(\tau^2 + \theta^2)^{1/2}]} d\theta$	

$$\frac{\Delta E}{k_B T} = (A_s \sigma_s^2 + A_c \sigma_c^2 + A_{sc} \sigma_s \sigma_c) / A_{den}$$

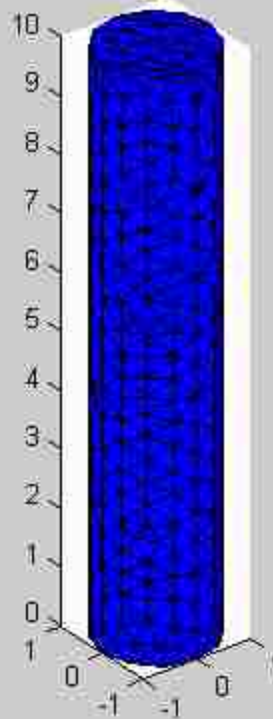
length of the cylinder. Therefore, the imposed boundary condition does not significantly influence the computed Boltzmann factor (figure 7.3). To compare the validity of the finite-element analysis, the solution is compared with the analytical solution developed by Smith and Deen for a linearized Poisson-Boltzmann equation. The analytical solution to the problem is provided in a tabular form in Table 7.1. The analytical solution is compared with the finite-element solution in figure 7.4. The basis of the finite element for solving partial differential equations (PDE) is the discretization of the domain into finite spaces or elements. In 3D, these elements are tetrahedrons, and it subdivides the geometry into mesh faces, mesh edges, and mesh vertices. Nodes are then assigned to each element. The selection of the elements and nodes are often a matter of judgment and prior experience. The order of the elements specifies the nodal points on the element. For example, order one would have one node point at each vertex of a tetrahedron; order two would have nodes at each vertex and midpoint²³⁵ of the sides of each element. For each of these node points, p_i , there exists a degree of freedom $\Psi_i = \psi(p_i)$ and a basis function ϕ_i such that: $\psi = \sum \Psi_i \phi_i$. It is apparent that the accuracy of a finite-element analysis will depend on the fineness of the mesh, and the number of nodal points considered, often at the cost of computing speed. The Matlab interface allows one to vary the mesh size by a parameter h_{\max} , which denotes the maximum height of each element in the mesh. By varying this parameter, it is possible to generate finer meshes. The meshes used for the calculations are shown in figure 7.4. The finer-mesh size increases the accuracy of the solution (in this case deviation from the analytical solution), but increased the computational time considerably as shown in figure 7.5. An optimization between fineness of the mesh and computation time was found with $h_{\max} = 0.25$. This finite-element analysis could not differentiate between the linear and nonlinear forms of the PB equation, (i.e. both forms of the equation provided similar solutions). The nonlinear form of the PB equation often becomes extremely important when considering near field forces, especially in predicting protein or macro-molecule conformation,²³⁶ but is of less significance when far-field forces are considered.²³⁷ Perhaps stringent error analysis and mesh refinements are required for accurate solution of the nonlinear PB equation.

3D mesh with $H_{max}=1$



(a)

3D mesh with $h_{max}=0.5$



(b)

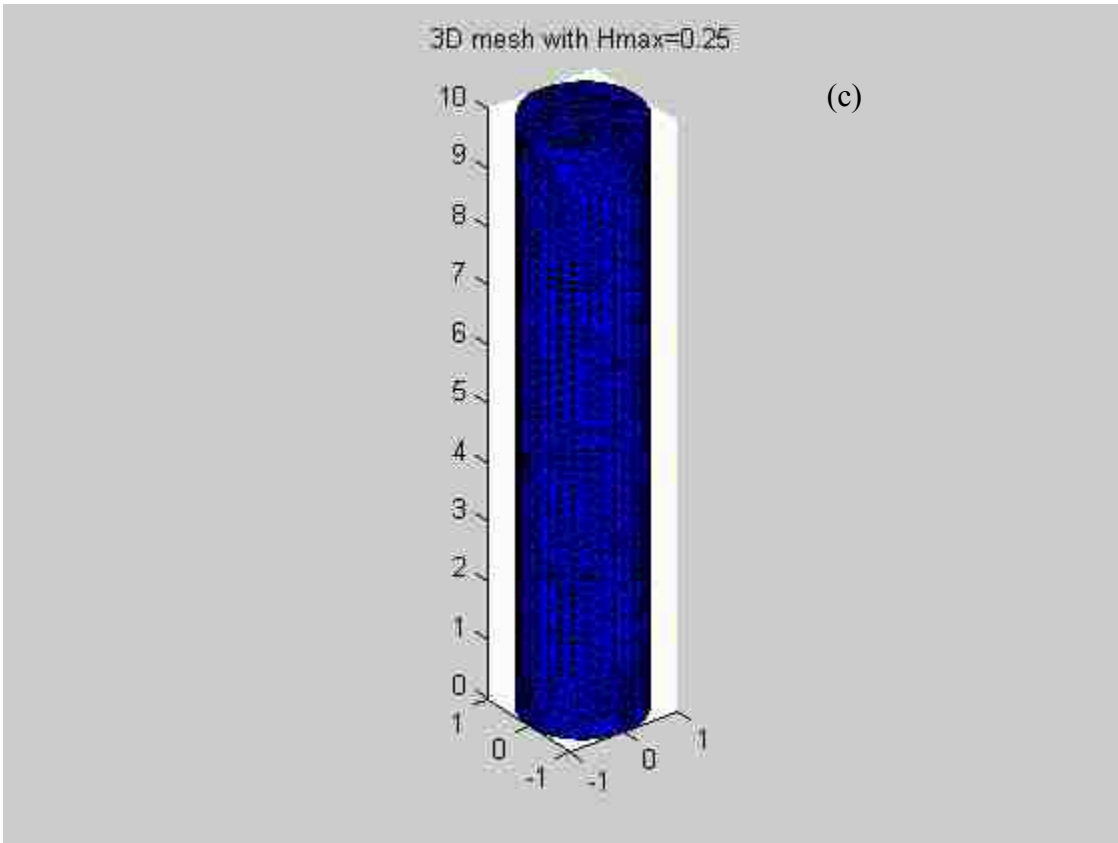


Figure 7.4 Quadratic Lagrangian elements used for generating the mesh for the finite element analysis. The mesh can be made finer by decreasing the maximum height (h_{\max}) of the element. Finer meshes require longer computational time, but the errors are minimized.

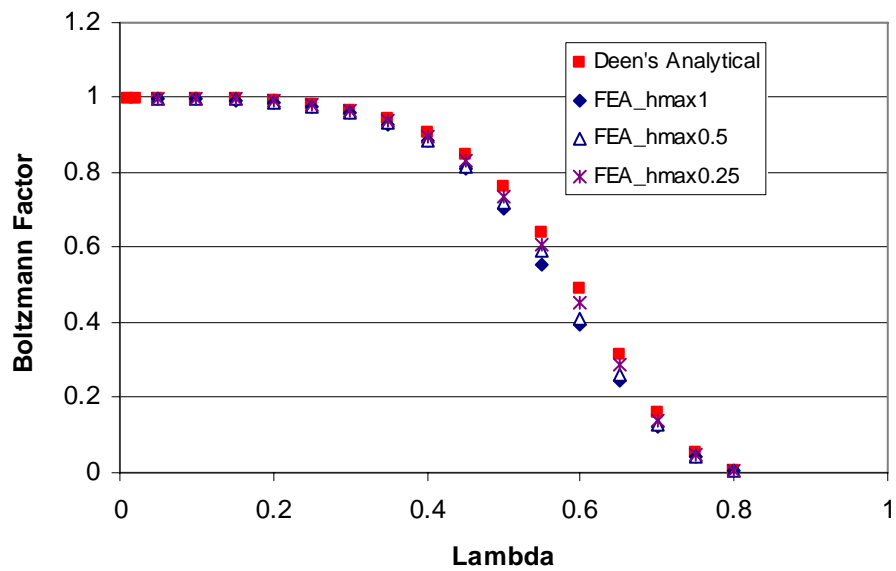


Figure 7.5 Comparison of Deen's analytical solution to the Finite-Element Analysis in this study. Calculations are for a cylinder with 10 nm pore radius with a charge density of $0.5 \times 10^{-2} \text{ C/m}^2$ and spherical particle with 1.02×10^{-2} charge density in presence of 0.1M of a 1:1 electrolyte. The maximum height of the mesh utilized for the finite element calculations is denoted by h_{max} .

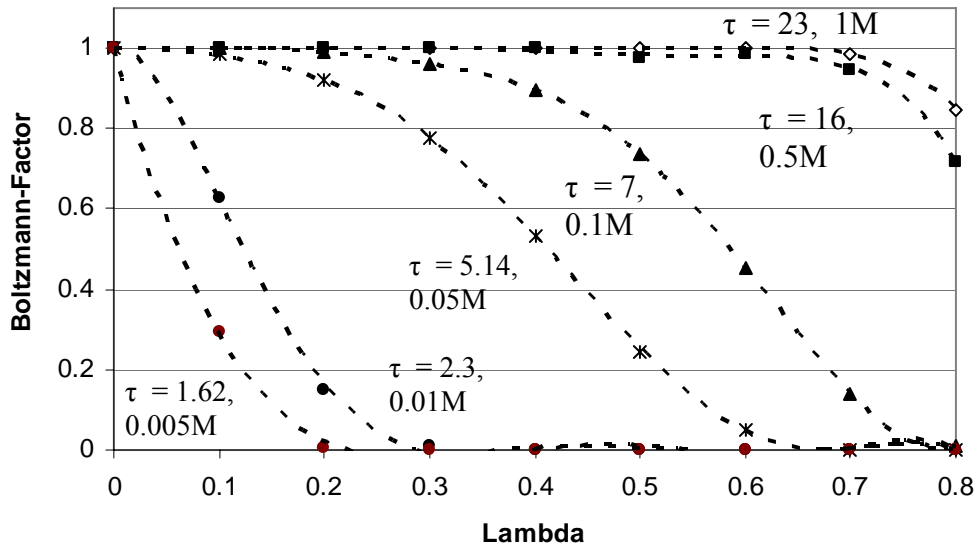


Figure 7.6 Boltzmann factor for a charged-spherical particle (charge density $1.02 \times 10^{-2} \text{ C/m}^2$) inside a cylindrical pore of 10 nm diameter with charge density ($5 \times 10^{-3} \text{ C/m}^2$). Partition co-efficient calculations are for different concentration of the screening (1:1) electrolyte. As expected, at higher concentration of the electrolyte, the charges are screened and the electrostatic effects are diminished. Values close to one indicate minimum interaction and values close to zero indicate that the particles are totally rejected by the charged pore especially at low values of τ .

7.3.2 Partition co-efficient as a function of Debye screening length

The presence of small mobile ionic charges in the form of electrolytes can significantly alter the charged double layer at the charged surface. The analysis in this work is carried out within the Gouy-Chapman framework of the double-layer model. Unlike the Stern model, where a fixed counter-ion layer adjacent to the charges on the surface is considered, the Gouy-Chapman model does not account for this fixed counter ion layer. The Debye length, which physically represents the characteristic length scale of Coulombic interactions, can be as large as 13 nm for 0.0005M to 0.3 nm for a 1M of 1:1 electrolyte. The effect of charge screening becomes especially important when the pore radii approach the dimensions of the Debye length. Ionic transport through porous systems with dimensions close to Debye length have been studied numerically for point charges.¹⁰⁸ However, interest also lies in finite size of the permeating species in porous systems with pore dimensions close to the Debye length. This is because the charged permeate will also significantly alter the double-layer charge distribution. This requires application of the electrostatic-partitioning theory in analyzing this problem. In this finite-element analysis, a pore of 10 nm radius is considered. The reduced pore diameter (λ) is the size of the permeate to the size of the pore, whereas, the dimensionless parameter τ is the ratio of the pore radius to the Debye-screening length.

Increase in ionic strength decreases the Debye screening length and leads to an increase in τ . Consider, for example, a particle with a diameter of 2 nm corresponding to $\lambda=0.2$ in figure 7.6. The surface charge on the cylindrical pore will electrostatically reject it at low-ionic strength ($\sim 0.005M$), but will be electrostatically unhindered in higher-ionic strength ($\sim 0.1M$). As the ionic strength increases and the charge on the pore and the sphere is screened, it will diffuse through the pores electrostatically unhindered. However, the hydrodynamic hindrance will be present as usual, (i.e. the steric effects would remain unaffected by these changes in the double layer structure). As expected, increase in the size of the permeate increases the electrostatic hindrance effect.

7.3.3 Effect of Particle Shape: Sphere, Cube and Cylinder

Until now, discussions have concerned spheres as the permeating species, which often is not the case. The norm has been to use the equivalent-spherical diameter or the

Stokes-Einstein diameter in hindered-diffusion analysis. The finite-element approach allows numerical solutions for the electrostatic-hindrance effects for permeating species of different geometries. As a demonstrative case, the Boltzmann factor has been calculated for three shapes with $L/D = 1$ (i.e. a sphere, cube and a cylinder (figure 7.7)). For similar charge density on the pore and the permeate, the calculations indicate that the cubical geometry is the most electrostatically hindered, while the sphere is least. A reason for this is that the surface areas of these three shapes are in the order cube > cylinder > sphere. Though the example shown here is rather simplistic, it should be possible to study electrostatic partitioning of complex macromolecules in pores using a similar approach and could find applications in predicting transport through charged ultrafiltration membranes.

7.3.4 Transport of Ions in Segmented and Sandwich Membranes

This dissertation has demonstrated the extremely fast mass-transport characteristics of the CNT membrane and a method to functionalize the tips and core of the membrane. Further, it has shown that core-grafted membrane slowed down the pressure-driven flux considerably through CNT membranes, as discussed in Chapter 2. While it is imperative to introduce chemical functionality for different separation purposes, it slows the throughput due to increased interaction of the solvent with the functional molecule. In this scheme, it is essential to preserve the non-interactive nature of the graphite cores and to force chemical functionality only at the CNT tips. Plasma-oxidization of membranes does preserve both of these aspects. However, for membranes with higher, functional density, another approach of forcing diazonium grafting chemistry at the tips by the fast fluid flow was described in Chapters 2 and the effects of chemical functionalization on mass transport through the membrane have been described in Chapters 3, 5 & 6. For designing a new class of membranes with exceptionally high selectivity and permeability, it is essential to strike a compromise with the extent of functionalization and decreased permeability. To this end, electrostatic partitioning of a charged molecule as a function of position in two-segmented pore geometry was studied using the finite-element approach. The segmented membrane has a constant surface charge at one end, while there is a zero surface charge on the other and is depicted in

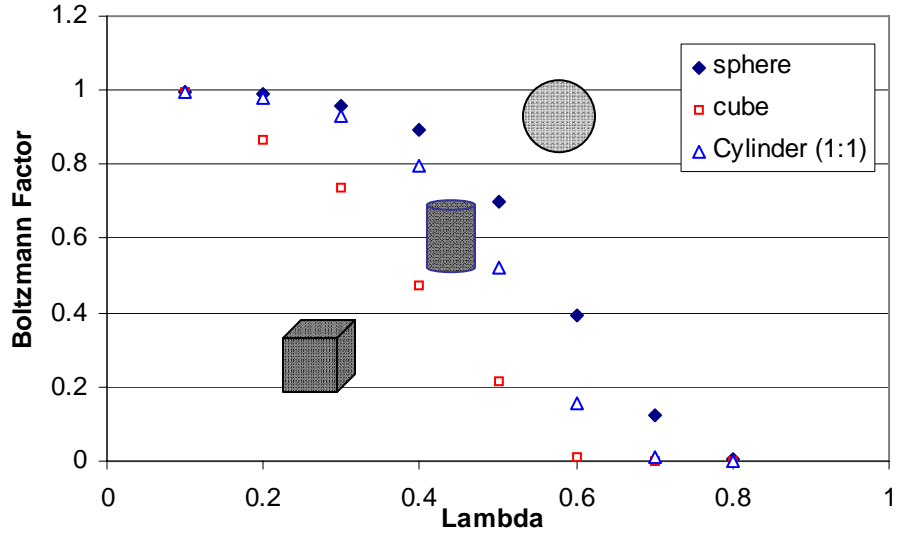


Figure 7.7 Boltzmann factor for different shapes of the particle: sphere, cube and cylinder ($L/D = 1$). For similar charge densities on the membrane ($1.02 \times 10^{-2} \text{ C/m}^2$) and on the cubical shape is electrostatically most hindered.

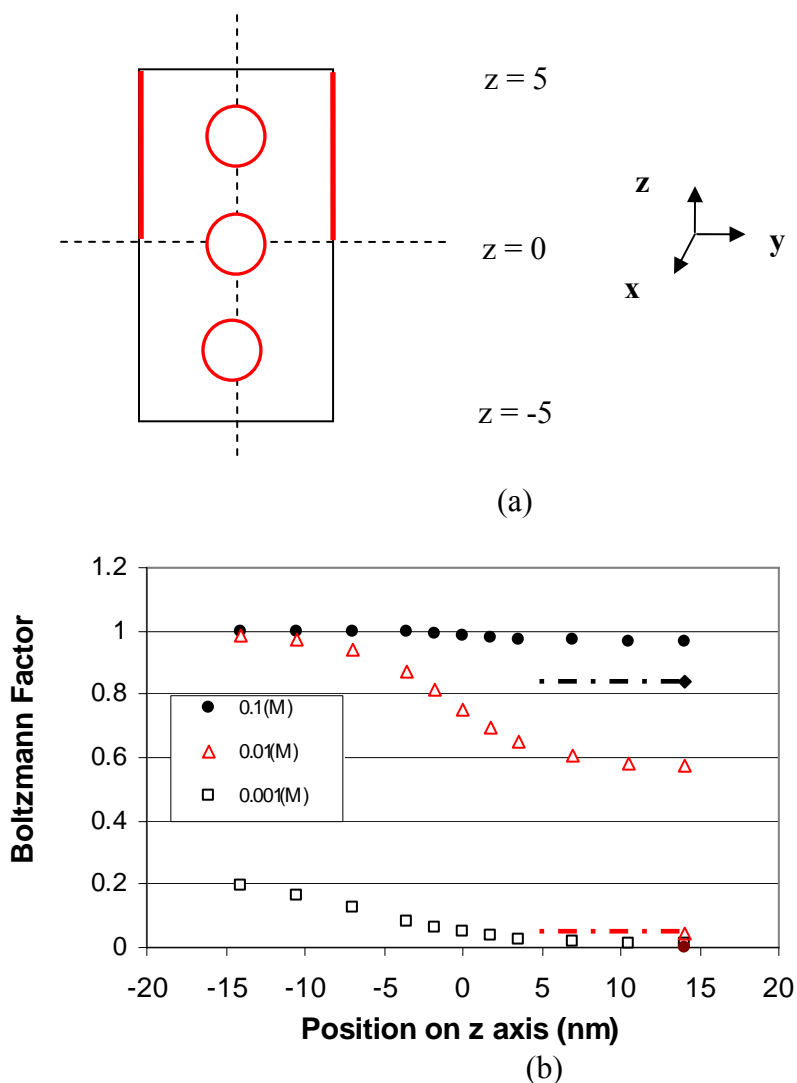


Figure 7.8 (a) Schematic of the computational geometry for calculating the partition coefficient as a function of position inside the pore. The red color indicates the presence of a charged-boundary condition, while the black line indicates a zero-charge boundary condition. A pore radius of 3.5 nm with a surface-charge density of $3.2 \times 10^{-3} \text{ C/m}^2$ and reduced-molecule radius of 0.135 with surface-charge density of 0.113 C/m^2 are considered. These values are analogous to those for a plasma-oxidized CNT membrane and $\text{Ru}(\text{bipy})_3^{2+}$. Ionic concentrations of 0.1M, 0.01M and 0.001M of 1:1 electrolyte are considered. (b) The Boltzmann factor for the molecule as a function of position in the segmented pore geometry. In this figure, the calculated Boltzmann factor is plotted against the dimensional position. Also shown by dashed line in the figure, is the Boltzmann factor for a homogenous cylinder for a position $z=14 \text{ nm}$.

figure 7.8 (a). A pore with radius of 3.5 nm and surface charge density of $3.2 \times 10^{-3} \text{ C/m}^2$ and reduced-molecule radius of 0.1357 with surface-charge density of 0.113 C/m^2 is considered. These values are analogous to those for plasma-oxidized membrane for $\text{Ru}(\text{bipy})_3^{2+}$. Though there is an attractive partitioning between the negatively-charged plasma oxidized membrane and the positively-charged molecule, for the sake of easy interpretation, the calculations are performed for repulsive interaction, (i.e. the pore and the molecule both have positive charge densities). The calculations indicate that the electrostatic effects are prominent for 0.001M, while being screened considerably for 0.1M of the electrolyte. For 0.001M of the screening electrolyte, the similarly-charged molecule would be electrostatically repelled by the charge density provided by the plasma-oxidized membranes. The electrostatic interactions also decline as the molecule enters into the pore area with a zero-charge boundary condition ($z < 0$). However, a significant amount of electrostatic interaction remains in this region too, exceeding the Debye screening length ($\sim 9 \text{ nm}$ for 0.001M electrolyte). For 0.01M concentration of the electrolyte, a curve showing the gradual transition from electrostatically influenced (partition co-efficient ~ 0.6) to electrostatically non-influenced (partition co-efficient > 0.95) is obtained. Next we turn our attention to another hypothetical pore structure, with pore radius of $\sim 1.5 \text{ nm}$, having a sandwich structure of a charged layer of 1.5 nm bounded by segments of no-charge with 4.5 nm length as shown schematically in figure 7.9 (a). The choice of pore radius is arbitrary, but motivated by the fact that the functional molecules on the nanotubes can shrink the pore size. The choice of the sandwich structure is to get a feel of the transition length from electrostatic interaction to non-interaction. The size and charge of the permeating sphere is the same as those for $\text{Ru}(\text{bi-py})_3^{2+}$. The charge density on the CNTs are assumed to be $1.28 \times 10^{-2} \text{ C/m}^2$ and $7.72 \times 10^{-2} \text{ C/m}^2$. The charge density of $1.28 \times 10^{-2} \text{ C/m}^2$ is based on four times the charge density of the plasma-oxidized membrane (i.e. close to dye functionalized CNT membrane), since the dye molecule has four charge units per molecule. The length of functionalization is 10% of the total length of the structure. Note that the experimentally-determined functionalization is $\sim 14 \%$ and has been used in the modeling of transport in Chapters 2 and 3. The charge density of $7.72 \times 10^{-2} \text{ C/m}^2$ corresponds to the charge density of diazo-grafted membrane times the charge on each dye molecule. It is easily the

highest-achievable charge density within the premises of the present dissertation. The calculations are shown in figure 7.9 (b) and (c). Also shown is the partition co-efficient calculated for the case of a homogenous cylinder, shown by dotted lines. The maximum electrostatic effects are observed at the center ($z = 0$) of the sandwich structure. However, it declines rapidly with position, and is prominent both for 0.1 and 0.01M of the electrolyte. Comparison of figures 7.9(b) and (c) show that for the higher the charge density on the sandwich structure, the ionic screening effects are less prominent. There was a 30% change in the Boltzmann factor, when the electrolyte was changed from 0.1M to 0.01M for the higher charge density calculations; whereas, a 42% change was observed for the calculation using $1.28 \times 10^{-2} \text{ C/m}^2$ at $z = 0$. These calculations indicate that the magnitude of the charge density is extremely important in electrostatic partitioning. If it is high enough, the electrolyte-screening effects might not influence the transport properties significantly.

Shown in figures 7.9 (b) and (c) are also the calculated Boltzmann factor for a uniform cylinder of similar charge density. There is $\sim 30\text{-}35\%$ less partitioning in the sandwich structure, compared to the uniformly charged cylinder as shown in figure 7.9(b) and 10% less partitioning as shown in figure 7.9(c). In the case of a segmented-pore structure, in figure 7.8 (b), there is significant deviation ($> 90\%$ for the calculated partition coefficient) considering a homogenous cylinder at a position where maximum electrostatic effects are observed. It suggests that the electric-field gradient effects in the segmented or sandwich structure are more prominent for lower-charge density on the structure.

Also pertinent to this discussion would be length scales associated with the electrostatic effects. The sandwich structure has a thin layer of charge at the centre of the structure and as such a symmetric distribution of the Boltzmann factor is obtained, with the maximum electrostatic effects (minimum partitioning) observed at the centre of the structure. A length scale associated with most electrostatic effects is the Debye-screening length, discussed in some details in Chapter 4 and earlier in this chapter. In brief, the Debye length is $\sim 3 \text{ nm}$ for 0.01M and $\sim 1 \text{ nm}$ for 0.1M of a 1:1 electrolyte. The discussion will center on the percent increase in electrostatic partitioning from the minima observed in the calculated curves of figures 7.9(b) and (c). In figure 7.9(b), at a

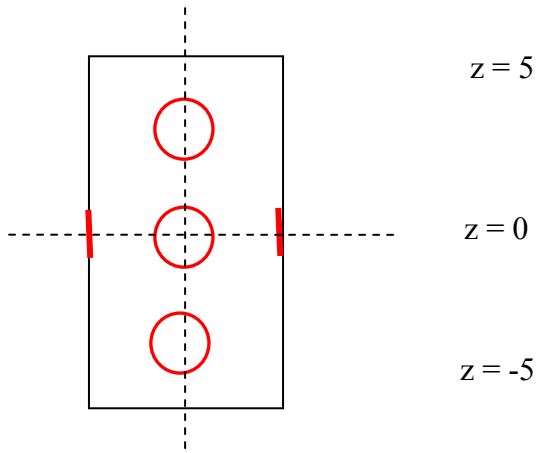
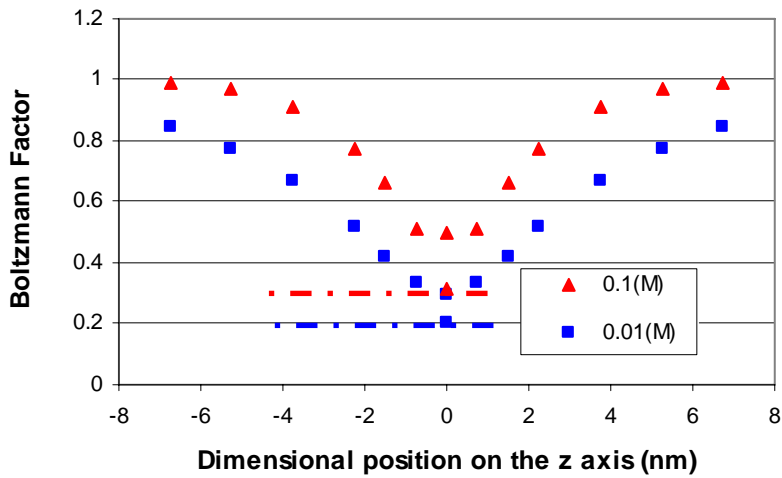
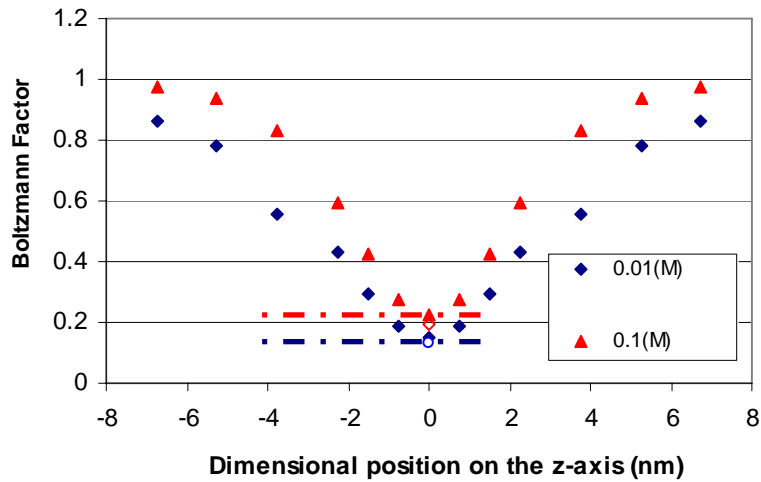


Figure 7.9 (a) A sandwich pore structure of radius 1.5 nm with surface charge density of $1.28 \times 10^{-2} \text{ C/m}^2$ and $7.72 \times 10^{-2} \text{ C/m}^2$, reduced molecule radius of 0.31 with surface charge density of 0.113 C/m^2 are considered.



(b)



(c)

Figure 7.9 Boltzmann factor as a function of the dimensional position of the sphere in the sandwich-pore structure for charge density of (b) 1.28×10^{-2} and (c) $7.72 \times 10^{-2} \text{ C/m}^2$ on the 1.5 nm pore. The red legends are for 0.1M and the blue legends are for 0.01M of the screening electrolyte. Calculations were performed for the blue legend on either side of the sandwich structure for figure 7.9 (a) and was found to be symmetric. Therefore, calculations were performed only for the negative z axis, while for positive values they were substituted from the symmetry of the solution. The Boltzmann factor has also been calculated for a uniformly-charged cylinder for the position $z=0$. Since the partition coefficient should not change for a uniformly charged sphere, it is denoted by dashed lines.

length of ~ 1 nm, for the 0.1M electrolyte, the partition coefficient declined by $\sim 45\%$ and is close to that observed in figure 7.9 (c) ($\sim 56\%$). For 0.01M of the electrolyte, a 100% decline was observed for the lower charge density (figure 7.9 (b)) and $\sim 230\%$ for the higher-charge density (figure 7.9 (c)) at a Debye length of 3 nm. It is difficult to generalize the observed transition by the present analysis. However, the statement that the charge effects were screened at few Debye lengths from the charged interface is generally valid.

An average partition coefficient of the charged sphere in the charged pore can also be calculated based on a series resistance model discussed in Chapters 2 &3 using the equation

$$\frac{1}{\phi_{eq}} = \frac{1}{L} \int_0^L \frac{dz}{\phi(z)} \quad [7.14]$$

where ϕ_{eq} , is the equivalent electrostatic partition coefficient and $\phi(z)$, is the calculated electrostatic partition coefficient as a function of position in the pore. For these calculations, the function, $\phi(z)$, is obtained by fitting a fourth-order polynomial to the calculated values in excel and then using a quadrature numerical method for carrying out the integral in Matlab. The average electrostatic partition coefficient is ~ 0.98 in 0.1(M), which decreases to ~ 0.76 in 0.01M and to 0.034 in 0.001M of the electrolyte in figure 7.8 (b). As expected, better separations (lower-partition coefficients) are seen at lower ionic strengths due to longer Debye screening lengths. Considerable electrostatic separations can be achieved in this hypothetical pore structure for the finite sizes and charge densities considered. It is important to point out that the length of pore segments with the charge density is 50% of the total length of the entire pore. For the sandwich structure in figure 7.9 (c), it is ~ 0.41 for the sandwich structure in 0.01M and decreases to ~ 0.58 in 0.1 (M) electrolyte for the pore with $7.72 \times 10^{-2} \text{ C/m}^2$. Similar analysis for the pore with $1.28 \times 10^{-2} \text{ C/m}^2$ shows that the average partition factor is ~ 0.55 for 0.01M and increases to 0.8 in 0.1M electrolyte. These calculations are for 10% of the functional length in the sandwich structure. These partition coefficients will be considerably less if this length of

the charged region is decreased. A simple approximation for the contribution of a thin barrier layer in a two diffusion barrier problem is ²³⁸

$$\frac{C_b}{C_o} = \frac{1}{1 + \frac{D_2}{D_1} \times \frac{L_1}{L_2}} \quad [7.15]$$

where C_b is the concentration after thin barrier layer and D_1, L_1, D_2, L_2 are the diffusion coefficients and path lengths of thin ‘gate-keeper’ region (~1nm) and nanotube length (~50um), respectively. From figure 7.9 (c), a partition factor of ~.15 (~ D_1/D_2) and barrier thickness of 4nm are approximated. Using equation 7.16 gives the ‘gate-keepers’ a relative partition of 0.9996, which is insignificant (a value of 1 would be for no thin barrier). Such a thin layer of charged ‘gate-keeper’ is the likely intended result of flow grafting of the membranes, where functionalization reaction is confined to the tips of the CNTs. Therefore, the voltage-dependent separations observed and discussed in Chapter 5?, especially for the flow-grafted membranes, cannot be simply electrostatic transport effects. The conformation of the charged-dye molecule, does significantly contribute to a decreased pore size and a steric blockage of the transporting channels.

7.4 Conclusions and Future Work

A finite-element method has been devised for solving electrostatic partitioning problems of charged particles in charged cylinders and validated to Deen’s analytical solution. The boundary conditions solved for were constant surface-charge density at the sphere and constant surface-charge density at the wall. The method captures the importance of double-layer screening in transport of charged species through charged pores. Unlike the analytical method, this numerical technique can also solve for other simple geometries like cubes and cylinders and non-uniform charge density on the cylindrical pores. The technique has been used for solving partition coefficients in a pore geometry consisting of a thin section of constant surface charge density analogous to the ‘gate-keeper’ concept in membrane separations. The results indicate the electrostatic effects decline within a few screening lengths, but functionalization length charge density

and ionic screening concentration are extremely important parameters for obtaining electrostatic effects. This can be the basis of designing novel-membrane structure based on the concept of ‘highly charged’ ‘gate-keepers’ up to a certain length, while allowing high-liquid flow through the rest of the noninteracting cores. From these calculations it became apparent that the electrostatic effects for a thin layer of charge on the CNT tips would not be enough to cause strong overall changes in diffusional flux across the entire membrane structure. Therefore, steric interactions are deemed necessary for the concept of ‘gatekeepers’ to provide meaningful changes in flux or separation through the membrane structure. Though not demonstrated here, the finite-element approach described here is useful in incorporating other boundary conditions like constant potential at the walls of the pore. It can provide a basic framework to study ‘voltage-gated’ transport through conducting membranes. However, in-depth study of the conformation of the ‘gate-keeper’ molecule and its effect on the transport through the membrane would require additional simulation techniques like Molecular Dynamics or Brownian Dynamics.

Chapter 8

Conclusions and Future Work

This Ph.D. dissertation has primarily focused on mass transport through a novel membrane structure composed of vertically oriented and open-ended CNTs with ~ 7 nm core diameter. The major attributes of the CNT-membrane structure are: that the pore size is set by the inner core of the CNT, allowing exceptional control over pore-size distribution; the graphitic non-interacting inner core allows less interaction between transporting molecules, which results in high-transport rates; the possibility of placement of selective chemistry; and electrical conductivity of the membrane due to crossing of the CNTs. The dissertation lays the foundation for understanding and manipulating molecular transport through this unique membrane structure. The following are the major conclusions of the dissertation:

- (i) Extremely fast mass transport exceeding conventional predictions in nano-scale channels by orders of magnitude is demonstrated in Chapter 3. However, progressive functionalization of the tips and cores introduces enhanced interaction between the solvent and pore walls to decrease the exceptional flow velocity. Ionic diffusion through the membrane structure is controlled by ‘gate-keeper’ type molecular interaction and gases are transported ~ 1 order of magnitude faster than Knudsen-Diffusion predictions.
- (ii) Application of facile ‘protein-chemistry’ (carbodiimide chemistry) approaches the CNT membrane structure for covalently attaching functional molecules, changing chain length, hydrophilicity, hydrophobicity, etc. with concomitant changes in selectivity and flux as demonstrated in Chapter 4.
- (iii) The CNT membranes are electronically conducting. Therefore, electrochemical functionalization using diazonium grafting chemistry can increase the density of functional groups. This concept is demonstrated in Chapter 4.
- (iv) Controlled actuation of macro-molecular tethers attached to the membranes with enhanced functional density can provide ‘voltage-gated’ control of transport through CNT membranes as shown in Chapter 6. This actuation

behavior has been further complimented by electrochemical impedance spectroscopy and has been discussed in Chapter 5.

- (v) Electrically-facilitated transport through the CNT membrane is electro-osmotically controlled.

With the extremely high transport rates through the CNT membrane, the applications are myriad. A potentially-interesting application is in ionic separations. Demonstrated in this dissertation is evidence of electrostatic interactions between permeating probe molecules and fixed charges on the membranes. A series-in-resistance model consisting of electrostatically-hindered diffusion at the pore entrance while close to bulk diffusivity inside the core could quantitatively explain the fluxes. Also demonstrated are techniques for increasing the charge density on the CNT walls to increase this electrostatic interaction. However, a caveat is that the functional molecules will cause the solvent to interact strongly with the walls and will greatly reduce the most attractive attribute (i.e. exceptionally high mass transport). Therefore, the best approach would be to have a highly-selective chemistry at the CNT entrance, while leaving the core of the CNT intact. More work is needed to understand how to increase selectivity without affecting the permeability through the CNT cores. As such, the large (~ 7nm core dia) membranes seem to be more suitable for separation of large molecules or macro-molecules. The pore sizes are too large to realize gas-separation applications, though functionlization chemistry could possibly introduce some selectivity.

As discussed earlier, a major attribute of the membrane structure is that it is electronically conducting. Electrochemical functionalization and characterization are potentially attractive tools of investigation. Demonstrated in this dissertation is controlled voltage, induced-conformational change of macro-molecular tethers attached to the CNT membranes for voltage-gated membrane channels. Future research has to be directed towards optimization of the functional density and size of the macro-molecule to increase the efficiency of the device for drug-delivery applications. It appears that the strategy for the device has to be on a case-by-case basis (i.e. different functional molecules for different permeant). Other potential applications would entail utilization of the electrochemical catalytic and fast-transport property of the membrane structure. The CNTs could easily serve as catalyst carriers and the resultant-membrane structure could be

utilized as membrane reactors, where mass transport and heterogenous electrochemical catalysis could be combined for realizing Electrochemical Membrane Reactors. Such devices could be interesting for fuel cell or environmental applications.

The finite-element work discussed in Chapter 7 provides the basic framework for carrying out simulations of transport studies through the CNT membrane. Most of the work has been implemented for constant surface-charge, density-boundary conditions, though some unsuccessful attempts have been made to solve the PB equation with the constant potential-boundary condition. The simulations significantly overestimated the partition coefficient observed in 3.2 nm gold nanotubule membranes.⁷⁶ It is therefore important to incorporate the Stern-layer model into this framework (i.e use modified PB equations). Besides, as stated in the previous chapter, the potential induced conformation change cannot be studied by the finite-element approach and would possibly require coupling to Brownian or molecular-dynamic approaches.

In summary, this dissertation is the first comprehensive experimental study on transport through CNT membranes and is complimented by modeling approaches to quantitatively understand mass-transport properties. It should serve as an important source of information for future researchers in the field of ‘carbon nanotube membranes’.

APPENDICES

A3 Appendix to Chapter 3

A3.1 UV-vis Calibration for Ionic Transport Measurements

Calibration of the UV-vis spectrophotometer was carried out using a fixed concentration (5×10^{-4} M to 1×10^{-3} M) of the analyte in the quartz cuvette. The analyte was diluted progressively with D.I. water and the resulting change in weight was accounted for in a balance. Performing a mass balance on each dilution level, the concentration of the analyte was calculated. It was then plotted against the observed absorbance at the respective wavelengths to obtain the calibration curve. The calibration curve in the region of the experimentally-observed (shown in figures A3.1.1 to A3.1.3) absorbances in the diffusion experiments was used for obtaining the transport rates. The following wavelengths were used for the estimation: 260 nm for MV^{2+} ; 452 nm for $Ru(bipy)_3^{2+}$; 230 nm for NDS^{2-} ; 620 nm for Dye^{2-} ; 456 nm for Rhodamine B.

Estimation of $Ru(bipy)_3^{2+}$ and MV^{2+} from their mixtures posed a slight challenge due to overlapping peaks at 260 nm (MV^{2+}) and 286 nm ($Ru(bipy)_3^{2+}$). Therefore the non-interfering peak at 452 nm was used for estimation of $Ru(bipy)_3^{2+}$. Thereafter, the absorbance at 260 nm due to absorbance at 452 nm ($Ru(bipy)_3^{2+}$ peak) was subtracted from the peak at 260 nm to obtain the corrected MV^{2+} absorbance at 260 nm and was converted to concentrations using the calibration curve. This methodology has been used in Chapters 3 & 4.

However, for the voltage-gating experiments in Chapter 6, a different protocol was followed. In those experiments, often the absorbance at 452 nm was very weak due the slow transport rate of $Ru(bipy)_3^{2+}$, which necessitated the use of the stronger peak at 286 nm. The following protocol was used: MV^{2+} was estimated from the peak at 260 nm. Then the contribution of 260 peak at 286 nm was subtracted to obtain the corrected $Ru(bipy)_3^{2+}$ absorbance at 286 nm, which was used estimate the $Ru(bipy)_3^{2+}$ quantitatively. To test this protocol a solution of MV^{2+} of $\sim 1.96 \times 10^{-5}$ M was taken and small amounts of $Ru(bipy)_3^{2+}$ of concentration $\sim 3.84 \times 10^{-5}$ M was added to it to vary the ratio of MV^{2+} to $Ru(bipy)_3^{2+}$. Shown in figure A3.1.1(c) is the predicted/actual separation factor (ratio of $MV^{2+}/Ru(bipy)_3^{2+}$) to the actual separation factor in these

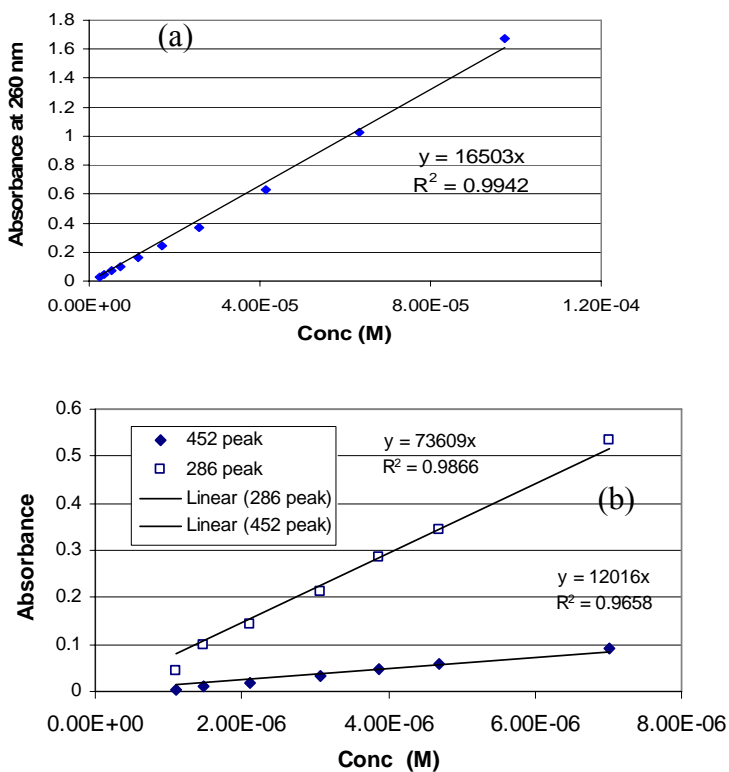


Figure A3.1.1 Calibration curve of (a) MV^{2+} absorbance (at 260 nm); (b) $Ru(bipy)_3^{2+}$ absorbance (at 286 and 452 nm) in the Ocean Optics USB-UVvis.

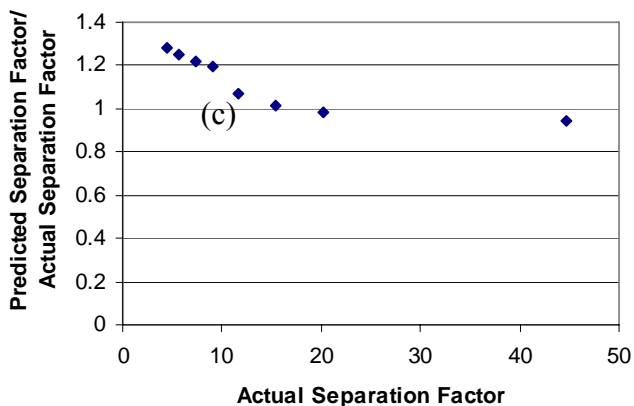


Figure A3.1.1 (c) Predicted/actual separation factor of MV^{2+} to $Ru(bipy)_3^{2+}$, from the protocol used for estimation of $Ru(bipy)_3^{2+}$ and MV^{2+} from the peaks at 286 and 260 nm as in Chapter 6. Note that the protocol successfully predicts the separation factor at higher ratio of MV^{2+} to $Ru(bipy)_3^{2+}$, but overestimates the separation factor at lower values of the separation factor.

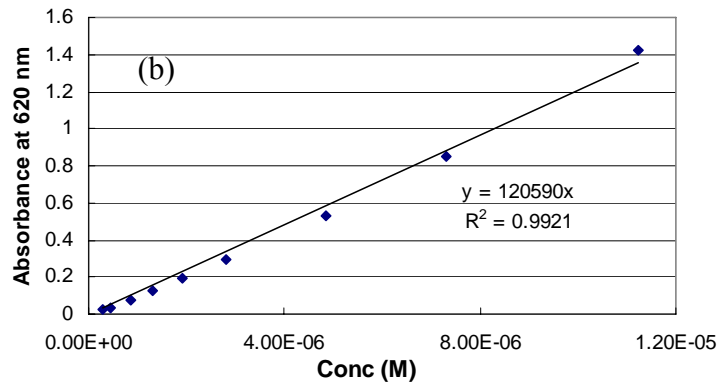
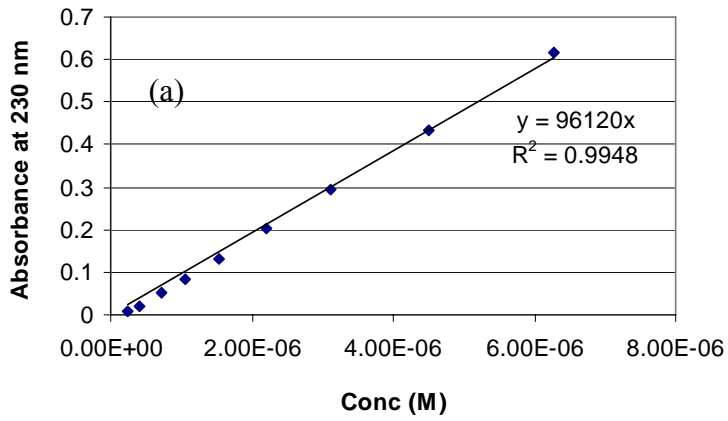


Figure A3.1.2 Calibration curve of (a) NDS⁻² absorbance (at 230 nm) and (b) Dye⁻² absorbance (at 620 nm) in the Ocean Optics USB-UVvis.

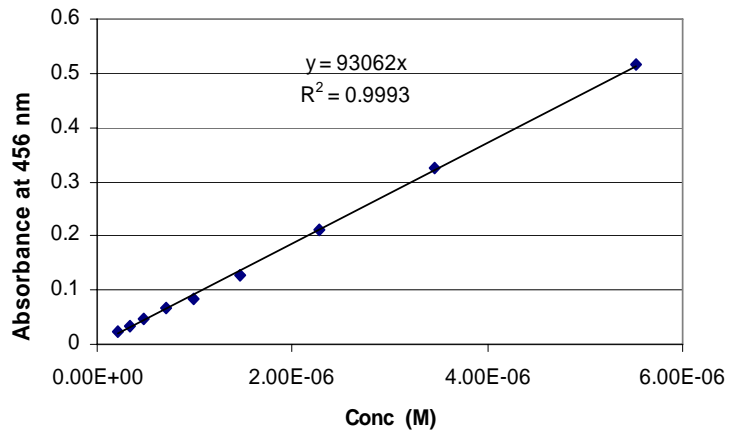


Figure A3.1.3 Calibration curve of Rhodamine B absorbance (at 456 nm) in the Ocean Optics USB-UVvis.

calibration experiments. The protocol predicts the separation factor (predicted/actual ~ 1) very well at high separation factors, (up to ~ 10), but overestimates the separation factor (by 20-25 %) at lower values of the separation factor. Therefore, ideally one should have used different protocols for different ratios. However, it would have rendered the analysis of the experiments very complicated and uncertain. For this reason, the same protocol has been consistently used in analyzing all the experimental observations and should not pose problems to the interpretation or conclusions of the experiments.

A3.2 Liquid-Flow Decline Studies Through the CNT Membrane

In prior experiments, a gas cylinder (containing N_2) was used to pressurize the water through the CNT membrane. An intriguing result was obtained. The flux through the CNT membrane was found to decline by an order of magnitude at a constant pressure of 10 psi shown in figure A3.2.1(a). This was not a typical fouling phenomenon, since the salt diffusion experiments before and after the pressure-flow experiments were not significantly different. Even more surprising was that the flow revived when the pressure was released (by closing the pressure regulator on the gas-cylinder) and restarted after 2 to 3 minutes as indicated in figure A3.2.1(b). In this figure, the arrows indicate the time at which the release and restart operation was conducted. Further experiments were carried out as per the experimental procedure detailed in Sec. 3.2.4 using a syringe pump. To test the flow-measurement apparatus described in Sec.3.2.4, pressure flow studies were also conducted on commercially available membranes, as shown in figure A3.2.2. Of particular concern was to test whether fouling or air bubble formation would slow observed flow rates for porous membranes of similar pore size. This was not observed in either case, indicating that the experimental method eliminates fouling particles and absorbed air. The experimentally-obtained flow data for the different solvents through CNT membrane are shown in figure A3.2.3. Shown in figure A3.2.4 is the experimentally-obtained permeability from the pressure driven flow of liquids through CNT membrane. The experiments using the syringe pumps are different from the experiments using nitrogen gas in that (i) the liquid was vacuum boiled to eliminate traces of dissolved air during experiments with the syringe pump and (ii) the nitrogen-pressurization experiments will inherently allow significant amount of dissolved air in the

liquids. Permeability declines by almost an order of magnitude were also observed in this case, but less pronounced than with the nitrogen-pressurization experiments. Also, the flow could not be revived by turning off and on the syringe pump, as was observed for the nitrogen pressurization experiments. During the syringe pump experiment, the vacuum-pumped solvents were exposed to ambient conditions while loading the solvent into the cell, presumably introducing some absorbed gas. It might be potentially interesting to investigate methods to turn 'on' and 'off' this pressure-driven flow. However, the hexane or decane permeability remained steady during the trials. Experiments with KCl-containing water showed insignificant permeability decline. One might speculate the formation of ordered water inside the CNTs, but the kinetics appear to be too slow for such a phenomena and was not observed in smaller DWCNTs.¹⁰² It appears that an air interface at the hydrophobic surface²³⁹ responsible for the dewetting expands, leading to decreases in the flux of the solvents in particular water. Potassium chloride is known to reduce bubble formation in water. For solvents that favorably wet the nanotube (like hexane or decane) the formation of this interface is reduced considerably, and the flow decline is not observed.

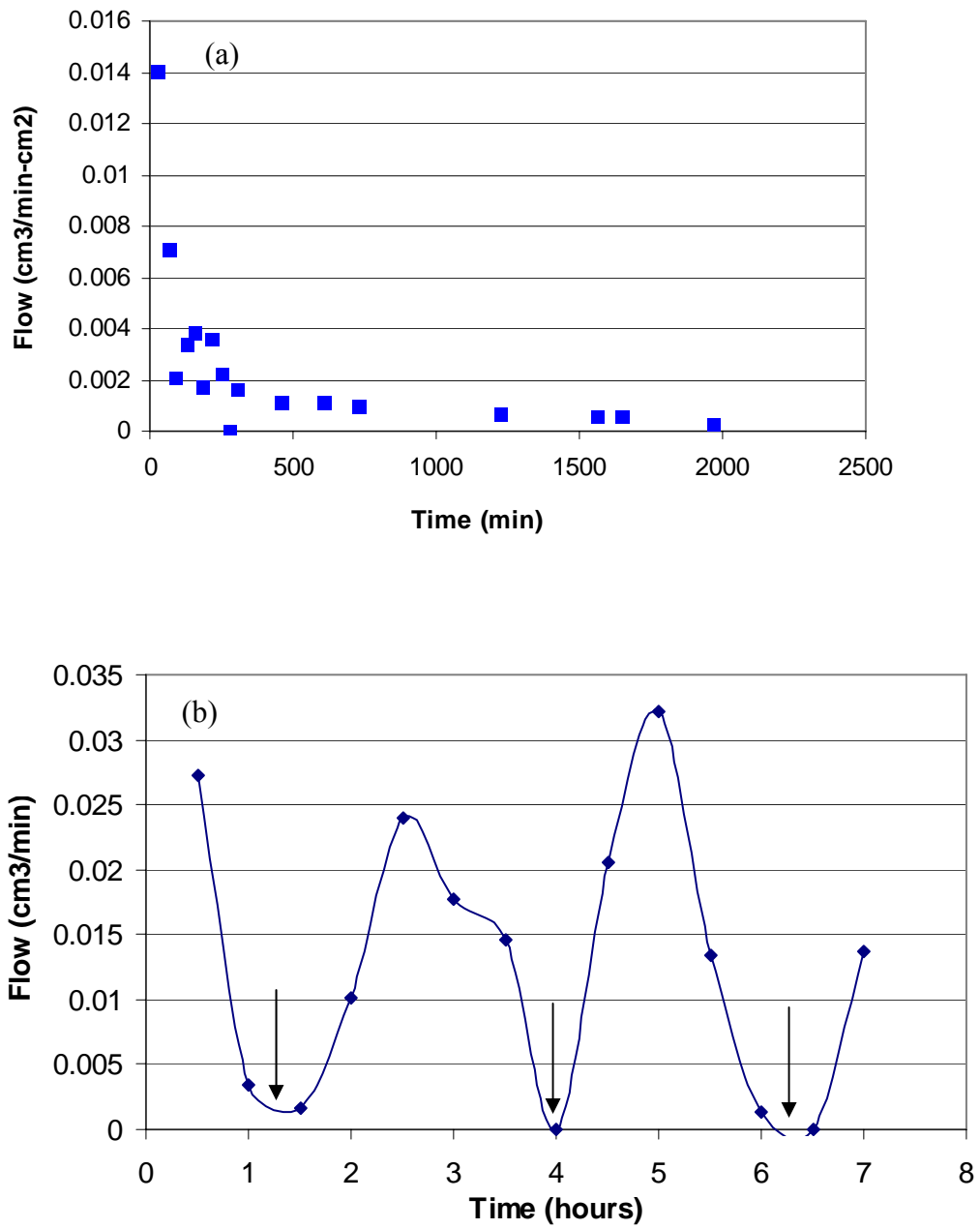


Figure A3.2.1 (a) Flow decline kinetics of water through CNT membrane and (b) flow revival when the flow system was de-pressurized.

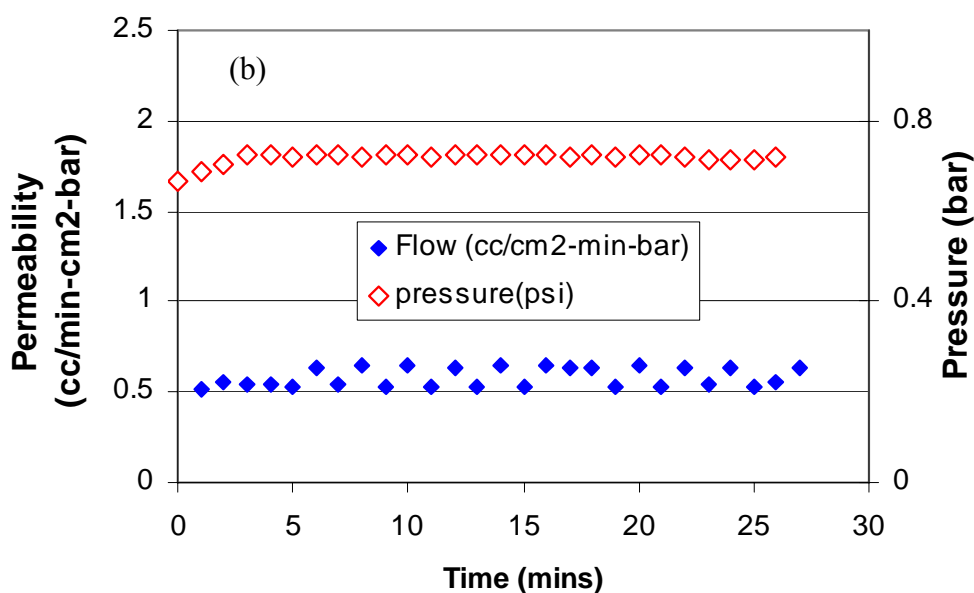
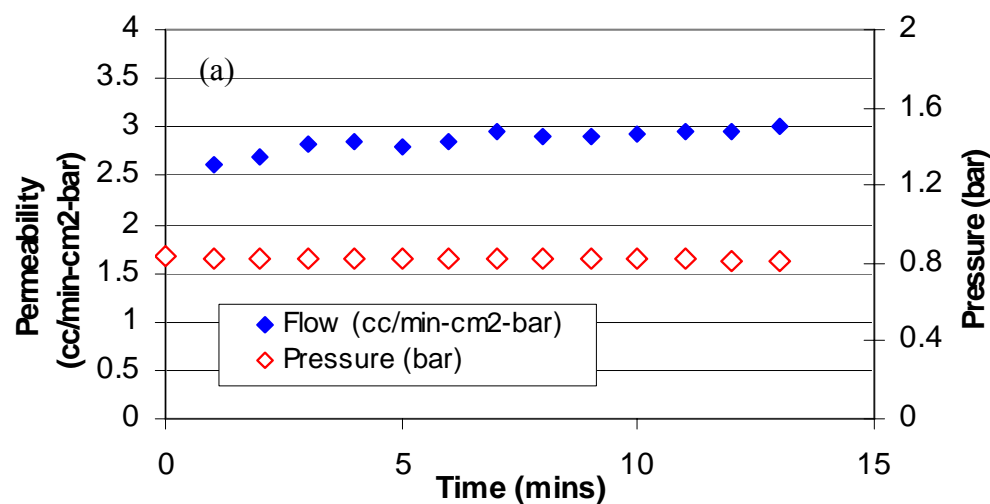


Figure A3.2.2 Water-flow measurements using vacuum-treated DI water in the flow set-up through two commercial membranes (a) Anodised alumina oxide membrane (with 20 nm top pores and 200 nm bottom pores) and (b) PAN membrane (24,000 molecular weight cutoff) showed a constant permeability and stable pressure with time. The water permeabilities are close to the specifications provided by the manufacturers.

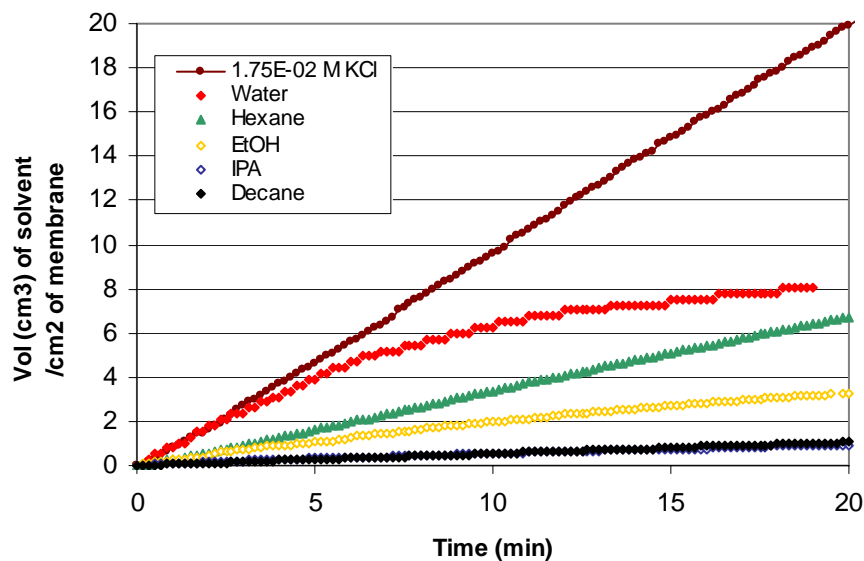
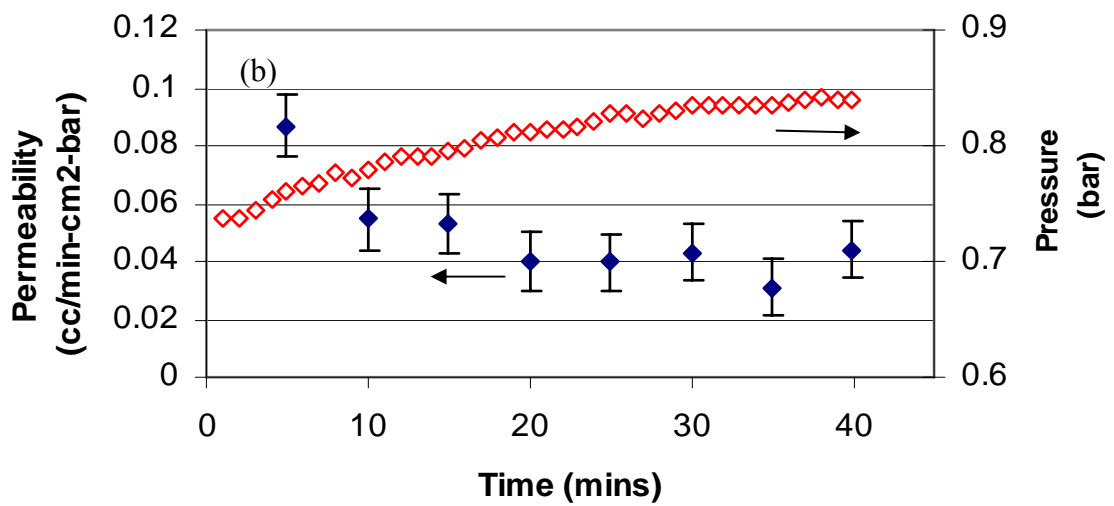
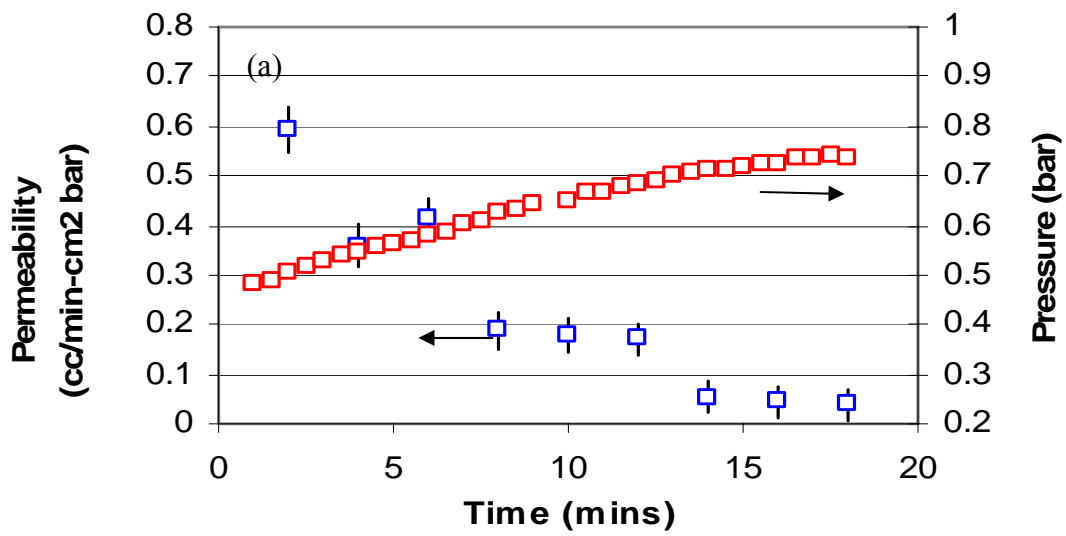


Figure A3.2.3 Cumulative volume of different solvents collected over a balance per unit area (cm^3/cm^2) of the membrane flowing through the CNT membrane as a function of time at (0.7-1bar applied pressure). Water flow data shown here has been normalized by permeable pore density. Reduction in the flow of associated liquids (water and alcohols) with time can be attributed to flow-induced solvent ordering or formation of bubbles. This mechanism is currently under investigation.



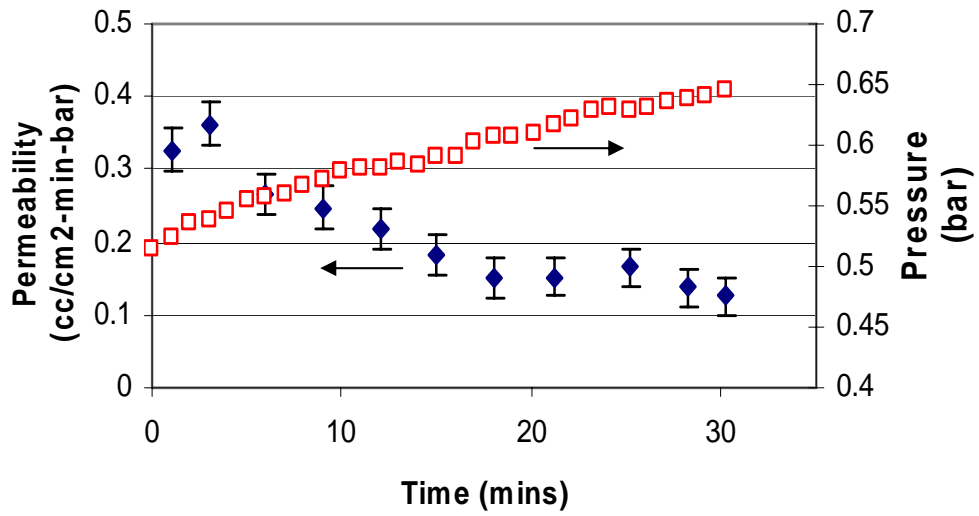


Figure A3.2.4 Permeability decline during measurement of (a) water; (b) iso-propyl alcohol, and (c) ethyl alcohol using the apparatus described in Section 3.2.4?. The error bars represent the error in measurement of the liquid permeability resulting from the weight of each drop of the liquid coming out of the flow cell.

A3.3 Estimation of Permeable Pore Density

The permeable pore density or the porosity is an important parameter in quantifying the transport properties of the CNT membrane. The method is explained in Sec. 2.2.6. Figure A3.3.1 shows a typical experimentally-obtained KCl diffusion flux through CNT membrane.

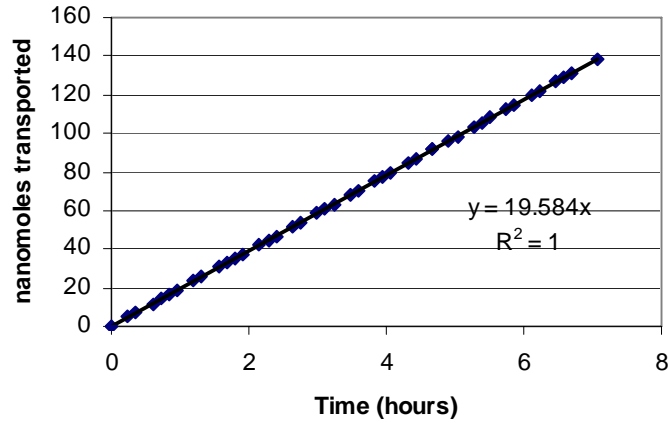
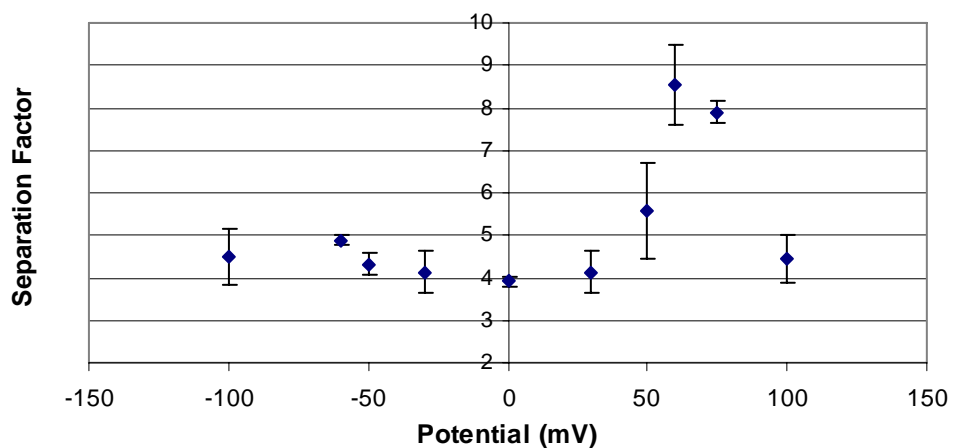


Figure A3.3 1 Representative plot of KCl diffusion, as measured by the conductivity of the permeate solution as a function of time.

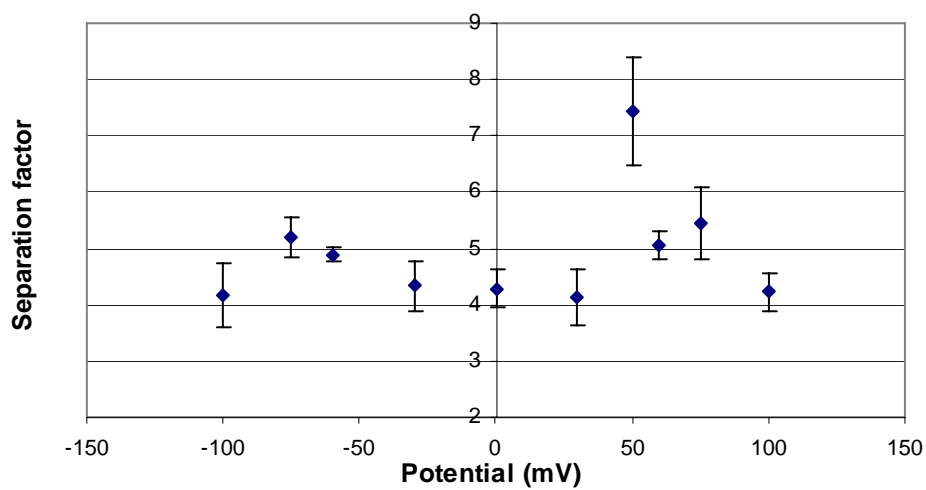
Appendix to Chapter 6

A6.1 Effect of position of the ‘gate-keeper’ chemistry: feed side and permeate side

The flow-grafted CNT membrane had an asymmetry due to confinement of the diazonium-grafting chemistry to the CNT tips. We studied the effect of the ‘gate-keeper’ chemistry either on the feed side or the permeate side of the U-tube diffusion cell. All experiments described in Chapter 6, were with the ‘gate-keeper’ chemistry on the permeate side. In a different set of experiments, the diazonium flow grafting was carried out with slightly higher (~ 20 cm) column of liquid on the feed side (see figure 2.7 (b)). Two series of transport experiments of MV^{+2} and $Ru(bipy)_3^{2+}$ as a function of applied potential to the CNT-FG-spacer-dye (see figure 2.9 for the chemistry) membrane were carried out: (i) with the grafted side facing the permeate (i.e. similar to experiments as described in section 2.15, figure 2.10), and (ii) with the grafted side on the feed side. The membrane rested on a conducting copper-tape attached to a perforated glass slide. In these experiments, the membrane served as the working electrode in the three-electrode assembly and connection to the membrane was made via an electrical connection to the copper tape. It was hypothesized that in the second case, with the chemistry side on the feed side, the actuator molecules would be closer to the copper electrode and contributes to greater actuation. There was no discernible difference between the observed separation factor and fluxes for the two geometries within the errors of the experiment (figure A6.1 and figure A6.2)

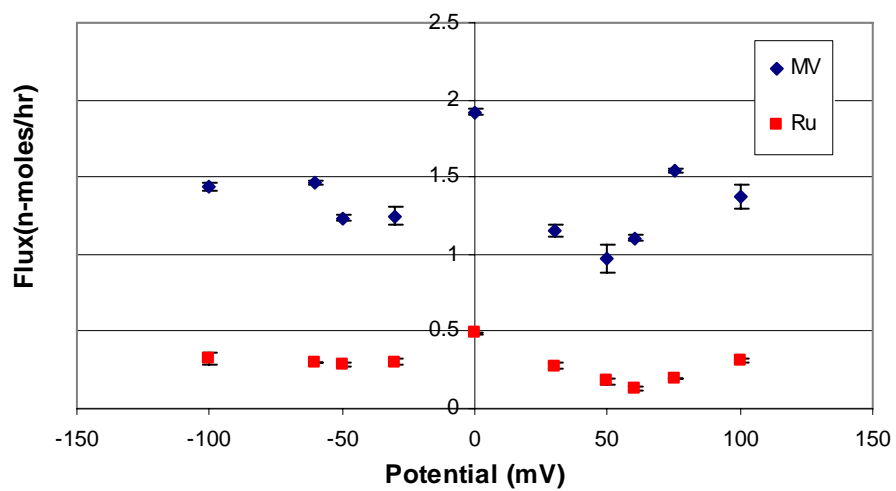


(a)

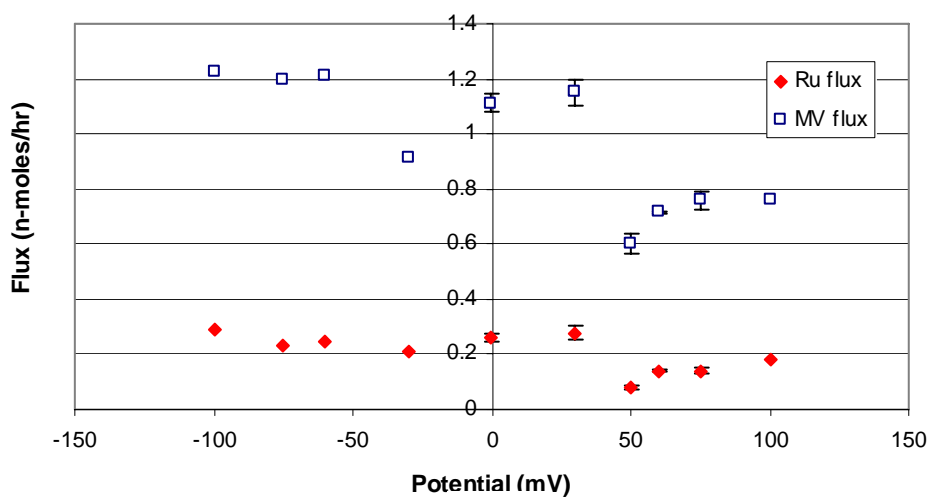


(b)

Figure A6.1 Separation factor between MV^{2+} and $Ru(bipy)_3^{2+}$ as a function of applied potential to the CNT-FG-spacer-dye membrane with (a) Chemistry side on the permeate; (b) Chemistry side on the feed



(a)



(b)

Figure A6.2 Fluxes of the probe molecules through CNT-FG-spacer-dye as a function of applied potential for (a) chemistry side on the permeate; (b) Chemistry side on the feed.

A7 Appendix to Chapter 7

A7.1 Matlab with Femlab program for evaluation of the energy of the sphere and cylinder in the sphere in cylinder system as a function of reduced pore diameter

```
clear fem
% The geometry of the pore with 1 radius and length 10
>> s1=circ2(0,0,1)
>> Cyl1=extrude(s1,'distance',10)
% The colloid at the centre of the cylinder with radius r
>> dq=zeros(1,0);
>> for r=0.05:0.05:0.8;
>> S3 = sphere3(r,'pos',[0 0 5],'axis',[0 0 1],'rot',0);
% The composite object
>> S = Cyl1-S3;
% Plot with numbering of the faces
>> geomplot(S,'facelabels','on');
>> fem.geom = S;
% Using Lagrange Elements
>> fem.shape = shlag(2,'u');
% initialising mesh
>> fem.mesh=meshinit(fem, 'hmax', 1);
% The source term of the Poisson Boltzmann Equation
>> fem.equ.f={'53.04*sinh(u)'};
>> fem.equ.c=-1;
% Constant charge density boundary conditions, face, cylinder, sphere
>> fem.bnd.g={'0' '-2.75' '-5.61'};
% Grouping of the BCs face, cylinder, sphere
>> fem.bnd.ind([3 4])=1;
>> fem.bnd.ind([1 2 9 14])=2;
>> fem.bnd.ind([5 6 7 8 10 11 12 13])=3;
%Solving the problem
>> fem.xmesh=meshextend(fem);
>> fem.sol=femlin(fem);
% Plotting the mesh
>> meshplot(fem);
% Plotting the solution
>> postplot(fem,'slicedata','u');
% Evaluating the surface integral over the sphere
>> Esp = postint(fem,'2.805*u','dl',[5 6 7 8 10 11 12 13],'edim',2);
% Evaluating the surface integral over the cylinder
>> Eps = postint(fem,'1.375*u','dl',[1 2 9 14],'edim',2);
disp([r Esp Eps]);
dq=[dq Esp];
end;
```

A7.2 Matlab with Femlab program for evaluation of the energy of the sphere with zero charge on the cylinder as a function of reduced pore diameter

```

clear fem
%Calculating the energy of the sphere alone
% The geometry of the pore with 1 radius and length 10
>> s1=circ2(0,0,1)
>> Cyl1=extrude(s1,'distance',10)
% The colloid at the centre of the cylinder with radius r
>> dq=zeros(1,0);
>> for r=0.1:0.1:0.8;
>> S3 = sphere3(r,'pos',[0 0 5],'axis',[0 0 1],'rot',0);
% The composite object
>> S = Cyl1-S3;
% Plot with numbering of the faces
>> geomplot(S,'facelabels','on');
>> fem.geom = S;
% Using Lagrange Elements
>> fem.shape = shlag(2,'u');
% initialising mesh
>> fem.mesh=meshinit(fem, 'hmax', 0.25);
% The source term of the Poisson Boltzmann Equation
>> fem.equ.f={'53.04*sinh(u)'};
>> fem.equ.c=-1;
% Constant charge density boundary conditions, face, cylinder, sphere
>> fem.bnd.g={'0' '0' '-5.61'};
% Grouping of the BCs face, cylinder, sphere
>> fem.bnd.ind([3 4])=1;
>> fem.bnd.ind([1 2 9 14])=2;
>> fem.bnd.ind([5 6 7 8 10 11 12 13])=3;
%Solving the problem
>> fem.xmesh=meshextend(fem);
>> fem.sol=femlin(fem);
% Plotting the mesh
>> meshplot(fem);
% Plotting the solution
>> postplot(fem,'slicedata','u');
% Evaluating the surface integral over the sphere
>> Esp = postint(fem,'2.805*u','dl',[5 6 7 8 10 11 12 13],'edim',2);
% Evaluating the surface integral over the cylinder
>> Eps = postint(fem,'0*u','dl',[1 2 9 14],'edim',2);
disp([r Esp Eps]);
dq=[dq Esp];
end;

```

A7.3 Matlab with Femlab program for evaluation of the energy of the cylinder with zero charge on the sphere, as a function of reduced pore diameter

```
clear fem
% Cylinder only
% The geometry of the pore with 1 radius and length 10
>> s1=circ2(0,0,1)
>> Cyl1=extrude(s1,'distance',10)
% The colloid at the centre of the cylinder with radius r
>> dq=zeros(1,0);
>> for r=0.1:0.1:0.8;
>> S3 = sphere3(r,'pos',[0 0 5],'axis',[0 0 1],'rot',0);
% The composite object
>> S = Cyl1-S3;
% Plot with numbering of the faces
>> geomplot(S,'facelabels','on');
>> fem.geom = S;
% Using Lagrange Elements
>> fem.shape = shlag(2,'u');
% initialising mesh
>> fem.mesh=meshinit(fem, 'hmax', 0.25);
% The source term of the Poisson Boltzmann Equation
>> fem.equ.f={'0.53*sinh(u)'};
>> fem.equ.c=-1;
% Constant charge density boundary conditions, face, cylinder, sphere
>> fem.bnd.g={'0' '-2.75' '0'};
% Grouping of the BCs face, cylinder, sphere
>> fem.bnd.ind([3 4])=1;
>> fem.bnd.ind([1 2 9 14])=2;
>> fem.bnd.ind([5 6 7 8 10 11 12 13])=3;
%Solving the problem
>> fem.xmesh=meshextend(fem);
>> fem.sol=femlin(fem);
% Plotting the mesh
>> meshplot(fem);
% Plotting the solution
>> postplot(fem,'slicedata','u');
% Evaluating the surface integral over the sphere
>> Esp = postint(fem,'0*u','dl',[5 6 7 8 10 11 12 13],'edim',2);
% Evaluating the surface integral over the cylinder
>> Eps = postint(fem,'1.375*u','dl',[1 2 9 14],'edim',2);
disp([r Esp Eps]);
dq=[dq Esp];
end;
```

REFERENCES

-
- ¹ Kroto, H. W.; Heath, J. R.; O'Brien, S. C.; Curl, R. F.; Smalley, R. E., C60: Buckminsterfullerene. *Nature* **1985**, 318, (6042), 162-163.
- ² Heath, J. R.; O'Brien, S. C.; Zhang, Q.; Liu, Y.; Curl, R. F.; Tittel, F. K.; Smalley, R. E., Lanthanum complexes of spheroidal carbon shells. *J. Am. Chem. Soc.* **1985**, 107, (25), 7779-7780.
- ³ Shinohara, H., Endohedral metallofullerenes. *Reports on Progress in Physics* **2000**, 63, (6), 843-892.
- ⁴ Kroto, H. W.; McKay, K., The formation of quasi-icosahedral spiral shell carbon particles. *Nature* **1988**, 331, (6154), 328-331.
- ⁵ Ugarte, D., Curling and closure of graphitic networks under electron-beam irradiation. *Nature* **1992**, 359, (6397), 707-709.
- ⁶ Kratschmer, W.; Lamb, L. D.; Fostiropoulos, K.; Huffman, D. R., Solid C60: a new form of carbon. *Nature* **1990**, 347, (6291), 354-358.
- ⁷ Iijima, S., Helical microtubules of graphitic carbon. *Nature* **1991**, 354, (6348), 56-58.
- ⁸ Iijima, S.; Ichihashi, T., Single-shell carbon nanotubes of 1-nm diameter. *Nature* **1993**, 363, (6430), 603-605.
- ⁹ Bethune, D. S.; Klang, C. H.; de Vries, M. S.; Gorman, G.; Savoy, R.; Vazquez, J.; Beyers, R., Cobalt-catalysed growth of carbon nanotubes with single-atomic-layer walls. *Nature* **1993**, 363, (6430), 605-607.
- ¹⁰ Smalley, R. Discovering the fullerene, Nobel Lecture, December 7, 1996. Stockholm, Sweden
- ¹¹ Curl, R. Banquet Dinner, Nobel Lecture, November 10, 1996, Stockholm, Sweden
- ¹² Oberlin, A.; Endo, M.; Koyama, T., Filamentous growth of carbon through benzene decomposition. *Journal of Crystal Growth* **1976**, 32, (3), 335-349.
- ¹³ Monthieux, M.; Kuznetsov, V. L., Who should be given the credit for the discovery of carbon nanotubes? *Carbon* **2006**, 44, (9), 1621-1623.
- ¹⁴ Fischer, J. E.; Dai, H.; Thess, A.; Lee, R.; Hanjani, N. M.; Dehaas, D. L.; Smalley, R. E., Metallic resistivity in crystalline ropes of single-wall carbon nanotubes. *Physical Review B* **1997**, 55, (8), R4921.

-
- ¹⁵ Dai, H.; Wong, E. W.; Lieber, C. M., Probing Electrical Transport in Nanomaterials: Conductivity of Individual Carbon Nanotubes. *Science* **1996**, 272, (5261), 523-526.
- ¹⁶ Frank, S.; Poncharal, P.; Wang, Z. L.; Heer, W. A. de, Carbon Nanotube Quantum Resistors. *Science* **1998**, 280, (5370), 1744-1746.
- ¹⁷ Ajayan, P. M.; Iijima, S., Capillarity-Induced Filling of Carbon Nanotubes. *Nature* **1993**, 361, (6410), 333-334.
- ¹⁸ Ajayan, P. M.; Ebbesen, T. W.; Ichihashi, T.; Iijima, S.; Tanigaki, K.; Hiura, H., Opening Carbon Nanotubes with Oxygen and Implications for Filling. *Nature* **1993**, 362, (6420), 522-525.
- ¹⁹ Ajayan, P. M.; Stephan, O.; Redlich, P.; Colliex, C., Carbon Nanotubes as Removable Templates for Metal-Oxide Nanocomposites and Nanostructures. *Nature* **1995**, 375, (6532), 564-567.
- ²⁰ Dujardin, E.; Ebbesen, T. W.; Hiura, H.; Tanigaki, K., Capillarity and Wetting of Carbon Nanotubes. *Science* **1994**, 265, (5180), 1850-1852.
- ²¹ Dujardin, E.; Ebbesen, T. W.; Krishnan, A.; Treacy, M. M. J., Wetting of single shell carbon nanotubes. *Advanced Materials* **1998**, 10, (17), 1472-1475.
- ²² Skoulidas, A. I.; Ackerman, D. M.; Johnson, J. K.; Sholl, D. S., Rapid transport of gases in carbon nanotubes. *Physical Review Letters* **2002**, 89, (18).
- ²³ Mao, Z.; Sinnott, S. B., A Computational Study of Molecular Diffusion and Dynamic Flow through Carbon Nanotubes. *J. Phys. Chem. B* **2000**, 104, (19), 4618-4624.
- ²⁴ Mao, Z.; Sinnott, S. B., Predictions of a Spiral Diffusion Path for Nonspherical Organic Molecules in Carbon Nanotubes. *Physical Review Letters* **2002**, 89, (27), 278301.
- ²⁵ Sokhan, V. P.; Nicholson, D.; Quirke, N., Fluid flow in nanopores: An examination of hydrodynamic boundary conditions. *Journal of Chemical Physics* **2001**, 115, (8), 3878-3887.
- ²⁶ Sokhan, V. P.; Nicholson, D.; Quirke, N., Fluid flow in nanopores: Accurate boundary conditions for carbon nanotubes. *Journal of Chemical Physics* **2002**, 117, (18), 8531-8539.
- ²⁷ Supple, S.; Quirke, N., Rapid imbibition of fluids in carbon nanotubes. *Physical Review Letters* **2003**, 90, (21).
- ²⁸ Hummer, G.; Rasaiah, J. C.; Noworyta, J. P., Water conduction through the hydrophobic channel of a carbon nanotube. *Nature* **2001**, 414, (6860), 188-190.

-
- ²⁹ Kalra, A.; Garde, S.; Hummer, G., From The Cover: Osmotic water transport through carbon nanotube membranes. *PNAS* **2003**, 100, (18), 10175-10180.
- ³⁰ Zhu, F.; Schulten, K., Water and Proton Conduction through Carbon Nanotubes as Models for Biological Channels. *Biophys. J.* **2003**, 85, (1), 236-244.
- ³¹ Ghosh, S.; Sood, A. K.; Kumar, N., Carbon Nanotube Flow Sensors, *Science* **2003**, 299, (5609), 1042-1044.
- ³² Megaridis, C. M.; Yazicioglu, A. G.; Libera, J. A.; Gogotsi, Y., Attoliter fluid experiments in individual closed-end carbon nanotubes: Liquid film and fluid interface dynamics. *Physics of Fluids* **2002**, 14, (2), L5-L8.
- ³³ Rossi, M. P.; Ye, H. H.; Gogotsi, Y.; Babu, S.; Ndungu, P.; Bradley, J. C., Environmental scanning electron microscopy study of water in carbon nanopipes. *Nano Letters* **2004**, 4, (5), 989-993.
- ³⁴ Naguib, N.; Ye, H.; Gogotsi, Y.; Yazicioglu, A. G.; Megaridis, C. M.; Yoshimura, M., Observation of Water Confined in Nanometer Channels of Closed Carbon Nanotubes. *Nano Lett.* **2004**, 4, (11), 2237-2243.
- ³⁵ Sun, L.; Crooks, R. M., Single Carbon Nanotube Membranes: A Well-Defined Model for Studying Mass Transport through Nanoporous Materials. *J. Am. Chem. Soc.* **2000**, 122, (49), 12340-12345.
- ³⁶ Ito, T.; Sun, L.; Crooks, R. M., Simultaneous Determination of the Size and Surface Charge of Individual Nanoparticles Using a Carbon Nanotube-Based Coulter. *Analytical Chemistry* **2003**, 75, (10), 2399-2406.
- ³⁷ Whitby, M.; Quirke, N., Fluid flow in carbon nanotubes and nanopipes. *Nature Nanotechnology* **2007**, 2, (2), 87-94.
- ³⁸ deHeer, W. A.; Bacsá, W. S.; Chatelain, A.; Gerfin, T.; Humphrey-Baker, R.; Forro, L.; Ugarte, D., Aligned Carbon Nanotube Films: Production and Optical and Electronic Properties. *Science* **1995**, 268, (5212), 845-847.
- ³⁹ Li, W. Z.; Xie, S. S.; Qian, L. X.; Chang, B. H.; Zou, B. S.; Zhou, W. Y.; Zhao, R. A.; Wang, G., Large-Scale Synthesis of Aligned Carbon Nanotubes. *Science* **1996**, 274, (5293), 1701-1703.
- ⁴⁰ Ren, Z. F.; Huang, Z. P.; Xu, J. W.; Wang, J. H.; Bush, P.; Siegal, M. P.; Provencio, P. N., Synthesis of Large Arrays of Well-Aligned Carbon Nanotubes on Glass. *Science* **1998**, 282, (5391), 1105-1107.

-
- ⁴¹ Sen, R., Govindaraj, A. & Rao, C. N. R. Carbon nanotubes by the metallocene route. *Chemical Physics Letters* **267**, 276-280 (1997).
- ⁴² Andrews, R.; Jacques, D.; Rao, A. M.; Derbyshire, F.; Qian, D.; Fan, X.; Dickey, E. C.; Chen, J., Continuous production of aligned carbon nanotubes: a step closer to commercial realization. *Chemical Physics Letters* **1999**, 303, (5-6), 467-474.
- ⁴³ Sinnott, S. B.; Andrews, R.; Qian, D.; Rao, A. M.; Mao, Z.; Dickey, E. C.; Derbyshire, F., Model of carbon nanotube growth through chemical vapor deposition. *Chemical Physics Letters* **1999**, 315, (1-2), 25-30.
- ⁴⁴ Jin, L.; Bower, C.; Zhou, O., Alignment of carbon nanotubes in a polymer matrix by mechanical stretching. *Applied Physics Letters* **1998**, 73, (9), 1197-1199.
- ⁴⁵ Thostenson, E. T.; Chou, T.-W., Aligned multi-walled carbon nanotube-reinforced composites: processing and mechanical characterization. *Journal of Physics D: Applied Physics* **2002**, 35, (16), L77-L80.
- ⁴⁶ Smith, B. W.; Benes, Z.; Luzzi, D. E.; Fischer, J. E.; Walters, D. A.; Casavant, M. J.; Schmidt, J.; Smalley, R. E., Structural anisotropy of magnetically aligned single wall carbon nanotube films. *Applied Physics Letters* **2000**, 77, (5), 663-665.
- ⁴⁷ Casavant, M. J.; Walters, D. A.; Schmidt, J. J.; Smalley, R. E., Neat macroscopic membranes of aligned carbon nanotubes. *Journal of Applied Physics* **2003**, 93, (4), 2153-2156.
- ⁴⁸ Y.W.Chung, *Introduction to Materials Science and Engineering*. 1 ed.; CRC press, Taylor and Francis: 2007; p 200-203.
- ⁴⁹ O'Sullivan, J. P.; Wood, G. C., The Morphology and Mechanism of Formation of Porous Anodic Films on Aluminium. *Proceedings of the Royal Society of London. Series A, Mathematical and Physical Sciences (1934-1990)* **1970**, 317, (1531), 511-543.
- ⁵⁰ Thompson, G. E., Porous anodic alumina: fabrication, characterization and applications. *Thin Solid Films* **1997**, 297, (1-2), 192-201.
- ⁵¹ Yuan, J. H.; He, F. Y.; Sun, D. C.; Xia, X. H., A Simple Method for Preparation of Through-Hole Porous Anodic Alumina Membrane. *Chemistry of Materials* **2004**, 16, (10), 1841-1844.
- ⁵² Kirchner, A.; MacKenzie, K. J. D.; Brown, I. W. M.; Kemmitt, T.; Bowden, M. E., Structural characterisation of heat-treated anodic alumina membranes prepared using a simplified fabrication process. *Journal of Membrane Science* **2007**, 287, (2), 264-270.
- ⁵³ Mulder, M., *Basic Principles of Membrane Technology*. Kluwer Academic Publisher

-
- ⁵⁴ Knaack, S. A.; Redden, M.; Onellion, M., AAO nanopore arrays: A practical entrance to nanostructures. *American Journal of Physics* **2004**, 72, (7), 856-859.
- ⁵⁵ Li, A. P.; Muller, F.; Birner, A.; Nielsch, K.; Gosele, U., Hexagonal pore arrays with a 50--420 nm interpore distance formed by self-organization in anodic alumina. *Journal of Applied Physics* **1998**, 84, (11), 6023-6026.
- ⁵⁶ Masuda, H. F., Kenji, Ordered nano-hole arrays made by a two step replication of honeycomb structure of anodic alumina. *Science* **1995**, 268, (5216), 1466-68.
- ⁵⁷ Choi, J.; Sauer, G.; Nielsch, K.; Wehrspohn, R. B.; Gosele, U., Hexagonally Arranged Monodisperse Silver Nanowires with Adjustable Diameter and High Aspect Ratio. *Chemistry of Materials* **2003**, 15, (3), 776-779.
- ⁵⁸ Martin, C. R., Membrane-based synthesis of nanomaterials. *Chemistry of Materials* **1996**, 8, (8), 1739-1746.
- ⁵⁹ Sano, T.; Iguchi, N.; Iida, K.; Sakamoto, T.; Baba, M.; Kawaura, H., Size-exclusion chromatography using self-organized nanopores in anodic porous alumina. *Applied Physics Letters* **2003**, 83, (21), 4438-4440.
- ⁶⁰ Cho, S.-H.; Walther, N. D.; Nguyen, S. T.; Hupp, J. T., Anodic aluminium oxide catalytic membranes for asymmetric epoxidation. *Chemical Communications* **2005**, (42), 5331-5333.
- ⁶¹ Price, P. B.; Walker, R. M., Observations of Charged-Particle Tracks in Solids. *Journal of Applied Physics* **1962**, 33, (12), 3400-3406.
- ⁶² Price, P. B.; Walker, R. M., Chemical Etching of Charged-Particle Tracks in Solids. *Journal of Applied Physics* **1962**, 33, (12), 3407-3412.
- ⁶³ Beck, R. E., Jerome S., Hindered Diffusion in Microporous Membranes with known geometry. *Science* **1970**, 170, (3964), 1302-05.
- ⁶⁴ Kathawalla, I. A.; Anderson, J. L.; Lindsey, J. S., Hindered diffusion of porphyrins and short-chain polystyrene in small pores. *Macromolecules* **1989**, 22, (3), 1215-1219.
- ⁶⁵ W. M. Deen, M. P. Brenner. N. B. E., Effects of molecular size and configuration on diffusion in microporous membranes. *AIChE. J* **1981**, 27, (6), 952-959.
- ⁶⁶ Bean, C. P.; Doyle, M. V.; Entine, G., Etching of Submicron Pores in Irradiated Mica. *Journal of Applied Physics* **1970**, 41, (4), 1454-1459.

-
- ⁶⁷ Knudstrup, T. G.; Bitsanis, I. A.; Westermann-Clark, G. B., Pressure-Driven Flow Experiments in Molecularly Narrow, Straight Pores of Molecular Dimension in Mica. *Langmuir* **1995**, 11, (3), 893-897.
- ⁶⁸ Quinn, J. A.; Anderson, J. L.; Ho, W. S.; Petzny, W. J., Model Pores of Molecular Dimension: The Preparation and Characterization of Track-Etched Membranes. *Biophysical Journal* **1972**, 12, (8), 990-1007.
- ⁶⁹ V. Kulshrestha, et al., Swift heavy ion irradiated polymeric membranes for gas permeation. *J. Appl. Polymer. Sci.* **2006**, 102, (3), 2386-2390.
- ⁷⁰ Siwy, Z.; Gu, Y.; Spohr, H. A.; Baur, D.; Wolf-Reber, A.; Spohr, R.; Apel, P.; Korchev, Y. E., Rectification and voltage gating of ion currents in a nanofabricated pore. *Europhys. Lett.* **2002**, 60, (3), 349-55.
- ⁷¹ Siwy, Z. , Ion-Current Rectification in Nanopores and Nanotubes with Broken Symmetry. *Advanced Functional Materials* **2006**, 16, (6), 735-746.
- ⁷² Jirage, K. B.; Hulteen, J. C.; Martin, C. R., Nanotubule-Based Molecular-Filtration Membranes. *Science* **1997**, 278, (5338), 655-658.
- ⁷³ Nishizawa, M.; Menon, V. P.; Martin, C. R., Metal Nanotubule Membranes with Electrochemically Switchable Ion-Transport Selectivity. *Science* **1995**, 268, (5211), 700-702.
- ⁷⁴ Hulteen, J. C.; Jirage, K. B.; Martin, C. R., Introducing Chemical Transport Selectivity into Gold Nanotubule Membranes. *J. Am. Chem. Soc.* **1998**, 120, (26), 6603-6604.
- ⁷⁵ Jirage, K. B.; Hulteen, J. C.; Martin, C. R., Effect of Thiol Chemisorption on the Transport Properties of Gold Nanotubule Membranes. *Analytical Chemistry* **1999**, 71, (21), 4913-4918.
- ⁷⁶ Kang, M.-S.; Martin, C. R., Investigations of Potential-Dependent Fluxes of Ionic Permeates in Gold Nanotubule Membranes Prepared via the Template Method. *Langmuir* **2001**, 17, (9), 2753-2759.
- ⁷⁷ Siwy, Z.; Heins, E.; Harrell, C. C.; Kohli, P.; Martin, C. R., Conical-Nanotube Ion-Current Rectifiers: The Role of Surface Charge. *J. Am. Chem. Soc.* **2004**, 126, (35), 10850-10851.
- ⁷⁸ Alsyouri, H. M.; Langheinrich, C.; Lin, Y. S.; Ye, Z.; Zhu, S., Cyclic CVD Modification of Straight Pore Alumina Membranes. *Langmuir* **2003**, 19, (18), 7307-7314.

-
- ⁷⁹ Miller, S. A.; Young, V. Y.; Martin, C. R., Electroosmotic flow in template-prepared carbon nanotube membranes. *Journal of the American Chemical Society* **2001**, 123, (49), 12335-12342.
- ⁸⁰ Hinds, B. J.; Chopra, N.; Rantell, T.; Andrews, R.; Gavalas, V.; Bachas, L. G., Aligned Multiwalled Carbon Nanotube Membranes. *Science* **2004**, 303, (5654), 62-65.
- ⁸¹ Holt, J. K.; Noy, A.; Huser, T.; Eaglesham, D.; Bakajin, O., Fabrication of a Carbon Nanotube-Embedded Silicon Nitride Membrane for Studies of Nanometer-Scale Mass Transport. *Nano Lett.* **2004**, 4, (11), 2245-2250.
- ⁸² Ajayan, P. M.; Tour, J. M., Materials Science: Nanotube composites. *Nature* **2007**, 447, (7148), 1066-1068.
- ⁸³ Milo S. P. Shaffer, A. H. W., Fabrication and Characterization of Carbon Nanotube/Poly(vinyl alcohol) Composites. *Advanced Materials* **1999**, 11, (11), 937-941.
- ⁸⁴ Qian, D.; Dickey, E. C.; Andrews, R.; Rantell, T., Load transfer and deformation mechanisms in carbon nanotube-polystyrene composites. *Applied Physics Letters* **2000**, 76, (20), 2868-2870.
- ⁸⁵ Ajayan, P. M.; Stephan, O.; Colliex, C.; Trauth, D., Aligned Carbon Nanotube Arrays Formed by Cutting a Polymer Resin--Nanotube Composite. *Science* **1994**, 265, (5176), 1212-1214.
- ⁸⁶ Jung, Y. J.; Kar, S.; Talapatra, S.; Soldano, C.; Viswanathan, G.; Li, X. S.; Yao, Z. L.; Ou, F. S.; Avadhanula, A.; Vajtai, R.; Curran, S.; Nalamasu, O.; Ajayan, P. M., Aligned carbon nanotube-polymer hybrid architectures for diverse flexible electronic applications. *Nano Letters* **2006**, 6, (3), 413-418.
- ⁸⁷ Raravikar, N. R.; Schadler, L. S.; Vijayaraghavan, A.; Zhao, Y.; Wei, B.; Ajayan, P. M., Synthesis and Characterization of Thickness-Aligned Carbon Nanotube-Polymer Composite Films. *Chemistry of Materials* **2005**, 17, (5), 974-983.
- ⁸⁸ B. Safadi, R. Andrews. E. A. Grulke., Multiwalled carbon nanotube polymer composites: Synthesis and characterization of thin films. *J. Appl. Polymer Sci.* **2002**, 84, (14), 2660-2669.
- ⁸⁹ Huang, S.; Dai, L., Plasma Etching for Purification and Controlled Opening of Aligned Carbon Nanotubes. *Journal of Physical Chemistry B* **2002**, 106, (14), 3543-3545.
- ⁹⁰ Chiang, I. W.; Brinson, B. E.; Smalley, R. E.; Margrave, J. L.; Hauge, R. H., Purification and Characterization of Single-Wall Carbon Nanotubes. *Journal of Physical Chemistry B* **2001**, 105, (6), 1157-1161.

-
- ⁹¹ Chopra, N. PhD dissertation, University of Kentucky, 2006
- ⁹² Application Note, AC-1, EG&G Princeton Applied Research, Princeton, NJ, 1985
- ⁹³ Liu, Z.; Shen, Z.; Zhu, T.; Hou, S.; Ying, L.; Gu, Z. Organizing Single-Walled Carbon Nanotubes on Gold Using a Wet Chemical Self-Assembling Technique, *Langmuir*, **2000**, 16, 3569-3573
- ⁹⁴ Marwan, J.; Addou, T.; Belanger, D., Functionalization of glassy carbon electrodes with metal-based species. *Chemistry of Materials* **2005**, 17, (9), 2395-2403.
- ⁹⁵ Tesema, Y. S. I., R.J., Bone cell viability on collagen immobilized poly(3-hydroxybutyrate-co-3-hydroxyvalerate) membrane: Effect of surface chemistry. *Journal of Applied Polymer Science* **2004**, 93, (5), 2445-2453.
- ⁹⁶ Furneaux, R. C.; Rigby, W. R.; Davidson, A. P., The formation of controlled-porosity membranes from anodically oxidized aluminium. *Nature* **1989**, 337, (6203), 147-149.
- ⁹⁷ Itaya, K.; Sugawara, S.; Arai, K.; Saito, S., Properties of Porous Anodic Aluminium Oxide Films as Membranes. *J. Chem. Eng. Jpn* **1984**, 17, 514-520.
- ⁹⁸ Quinn, J. A.; Anderson, J. L.; Ho, W. S.; Petzny, W. J., Model Pores of Molecular Dimension: The Preparation and Characterization of Track-Etched Membranes. *Biophysical Journal* **1972**, 12, (8), 990-1007.
- ⁹⁹ Phillip, W. A.; Rzaev, J.; Hillmyer, M. A.; Cussler, E. L., Gas and water liquid transport through nanoporous block copolymer membranes. *Journal of Membrane Science* **2006**, 286, (1-2), 144-152.
- ¹⁰⁰ Koganti, V. R.; Dunphy, D.; Gowrishankar, V.; McGehee, M. D.; Li, X. F.; Wang, J.; Rankin, S. E., Generalized coating route to silica and titania films with orthogonally tilted cylindrical nanopore arrays. *Nano Letters* **2006**, 6, (11), 2567-2570.
- ¹⁰¹ Sholl, D. S.; Johnson, J. K., MATERIALS SCIENCE: Making High-Flux Membranes with Carbon Nanotubes. *Science* **2006**, 312, (5776), 1003-1004.
- ¹⁰² Holt, J. K.; Park, H. G.; Wang, Y.; Stadermann, M.; Artyukhin, A. B.; Grigoropoulos, C. P.; Noy, A.; Bakajin, O., Fast Mass Transport Through Sub-2-Nanometer Carbon Nanotubes. *Science* **2006**, 312, (5776), 1034-1037.
- ¹⁰³ Majumder, M.; Chopra, N.; Andrews, R.; Hinds, B. J., Nanoscale hydrodynamics: Enhanced flow in carbon nanotubes. *Nature* **2005**, 438, (7064), 44.

-
- ¹⁰⁴ Nednoor, P.; Chopra, N.; Gavalas, V.; Bachas, L. G.; Hinds, B. J., Reversible Biochemical Switching of Ionic Transport through Aligned Carbon Nanotube Membranes. *Chem. Mater.* **2005**, 17, (14), 3595-3599.
- ¹⁰⁵ Majumder, M.; Chopra, N.; Hinds, B. J., Effect of Tip Functionalization on Transport through Vertically Oriented Carbon Nanotube Membranes. *J. Am. Chem. Soc.* **2005**, 127, (25), 9062-9070.
- ¹⁰⁶ Majumder, M.; Zhan, X.; Andrews, R.; Hinds, B. J., Voltage Gated Carbon Nanotube Membranes. *Langmuir* **2007**.
- ¹⁰⁷ Bryant, M. A. C., R.M., Determination of Surface pKa Values of Surface-Confined Molecules Derivatized with pH-Sensitive Pendant Groups. *Langmuir* **1993**, 9, 385-387.
- ¹⁰⁸ Gerischer, H.; McIntyre, R.; Scherson, D.; Storck, W., Density of the Electronic States of Graphite: Derivation from Differential Capacitance Measurements. *J. Phys. Chem.* **1987**, 91, 1930-35.
- ¹⁰⁹ Holmes-Farley, S. R.; Reamey, R. H.; McCarthy, T. J.; Deutch, J.; Whitesides, G. M., Acid-Base Behavior of Carboxylic Acid Groups Covalently Attached at the Surface of Polyethylene: The Usefulness of Contact Angle in Following the Ionization of Surface Functionality. *Langmuir* **1985**, 1, 725-40.
- ¹¹⁰ Marshall, M. W.; Popa-Nita, S.; Shapter, J. G., Measurement of functionalised carbon nanotube carboxylic acid groups using a simple chemical process. *Carbon* **2006**, 44, (7), 1137-1141.
- ¹¹¹ Fievet, P.; Szymczyk, A.; Labbez, C.; Aoubiza, B.; Simon, C.; Foissy, A.; Pagetti, J., Determining the Zeta Potential of Porous Membranes Using Electrolyte Conductivity inside Pores. *Journal of Colloid and Interface Science* **2001**, 235, (2), 383-390.
- ¹¹² Lauga, E. B., M.P.; Stone, H.A., *The no-slip boundary condition- A review in The Handbook of experimental fluid dynamics*. Springer: 2005.
- ¹¹³ Smith III, F. G.; Deen, W. M., Electrostatic double-layer interactions for spherical colloids in cylindrical pores. *Journal of Colloid and Interface Science* **1980**, 78, (2), 444-465.
- ¹¹⁴ Douglas B. Burns, A. L. Z., Contributions to electrostatic interactions on protein transport in membrane systems. *AIChE Journal* **2001**, 47, (5), 1101-1114.
- ¹¹⁵ Nghiem, L. D.; Schafer, A. I.; Elimelech, M., Role of electrostatic interactions in the retention of pharmaceutically active contaminants by a loose nanofiltration membrane. *Journal of Membrane Science* **2006**, 286, (1-2), 52-59.

-
- ¹¹⁶ Domingo-Garcia, M.; Lopez-Garzon, F. J.; Perez-Mendoza, M., Effect of Some Oxidation Treatments on the Textural Characteristics and Surface Chemical Nature of an Activated Carbon. *Journal of Colloid and Interface Science* **2000**, 222, (2), 233-240.
- ¹¹⁷ Steinle, E. D.; Mitchell, D. T.; Wirtz, M.; Lee, S. B.; Young, V. Y.; Martin, C. R., Ion Channel Mimetic Micropore and Nanotube Membrane Sensors. *Anal. Chem.* **2002**, 74, (10), 2416-2422.
- ¹¹⁸ Fu, Y.; Ye, F.; Sanders, W. G.; Collinson, M. M.; Higgins, D. A., Single Molecule Spectroscopy Studies of Diffusion in Mesoporous Silica Thin Films. *J. Phys. Chem. B* **2006**, 110, (18), 9164-9170.
- ¹¹⁹ Peter, C.; Hummer, G., Ion Transport through Membrane-Spanning Nanopores Studied by Molecular Dynamics Simulations and Continuum Electrostatics Calculations *Biophys. J.* **2005**, 89, (4), 2222-2234.
- ¹²⁰ Lauga, E.; Brenner, M. P., Dynamic mechanisms for apparent slip on hydrophobic surfaces. *Physical Review E (Statistical, Nonlinear, and Soft Matter Physics)* **2004**, 70, (2), 026311-7.
- ¹²¹ de Gennes, P. G., On Fluid/Wall Slippage. *Langmuir* **2002**, 18, (9), 3413-3414.
- ¹²² Bandurp, J.; Immergut, E.H.; Grulke, E.A., *Polymer Handbook, fourth edition*. John Wiley and Sons, Inc.: New York, 1999; p VII/675-711.
- ¹²³ Mattia, D.; Bau, H. H.; Gogotsi, Y., Wetting of CVD Carbon Films by Polar and Nonpolar Liquids and Implications for Carbon Nanopipes. *Langmuir* **2006**, 22, (4), 1789-1794.
- ¹²⁴ Zhu, Y.; Granick, S., Rate-Dependent Slip of Newtonian Liquid at Smooth Surfaces. *Physical Review Letters* **2001**, 87, (9), 096105.
- ¹²⁵ de Lange, R. S. A.; Keizer, K.; Burggraaf, A. J., Analysis and theory of gas transport in microporous sol-gel derived ceramic membranes. *Journal of Membrane Science* **1995**, 104, (1-2), 81-100.
- ¹²⁶ Cussler, E. L., *Diffusion: Mass Transfer in Fluid Systems*. Second ed.; Cambridge University Press: 2003; p 176-179.
- ¹²⁷ Rao, M. B.; Sircar, S., Nanoporous carbon membranes for separation of gas mixtures by selective surface flow. *Journal of Membrane Science* **1993**, 85, (3), 253-264.
- ¹²⁸ Fuertes, A. B., Adsorption-selective carbon membrane for gas separation. *Journal of Membrane Science* **2000**, 177, (1-2), 9-16.

-
- ¹²⁹ Conversion factor: $1 \text{ cm}^3/\text{cm}^2\text{-min-psi} \sim 1.07 \times 10^{-6} \text{ moles/m}^2\text{-s-Pa}$
- ¹³⁰ Yaws, C. L.; *Matheson Gas Handbook*. 7th ed.; Mc. Graw Hill: NY, 2001.
- ¹³¹ Bittner, E. W.; Smith, M. R.; Bockrath, B. C., Characterization of the surfaces of single-walled carbon nanotubes using alcohols and hydrocarbons: a pulse adsorption technique. *Carbon* **2003**, 41, (6), 1231-1239.
- ¹³² Matranga, C.; Bockrath, B.; Chopra, N.; Hinds, B. J.; Andrews, R., Raman Spectroscopic Investigation of Gas Interactions with an Aligned Multiwalled Carbon Nanotube Membrane. *Langmuir* **2006**, 22, (3), 1235-1240.
- ¹³³ Roy, S.; Raju, R.; Chuang, H. F.; Cruden, B. A.; Meyyappan, M., Modeling gas flow through microchannels and nanopores. *Journal of Applied Physics* **2003**, 93, (8), 4870-4879.
- ¹³⁴ Bhatia, S. K.; Chen, H. B.; Sholl, D. S., Comparisons of diffusive and viscous contributions to transport coefficients of light gases in single-walled carbon nanotubes. *Molecular Simulation* **2005**, 31, (9), 643-649.
- ¹³⁵ Cooper, S. M.; Cruden, B. A.; Meyyappan, M.; Raju, R.; Roy, S., Gas Transport Characteristics through a Carbon Nanotubule. *Nano Lett.* **2004**, 4, (2), 377-381.
- ¹³⁶ Arya, G.; Chang, H.-C.; Maginn, E. J., Knudsen Diffusivity of a Hard Sphere in a Rough Slit Pore. *Physical Review Letters* **2003**, 91, (2), 026102-4.
- ¹³⁷ Arya, G.; Chang, H.-C.; Maginn, E. J., Molecular Simulations of Knudsen Wall-slip: Effect of Wall Morphology. *Molecular Simulation* **2003**, 29, (10/11), 697.
- ¹³⁸ Ackerman, D. M.; Skoulidas, A. I.; Sholl, D. S.; Johnson, J. K., Diffusivities of Ar and Ne in carbon nanotubes. *Molecular Simulation* **2003**, 29, (10-11), 677-684.
- ¹³⁹ Roy, S.; Cooper, S. M.; Meyyappan, M.; Cruden, B. A., Single component gas transport through 10 nm pores: Experimental data and hydrodynamic prediction. *Journal of Membrane Science* **2005**, 253, (1-2), 209-215.
- ¹⁴¹ Davis, M.E. Organizing for better synthesis, *Nature*, **1993**,364, 391
- ¹⁴² Martin, C.R.; Kohli, P.The Emerging Field of Nanotube Biotechnology, *Nature*, **2003**,2, 29-37
- ¹⁴³ Brinker, C.J.; Lu, Y.; Sellinger, A.; Fan, H.Evaporation-Induced Self –Assembly: Nanostructures Made Easy *Advanced Materials*, **1999**, 11, 579-585

-
- ¹⁴⁴ Tolbert, S.H.; Firouzi, A.; Stucky, G.D.; Chemlka, B.D. Magnetic Field Alignment of Ordered Silicate-Surfactant Composites and Mesoporous Silica *Science*, **1997**, 278, 264-267
- ¹⁴⁵ Hulteen, J.C.; Martin, C.R. A general template-based method for the preparation of nanomaterials *J. Mater. Chem.*, **1997**, 7, 1075-1087
- ¹⁴⁶ Cheung, C.L. ; Kurtz, H.P.; Leiber, C.M., Diameter controlled Synthesis of Carbon Nanotube, *J. Phys. Chem. B.*, **2002**, 106, 2429-2433
- ¹⁴⁷ Lee, S. B.; Mitchell, D.T.; Trofin, L.; Nevanen, T.K. ; Soderland, H.; Martin, C.R. Antibody-Based Bio-Nanotube Membranes for Enantiomeric Drug Separations *Science*, **2002**, 296, 2198-2200
- ¹⁴⁸ Randon, J.; Patterson, R. Preliminary studies on the potential for gas separation by mesoporous ceramic oxide membranes surface modified by alkyl phosphonic acids, *J. Memb. Sci.*, **1997**, 134, 219-223
- ¹⁴⁹ Feng, X.; Fryxell, G.E.; Wang, L.-Q; Kim, A.Y.; Liu, J.; Kemner, K.M. Functionalized Monolayers on Ordered Mesoporous Supports, *Science*, **1997** 276, 923-926
- ¹⁵⁰ Jacobson, G.; Zubay, G. Mechanisms of Membrane Transport in Biochemistry, 4th edition, Wm.C. Brown Publishers
- ¹⁵¹ Jiang, Y; Ruta, V.; Chen, J; Lee, A.; Mackinnon, R. The principle of gating charge movement in a voltage dependent K⁺ channel, *Nature*, **2003**, 423, 42-48
- ¹⁵² Joshep, S.; Mashi, R.J.; Jakobsson, E.; Aluru, N. Electrolytic Transport in Modified Carbon Nanotubes, *NanoLetters*, **2003**, 3, 1399-1403
- ¹⁵³ Basiuk, E. V.; Basiuk, V. A.; Banuelos, J.-G.; Saniger-Blesa, J.-M.; Pokrovskiy, V. A.; Gromovoy, T. Y.; Mischanchuk, A. V.; Mischanchuk, B. G., Interaction of Oxidized Single-Walled Carbon Nanotubes with Vaporous Aliphatic Amines. *J. Phys. Chem. B* **2002**, 106, (7), 1588-1597.
- ¹⁵⁴ Pavia, D.L.; Lampman, V.; Kriz, S.G. in *Introduction to Organic Laboratory Techniques-contemporary approach*, Appendix 3, second edition, Saunders College Publishing.
- ¹⁵⁵ Liu, Y.; Gao, L., A study of the electrical properties of carbon nanotube-NiFe₂O₄ composites: Effect of the surface treatment of the carbon nanotubes. *Carbon* **2005**, 43, (1), 47-52.

-
- ¹⁵⁶ Reisdorf, W.C.; Krimm S. Infrared Amide I Band of the Coiled Coil *Biochemistry*, **1996**, 35,1383-1386
- ¹⁵⁷ Bath, B. D.; White, H. S.; Scott, E. R., Electrically Facilitated Molecular Transport. Analysis of the Relative Contributions of Diffusion, Migration, and Electroosmosis to Solute Transport in an Ion-Exchange Membrane. *Anal. Chem.* **2000**, 72, (3), 433-442.
- ¹⁵⁸ Liu, J.; Shin, Y.; Nie, Z.; Chang, J. H.; Wang, L.-Q.; Fryxell, G. E.; Samuels, W. D.; Exarhos, G. J., Molecular Assembly in Ordered Mesoporosity: A New Class of Highly Functional Nanoscale Materials. *J. Phys. Chem. A* **2000**, 104, (36), 8328-8339.
- ¹⁵⁹ Bhanushali, D., Kloos, S., Kurth, C.; Bhattacharyya, D. Performance of solvent-resistant membranes for non-aqueous systems: solvent permeation results and modeling, *J. Memb. Sci.*, **2001**,199, 1-21
- ¹⁶⁰Craig, V.S.J; Ninham, B.W; Pashley, R.M.; The Effect of Electrolytes on Bubble Coalescence in Water, *J. Phys. Chem.* **1993**,97, 10192-10197)
- ¹⁶¹ Maheswari, R.; Dhathathreyan, A. Influence of ammonium nitrate in phase transitions of Langmuir and Langmuir-Blodgett films at air/solution and solid/solution interfaces, *J. Colloid Interf. Sci.*, **2004**,275,270-276
- ¹⁶² Martin, C.R.; Rubunstein, I. ;Bard, A.J. The heterogenous rate constant for the Ru(bpy)₃^{3+/2+} couple at a glassy carbon electrode in aqueous solution, *J. Electroanal. Chem.*, **1983**,151,267-271
- ¹⁶³ Moghaddam, M. J.; Taylor, S.; Gao, M.; Huang, S. M.; Dai, L. M.; McCall, M. J. Highly efficient binding of DNA on the sidewalls and tips of carbon nanotubes using photochemistry *Nano Letters*, **2004**, 4, 89-93
- ¹⁶⁴ Chopra, N., Majumder, M. & Hinds, B. J. Bifunctional carbon nanotubes by sidewall protection. *Advanced Functional Materials* **15**, 858-864 (2005)..
- ¹⁶⁵ Miyoshi, H. Donnan dialysis with ion-exchange membranes. III. Diffusion coefficients using ions of different valence" *Separation Science and Technology* **1999**, 34, 231-241.
- ¹⁶⁶Wei, C.; Srivastava, D., Theory of Transport of Long Polymer Molecules through Carbon Nanotube Channels. *Physical Review Letters* **2003**, 91, (23), 235901-4.
- ¹⁶⁷ Lefebvre, X.; Palmeri, J.; David, P., Nanofiltration Theory: An Analytic Approach for Single Salts. *Journal of Physical Chemistry B* **2004**, 108, (43), 16811-16824.

-
- ¹⁶⁸ Hollman, A. M.; Bhattacharyya, D., Pore assembled multilayers of charged polypeptides in microporous membranes for ion separation. *Langmuir* **2004**, 20, (13), 5418-5424.
- ¹⁶⁹ Xu, T., Ion exchange membranes: State of their development and perspective. *Journal of Membrane Science* **2005**, 263, (1-2), 1-29.
- ¹⁷⁰ Daiguji, H.; Yang, P.; Szeri, A. J.; Majumdar, A., Electrochemomechanical Energy Conversion in Nanofluidic Channels. *Nano Lett.* **2004**, 4, (12), 2315-2321.
- ¹⁷¹ S. Banerjee, T. H.-B., S.S. Wong,, Covalent Surface Chemistry of Single-Walled Carbon Nanotubes. *Advanced Materials* **2005**, 17, (1), 17-29.
- ¹⁷² Tasis, D.; Tagmatarchis, N.; Bianco, A.; Prato, M., Chemistry of Carbon Nanotubes. *Chem. Rev.* **2006**, 106, (3), 1105-1136.
- ¹⁷³ Liu, J.; Rinzler, A. G.; Dai, H.; Hafner, J. H.; Bradley, R. K.; Boul, P. J.; Lu, A.; Iverson, T.; Shelimov, K.; Huffman, C. B.; Rodriguez-Macias, F.; Shon, Y.-S.; Lee, T. R.; Colbert, D. T.; Smalley, R. E., Fullerene Pipes. *Science* **1998**, 280, (5367), 1253-1256.
- ¹⁷⁴ Chen, J.; Hamon, M. A.; Hu, H.; Chen, Y.; Rao, A. M.; Eklund, P. C.; Haddon, R. C., Solution Properties of Single-Walled Carbon Nanotubes. *Science* **1998**, 282, (5386), 95-98.
- ¹⁷⁵ Chen, Q.; Dai, L.; Gao, M.; Huang, S.; Mau, A., Plasma Activation of Carbon Nanotubes for Chemical Modification. *J.Phys. Chem. B* **2001**, 105, (3), 618-622.
- ¹⁷⁶ Mickelson, E. T.; Huffman, C. B.; Rinzler, A. G.; Smalley, R. E.; Hauge, R. H.; Margrave, J. L., Fluorination of single-wall carbon nanotubes. *Chemical Physics Letters* **1998**, 296, (1-2), 188-194.
- ¹⁷⁷ Alison J. Downard, Electrochemically Assisted Covalent Modification of Carbon Electrodes. *Electroanalysis* **2000**, 12, (14), 1085-1096.
- ¹⁷⁸ Deinhammer, R. S.; Ho, M.; Anderegg, J. W.; Porter, M. D., Electrochemical oxidation of amine-containing compounds: a route to the surface modification of glassy carbon electrodes. *Langmuir* **1994**, 10, (4), 1306-1313.
- ¹⁷⁹ Delamar, M.; Hitmi, R.; Pinson, J.; Saveant, J. M., Covalent modification of carbon surfaces by grafting of functionalized aryl radicals produced from electrochemical reduction of diazonium salts. *J. Am. Chem. Soc.* **1992**, 114, (14), 5883-5884.

-
- ¹⁸⁰ Andrieux, C. P.; Gonzalez, F.; Saveant, J. M., Derivatization of Carbon Surfaces by Anodic Oxidation of Arylacetates. Electrochemical Manipulation of the Grafted Films. *J. Am. Chem. Soc.* **1997**, 119, (18), 4292-4300.
- ¹⁸¹ Combellas, C.; Kanoufi, F.; Pinson, J.; Podvorica, F. I., Time-of-Flight Secondary Ion Mass Spectroscopy Characterization of the Covalent Bonding between a Carbon Surface and Aryl Groups. *Langmuir* **2005**, 21, (1), 280-286.
- ¹⁸² Allongue, P.; Delamar, M.; Desbat, B.; Fagebaume, O.; Hitmi, R.; Pinson, J.; Saveant, J.-M., Covalent Modification of Carbon Surfaces by Aryl Radicals Generated from the Electrochemical Reduction of Diazonium Salts. *J. Am. Chem. Soc.* **1997**, 119, (1), 201-207.
- ¹⁸³ Bahr, J. L.; Yang, J.; Kosynkin, D. V.; Bronikowski, M. J.; Smalley, R. E.; Tour, J. M., Functionalization of Carbon Nanotubes by Electrochemical Reduction of Aryl Diazonium Salts: A Bucky Paper Electrode. *J. Am. Chem. Soc.* **2001**, 123, (27), 6536-6542.
- ¹⁸⁴ Lee, C.-S.; Baker, S. E.; Marcus, M. S.; Yang, W.; Eriksson, M. A.; Hamers, R. J., Electrically Addressable Biomolecular Functionalization of Carbon Nanotube and Carbon Nanofiber Electrodes. *Nano Lett.* **2004**, 4, (9), 1713-1716
- ¹⁸⁵ D'Amours, M.; Belanger, D., Stability of Substituted Phenyl Groups Electrochemically Grafted at Carbon Electrode Surface. *J. Phys. Chem. B* **2003**, 107, (20), 4811-4817.
- ¹⁸⁶ Kariuki, J. K.; McDermott, M. T., Formation of Multilayers on Glassy Carbon Electrodes via the Reduction of Diazonium Salts. *Langmuir* 2001, 17, (19), 5947-5951.
- ¹⁸⁷ Wu, K.; Ji, X.; Fei, J.; Hu, S., The fabrication of a carbon nanotube film on a glassy carbon electrode and its application to determining thyroxine. *Nanotechnology* **2004**, 15, (3), 287-291.
- ¹⁸⁸ Tsai, Y. C.; Li, S. C.; Chen, J. M., Cast Thin Film Biosensor Design Based on a Nafion Backbone, a Multiwalled Carbon Nanotube Conduit, and a Glucose Oxidase Function. *Langmuir* **2005**, 21, (8), 3653-3658.
- ¹⁸⁹ Zhang, M.; Gorski, W., Electrochemical Sensing Platform Based on the Carbon Nanotubes/Redox Mediators-Biopolymer System. *J. Am. Chem. Soc.* **2005**, 127, (7), 2058-2059.
- ¹⁹⁰ Monk, P. S., *Fundamentals of Electroanalytical Chemistry*. Wiley: West Sussex, 2001.
- ¹⁹¹ Evgenij Barasoukov, J. R. Mc Donald., *Impedance Spectroscopy: Theory, Experiment and Applications*. John Wiley & Sons, Inc.: Hoboken, New Jersey, 2005.

¹⁹² Zhang, H.; Cao, G. P.; Yang, Y. S., Using a cut & paste method to prepare a carbon nanotube fur electrode. *Nanotechnology* **2007**, 18, (19), 195607.

¹⁹³ Kim, Y.-T.; Ito, Y.; Tadai, K.; Mitani, T.; Kim, U.-S.; Kim, H.-S.; Cho, B.-W., Drastic change of electric double layer capacitance by surface functionalization of carbon nanotubes. *Applied Physics Letters* **2005**, 87, (23), 234106-3.

¹⁹⁴ Barisci, J. N.; Wallace, G. G.; Baughman, R. H., Electrochemical studies of single-wall carbon nanotubes in aqueous solutions. *Journal of Electroanalytical Chemistry* **2000**, 488, (2), 92-98.

¹⁹⁵ Ago, H.; Kugler, T.; Cacialli, F.; Salaneck, W. R.; Shaffer, M. S. P.; Windle, A. H.; Friend, R. H., Work Functions and Surface Functional Groups of Multiwall Carbon Nanotubes. *Journal of Physical Chemistry B* **1999**, 103, (38), 8116-8121.

¹⁹⁶ Wong, S. S.; Joselevich, E.; Woolley, A. T.; Cheung, C. L.; Lieber, C. M., Covalently functionalized nanotubes as nanometre- sized probes in chemistry and biology. *Nature* **1998**, 394, (6688), 52-55.

¹⁹⁷ Abiman, P.; Crossley, A.; Wildgoose, G. G.; Jones, J. H.; Compton, R. G., Investigating the Thermodynamic Causes Behind the Anomalously Large Shifts in pKa Values of Benzoic Acid-Modified Graphite and Glassy Carbon Surfaces. *Langmuir* **2007**.

¹⁹⁹ Hou, C.-H.; Liang, C.; Yiaccoumi, S.; Dai, S.; Tsouris, C., Electrosorption capacitance of nanostructured carbon-based materials. *Journal of Colloid and Interface Science* **2006**, 302, (1), 54-61.

²⁰⁰ Oren, Y.; Tobias, H.; Soffer, A., The electrical double layer of carbon and graphite electrodes: Part I. Dependence on electrolyte type and concentration. *Journal of Electroanalytical Chemistry* **1984**, 162, (1-2), 87-99.

²⁰¹ Charge Density estimated was estimated from the Poisson-Boltzmann equation:

$$\sigma_c = \varepsilon_0 \varepsilon_r K \times \left(\frac{2kT}{e} \right) \times \sinh \left(\frac{e\Delta V}{2kT} \right), \text{ where } K = e \left(\frac{2n^0}{\varepsilon_0 \varepsilon_r kT} \right)^{\frac{1}{2}} \text{ is the reciprocal Debye}$$

length for a 1:1 electrolyte solution with dielectric constant ε_r , n^0 is the number density of monovalent cations, e the electronic charge, ε_0 is the permittivity of vacuum, ΔV is the potential of zero-charge, k is the Boltzmann Constant and T is the temperature.

²⁰² $K = \left[\frac{F^2}{\varepsilon RT} \sum (z_i^2 C_{i0}) \right]^{1/2}$ where $(1/K)$ is the Debye screening length, F is the Faraday constant, ε is the solvent dielectric permittivity, R is the Universal gas constant, T is the temperature, z_i is the charge on the ions and C_i is the concentration.

-
- ²⁰³ Huber, D. L.; Manginell, R. P.; Samara, M. A.; Kim, B.-I.; Bunker, B. C., Programmed Adsorption and Release of Proteins in a Microfluidic Device. *Science* **2003**, 301, (5631), 352-354.
- ²⁰⁴ Mao, Y.; Luo, C.; Deng, W.; Jin, G.; Yu, X.; Zhang, Z.; Ouyang, Q.; Chen, R.; Yu, D., Reversibly switchable DNA nanocompartment on surfaces. *Nucleic Acids Research* **2004**, 32, (19), e144-.
- ²⁰⁵ Blinov, L. M.; Barberi, R.; Palto, S. P.; De Santo, M. P.; Yudin, S. G., Switching of a ferroelectric polymer Langmuir-Blodgett film studied by electrostatic force microscopy. *Journal of Applied Physics* **2001**, 89, (7), 3960-3966.
- ²⁰⁶ Lahann, J.; Mitragotri, S.; Tran, T.-N.; Kaido, H.; Sundaram, J.; Choi, I. S.; Hoffer, S.; Somorjai, G. A.; Langer, R., A Reversibly Switching Surface. *Science* **2003**, 299, (5605), 371-374.
- ²⁰⁷ Rant, U.; Arinaga, K.; Fujita, S.; Yokoyama, N.; Abstreiter, G.; Tornow, M., Dynamic Electrical Switching of DNA Layers on a Metal Surface. *Nano Lett.* **2004**, 4, (12), 2441-2445.
- ²⁰⁸ Joseph, W., Carbon-Nanotube Based Electrochemical Biosensors: A Review. *Electroanalysis* **2005**, 17, (1), 7-14.
- ²⁰⁹ Craig E. Banks; Trevor J. Davies; and, G. G. W.; Compton, R. G., Electrocatalysis at graphite and carbon nanotube modified electrodes: edge-plane sites and tube ends are the reactive sites. *Chem. Commun.*, **2005**, 7, 829-41.
- ²¹⁰ Evgenij Barasoukov, J. R. M., *Impedance Spectroscopy: Theory, Experiment and Applications*. John Wiley & Sons, Inc.: Hoboken, New Jersey, 2005.
- ²¹¹ Monk, P. S., *Fundamentals of Electroanalytical Chemistry*. Wiley: West Sussex, 2001.
- ²¹² Peng, D. K.; Yu, S. T.; Alberts, D. J.; Lahann, J., Switching the Electrochemical Impedance of Low-Density Self-Assembled Monolayers. *Langmuir* **2007**, 23, (1), 297-304.
- ²¹³ Eugenii Katz, I. W., Probing Biomolecular Interactions at Conductive and Semiconductive Surfaces by Impedance Spectroscopy: Routes to Impedimetric Immunosensors, DNA-Sensors, and Enzyme Biosensors. *Electroanalysis* **2003**, 15, (11), 913-947.
- ²¹⁴ Raistrick, I. D., Application of Impedance Spectroscopy to Materials Science. *Ann. Rev. Mater. Sci.* **1986**, 16, 343-70.

-
- ²¹⁵ Min, S.; Sastry, S. K.; Balasubramaniam, V. M., In situ electrical conductivity measurement of select liquid foods under hydrostatic pressure to 800 MPa. *Journal of Food Engineering* **2007**, 82, (4), 489-497.
- ²¹⁶ Yellen, G., The moving parts of voltage-gated ion channels. *Quarterly Reviews of Biophysics* **1998**, 31, 239-96.
- ²¹⁷ Perozo, E.; Marien, D.; Cortes; Cuello, L. G., Structural Rearrangements Underlying K⁺-Channel Activation Gating. *Science* **1999**, 285, (5424), 73-78.
- ²¹⁸ del Camino, D.; Yellen, G., Tight Steric Closure at the Intracellular Activation Gate of a Voltage-Gated K⁺ Channel. *Neuron* **2001**, 32, (4), 649-656.
- ²¹⁹ Hector, R. S.; Gin, M. S., Signal-Triggered Transmembrane Ion Transport through Synthetic Channels. *Supramolecular Chemistry* **2005**, 17, (1/2), 129-134.
- ²²⁰ Hollman, A. M.; Bhattacharyya, D., Pore Assembled Multilayers of Charged Polypeptides in Microporous Membranes for Ion Separation. *Langmuir* **2004**, 20, (13), 5418-5424.
- ²²¹ Rant, U.; Arinaga, K.; Fujita, S.; Yokoyama, N.; Abstreiter, G.; Tornow, M., Dynamic Electrical Switching of DNA Layers on a Metal Surface. *Nano Lett.* **2004**, 4, (12), 2441-2445.
- ²²² Harrell, C. C.; Kohli, P.; Siwy, Z.; Martin, C. R., DNA-Nanotube Artificial Ion Channels. *J. Am. Chem. Soc.* **2004**, 126, (48), 15646-15647.
- ²²³ Wang, G.; Zhang, B.; Wayment, J. R.; Harris, J. M.; White, H. S., Electrostatic-Gated Transport in Chemically Modified Glass Nanopore Electrodes. *J. Am. Chem. Soc.* **2006**, 128, (23), 7679-7686.
- ²²⁴ Matrab, T.; Chancolon, J.; L'hermite, M. M.; Rouzard, J.-N.; Deniau, G.; Boudou, J.-P.; Chehimi, M. M.; Delamar, M., Atom transfer radical polymerization (ATRP) initiated by aryl diazonium salts: a new route for surface modification of multiwalled carbon nanotubes by tethered polymer chains. *Colloids and Surfaces A: Physicochemical and Engineering Aspects* **2006**, 287, (1-3), 217-221.
- ²²⁵ Farhat, T. R. S., J.B., Ion Transport and Equilibria in Polyelectrolyte Multilayers. *Langmuir* **2001**, 17, (4), 1184-1192.
- ²²⁶ Kontturi, K.; Mafe, S.; Manzanares, J. A.; Svarfvar, B. L.; Viinikka, P., Modeling of the Salt and pH Effects on the Permeability of Grafted Porous Membranes. *Macromolecules* **1996**, 29, (17), 5740-5746.

-
- ²²⁷ Bird, B. R.; Stewart, W.E.; Lightfoot, E.N., *Transport Phenomena*. John Wiley & Sons, Inc. : 2002.
- ²²⁸ Smith, I., Frank G.; Deen, W. M., Electrostatic effects on the partitioning of spherical colloids between dilute bulk solution and cylindrical pores. *Journal of Colloid and Interface Science* **1983**, 91, (2), 571-590.
- ²²⁹ Pujar, N. S.; Zydney, A. L., Electrostatic and Electrokinetic Interactions during Protein Transport through Narrow Pore Membranes. *Ind. Eng. Chem. Res.* **1994**, 33, (10), 2473-2482.
- ²³⁰ Warszynski, P.; Adamczyk, Z., Calculations of Double-Layer Electrostatic Interactions for the Sphere/Plane Geometry. *Journal of Colloid and Interface Science* **1997**, 187, (2), 283-295.
- ²³¹ Das, P. K.; Bhattacharjee, S.; Moussa, W., Electrostatic Double Layer Force between Two Spherical Particles in a Straight Cylindrical Capillary: Finite Element Analysis. *Langmuir* **2003**, 19, (10), 4162-4172.
- ²³² Gray, J. J.; Chiang, B.; Bonnacaze, R. T., Colloidal particles: Origin of anomalous multibody interactions. *Nature* **1999**, 402, (6763), 750-750.
- ²³³ Chen, S. B., Electrostatic Interaction and Hindered Diffusion of Ion-Penetrable Spheres in a Slit Pore. *Journal of Colloid and Interface Science* **1998**, 205, (2), 354-364.
- ²³⁴ Myung-Suk Chun, R. J. P., Electrostatic partitioning in slit pores by Gibbs ensemble Monte Carlo simulation. *AIChE Journal* **1997**, 43, (5), 1194-1203.
- ²³⁵ Kenneth H. Huebner, D. L. D., Douglas E. Smith, Ted G. Byron, *The finite element method for engineers*. John Wiley: New York, 2001.
- ²³⁶ Bertonati, C.; Honig, B.; Alexov, E., Poisson-Boltzmann Calculations of Nonspecific Salt Effects on Protein-Protein Binding Free Energies. *Biophysical Journal* **2007**, 92, (6), 1891-1899.
- ²³⁷ Chapot, D.; Bocquet, L.; Trizac, E., Electrostatic potential around charged finite rodlike macromolecules: nonlinear Poisson-Boltzmann theory. *Journal of Colloid and Interface Science* **2005**, 285, (2), 609-618.
- ²³⁷ Cussler, E. L., *Diffusion: Mass Transfer in Fluid Systems*. Second ed.; Cambridge University Press: 2003; p 28
- ²³⁹ Zhang, X. H.; Li, G.; Maeda, N.; Hu, J., Removal of Induced Nanobubbles from Water/Graphite Interfaces by Partial Degassing. *Langmuir* **2006**, 22, (22), 9238-9243.

Vita

Mainak Majumder was born on February 18, 1976, in Calcutta, India. He received a BS (Ceramic Engineering) from the Calcutta University in 1999 with first class honors. He attended the Institute of Technology-Banaras Hindu University for a MS (Ceramic Engineering) with a gold medal in 2001. From 2001 to 2003, he worked as a staff scientist at a National Laboratory of India (Central Glass and Ceramic Research Institute, www.cgcri.res.in). In the fall of 2003, he joined the University of Kentucky to pursue a PhD degree in Materials Engineering with a minor in Chemical Engineering. His research interests are at the interface of Chemical and Materials Engineering, specifically in surface-chemistry, CNT functionalization, electrochemistry, micro-fabrication techniques, sol-gel synthesis, membrane based separation processes and in numerical techniques like finite element analysis. He has received the dissertation year fellowship from the University of Kentucky in 2006 and the North American Membrane Society Annual Travel Award (competitive with young faculty, post-docs and senior graduate students) in 2007. He has published the following papers in peer reviewed journals:

1. **M. Majumder**, K. Keis, J. Cole, X. Zhan, B.J. Hinds, "Electrostatic modulation of transport through CNT membrane by diazonium grafting chemistry" invited article, *Journal of Membrane Science*, **2007** (in revision)
2. **M. Majumder**, X. Zhan, R. Andrews, B.J. Hinds "Voltage Gated Carbon Nanotube Membranes", *Langmuir*, **2007**, 23,16, 8624-31
3. **M. Majumder**, N. Chopra, R. Andrews, B.J. Hinds, "Nanoscale Hydrodynamics: Enhanced Flow in Carbon Nanotubes", *Nature*, **2005**, 438, 3, 44
4. **M. Majumder**, N.Chopra, B.J. Hinds, "Effect of Tip Functionalization on Transport through Vertically Oriented Carbon Nanotube Membranes" *J. Amer. Chem. Soc.*, **2005**,127,9062-70
5. N. Chopra, **M. Majumder**, B.J. Hinds, "Bi-functional Carbon Nanotubes by Sidewall Protection", *Adv. Funct. Mat.*,**2005**,15,858-64
6. **M. Majumder**, S. Mukhopadhyay, O.Parkash, D.Kumar, "Sintering and Crystallization Behavior of Chemically Prepared Cordierite for Application in Electronic Packaging", *Ceram. Inter.*, **2004**, 30, 1067-1070
7. S. Mukhopadhyay, S. Dutta, **M. Majumder**, A. Kundu and S.K. Das, "Synthesis and Characterisation of Alumina Bearing Sol for Application in Refractory Castables", *Industrial Ceramics*, **2000**, 20,2,88-92

The following papers are in preparation:

8. M. Majumder, N. Chopra, B.J. Hinds “Mass Transport Through Carbon Nanotube Membranes in three different regimes: ionic, liquid, and gas”

9. M. Majumder, K. Keis X. Zhan and B.J. Hinds, “Switchable Impedance Spectroscopy of functionalized vertically oriented CNT membrane/electrode”

10. M. Majumder and B.J. Hinds, “Electrically-facilitated Transport in Carbon Nanotube Membranes”

11. M. Majumder et al. “Finite Element Analysis of Electro-static Partitioning by Solving Non-linear Poisson-Boltzmann Equation in 3D ”